

# **Mapping and Predicting the Earth's Ionosphere Using the Global Positioning System**

Inauguraldissertation  
der Philosophisch-naturwissenschaftlichen Fakultät  
der Universität Bern

vorgelegt von

**Stefan Schaer**

von Trubschachen BE

Leiter der Arbeit: Prof. Dr. G. Beutler, PD Dr. M. Rothacher  
Astronomisches Institut der Universität Bern



# Mapping and Predicting the Earth's Ionosphere Using the Global Positioning System

Inauguraldissertation  
der Philosophisch-naturwissenschaftlichen Fakultät  
der Universität Bern

vorgelegt von

**Stefan Schaer**

von Trubschachen BE

Leiter der Arbeit: Prof. Dr. G. Beutler, PD Dr. M. Rothacher  
Astronomisches Institut der Universität Bern

Von der Philosophisch-naturwissenschaftlichen Fakultät angenommen.

Der Dekan:

Bern, den 25. März 1999

Prof. Dr. A. Pfiffner



# Contents

<b>List of Figures</b>	<b>v</b>
<b>List of Tables</b>	<b>xi</b>
<b>Frequently Used Acronyms</b>	<b>xiii</b>
<b>1. Introduction and Motivation</b>	<b>1</b>
<b>I The GPS as a Tool for Ionospheric Mapping—Theory</b>	<b>7</b>
<b>2. Basics of the GPS Data Analysis</b>	<b>9</b>
2.1 The Global Positioning System—Current Status . . . . .	9
2.2 GPS Institutions Relevant to this Work . . . . .	14
2.2.1 The International GPS Service (IGS) . . . . .	14
2.2.2 The Center for Orbit Determination in Europe . . . . .	16
2.2.3 The IGS Ionosphere Working Group . . . . .	17
2.3 Modeling the GPS Observables . . . . .	18
2.3.1 Fundamental Observation Equations . . . . .	19
2.3.2 Forming Differences . . . . .	22
2.3.3 Linear Combinations and Their Characteristics . . . . .	25
2.3.4 Ambiguity Resolution . . . . .	30
2.4 Least-Squares Adjustment Recapitulated . . . . .	34
<b>3. Extracting Ionospheric Information from GPS Data</b>	<b>41</b>
3.1 The Earth’s Ionosphere . . . . .	41
3.1.1 Ionization Processes and Vertical Profile . . . . .	41
3.1.2 Solar Activity . . . . .	47
3.1.3 Integrated Electron Density . . . . .	48
3.2 Wave Propagation Delays due to the Ionosphere . . . . .	50
3.2.1 Effect on Linear Combinations . . . . .	52
3.2.2 Effect on Single-Frequency Baseline Solutions . . . . .	53

3.3	Single-Layer Model and Mapping Function . . . . .	54
3.3.1	GPS Satellite Visibility and Probed Ionospheric Centroid . . . . .	56
3.3.2	Ionospheric Mapping Functions . . . . .	57
3.4	Observation Equations for Absolute TEC Determination . . . . .	64
3.5	Total Electron Content Parameterization Methods . . . . .	65
3.5.1	Local TEC Representation . . . . .	65
3.5.2	Global TEC Representation . . . . .	66
3.5.3	Other Global TEC Parameterization Methods . . . . .	67
3.6	Variance-Covariance Study Concerning Different Ionospheric GPS Observables . . . . .	70
<b>II</b>	<b>GPS-Derived Ionospheric Information—Results</b>	<b>73</b>
<b>4.</b>	<b>Time Series of CODE Ionosphere Products</b>	<b>75</b>
4.1	IGS Data Processing at CODE—An Overview . . . . .	75
4.1.1	Rapid IGS Data Processing . . . . .	75
4.1.2	Final IGS Data Processing . . . . .	77
4.1.3	European IGS Data Processing . . . . .	80
4.2	CODE Ionosphere Products . . . . .	81
4.2.1	TEC Parameterization and Estimation . . . . .	82
4.2.2	Examples of CODE TEC Maps . . . . .	83
4.2.3	Data Formats . . . . .	85
4.2.4	IGS IONEX Files . . . . .	87
4.2.5	The Ionosphere Map Exchange (IONEX) Format . . . . .	88
4.2.6	Automatically Updated WWW Site Showing CODE GIMs . . . . .	90
4.2.7	History of the CODE Ionospheric Solutions . . . . .	90
4.3	Selected Global TEC Parameters . . . . .	93
4.3.1	Mean TEC of the Earth’s Ionosphere . . . . .	94
4.3.2	Deriving Mean TEC From Global IONEX Data . . . . .	97
4.3.3	Mean TEC of the Northern and Southern Hemisphere . . . . .	97
4.3.4	Maximum TEC . . . . .	98
4.3.5	Higher-Degree SH Coefficients . . . . .	101
4.4	TEC as a Function of Geographic Coordinates and Time . . . . .	104
4.4.1	Daily TEC Profiles . . . . .	105
4.4.2	Monthly Averaged TEC Profiles and Day-to-Day Variability . . . . .	106
4.5	Estimating a Global Single-Layer Height . . . . .	108
4.6	IGS Receiver Performance in the Equatorial Region . . . . .	109
4.7	Differential Code Biases . . . . .	111
4.7.1	DCBs of the GPS Spacecrafts . . . . .	112
4.7.2	DCBs of the IGS Receivers . . . . .	119
4.7.3	DCBs of the GLONASS Spacecrafts . . . . .	120
4.8	Use of Satellite DCB Information . . . . .	121

<b>5. Predicting Global TEC Parameters and Maps</b>	<b>123</b>
5.1 Mathematical Principle . . . . .	123
5.2 TEC Trend Function . . . . .	126
5.3 Resulting Autocovariance Functions . . . . .	128
5.4 TEC Prediction Procedure . . . . .	129
5.5 Examples . . . . .	131
5.5.1 Long-Term Prediction . . . . .	131
5.5.2 Short-Term Prediction . . . . .	131
5.6 Predicting DCBs for GPS Spacecrafts . . . . .	137
<b>6. Validating the CODE Ionospheric Parameters and Maps</b>	<b>139</b>
6.1 An Introductory Example . . . . .	139
6.1.1 Deterministic Component of the TEC . . . . .	139
6.1.2 Stochastic Component of the TEC . . . . .	141
6.1.3 Formal Accuracy of the Double-Difference TEC Determination . . . . .	145
6.2 Comparing and Correlating CODE With IGS Global TEC Parameters and Maps . . . . .	147
6.2.1 Mean Total Electron Content . . . . .	147
6.2.2 Total Electron Content Above Europe . . . . .	151
6.3 Comparing CODE With JPL Global TEC Maps . . . . .	153
6.4 Correlation of TEC With Solar Parameters . . . . .	159
6.5 Comparing and Combining IGS Satellite DCB Results . . . . .	163
<b>7. Summary, Conclusions, and Outlook</b>	<b>165</b>
<b>Acknowledgements</b>	<b>171</b>
<b>III Appendices</b>	<b>173</b>
<b>A. Time Series of CODE Total Electron Content Parameters</b>	<b>175</b>
A.1 Global TEC Parameters . . . . .	175
A.2 Monthly Averaged European TEC Profiles . . . . .	175
<b>B. Time Series of CODE Differential Code Biases</b>	<b>183</b>
B.1 Differential Code Biases of the GPS Spacecrafts . . . . .	183
B.2 Differential Code Biases of Some IGS Stations Processed by CODE . . . . .	183
<b>Bibliography</b>	<b>197</b>





# List of Figures

2.1	Block-I, Block-II, and Block-IIR GPS spacecrafts. . . . .	10
2.2	GPS satellite orbits viewed from a latitude $\beta$ . . . . .	10
2.3	Sub-satellite trajectories of all GPS satellites for June 1, 1998. . . . .	11
2.4	Approximate GPS satellite constellation on June 1, 1998 at 00:00 UT. . . . .	12
2.5	Globally distributed IGS tracking stations processed by CODE. . . . .	17
2.6	Four one-way observations needed to form a double difference. . . . .	23
3.1	Chapman ion production rate for solar zenith angles $\chi$ of $0^\circ$ , and $5^\circ$ to $85^\circ$ in steps of $5^\circ$ . . . . .	44
3.2	Vertical electron density distribution of a Chapman layer for solar zenith angles $\chi$ of $0^\circ$ , and $5^\circ$ to $85^\circ$ in steps of $5^\circ$ . . . . .	45
3.3	Monthly smoothed sunspot number [ <i>SIDC</i> , 1998]. . . . .	48
3.4	Vertical TEC $E_v$ of a Chapman layer as a function of the solar time, in units of $E_v(\chi = 0)$ . . . . .	49
3.5	Single-layer model for the ionosphere. . . . .	55
3.6	GPS satellite visibility as a function of the geographic latitude $\beta$ . . . . .	58
3.7	GPS-probed part of the ionospheric centroid as a function of the geographic latitude $\beta$ . . . . .	59
3.8	Ionospheric mapping functions compared. . . . .	61
3.9	Deviations of ionospheric mapping functions with respect to the single-layer model mapping function at $H = 350$ km. . . . .	62
3.10	Deviation of the modified SLM mapping function with respect to the reference Chapman profile mapping function. . . . .	64
3.11	Two methods for parameterizing time-dependent parameters. . . . .	68
4.1	Flow chart of the rapid IGS data processing at CODE. . . . .	76
4.2	Flow chart of the final IGS data processing at CODE. . . . .	78
4.3	Number of IGS stations daily processed by CODE, from January 1996 to July 1998. . . . .	79
4.4	Globally distributed IGS stations processed by CODE and GPS-probed ionospheric regions. . . . .	80
4.5	24-hour European TEC map for November 14, 1998. . . . .	83

4.6	2-hourly global TEC snapshots for January 17, 1998, taken at 01:00, 03:00, 05:00, ..., 23:00 UT. . . . .	85
4.7	Global TEC on January 17, 1998 at 13:00 UT. . . . .	86
4.8	2-hourly global RMS snapshots for January 17, 1998, taken at 01:00, 03:00, 05:00, ..., 23:00 UT. . . . .	87
4.9	BGS ionosphere (ION) file <code>g1_98152.ion</code> . . . . .	88
4.10	BGS DCB file <code>z1n98152.dcb</code> . . . . .	89
4.11	Header section of the IGS IONEX file <code>codg1520.98i</code> . . . . .	90
4.12	Data section of the IGS IONEX file <code>codg1520.98i</code> . . . . .	91
4.13	Bivariate interpolation using the four nearest TEC grid values $E_{i,j}$ . . . . .	92
4.14	Mean vertical TEC of the Earth's ionosphere computed by CODE, from January 1995 to November 1998. . . . .	94
4.15	Amplitude spectrum of the mean TEC. . . . .	95
4.16	Amplitude spectrum of the mean TEC, for periods below 40 days. . . . .	96
4.17	Mean TEC of both hemispheres, from January 1995 to November 1998. . . . .	98
4.18	Amplitude spectrum of the mean TEC of both hemispheres. . . . .	99
4.19	Maximum vertical TEC, from January 1995 to November 1998. . . . .	100
4.20	Amplitude spectrum of the maximum TEC. . . . .	100
4.21	Amplitude spectrum of the maximum TEC, for periods below 40 days. . . . .	101
4.22	Normalized cosine coefficient $\tilde{C}_{1,0}$ . . . . .	101
4.23	Amplitude spectrum of the sectorial SH coefficients $\tilde{C}_{1,1}$ and $\tilde{S}_{1,1}$ , for periods below 40 days. . . . .	103
4.24	Amplitude spectrum of the sectorial SH coefficients $\tilde{C}_{2,2}$ and $\tilde{S}_{2,2}$ , for periods below 40 days. . . . .	104
4.25	Daily TEC profiles evaluated at $(\beta, \lambda) = (50^\circ, 7.5^\circ)$ , for June 1998. . . . .	105
4.26	Daily TEC profiles evaluated at $(\beta, \lambda) = (50^\circ, 7.5^\circ)$ as a function of local time, for June 1998. . . . .	106
4.27	Monthly averaged TEC profile and day-to-day TEC variability evaluated at $(\beta, \lambda) = (50^\circ, 7.5^\circ)$ , for June 1998. . . . .	107
4.28	Monthly averaged TEC profile and day-to-day TEC repeatability evaluated at $(\beta, \lambda) = (50^\circ, 7.5^\circ)$ , for June 1998. . . . .	108
4.29	Daily estimated global single-layer heights based on G1H solutions, from January 1995 to March 1998. . . . .	109
4.30	Average number of GPS satellites successfully tracked by receivers in the IGS network as a function of local time and geographic latitude, for September 1998. . . . .	110
4.31	Average number of GPS satellites successfully tracked by "equatorial" receivers in the IGS network with geographic latitudes between $-20^\circ$ and $+20^\circ$ , for September 1998. . . . .	111
4.32	Daily DCB estimates (dots) of the GPS spacecrafts and combined values (circles) based on Z1N solutions, from June 1998 to November 1998. . . . .	113

4.33	Daily DCB residuals of the GPS spacecrafts with respect to combined values based on Z1N solutions, from June 1998 to November 1998. . . . .	114
4.34	DCB of PRN 23. . . . .	114
4.35	DCB of PRN 8. . . . .	114
4.36	Obliquity factor for the Z-axis satellite antenna offset. . . . .	117
4.37	Obliquity factor for the X/Y-axis satellite antenna offset. . . . .	118
4.38	DCB of the station ALG0 (Algonquin, Canada). . . . .	119
5.1	Components of the least-squares collocation: noise $n$ , signal $s$ , predicted signal $s'$ , and trend function. . . . .	124
5.2	Mean TEC $\tilde{C}_{0,0}$ and related 7-parameter trend function $\Psi(t)$ , from January 1995 to November 1998. . . . .	127
5.3	Autocovariance function of the SH coefficient $\tilde{C}_{0,0}$ . . . . .	128
5.4	Autocovariance function of the SH coefficient $\tilde{C}_{1,0}$ . . . . .	128
5.5	Autocovariance function of the SH coefficient $\tilde{C}_{2,0}$ . . . . .	129
5.6	Long-term as well as short-term prediction of the mean TEC, based on (a) 35, (b) 41, and (c) 47 months of global TEC observations. . . . .	132
5.7	Mean TEC $\tilde{C}_{0,0}$ and trend function $\Psi(t)$ , fitted to 4 years of global TEC observations and extrapolated for the next 7 years. . . . .	133
5.8	Least-squares interpolated and 2-day extrapolated SH coefficient $\tilde{C}_{0,0}$ based on Z1 and G1 solutions, for June 1998. . . . .	134
5.9	Least-squares interpolated and 2-day extrapolated SH coefficient $\tilde{C}_{1,0}$ based on Z1 and G1 solutions, for June 1998. . . . .	135
5.10	1-day and 2-day predicted TEC profiles at $(\beta, \lambda) = (50^\circ, 7.5^\circ)$ derived from Z1 or G1 solutions of June 1998. . . . .	136
6.1	Baseline-specific TEC map (before and after ambiguity resolution) derived from the baseline Kootwijk-Wetzell, for January 25, 1994. . . . .	140
6.2	Double-differenced L1 ionospheric corrections as reflected by the Kootwijk-Wetzell TEC map, for January 25, 1994. . . . .	141
6.3	Double-differenced L1 ionospheric path delays and double-differenced TEC on the baseline Kootwijk-Wetzell, for January 25, 1994. . . . .	143
6.4	Medium-scale traveling ionospheric disturbances (MSTIDs) on the baseline Kootwijk-Wetzell, for January 25, 1994 (08:00 to 12:00 UT). . . . .	144
6.5	Ionosphere-induced errors related to the L1/L2 ambiguities of the baseline Kootwijk-Wetzell, for January 25, 1994. . . . .	145
6.6	Mean TEC $\bar{E}$ computed by the IGS ionosphere ACs, from August 28, 1998 to January 31, 1999. . . . .	148
6.7	2-hourly mean TEC $\bar{E}$ (aligned values) computed by the IGS ionosphere ACs, from September 22 to October 1, 1998. . . . .	149
6.8	Global maps of the standard deviation between COD(Z1) and JPL GIMs referring to 01:00, 03:00, 05:00, ..., 23:00 UT each, from August 28, 1998 to January 31, 1999. . . . .	154

6.9	Global map of the standard deviation between COD(Z1) and JPL GIMs referring to 13:00 UT each, from August 28, 1998 to January 31, 1999. . .	155
6.10	Day-to-day TEC variability at $(\beta, \lambda) = (50^\circ, 7.5^\circ)$ derived from Z1 or G1 solutions of June 1998. . . . .	156
6.11	Global maps of the difference between COD(Z1) and JPL GIMs referring to 01:00, 03:00, 05:00, ..., 23:00 UT each, from August 28, 1998 to January 31, 1999. . . . .	157
6.12	Global map of the difference between COD(Z1) and JPL GIMs referring to 13:00 UT each, from August 28, 1998 to January 31, 1999. . . . .	158
6.13	Solar flux and sunspot number, from January 1995 to November 1998 [NGDC, 1998]. . . . .	160
6.14	Reduced mean TEC $\bar{E}'$ (without semi-annual component) determined by CODE, from January 1995 to November 1998. . . . .	161
6.15	Correlation coefficients of reduced mean TEC $\bar{E}'$ with respect to solar flux $\phi_{\text{obs}}$ and sunspot number $R$ , for lags between $-10$ and $+10$ days. . .	161
6.16	Solar flux $\phi_{\text{obs}}$ and sunspot number $R$ versus reduced mean TEC $\bar{E}'$ , from January 1995 to November 1998. . . . .	162
6.17	WRMS errors obtained from daily satellite DCB combinations, from June 1, 1998 to January 31, 1999. . . . .	163
7.1	Mean vertical TEC of the Earth's ionosphere computed by CODE, from January 1995 to February 1999. . . . .	166
A.1	SH coefficient $\tilde{C}_{0,0}$ (or mean TEC $\bar{E}$ ). . . . .	175
A.2	SH coefficient $\tilde{C}_{1,0}$ . . . . .	176
A.3	SH coefficient $\tilde{C}_{1,1}$ . . . . .	176
A.4	SH coefficient $\tilde{S}_{1,1}$ . . . . .	176
A.5	SH coefficient $\tilde{C}_{2,0}$ . . . . .	177
A.6	SH coefficient $\tilde{C}_{2,1}$ . . . . .	177
A.7	SH coefficient $\tilde{S}_{2,1}$ . . . . .	177
A.8	SH coefficient $\tilde{C}_{2,2}$ . . . . .	178
A.9	SH coefficient $\tilde{S}_{2,2}$ . . . . .	178
A.10	Monthly averaged European TEC profile, for December 1997. . . . .	178
A.11	Monthly averaged European TEC profile, for January 1998. . . . .	179
A.12	Monthly averaged European TEC profile, for February 1998. . . . .	179
A.13	Monthly averaged European TEC profile, for March 1998. . . . .	179
A.14	Monthly averaged European TEC profile, for April 1998. . . . .	180
A.15	Monthly averaged European TEC profile, for May 1998. . . . .	180
A.16	Monthly averaged European TEC profile, for June 1998. . . . .	180
A.17	Monthly averaged European TEC profile, for July 1998. . . . .	181
A.18	Monthly averaged European TEC profile, for August 1998. . . . .	181
A.19	Monthly averaged European TEC profile, for September 1998. . . . .	181
A.20	Monthly averaged European TEC profile, for October 1998. . . . .	182

A.21 Monthly averaged European TEC profile, for November 1998. . . . .	182
B.1 DCB of PRN 1. . . . .	183
B.2 DCB of PRN 2. . . . .	184
B.3 DCB of PRN 3. . . . .	184
B.4 DCB of PRN 4. . . . .	184
B.5 DCB of PRN 5. . . . .	185
B.6 DCB of PRN 6. . . . .	185
B.7 DCB of PRN 7. . . . .	185
B.8 DCB of PRN 8. . . . .	186
B.9 DCB of PRN 9. . . . .	186
B.10 DCB of PRN 10. . . . .	186
B.11 DCB of PRN 13. . . . .	187
B.12 DCB of PRN 14. . . . .	187
B.13 DCB of PRN 15. . . . .	187
B.14 DCB of PRN 16. . . . .	188
B.15 DCB of PRN 17. . . . .	188
B.16 DCB of PRN 18. . . . .	188
B.17 DCB of PRN 19. . . . .	189
B.18 DCB of PRN 21. . . . .	189
B.19 DCB of PRN 22. . . . .	189
B.20 DCB of PRN 23. . . . .	190
B.21 DCB of PRN 24. . . . .	190
B.22 DCB of PRN 25. . . . .	190
B.23 DCB of PRN 26. . . . .	191
B.24 DCB of PRN 27. . . . .	191
B.25 DCB of PRN 29. . . . .	191
B.26 DCB of PRN 30. . . . .	192
B.27 DCB of PRN 31. . . . .	192
B.28 DCB of the station ALGO (Algonquin, Canada). . . . .	192
B.29 DCB of the station CHAT (Chatham Island, New Zealand). . . . .	193
B.30 DCB of the station DRAO (Dominion Radio Astrophysical Observatory, Penticton, Canada). . . . .	193
B.31 DCB of the station GODE (Goddard Geophysical and Astronomical Obser- vatory, Greenbelt, USA). . . . .	193
B.32 DCB of the station JOZE (Jozefoslaw, Poland). . . . .	194
B.33 DCB of the station KOSG (Kootwijk Observatory for Satellite Geodesy, The Netherlands). . . . .	194
B.34 DCB of the station NLIB (North Liberty, USA). . . . .	194
B.35 DCB of the station USNO (U. S. Naval Observatory, USA). . . . .	195
B.36 DCB of the station WSRT (Westerbork Synthesis Radio Telescope, The Netherlands). . . . .	195
B.37 DCB of the station WTZR (Wettzell, Germany). . . . .	195



# List of Tables

2.1	Active GPS spacecrafts as of mid 1998. . . . .	12
2.2	Linear combinations $\kappa_1 L_1 + \kappa_2 L_2$ and their error characteristics. . . . .	28
3.1	Ionospheric path delay caused by 1 TECU of free electrons. . . . .	53
3.2	Ionosphere-induced scale bias of single-frequency GPS network solutions when neglecting the ionosphere. . . . .	54
3.3	Semi-diameter of the ionospheric cap probed by a single GPS station. . . . .	56
3.4	Altitudes $H_{\text{opt}}$ for the SLM mapping function best fitting the reference Chapman profile mapping function. . . . .	62
3.5	Altitudes $H_{\text{opt}}$ and factors $\alpha_{\text{opt}}$ for the modified SLM mapping function best fitting the reference Chapman profile mapping function. . . . .	63
3.6	Comparison of the smallest formal uncertainties of the vertical TEC $E_v(\beta, s)$ , the satellite DCBs $\Delta b^k$ , the receiver DCB $\Delta b_i$ , and the ambiguity biases $B_{i,4}^k$ . . . . .	71
4.1	CODE ionospheric solutions, the maximum degree $n_{\text{max}}$ and order $m_{\text{max}}$ of the SH expansion, the period $\Delta t$ of validity, the total number $u$ of TEC and DCB parameters estimated each day, and TEC parameter constraints $\sigma_{E,\text{abs}}$ and $\sigma_{E,\text{rel}}$ . . . . .	82
4.2	Combined DCB values of the GPS spacecrafts and RMS errors of the daily Z1N estimation, from June 1998 to November 1998. . . . .	115
6.1	AC-specific offsets of the mean TEC $\bar{E}$ , from August 28, 1998 to January 31, 1999. . . . .	147
6.2	Correlation coefficients between the mean TEC values $\bar{E}$ of the COD(G1), COD(Z1), EMR, ESA, JPL, and UPC GIMs, from August 28, 1998 to January 31, 1999. . . . .	150
6.3	Standard deviations in TECU between the mean TEC values $\bar{E}$ of the COD(G1), COD(Z1), EMR, ESA, JPL, and UPC GIMs, from August 28, 1998 to January 31, 1999. . . . .	151
6.4	Adjusted standard deviations giving the accuracy of the mean TEC determination performed by the various IGS ionosphere ACs, from August 28, 1998 to January 31, 1999. . . . .	151

6.5	Standard deviations in TECU between TEC grid values extracted in the vicinity of $(\beta, \lambda) = (+50^\circ, +7.5^\circ)$ from different TEC products, from August 28, 1998 to January 31, 1999. . . . .	152
6.6	Adjusted standard deviations giving the accuracy of different TEC products for locations in Western Europe, from August 28, 1998 to January 31, 1999. . . . .	153
6.7	Correlation coefficients between mean TEC $\bar{E}$ , maximum TEC $E_{\max}$ , observed solar flux $\phi_{\text{obs}}$ , adjusted solar flux $\phi_{\text{adj}}$ , and sunspot number $R$ . Note that a dash indicates the removal of a semi-annual component. . . .	162
6.8	Mean RMS and WRMS errors obtained from daily satellite DCB combinations, from August 28, 1998 to January 31, 1999. . . . .	164



# Frequently Used Acronyms

AC	Analysis center
ACC	Analysis center coordinator
ACF	Autocovariance function (or autocorrelation function)
AIUB	Astronomical Institute of the University of Berne, Switzerland
AS	Anti-spoofing
BGS	Bernese GPS Software
BKG	Federal Agency of Cartography and Geodesy, Frankfurt, Germany
BPE	Bernese Processing Engine
bps	Bit(s) per second
C/A-code	Coarse/acquisition code (1.023 MHz)
CB	Central bureau
CBIS	Central bureau information system
CDDIS	Crustal Dynamics Data Information System, GSFC, NASA, USA
CODE	Center for Orbit Determination in Europe, AIUB, Berne, Switzerland
CPU	Central processing unit
CSTG	Commission on International Coordination of Space Techniques for Geodesy and Geodynamics
DCB	Differential code bias
DGPS	Differential GPS
DLR	Deutsches Zentrum für Luft- und Raumfahrt, Neustrelitz, Germany
DOF	Degree of freedom
DOMES	Directory of MERIT Sites
DOY	Day of year
EMR	Energy, Mines and Resources, Ottawa, Canada
ERP	Earth rotation parameter
ESA	European Space Agency, Darmstadt, Germany
ESOC	European Space Operations Centre, ESA, Darmstadt, Germany
EUREF	European Reference Frame
FARA	Fast Ambiguity Resolution Approach
FTP	File Transfer Protocol
GFZ	GeoForschungsZentrum, Potsdam, Germany
GIM	Global ionosphere map
GLONASS	GLOBAL Navigation Satellite System

GNSS	Global Navigation Satellite System
GPS	Global Positioning System
GPSEST	Main parameter estimation program of the BGS
GSFC	Goddard Space Flight Center, NASA, USA
IAG	International Association of Geodesy
IERS	International Earth Rotation Service
IGEX	International GLONASS EXperiment
IGN	Institut Géographique National, Paris, France
IGRF	International Geomagnetic Reference Frame
IGS	International GPS Service
ION	Institute of Navigation
IONANA	Ionosphere analysis program of the BGS
IONEX	IONosphere Map EXchange Format
IRI	International Reference Ionosphere
ITRF	IERS Terrestrial Reference Frame
ITRS	IERS Terrestrial Reference System
JPL	Jet Propulsion Laboratory, Pasadena, California, USA
L+T	Federal Office of Topography, Wabern, Switzerland
L1	L1 carrier (1575.42 MHz)
L2	L2 carrier (1227.60 MHz)
LAMBDA	Least-squares AMBiguity Decorrelation Adjustment
LC	Linear combination
LEO	Low-earth orbiter
LOD	Length of day
LRA	Laser reflector array
LSTID	Large-scale traveling ionospheric disturbance
LT	Local time
MERIT	Monitoring Earth Rotation and Intercomparison of Techniques
MF	Mapping function
MSTID	Medium-scale traveling ionospheric disturbance
NASA	National Aeronautics and Space Administration, USA
NAVSTAR	NAVigation Satellite Timing and Ranging
NGDC	National Geophysical Data Center, Boulder, Colorado, USA
NGS	National Geodetic Survey, Silver Spring, Maryland, USA
NOAA	National Oceanic and Atmospheric Administration, Silver Spring, Maryland, USA
NRCan	National Resources Canada, Ottawa, Canada
O–C	Observed-minus-computed
P-code	Precision code (10.23 MHz)
ppb	Part(s) per billion— $10^{-9}$
ppm	Part(s) per million— $10^{-6}$
PRN	Pseudo-random noise

QIF	Quasi-ionosphere-free (ambiguity resolution strategy)
RINEX	Receiver-INdependent EXchange Format
RMS	Root-mean-square (error)
RRE	Residual range error
SA	Selective availability
SH	Spherical harmonic
SIDC	Sunspot Index Data Center, Brussels, Belgium
SINEX	Solution-INdependent EXchange Format
SIO	Scripps Institution of Oceanography, San Diego, California, USA
SIP	Stochastic ionosphere parameter
SLM	Single-layer model
SLR	Satellite laser ranging
SSTID	Small-scale traveling ionospheric disturbance
SVN	Space vehicle number
TEC	Total electron content
TECU	Total electron content unit(s)— $10^{16} \text{ m}^{-2}$
TID	Traveling ionospheric disturbance
UNB	University of New Brunswick, Fredericton, Canada
UPC	Polytechnical University of Catalonia, Barcelona, Spain
UT	Universal time
VTEC	Vertical total electron content
WRMS	Weighted root-mean-square (error)
WWW	World Wide Web
Y-code	Encrypted P-code



# 1. Introduction and Motivation

The propagation of electromagnetic waves through the various atmospheric shells is a complex matter and is still the subject of much research. Whereas precise positioning with the Global Positioning System (GPS) requires careful consideration of the impact of the propagation media, the GPS used for “atmospheric” purposes, in turn, has become a unique tool for studying the Earth’s atmosphere, the troposphere (or neutral atmosphere) and, in particular, the *ionosphere*, which is the subject of this Ph.D. thesis.

The ionosphere covers the region between approximately 50 and 1500 kilometers above the Earth’s surface and is characterized by the presence of a significant number of free electrons and positively charged atoms and molecules called ions. For microwaves, the ionosphere is a dispersive medium, implying that the impact on the GPS signals—travelling from the GPS satellite through the ionosphere to the GPS receiver located on or near the Earth’s surface—is a function of the carrier frequency and the electron density along the signal path. Each GPS satellite transmits information for positioning purposes on two carriers: L1 and L2, centered at 1.57542 and 1.22760 GHz. Under most extreme ionospheric conditions, the ionospheric path delay at L1 may reach up to about 100 meters for low elevation angles. The basic GPS observables are the so-called pseudo-range (or code) and the carrier phase. Both may be viewed as biased measurements of the slant range between a GPS receiver and a GPS satellite. Due to the dispersive nature of the ionosphere, the ionospheric effect can be almost completely eliminated by forming the so-called ionosphere-free linear combination (LC) of simultaneous L1 and L2 measurements, provided that we have dual-frequency GPS receivers. On the other hand, by analyzing the so-called geometry-free LC, the difference between the L1 and L2 observable expressed in units of length, allows to extract information about the electron density from dual-frequency GPS data. However, it is not possible to directly derive ionospheric information, at least on an “absolute” level, without taking into account differential code biases and initial carrier phase ambiguities, respectively. This thesis introduces in a first, theoretical part state-of-the-art methods suited to map the Earth’s ionosphere using the GPS.

For a long time ionospheric refraction is considered as an important error source in the GPS error budget. In the time period when mainly single-frequency (L1) receivers were available, it was important to get insight into the biases introduced in a GPS network

solution by unmodeled ionospheric refraction [Beutler *et al.*, 1987, 1990]. Later on it became obvious that short-periodic variations in ionospheric refraction could harm GPS data analyses even if dual-frequency receivers were available [Beutler *et al.*, 1989]. In the latter paper, there were also clues that valuable information about the ionosphere could be extracted from dual-frequency GPS data.

Modeling and monitoring the ionosphere was the main topic of the Ph.D. thesis by Wild [1994]. In this thesis, it could be shown that local ionosphere models like those presented by Georgiadou and Kleusberg [1988] are very efficient to remove or greatly reduce the ionosphere-induced scale bias of GPS baseline solutions based on single-frequency receivers operating in the vicinity of one or more dual-frequency receivers, the data of which is used to establish a local ionosphere model. U. Wild computed such ionosphere models for a number of sites of the International GPS Service (IGS) network over an extended time span. He also describes a procedure to assess the stochastic behavior of the ionosphere in the vicinity of a GPS tracking station. He concluded that valuable information concerning the ionosphere could be extracted from the IGS network.

Let us very briefly review the ionospheric modeling technique used by Wild [1994]. The so-called single-layer (or thin-shell) model where one assumes that all free electrons are concentrated in a shell of infinitesimal thickness is used as a basis. The altitude of this idealized layer is usually set to 350, 400, or 450 kilometers above a spherical Earth, which approximately corresponds to the altitude of maximum electron density. The vertically integrated electron density, generally called vertical total electron content (VTEC or simply TEC), is then represented by a two-dimensional Taylor series expansion referring to a sun-fixed (or local-time) frame since the ionospheric density is relatively stationary in that frame.

Since 21 June 1992, the beginning of the IGS test campaign, the IGS produces and makes available uninterrupted time series of GPS observations from its world-wide GPS tracking network, highly accurate GPS ephemerides, earth rotation parameters (ERPs), satellite and receiver clock information, station coordinates and velocities, and other parameters of geophysical interest [Beutler *et al.*, 1994, 1995b, 1998b]. CODE (Center for Orbit Determination in Europe) is one of the seven IGS analysis centers (ACs) currently contributing with its products to the IGS service. It is a joint venture of four European institutions [Rothacher *et al.*, 1994]. The CODE AC is located at the AIUB in Berne, Switzerland.

For geodetic applications of the GPS system, interferometric data processing techniques are explicitly or implicitly used. CODE processes doubly differenced carrier phase measurements from currently more than 100 globally distributed IGS sites to generate its IGS core products. Consequently, cycle-slip-free L1 and L2 carrier phase measurements are readily available for every day. In [Schaer *et al.*, 1995] we could show that by analyzing the geometry-free LC of our double-difference IGS data—instead of the normally used ionosphere-free LC—and by setting up ionospheric parameters, it is possible to extract absolute TEC information even when applying an interferometric data processing

---

scheme. To do so, we had to replace the Taylor series expansion, used to locally represent TEC, by a spherical harmonic (SH) expansion which is better suited for global ionosphere maps (GIMs). In this context, we may mention that a pre-analysis for an ionospheric mapping technique using double differences was already performed by *Schaer* [1994] and *Mervart* [1995].

After implementing the GIM parameterization into the Bernese GPS Software [*Rothacher and Mervart*, 1996] at the end of 1996, CODE routinely generated daily GIMs and regional maps for Europe [*Schaer et al.*, 1996a, 1996c; *Rothacher et al.*, 1996]. These ionospheric maps are used in the CODE processing scheme to improve the quasi-ionosphere-free (QIF) resolution of the initial carrier phase ambiguities. Moreover, all 1995 IGS data was re-processed to obtain GIMs using the Bernese Processing Engine (BPE), a front-end of the Bernese GPS Software which allows to efficiently process GPS data in a fully automatic mode [*Rothacher and Mervart*, 1996]. The time series of daily global and regional ionosphere parameters covering a time span of more than 3.5 and 2.5 years during low ionospheric activity are presented and discussed in the second part of this thesis.

It is well known that the ionospheric activity is driven largely by the solar activity and therefore follows the sunspot cycle with the principal period of about 11 years. The most recent ionospheric minimum was observed in summer of 1996. The next solar maximum is expected for the years 2000–2001. Access to fast and up-to-date ionospheric information is required for many applications.

In order to coordinate the ionosphere activities within the IGS, an IGS ionosphere working group was established in May 1998. It is the declared goal of this working group, to continuously monitor the ionosphere for at least the next period of high solar activity and to study the impact of the ionosphere on the IGS core products. To this end, the IONosphere Map EXchange Format (IONEX), a format that allows the exchange of earth-fixed TEC snapshots, was developed by *Schaer et al.* [1998a]. The format was approved by the IGS community. Since 1 June 1998, several ACs, among them CODE, deliver daily IONEX files containing 12 2-hourly global TEC snapshots and a set of satellite-specific differential code biases (DCBs) to the CDDIS (Crustal Dynamics Data Information System), a global data center of the IGS. Since IONEX is a well-defined format, the IGS ionosphere products may be used by a larger user community. In the second part of this thesis, we will analyze first IGS IONEX results for validation purposes.

Ionosphere products are useful for many applications. Single-frequency GPS users may improve their results by applying global, regional, or local TEC maps. Space-borne applications, like altimetry, may benefit from the rapidly available global TEC maps. For ionosphere physicists, these maps are an alternative source of information about the deterministic behavior of the ionosphere that may be used to refine theoretical and semi-empirical ionosphere models. Last but not least, time series of global TEC parameters document the ionosphere's history and might possibly be of interest in the context of

global change studies [Rawer and Thiemann, 1997].

The present work has to be seen as a continuation of the ionosphere-related research work using GPS, performed at the AIUB. New aspects with respect to [Wild, 1994] are:

- global and regional ionospheric mapping,
- routine production of global, regional, and site-specific TEC maps embedded in the IGS data processing of CODE,
- time series of TEC parameters and maps,
- prediction of global TEC parameters and maps,
- estimation of DCBs for GPS/GLONASS satellites and receivers,
- time series of DCBs,
- IGS global ionosphere maps in IONEX form, and
- validation of TEC and DCB results.

Let us conclude with an outline of the subsequent chapters:

Chapter 2, *Basics of the GPS Data Analysis*, explains the current status of the GPS, introduces the GPS institutions that are relevant to this work, and highlights the most important aspects in modeling the GPS observables. Least-squares adjustment is recapitulated.

Chapter 3, *Extracting Ionospheric Information from GPS Data*, first gives a short introduction into the Earth's ionosphere, focuses on the ionospheric effects on GPS observables and solutions, reviews the single-layer model including the mapping function, and describes TEC parameterization methods. In addition, a covariance study concerning different ionospheric observables is performed.

Chapter 4, *Time Series of CODE Ionosphere Products*, sketches the IGS data processing scheme at CODE, lists the CODE ionosphere products, and presents and discusses selected TEC parameters, various types of temporal TEC profiles, and DCB results.

Chapter 5, *Predicting Global TEC Parameters and Maps*, develops a procedure to predict global TEC parameters, demonstrates long-term as well as short-term predictions, and shows resulting autocovariance functions.

Chapter 6, *Validating the CODE Ionospheric Parameters and Maps*, deals with the validation of CODE ionosphere products using an introductory example of a 600-kilometer baseline. CODE global and regional TEC information is compared with IGS IONEX data and the correlation of global TEC parameters with solar quantities is studied. Furthermore, IGS satellite DCB results are compared and combined.



---

Chapter 7, *Summary, Conclusions, and Outlook*, summarizes the essential results and conclusions of this work and points out aspects and ideas that might be of interest for future investigations.

Finally, Part III, consisting of Appendices A and B, includes numerous figures showing time series of CODE total electron content parameters and differential code biases.



## **Part I**

# **The GPS as a Tool for Ionospheric Mapping—Theory**



## 2. Basics of the GPS Data Analysis

### 2.1 The Global Positioning System—Current Status

The NAVigation Satellite Timing and Ranging Global Positioning System (NAVSTAR GPS or shortly GPS) is an all-weather, space-based radio navigation system deployed and operated by the United States for civilian and military purposes.

The first GPS satellite, PRN 4, was launched on 22 February 1978. PRN 4 was the first of a series of 11 so-called Block-I satellites that were used to build up the constellation. Although designed for 3-year lifetimes, several satellites operated for over 10 years. The last Block-I satellite, PRN 12, was active for about eleven and a half years till 26 March 1996. A major milestone in the development of the GPS system was 8 December 1993, when 24 satellites, 3 of them active spares, were successfully operating. The full constellation guarantees that at any time and for any location on or near the Earth's surface at least four satellites, required for a three-dimensional navigation solution, are simultaneously visible. In mid 1998, the GPS constellation actually consists of 27 satellites, 26 Block-II satellites plus a first Block-IIR satellite, PRN 13. The three types of GPS spacecrafts are reproduced in Figure 2.1. A fourth generation of NAVSTAR satellites, the Block-IIF series, is announced.

The Block-II satellites are arranged in six orbital planes which are inclined by about  $55^\circ$  with respect to the Earth's equator and equally separated by  $60^\circ$  on the equator. The satellite orbits are close to circular, with a semi-major axis of about 26 600 kilometers, corresponding to an altitude of approximately 20 200 kilometers above the Earth's surface. Figure 2.2 gives an impression of the size and orientation of the GPS satellite orbits around the Earth viewed from a latitude of  $35^\circ$  and from the north (or south) pole.

The orbital revolution period is, with about 11 hours 58 minutes, almost precisely half a sidereal day. Because the orbital period is an exact multiple of the rotation period of the Earth, the satellites complete two orbital revolutions while the Earth rotates by  $360^\circ$  with respect to inertial space, that is, the satellites' trajectories (or ground tracks) on the Earth as shown in Figure 2.3 repeat themselves daily. However, the satellites rise about 4 minutes earlier each solar day. The particular orbital period implies that all GPS satellites are in a deep 2:1 resonance with the Earth's rotation and therefore are

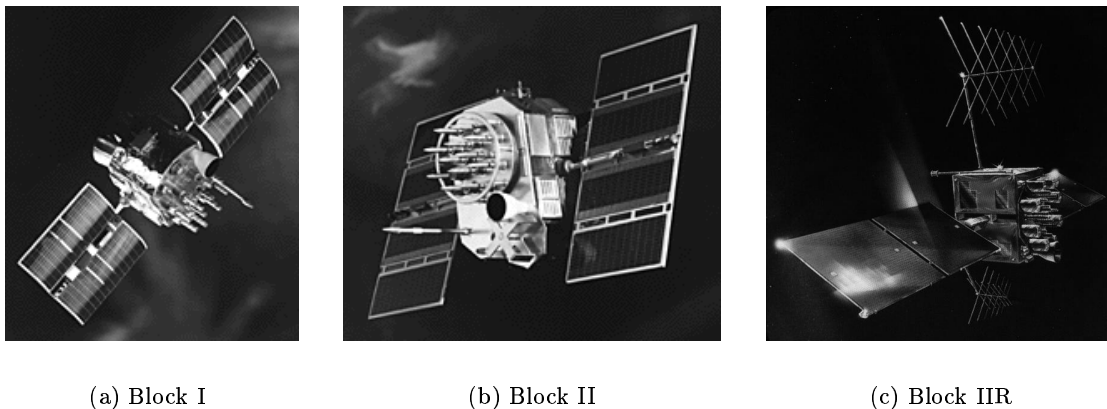


Figure 2.1: Block-I, Block-II, and Block-IIR GPS spacecrafts.

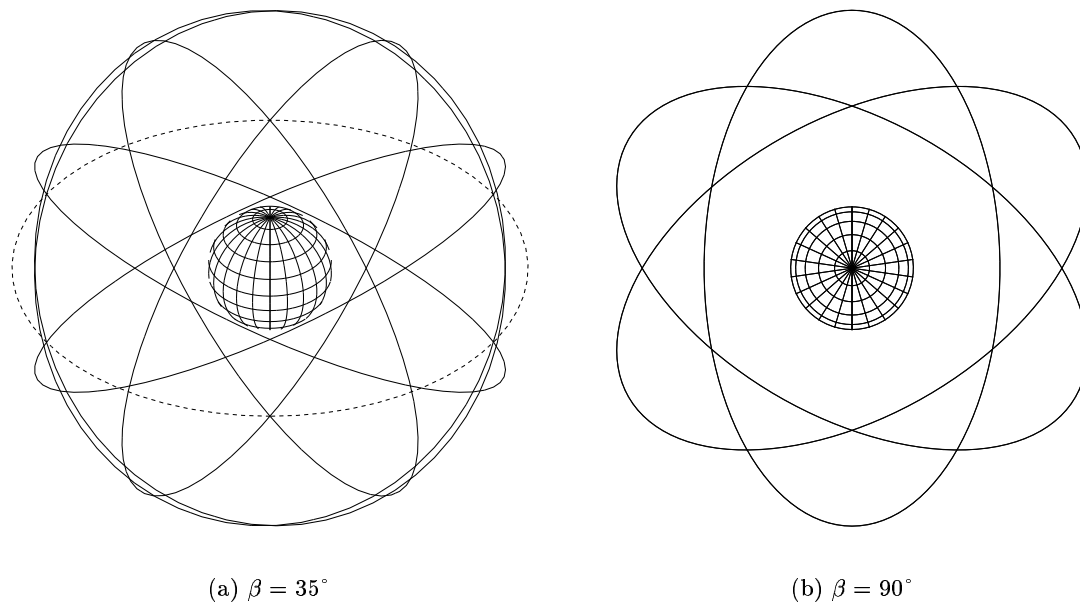


Figure 2.2: GPS satellite orbits viewed from a latitude  $\beta$ .

subject to pronounced secular or long-periodic perturbations in certain orbital elements [Beutler *et al.*, 1998a].

The GPS satellite constellation is schematically shown in Figure 2.4 for June 1, 1998 at

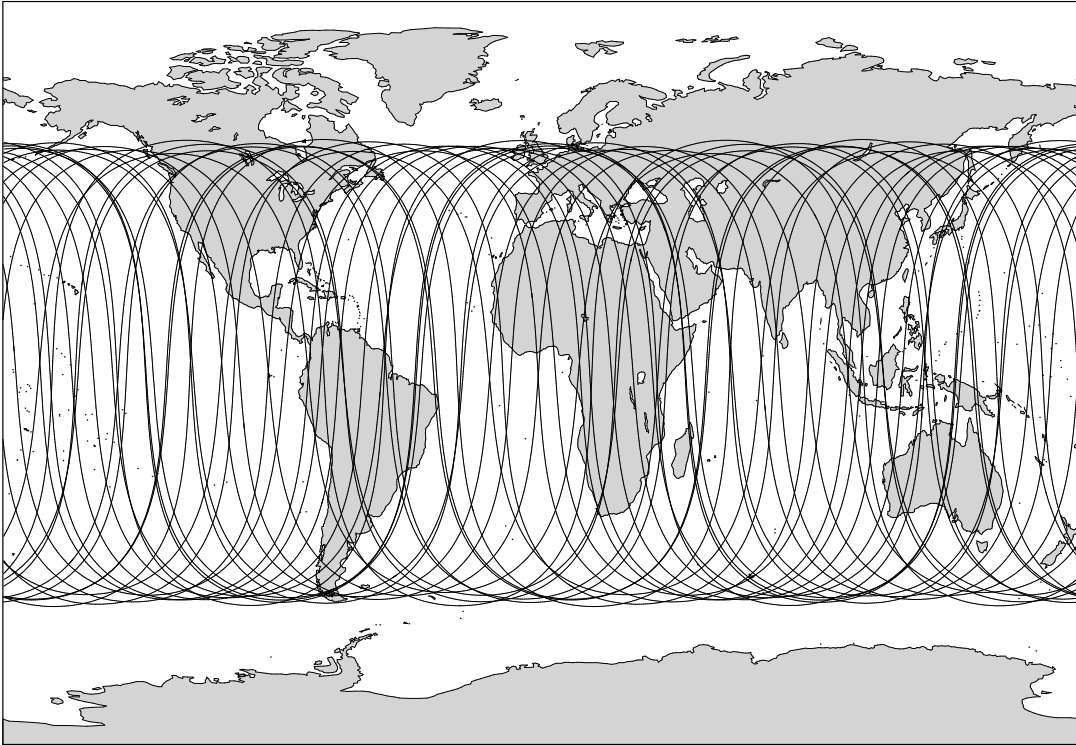


Figure 2.3: Sub-satellite trajectories of all GPS satellites for June 1, 1998.

00:00 UT. Each orbital plane, numbered from A to F, contains nominally 4 or effectively up to 5 satellites, identified by plane/slot and PRN numbers. The equatorial plane is indicated by the dashed line. To optimize global satellite visibility, the satellites are not equally spaced within the orbital planes. Note that because of the flattening of the Earth, the right ascension of the ascending node increases by about  $-0.039^\circ$  per day or  $-14.2^\circ$  per year [Beutler *et al.*, 1998a].

Table 2.1 lists the active GPS spacecrafts as of mid 1998. The 18 Block-IIA satellites are slightly modified Block-II satellites. Two GPS spacecrafts are equipped with a laser reflector array (LRA), namely SVN 35 and SVN 36. A laser reflector array allows to measure the distance between a ground station and a satellite using satellite laser ranging (SLR). Such line-of-sight distance measurements to GPS satellites, typically available with a centimeter accuracy, are very useful for absolute calibration purposes [Springer, 1998].

The “heart” of each GPS spacecraft is a high-quality oscillator, strictly speaking an ensemble of rubidium and cesium atomic clocks which is sequentially used to generate two coherent carriers L1 and L2 in the L-band. The two carrier frequencies  $\nu_1$  and  $\nu_2$

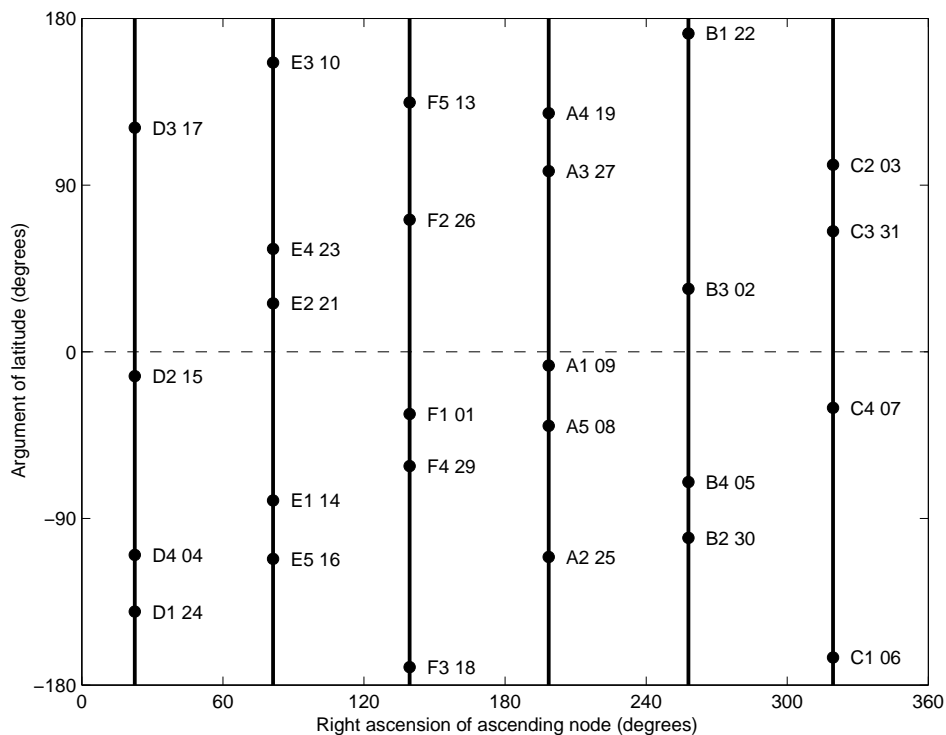


Figure 2.4: Approximate GPS satellite constellation on June 1, 1998 at 00:00 UT.

Table 2.1: Active GPS spacecrafts as of mid 1998.

PRN	SVN	Plane/slot	Block	LRA	PRN	SVN	Plane/slot	Block	LRA
1	32	F1	IIA		17	17	D3	II	
2	13	B3	II		18	18	F3	II	
3	11	C2	IIA		19	19	A4	II	
4	34	D4	IIA		21	21	E2	II	
5	35	B4	IIA	X	22	22	B1	IIA	
6	36	C1	IIA	X	23	23	E4	IIA	
7	37	C4	IIA		24	24	D1	IIA	
8	4	A5	IIA		25	25	A2	IIA	
9	39	A1	IIA		26	26	F2	IIA	
10	40	E3	IIA		27	27	A3	IIA	
13	43	F5	IIR		29	29	F4	IIA	
14	14	E1	II		30	30	B2	IIA	
15	15	D2	II		31	31	C3	IIA	
16	16	E5	II						



are derived from the fundamental frequency  $\nu_0 = 10.23$  MHz:

$$\nu_1 = 154 \nu_0 = 1575.42 \text{ MHz} \quad \text{with} \quad \lambda_1 = \frac{c}{\nu_1} \approx 190 \text{ mm} \quad (2.1a)$$

$$\nu_2 = 120 \nu_0 = 1227.60 \text{ MHz} \quad \text{with} \quad \lambda_2 = \frac{c}{\nu_2} \approx 244 \text{ mm} \quad (2.1b)$$

where

$\lambda_1, \lambda_2$  denote the corresponding wavelengths and

$c = 299\,792\,458$  m/s is the vacuum speed of light.

Note that the nominal frequency  $\nu_0$  is compensated for relativistic effects.

Two pseudo-random noise (PRN) codes are generated: (a) The coarse/acquisition (C/A) code is modulated on the carrier L1 with a chip rate of 1.023 Mbps, corresponding to one tenth of the fundamental frequency  $\nu_0$ . The C/A-code is an easy-to-acquire code. Its length per chip is about 293 meters. (b) The precision (P) code, or its encrypted version, the Y-code, is the principal code used for military positioning and navigation. It is modulated with a chip rate of 10.23 Mbps on both carriers L1 and L2. Its length per chip is about 29.3 meters. In addition, the navigation message, also called telemetry, is modulated with 50 bps on both carriers. It contains information on the ephemerides and clocks of the satellites, GPS time, and system status messages. The quality of the broadcast ephemerides is at present 2–4 meters.

In principle, the GPS is a one-way ranging system. A signal is transmitted by a NAVSTAR satellite and is observed by a suitable receiver. In essence, the GPS observable is the signal travelling time from satellite to receiver. Due to the lack of receiver clock synchronization, one cannot directly derive ranges from the code measurements, which therefore are called pseudo-ranges.

To prevent unauthorized GPS users from making use of the full potential of GPS, there are two options, namely:

- “selective availability” (SA), artificially deteriorating the satellite clocks, and
- “anti-spoofing” (AS), which encrypts the P-code observations.

SA and AS are usually activated. Essentially the civilian and commercial real-time applications of the GPS are affected by SA and AS, as opposed to the post-processing applications, which are only weakened by AS. Nowadays, methods are known, like differential GPS (DGPS), to get round part of the deteriorating effects. Due to the fact that GPS has become a significant and continuously growing economic sector, the U.S. government has announced in 1996 its intention to discontinue the use of SA within a decade.

For a thorough discussion of the GPS system, one may consult, e. g., [Hofmann-Wellenhof *et al.*, 1992; Kaplan, 1996; Leick, 1995; Parkinson and Spilker, 1996a, 1996b; Seeber, 1993; Teunissen and Kleusberg, 1998; Wells *et al.*, 1987]. The GPS error budget for a stand-alone receiver is well documented in [Langley, 1997].

### The Global Navigation Satellite System

The Russian analogue of the GPS, the GLObal NAVigation Satellite System (GLO-NASS), has similar characteristics. Incidentally, the term “Global Navigation Satellite System,” abbreviated as GNSS, is also used to label satellite systems for navigation and positioning in general.

The GLONASS satellites are arranged in three orbital planes which are inclined by about  $64.8^\circ$  to the equator and separated by  $120^\circ$ . They orbit about 1100 kilometers lower than the GPS counterparts, resulting in an orbital period of about 11 hours 16 minutes,  $8/17$  of a sidereal day. Each orbital plane nominally contains 8 satellites equally spaced, resulting in 24 satellites in total, as in the case of the GPS. At the beginning of 1996, the full satellite constellation was successfully operating for the first time. In mid 1998, only 14 satellites are still “healthy.” Nevertheless, the combination of GPS and GLONASS with  $27 + 14 = 41$  operational satellites is remarkable.

GLONASS offers a C/A-code (0.511 MHz) on L1 and P-codes (5.11 MHz) on L1 and L2. The GLONASS carrier frequencies  $\nu_1, \nu_2$  are not the same for all satellites but thus are related to a channel number  $i$  taking values 1 to 24:

$$\nu_{1,i} = 9(\nu + i \Delta\nu) \approx 1603\text{--}1616 \text{ MHz} \quad \text{with} \quad \lambda_{1,i} = \frac{c}{\nu_{1,i}} \approx 186\text{--}187 \text{ mm} \quad (2.2a)$$

$$\nu_{2,i} = 7(\nu + i \Delta\nu) \approx 1246\text{--}1257 \text{ MHz} \quad \text{with} \quad \lambda_{2,i} = \frac{c}{\nu_{2,i}} \approx 239\text{--}241 \text{ mm} \quad (2.2b)$$

where  $\nu = 178$  MHz and  $\Delta\nu = 0.0625$  MHz. The frequency ratio  $\nu_{1,i}/\nu_{2,i}$  (or the wavelength ratio  $\lambda_{2,i}/\lambda_{1,i}$ ) remains constant and is, with  $9/7 \approx 1.2857$ , very close to that of GPS, with  $77/60 \approx 1.2833$ . Also, the slightly different wavelengths result in a more complex resolution of the initial carrier phase ambiguities [Habrich, 1998].

It is worth mentioning that there is no SA or AS on GLONASS.

## 2.2 GPS Institutions Relevant to this Work

### 2.2.1 The International GPS Service (IGS)

Within the last decade, the GPS has come to play a major role in earth sciences. In the face of continued growth and diversification of GPS applications, the international scientific community has made an effort to promote international standards for GPS data acquisition and analysis, and to deploy and operate a common, comprehensive

global GPS tracking network. As a result of this effort, the International GPS Service (IGS) was established by the International Association of Geodesy (IAG) in 1993 and began its official operation on 1 January 1994 [Beutler *et al.*, 1994, 1995b; Neilan, 1995]. The IGS, with a multinational membership of organizations, agencies, and universities, makes available based on the contributions of seven analysis centers:

- highly accurate ephemerides of all active GPS satellites, distinguishing between a final, a rapid, and a 2-day predicted orbit product,
- earth rotation parameters (ERPs), as x- and y-component of polar wobble and length of day (LOD),
- IGS tracking station coordinates and velocities in SINEX (Solution-INdependent EXchange) format [Kouba *et al.*, 1996],
- satellite and station clock information, and
- since 26 January 1997 also station-specific tropospheric zenith path delay estimates [Gendt, 1998].

The mentioned products refer to the IERS Terrestrial Reference System (ITRS) realized by the IERS Terrestrial Reference Frame (ITRF), at present ITRF 96 [Boucher *et al.*, 1998]. The IGS final products are available within about two weeks of observations. Both IGS member institutions and the interested public can access them on the Internet through the information system (CBIS) maintained by the IGS central bureau (CB), which is sponsored by the National Aeronautic and Space Administration (NASA) and managed by the Jet Propulsion Laboratory (JPL) of the California Institute of Technology.

Let us point out that the raw data of the global IGS tracking network is a very valuable IGS product as well. It is collected, archived, and distributed using the RINEX (Receiver-INdependent EXchange) format [Gurtner, 1994].

In order to facilitate a combination of different GNSSs in the near future, a world-wide GLONASS campaign, the International GLONASS EXperiment (IGEX), has been scheduled and organized by CSTG (Commission on International Coordination of Space Techniques for Geodesy and Geodynamics), IGS, and ION (Institute of Navigation) [Willis *et al.*, 1998].

The IGS consists of components like network stations, global and regional data centers, analysis centers (ACs), analysis center coordinator (ACC), central bureau, governing board, and users to mention the most important ones [Neilan, 1995; IGS, 1998]. At present seven ACs contribute to the IGS service:

- COD, Center for Orbit Determination in Europe, AIUB, Berne, Switzerland,
- EMR, Energy, Mines and Resources, NRCan, Ottawa, Canada,

- ESA, European Space Agency, ESOC, Darmstadt, Germany,
- GFZ, GeoForschungsZentrum Potsdam, Germany,
- JPL, Jet Propulsion Laboratory, Pasadena, California, USA,
- NGS, National Geodetic Survey, NOAA, Silver Spring, Maryland, USA, and
- SIO, Scripps Institution of Oceanography, San Diego, California, USA.

Note that the 3-character acronyms at the beginning of each AC are used to identify the individual products.

For more information about the IGS or its products, we refer to the IGS annual reports, to the IGS workshop proceedings, and to the IGS WWW address <http://igs.cb.jpl.nasa.gov/>.

### 2.2.2 The Center for Orbit Determination in Europe

CODE, the Center for Orbit Determination in Europe, is a joint venture of the following four institutions:

- the Federal Office of Topography (L+T), Wabern, Switzerland,
- the Federal Agency of Cartography and Geodesy (BKG), Frankfurt, Germany,
- the Institut Géographique National (IGN), Paris, France, and
- the Astronomical Institute of the University of Berne (AIUB), Berne, Switzerland.

CODE is located at the AIUB. The computations are performed on a cluster of VAX/Alpha computers using the latest version of the Bernese GPS Software [*Rothacher and Mervart, 1996*], at present development version 4.1. Since 21 June 1992, the beginning of the IGS test campaign, and 1 November 1992, the beginning of the IGS pilot service, respectively, the CODE AC reliably contributes to the IGS with a complete range of products.

CODE justifies the word “Europe” in its name by including a large number of European IGS stations in its global data analysis which hopefully results in the best possible GPS orbits over Europe. The about 130 globally distributed IGS tracking stations processed at present by CODE are shown in Figure 2.5. That CODE puts considerable emphasis on Europe is also reflected by the fact that CODE plays an essential role in the maintenance and densification of the European Reference Frame (EUREF). For EUREF, CODE acts as one of currently ten associate ACs processing a subset of permanent European GPS tracking stations. In addition, it is responsible for the combination of the individual contributions to an official weekly EUREF solution [*Springer et al., 1997*]. The European

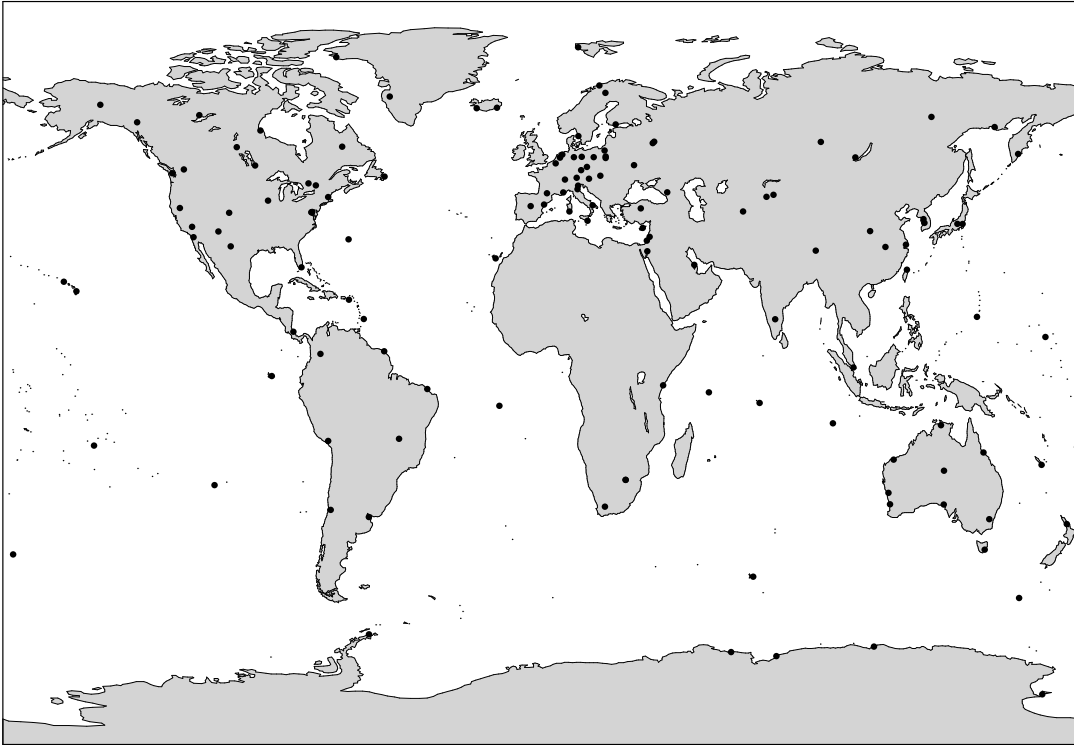


Figure 2.5: Globally distributed IGS tracking stations processed by CODE.

GPS tracking network is also used by CODE to regularly verify the quality of the CODE final orbits by processing large-area regional networks and to test and compare new, refined processing strategies [Rothacher *et al.*, 1998b]. The weekly comparisons of CODE final orbits with IGS combined orbits reveal an RMS consistency of 3–5 centimeters [Kouba, 1998].

For further information about CODE products and processing strategies, please consult the CODE annual reports [Rothacher *et al.*, 1995a, 1996, 1997, 1998a].

### 2.2.3 The IGS Ionosphere Working Group

The IGS community has been aware for a long time of the potential of the global IGS tracking network to extract information about the Earth's ionosphere. At the IGS workshops held in Potsdam, Germany, in May 1995, and in Silver Spring, Maryland, USA, in March 1996, sessions were dedicated to ionospheric issues. At the latter workshop, total electron content (TEC) maps delivered by COD, DLR (Deutsches Zentrum für Luft- und Raumfahrt, Neustrelitz, Germany), ESA, and UNB (University of New Brunswick, Fredericton, Canada) were compared. Only regional European maps and the corresponding

portion of global maps were considered [Feltens *et al.*, 1996]. As a consequence of this TEC comparison, a format for the exchange of ionosphere maps, called IONEX, was developed by Schaer *et al.* [1998a] and approved by the IGS-ionosphere community. IONEX allows the storage of snapshots of the electron density referring to particular epochs and to a two- or even three-dimensional, earth-fixed grid. Technique-related auxiliary data may be stored in IONEX files as well.

In the meantime, some IGS ACs began to produce global ionosphere maps and, as a by-product of the TEC determination, satellite and receiver differential code biases on a regular basis. At the IGS workshop in Darmstadt, Germany, in February 1998, it was concluded that the IGS should monitor the ionosphere for at least the next period of high solar activity and study in particular the impact of the ionosphere on IGS core products [Feltens and Schaer, 1998]. For that purpose, it was recommended to focus on two kinds of ionospheric products:

- 2-hourly global ionosphere maps (GIMs) in the form of two-dimensional grids and
- daily sets of differential code biases (DCBs) for the satellites.

In order to accomplish this and to coordinate the ionospheric activities within the IGS, an ionosphere working group was established in May 1998 [Schaer and Feltens, 1998]. The IGS ionosphere working group consists of representatives of each AC contributing to a future IGS ionosphere service, representatives of so-called ionospheric associate validation centers, representatives of the ionosphere research community, the IGS AC coordinator, and a representative of the IGS central bureau.

On 1 June 1998, COD, EMR, ESA, and, as an IGS ionospheric associate AC, UPC (Polytechnical University of Catalonia, Barcelona, Spain) began to deliver daily IONEX files to CDDIS. About three months later, JPL started to send its IONEX files to CDDIS as well. Whereas TEC information is supplied by currently all five ionospheric ACs, DCB information is supplied by four ACs only, namely COD, EMR, ESA, and JPL. First comparison and combination results may be expected from the IGS ionosphere combination center ESA by the end of 1998. This implies that the IGS ionosphere working group strives for an IGS combined ionosphere product [Schaer, 1998b]. The development of an IGS global ionosphere model, as stated in [Schaer and Feltens, 1998], may be seen as a long-term goal.

## 2.3 Modeling the GPS Observables

In this section, we briefly introduce the fundamental GPS observation equations, the interferometric GPS principle, different linear combinations, and ambiguity resolution. For a more detailed discussion, the reader is referred to the rich GPS literature, e. g., [Teunissen and Kleusberg, 1998].

### 2.3.1 Fundamental Observation Equations

The C/A-, P-, or Y-code, transmitted by satellite  $k$  at time  $t^k$  and registered by receiver  $i$  at time  $t_i$ , is defined as

$$P_i^k = c(t_i - t^k) = c\tau_i^k \quad (2.3)$$

where

$P_i^k$  denotes the pseudo-range (or code observation), expressed in units of length,

$c$  is the speed of light,

$t_i$  is the arrival (or observation) time of the signal, as measured by the clock of receiver  $i$ ,

$t^k$  is the transmission time of the signal, measured in the time frame of satellite  $k$ , and

$\tau_i^k = t_i - t^k$  is the signal travelling time—apart from satellite and receiver clock errors.

The pseudo-range  $P_i^k$  may be related to the slant range  $\rho_i^k$ , the geometric distance between receiver  $i$  at time  $t_i - \Delta t_i$  and the satellite  $k$  at time  $t^k - \Delta t^k$ , and to the delays due to the Earth's atmosphere:

$$P_i^k = \rho_i^k + c(\Delta t_i - \Delta t^k) + \Delta\rho_{i,\text{trop}}^k + \Delta\rho_{i,\text{ion}}^k + c(b^k + b_i) + \epsilon \quad (2.4)$$

where

$\Delta t_i, \Delta t^k$  are the offsets of the receiver and satellite clocks with respect to the GPS system time,

$\Delta\rho_{i,\text{trop}}^k$  is the delay of the signal due to the troposphere (or neutral atmosphere),

$\Delta\rho_{i,\text{ion}}^k$  is the delay of the signal due to the ionosphere,

$b^k, b_i$  are the satellite and receiver hardware delays, expressed in units of time, and

$\epsilon$  indicates a random error (or residual).

The term  $\rho_i^k$  also includes relativistic effects as, e. g., the periodic relativistic effect due to the eccentricity of the satellite orbits and the refraction due to the gravitational field [Rothacher, 1992]. In addition, antenna phase center offsets and variations have to be taken into account [Rothacher et al., 1995b].

Both hardware delays,  $b^k$  and  $b_i$ , are usually ignored or assumed to be zero, because they cannot be separated from the clock offsets  $\Delta t^k$  and  $\Delta t_i$ . Consequently, the clock offsets

implicitly compensate for the hardware delays. In principle, these hardware delays are time-dependent, although in practice they seem to be relatively stable, at least on time scales of days.

“Multipath,” caused by the fact that signals arrive at the receiver via multiple paths due to reflections, distorts code (and phase) observations and is a relevant error source in GPS. Multipath, a systematic effect when considering it over a short time span of several minutes, may be interpreted as measurement noise over long time periods and is therefore not explicitly listed in above observation equation.

Assuming a relative resolution of the measurements of one percent with respect to the chip length and the wavelength, respectively, one obtains an uncertainty of 3 meters for C/A-code, 0.3 meters for P-code, and about 2 millimeters for carrier phase measurements. These orders of magnitude reveal that for high-precision applications of the GPS, the carrier phase is the primary observable.

Let us repeat the observation equation (2.4) for the accumulated carrier phase observation  $L_i^k$ , expressed in units of length:

$$L_i^k = \rho_i^k + c(\Delta t_i - \Delta t^k) + \Delta\rho_{i,\text{trop}}^k - \Delta\rho_{i,\text{ion}}^k + \lambda B_i^k + \epsilon \quad (2.5)$$

where

$\lambda$  is the corresponding wavelength and

$B_i^k$  denotes a constant bias, expressed in cycles, principally containing the initial carrier phase ambiguity  $N_i^k$ .

Strictly speaking, the bias term  $\lambda B_i^k$  consists of  $\lambda(N_i^k + \delta N_i^k) + c(b^k + b_i)$ , where  $N_i^k$  is an integer and  $\delta N_i^k$  designates the effect due to “phase windup.” However, one cannot separate  $N_i^k$  from  $b^k$  and  $b_i$  and therefore has to substitute  $\lambda B_i^k$ , where  $B_i^k$  is now a real-valued number. In the general case, one unknown bias parameter  $B_i^k$  has to be determined per satellite pass, receiver, and frequency. If discontinuities in the carrier phase observations, so-called cycle-slips, are detected, which cannot be repaired, additional bias parameters  $B_i^k$  have to be set up. Comparing equations (2.4) and (2.5), one notices that the group delay and the phase advance caused by the ionospheric refraction  $\Delta\rho_{i,\text{ion}}^k$  are of equal size but opposite sign.

Equations (2.4) and (2.5), representing the fundamental GPS observation equations, reveal the “interdisciplinary” potential of the GPS [Beutler *et al.*, 1998b]:

- The slant range  $\rho_i^k$  contains the “geometrical” information, which allows to retrieve receiver positions, satellite orbits, ERPs, antenna phase center offsets and variations, etc.
- The terms  $\Delta t^k$  and  $\Delta t_i$  contain information related to satellite and receiver clocks, enabling time and frequency transfer up to intercontinental distances [Schildknecht *et al.*, 1990].



- The terms  $\Delta\rho_{i,\text{trop}}^k$  and  $\Delta\rho_{i,\text{ion}}^k$  contain information about the atmosphere.

Subsequently, we will mainly focus on the term  $\Delta\rho_{i,\text{ion}}^k$  which obviously contains the ionospheric information.

Because the ionosphere is a dispersive medium, ionospheric refraction depends on the frequency of the signal. To be more specific, the ionospheric refraction is proportional to  $1/\nu^2$ , where  $\nu$  is the carrier frequency, ignoring very small higher order terms. The observation equations for the set of observations provided by a dual-frequency geodetic GPS receiver may be written using a simplified, frequency-dependent notation by substituting

$$\rho_i^k + c(\Delta t_i - \Delta t^k) + \Delta\rho_{i,\text{trop}}^k = \rho_i^{\prime k} \quad (2.6)$$

and furthermore introducing the ionospheric variable  $I_i^k$ , which represents the ionospheric delay related to the first frequency  $\nu_1$ :

$$L_{i,1}^k = \rho_i^{\prime k} - I_i^k + \lambda_1 B_{i,1}^k \quad (2.7a)$$

$$L_{i,2}^k = \rho_i^{\prime k} - \xi I_i^k + \lambda_2 B_{i,2}^k \quad (2.7b)$$

$$P_{i,1}^k = \rho_i^{\prime k} + I_i^k + c(b^{k,1} + b_{i,1}) \quad (2.7c)$$

$$P_{i,2}^k = \rho_i^{\prime k} + \xi I_i^k + c(b^{k,2} + b_{i,2}) \quad (2.7d)$$

where

$L_{i,1}^k, L_{i,2}^k$  are the carrier phase observations on both frequencies,

$P_{i,1}^k, P_{i,2}^k$  are the P-code observations on both frequencies,

$\rho_i^{\prime k}$  is the geometric distance between receiver  $i$  and satellite  $k$  including the clock offsets  $\Delta t_i$  and  $\Delta t^k$  and tropospheric refraction  $\Delta\rho_{i,\text{trop}}^k$ ,

$\xi = \nu_1^2/\nu_2^2 \approx 1.647$  is a factor that depends on the frequency ratio  $\nu_1/\nu_2 = 77/60$ ,

$I_i^k$  is the epoch-specific,  $L_1$ -related ionospheric refraction, expressed in units of length, and

$B_{i,1}^k, B_{i,2}^k$  are the carrier phase ambiguity parameters of both frequencies.

In principle, the hardware delay terms  $c(b^{k,1} + b_{i,1})$  and  $c(b^{k,2} + b_{i,2})$  are still present in the observation equations (2.7c) and (2.7d). Disregarding these terms, the code observations, as opposed to the phase observations, are unambiguous. The phase observations are two to three orders of magnitude more accurate than the code observations. In order to keep the observation equations (2.7) and the following equations simple, the observation noise initially indicated by the term  $\epsilon$  is no longer included.

It is essential that each GPS receiver tracks several, ideally all satellites in view quasi-simultaneously. If SA is turned on, the requirement to simultaneity is relatively high

because of the satellite clocks dithering. State-of-the-art receivers keep their clocks synchronized with respect to GPS time within about one millisecond.

It is an IGS standard to record GPS observations every 30 seconds. For some special applications, like kinematic applications, a higher data sampling rate may be required.

### Pseudo-Range Smoothing

Based on a continuous time series of dual-frequency code and phase measurements, it is possible to create “new,” phase-smoothed code measurements with a significantly reduced noise compared to the noise of the original code measurements. The smoothed dual-frequency code measurements at epoch  $t$  can be written as

$$\tilde{P}_{i,1}^k(t) = \bar{P}_{i,1}^k + \Delta L_{i,1}^k(t) + 2 \frac{\nu_2^2}{\nu_1^2 - \nu_2^2} (\Delta L_{i,1}^k(t) - \Delta L_{i,2}^k(t)) \quad (2.8a)$$

$$\tilde{P}_{i,2}^k(t) = \bar{P}_{i,2}^k + \Delta L_{i,2}^k(t) + 2 \frac{\nu_1^2}{\nu_1^2 - \nu_2^2} (\Delta L_{i,1}^k(t) - \Delta L_{i,2}^k(t)) \quad (2.8b)$$

using the auxiliary expressions

$$\Delta L_{i,1}^k(t) = L_{i,1}^k(t) - \bar{L}_{i,1}^k \quad (2.9a)$$

$$\Delta L_{i,2}^k(t) = L_{i,2}^k(t) - \bar{L}_{i,2}^k \quad (2.9b)$$

where

$L_{i,1}^k(t), L_{i,2}^k(t)$  are the corresponding phase measurements at epoch  $t$ ,

$\bar{L}_{i,1}^k, \bar{L}_{i,2}^k$  are the mean phase measurements, and

$\bar{P}_{i,1}^k, \bar{P}_{i,2}^k$  are the mean code measurements, all averaged over a common, “cycle-slip-free” time interval.

The noise of the smoothed code measurements is dominated by that of the terms  $\bar{P}_{i,1}^k$  and  $\bar{P}_{i,2}^k$ , which is reduced by about a factor of  $\sqrt{n}$  with respect to that of unsmoothed code measurements, where  $n$  denotes the number of epochs taken into account. The phase measurements  $L_{i,1}^k$  and  $L_{i,2}^k$  are considered error-free. It is important to know that such code measurements, being derived from phase measurements, are highly correlated in time and therefore generally lead to underestimated standard deviations—when treated as uncorrelated.

### 2.3.2 Forming Differences

The difference of two phase (or code) observations quasi-simultaneously acquired to the satellite  $k$  by receivers  $i$  and  $j$

$$L_{ij}^k = L_i^k - L_j^k \quad (2.10)$$

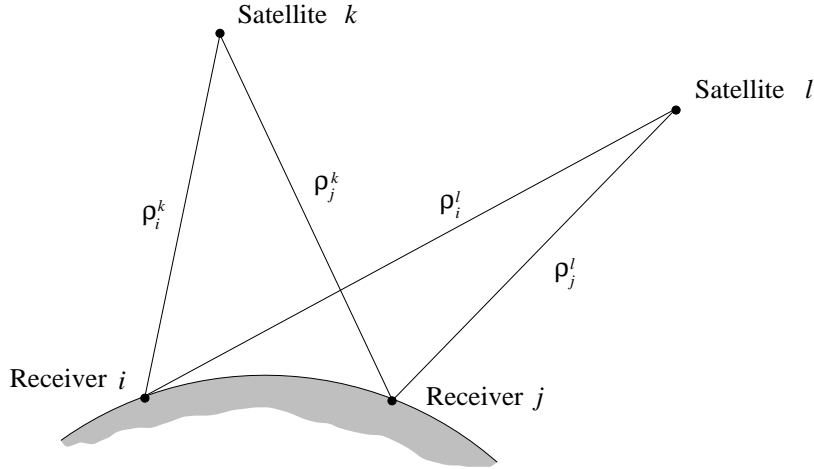


Figure 2.6: Four one-way observations needed to form a double difference.

almost completely eliminates the satellite clock offset  $\Delta t^k$  and does no longer contain the hardware delay  $b^k$ . Differences of this type are called *single differences*. They still contain the receiver clock offsets and are therefore well suited for time and frequency transfer.

The difference of two quasi-simultaneous phase (or code) single differences to the satellites  $k$  and  $l$

$$L_{ij}^{kl} = L_{ij}^k - L_{ij}^l = (L_i^k - L_j^k) - (L_i^l - L_j^l) \quad (2.11)$$

does not contain the receiver clock offsets  $\Delta t_i$  and  $\Delta t_j$  and hardware delays  $b_i$  and  $b_j$ . Differences of this type are called *double differences*.

Figure 2.6 shows four one-way observations, also called *zero differences*, which allow to form two single differences and one double difference, respectively. The line connecting the receivers is addressed as baseline.

Taking the difference of two double differences referring to two different epochs yields a *triple difference*. This latter type of differences has advantages for the initial processing and screening of the data. Differences between consecutive epochs as well as differences with respect to a particular epoch are conceivable. Note that phase ambiguity parameters cancel out when forming triple differences.

Interferometric GPS—processing of single, double, or triple differences—obviously yields the relative positions between the co-observing receivers, usually referred to as the baseline vectors between the stations. Remaining errors due to inaccurate satellite orbits, mismodeled troposphere and unmodeled ionosphere are considerably reduced by forming differences. In the “limiting case” of a zero-baseline, when two receivers are connected to one and the same antenna (or a very short baseline), these errors cancel out totally.

### Double-Difference Observation Equations

Doubly differencing zero-difference observation equations (2.7) in analogy to (2.11) leads to the following set of double-difference observation equations:

$$L_{ij,1}^{kl} = \rho_{ij}^{kl} - I_{ij}^{kl} + \lambda_1 N_{ij,1}^{kl} \quad (2.12a)$$

$$L_{ij,2}^{kl} = \rho_{ij}^{kl} - \xi I_{ij}^{kl} + \lambda_2 N_{ij,2}^{kl} \quad (2.12b)$$

$$P_{ij,1}^{kl} = \rho_{ij}^{kl} + I_{ij}^{kl} \quad (2.12c)$$

$$P_{ij,2}^{kl} = \rho_{ij}^{kl} + \xi I_{ij}^{kl} \quad (2.12d)$$

where

$\rho_{ij}^{kl} = \rho_{ij}^{kl} + \Delta\rho_{ij,\text{trop}}^{kl}$  represents the doubly differenced geometric term, consisting of geometric distance  $\rho_{ij}^{kl}$  and tropospheric refraction  $\Delta\rho_{ij,\text{trop}}^{kl}$ , and

$N_{ij,1}^{kl}, N_{ij,2}^{kl}$  are the double-difference phase ambiguity parameters of both frequencies, expressed in cycles.

Double-difference ambiguity parameters  $N_{ij}^{kl}$  are related to a satellite pair and a receiver pair (or baseline). They are of integer nature, because all clock offsets  $\Delta t$  and hardware delays  $b$  are eliminated (or greatly reduced).

The GPS satellites move by  $v = \sqrt{GM/a} \approx 3.9$  km/s in space.  $GM$  is the earth gravitational constant and  $a$  is the semi-major axis of the satellites. The maximum velocity with respect to the earth-fixed frame is about 3.2 km/s (or 3.2 mm/ $\mu$ s) and is reached at the equator; the minimum velocity is about 2.8 km/s at latitudes of  $\pm 55^\circ$ . Therefore the receiver clock offsets  $\Delta t_i$  must be applied with an accuracy better than one microsecond prior to differentiation. This is easily possible using code measurements. For very long baselines, the signal transmission epochs  $t^k$  (or the signal travelling times  $\tau_i^k$ ) may differ by up to several milliseconds, that is, the SA-induced errors may somewhat harm double differences. A first-order correction might be theoretically done by accounting for SA rates. In practice, one usually lives with this effect, hoping and assuming that it is of random nature, at least on a longer time scale.

In the Bernese GPS Software [Rothacher and Mervart, 1996], single differences are explicitly formed using sophisticated algorithms to find an optimal set of linearly independent baselines. Double and triple differences are then implicitly formed in the corresponding parameter estimation and pre-processing programs. However, the interferometric GPS principle can also be achieved by processing zero differences and simultaneously solving for epoch-specific satellite and receiver clock offsets. In the latter case, one has to handle a huge amount of clock parameters, what is actually no problem—apart from the computational burden. Using parameter pre-elimination algorithms, one can handle a big number of epoch-specific parameters. The processing of zero differences and the estimation of satellite and receiver clock parameters is supported by the latest version of the Bernese GPS Software as well.

### 2.3.3 Linear Combinations and Their Characteristics

#### Ionosphere-Free Linear Combination

It may be verified that the linear combination (LC) of the basic dual-frequency phase (or code) observables

$$L_3 = \kappa_{1,3} L_1 + \kappa_{2,3} L_2 \quad (2.13)$$

with the coefficients

$$\kappa_{1,3} = +\nu_1^2/(\nu_1^2 - \nu_2^2) \approx +2.546 \quad (2.14a)$$

$$\kappa_{2,3} = -\nu_2^2/(\nu_1^2 - \nu_2^2) \approx -1.546 \quad (2.14b)$$

eliminates the ionospheric refraction terms  $I$  and  $\xi I$  quoted in the zero-difference and double-difference observation equations (2.7) and (2.12).  $L_3$  is therefore called ionosphere-free LC (or observable). Forming the ionosphere-free LC from the undifferenced observation equations (2.7), taking into account (2.6), and neglecting the hardware delays  $b$ , leads to

$$L_{i,3}^k = \rho_i^k + \lambda_3 B_{i,3}^k \quad (2.15a)$$

$$P_{i,3}^k = \rho_i^k \quad (2.15b)$$

where

$\lambda_3 = c/(\nu_1 + \nu_2) \approx 107$  mm is the so-called narrow-lane wavelength and

$B_{i,3}^k$  is a real-valued ambiguity parameter, expressed in narrow-lane cycles.

The corresponding double-difference observation equations read as

$$L_{ij,3}^{kl} = \rho_{ij}^{kl} + \lambda_3 B_{ij,3}^{kl} \quad (2.16a)$$

$$P_{ij,3}^{kl} = \rho_{ij}^{kl} \quad (2.16b)$$

where

$$B_{ij,3}^{kl} = \frac{\kappa_{1,3} \lambda_1 N_{ij,1}^{kl} + \kappa_{2,3} \lambda_2 N_{ij,2}^{kl}}{\lambda_3} = \kappa_{1,5} N_{ij,1}^{kl} + \kappa_{2,5} N_{ij,2}^{kl} \quad (2.17)$$

is a non-integer ambiguity parameter. The multipliers  $\kappa_{1,5}$  and  $\kappa_{2,5}$  equal to

$$\kappa_{1,5} = +\nu_1/(\nu_1 - \nu_2) = +77/17 \approx +4.529 \quad (2.18a)$$

$$\kappa_{2,5} = -\nu_2/(\nu_1 - \nu_2) = -60/17 \approx -3.529 \quad (2.18b)$$

The ionosphere-free LC is certainly the most frequently used observable. Using the ionosphere-free LC leads to an observation noise about 3 times larger than that of  $L_1$  and  $L_2$ , assuming  $\sigma(L_2) = \sigma(L_1)$ :

$$\sigma(L_3) = \sqrt{\kappa_{1,3}^2 \sigma^2(L_1) + \kappa_{2,3}^2 \sigma^2(L_2)} = \sqrt{\kappa_{1,3}^2 + \kappa_{2,3}^2} \sigma(L_1) \approx 3 \sigma(L_1) \quad (2.19)$$

$\kappa_{1,3}$  and  $\kappa_{2,3}$  are given in (2.14).

Since GPS orbits with an excellent accuracy are available, tropospheric refraction, included in the term  $\rho'_{ij}{}^{kl}$  (or  $\rho'_i{}^k$ ), is the limiting error source in geodetic GPS, provided that dual-frequency data is present.

### Another Ionosphere-Free Observable

Having only single-frequency phase and code measurements  $L_1$  and  $P_1$ , one might form an ionosphere-free, but ambiguous observable by simply putting

$$L'_3 = \frac{L_1 + P_1}{2} \quad (2.20)$$

The noise of this special observable would be half as large as that of  $P_1$ , assuming  $L_1$  to be error-free compared to  $P_1$ . The observation equations (2.7a) and (2.12a) might be modified accordingly to

$$L'_{i,3}{}^k = \rho'_i{}^k + \lambda'_1 B_{i,1}{}^k \quad (2.21)$$

and

$$L'_{ij,3}{}^{kl} = \rho'_{ij}{}^{kl} + \lambda'_1 N_{ij,1}{}^{kl} \quad (2.22)$$

respectively, where  $\lambda'_1 = \lambda_1/2 \approx 95$  mm. In practice, it would be a non-trivial task to reliably detect cycle-slips in the carrier phase measurements  $L_1$  and thus making available cycle-slip-free portions of  $L_1$  measurements. This means that the LC (2.20) is of rather “academic” nature. Nevertheless, the LC (2.20) might be of interest for processing single-frequency GLONASS data because the number of presently operating dual-frequency GLONASS receivers is still small.

### Geometry-Free Linear Combination

By subtracting the phase (or code) observable of the second frequency from that of the first frequency, both expressed in units of length, the “geometric” term  $\rho'$  including clock offsets and tropospheric delay is eliminated. The “geometry-free” LC

$$L_4 = L_1 - L_2 = \kappa_{1,4} L_1 + \kappa_{2,4} L_2 \quad (2.23)$$

with  $\kappa_{1,4} = +1$  and  $\kappa_{2,4} = -1$ , only contains ionospheric refraction and ambiguity parameters (or hardware delays). This LC is of vital interest for ionospheric mapping. Therefore  $L_4$  is sometimes also called “ionospheric” LC (or observable). Applying the geometry-free LC to the observation equations (2.7) and (2.12) leads to the undifferenced observation equations

$$L_{i,4}{}^k = -\xi_4 I_i{}^k + B_{i,4}{}^k \quad (2.24a)$$

$$P_{i,4}{}^k = +\xi_4 I_i{}^k + c(\Delta b^k - \Delta b_i) \quad (2.24b)$$

where

$\xi_4 = 1 - \xi = 1 - \nu_1^2/\nu_2^2 \approx -0.647$  is the factor that converts the ionospheric delay in  $L_4$  to that of the first frequency,

$B_{i,4}^k = \lambda_1 B_{i,1}^k - \lambda_2 B_{i,2}^k$  is an ambiguity parameter with an undefined wavelength, therefore expressed in units of length,

$\Delta b^k = b^{k,1} - b^{k,2}$  is the differential, inter-frequency hardware delay in units of time, generally called differential code bias (DCB), of the satellite  $k$ , and

$\Delta b_i = b_{i,1} - b_{i,2}$  is the DCB of the receiver  $i$ ,

and to the corresponding double-difference observation equations

$$L_{ij,4}^{kl} = -\xi_4 I_{ij}^{kl} + B_{ij,4}^{kl} \quad (2.25a)$$

$$P_{ij,4}^{kl} = +\xi_4 I_{ij}^{kl} \quad (2.25b)$$

where

$$B_{ij,4}^{kl} = \lambda_1 N_{ij,1}^{kl} - \lambda_2 N_{ij,2}^{kl} \quad (2.26)$$

Note that neither satellite nor receiver DCBs occur in (2.25b), when modeling a double difference of geometry-free code observations. Furthermore, if the dual-frequency ambiguity parameters  $N_{ij,1}^{kl}$  and  $N_{ij,2}^{kl}$  of (2.26) are fixed to integers, the term  $B_{ij,4}^{kl}$  in (2.25a) is known. This in turn means that in the ambiguity-resolved case the only remaining unknown parameter  $I_{ij}^{kl}$ , representing the doubly differenced ionospheric delay on  $L_1$ , is determined with a few-millimeter accuracy.

The determination of the *absolute* ionosphere, however, is not a straightforward matter at all, despite the availability of dual-frequency observations. The theoretical background necessary for solving this task will be developed in Chapter 3.

### Wide-Lane Linear Combination

For ambiguity resolution, much is gained by forming the so-called wide-lane LC

$$L_5 = \kappa_{1,5} L_1 + \kappa_{2,5} L_2 \quad (2.27)$$

using the LC coefficients (2.18).

Wide-laning the double-difference observation equations (2.12) gives

$$L_{ij,5}^{kl} = \rho_{ij}^{kl} - \xi_5 I_{ij}^{kl} + \lambda_5 N_{ij,5}^{kl} \quad (2.28)$$

where

$\xi_5 = -\nu_1/\nu_2 \approx -1.283$  is the corresponding ionospheric conversion factor,

$\lambda_5 = c/\nu_5 = c/(\nu_1 - \nu_2) \approx 862$  mm is the wide-lane wavelength, and

Table 2.2: Linear combinations  $\kappa_1 L_1 + \kappa_2 L_2$  and their error characteristics.

LC	$\lambda$ (m)	$\kappa_1$ (m/m)	$\kappa_2$ (m/m)	Geometric error		Ionospheric error		Noise	
				(m)	(cycles)	(m)	(cycles)	(m)	(cycles)
$L_1$	0.190	+1.000	0.000	1.000	1.000	+1.000	+1.000	1.000	1.000
$L_2$	0.244	0.000	+1.000	1.000	0.779	+1.647	+1.283	1.000	0.779
$L_3$	0.107	+2.546	-1.546	1.000	1.779	0.000	0.000	2.978	5.299
$L_4$	0.054	+1.000	-1.000	0.000	0.000	-0.647	-2.283	1.414	4.991
$L_5$	0.862	+4.529	-3.529	1.000	0.221	-1.283	-0.283	5.742	1.268

$N_{ij,5}^{kl}$  is an integer ambiguity, expressed in wide-lane cycles.

The wide-lane ambiguity  $N_{ij,5}^{kl}$  is related to the original, dual-band ambiguities  $N_{ij,1}^{kl}$  and  $N_{ij,2}^{kl}$  as follows:

$$N_{ij,5}^{kl} = N_{ij,1}^{kl} - N_{ij,2}^{kl} \quad (2.29)$$

The major advantage of the wide-lane LC is that the ionospheric error  $\xi_5 I_{ij}^{kl}$  expressed in  $L_5$ -cycles is considerably smaller than the ionospheric errors  $I_{ij}^{kl}$  and  $\xi I_{ij}^{kl}$  expressed in  $L_1$ - and  $L_2$ -cycles, respectively, which means that the fixing of the wide-lane ambiguity  $N_{ij,5}^{kl}$  is less sensitive to ionospheric biases than that of the original ambiguities  $N_{ij,1}^{kl}$  and  $N_{ij,2}^{kl}$  listed in observation equations (2.12a) and (2.12b).

Once the wide-lane ambiguity  $N_{ij,5}^{kl}$  is resolved, the integer nature of the ambiguity term  $B_{ij,3}^{kl}$  in the ionosphere-free LC (2.16a) may be recovered by setting the second ambiguity  $N_{ij,2}^{kl} = N_{ij,1}^{kl} - N_{ij,5}^{kl}$  in (2.17), which results in

$$B_{ij,3}^{kl} = \kappa_{1,5} N_{ij,1}^{kl} + \kappa_{2,5} (N_{ij,1}^{kl} - N_{ij,5}^{kl}) = N_{ij,1}^{kl} - \kappa_{2,5} N_{ij,5}^{kl} \quad (2.30)$$

where  $N_{ij,1}^{kl}$  is denoted “narrow-lane” ambiguity, because of the relatively small wavelength  $\lambda_3 \approx 107$  mm.

All mentioned LCs are summarized in Table 2.2 listing the wavelength  $\lambda$ , the LC factors  $\kappa_1$  and  $\kappa_2$ , the geometric and ionospheric errors normalized to  $L_1$ , and the resulting observation noise assuming  $L_1$  and  $L_2$  expressed in units of length to be equally accurate and uncorrelated. The wavelengths specified for  $L_3$  and  $L_4$  result when the wide-lane ambiguities  $N_5$  are introduced as known and, for  $L_4$ , when the ionosphere is additionally neglected. The ionospheric error in meters is proportional to the ionospheric conversion factors 1,  $\xi$ , 0,  $\xi_4$ , and  $\xi_5$ . The noise value in meters corresponds to  $\sqrt{\kappa_1^2 + \kappa_2^2}$ . The subscripts “3,” “4,” and “5” denoting the ionosphere-free, geometry-free, and wide-lane LC stem from the terminology used in the Bernese GPS Software.



### Melbourne-Wübbena Linear Combination

There is a special LC of dual-band phase and code measurements yielding unbiased observation equation for the wide-lane ambiguity parameters  $N_{ij,5}^{kl}$ . The corresponding LC was introduced by *Melbourne* [1985] and independently by *Wübbena* [1985]. In principle, this LC may be generated on any differencing level, the doubly differenced LC

$$N_{ij,5}^{kl} = \frac{\kappa_{1,5} L_{ij,1}^{kl} + \kappa_{2,5} L_{ij,2}^{kl} + \kappa_{3,5} P_{ij,1}^{kl} + \kappa_{4,5} P_{ij,2}^{kl}}{\lambda_5} \quad (2.31)$$

using the code multipliers

$$\kappa_{3,5} = -\nu_1/(\nu_1 + \nu_2) = -77/137 \approx -0.562 \quad (2.32a)$$

$$\kappa_{4,5} = -\nu_2/(\nu_1 + \nu_2) = -60/137 \approx -0.438 \quad (2.32b)$$

being the one used for ambiguity fixing. The phase multipliers  $\kappa_{1,5}$  and  $\kappa_{2,5}$  are given in (2.18). The code multipliers are remarkably small, holding  $\sqrt{\kappa_{3,5}^2 + \kappa_{4,5}^2} \approx 0.713 < 1$ .

It can be easily verified that the Melbourne-Wübbena LC completely eliminates (a) the geometry, including troposphere and clock offsets, and (b) the ionosphere:

$$\kappa_{1,5} + \kappa_{2,5} + \kappa_{3,5} + \kappa_{4,5} = 0 \quad (2.33a)$$

$$-\kappa_{1,5} - \xi \kappa_{2,5} + \kappa_{3,5} + \xi \kappa_{4,5} = 0 \quad (2.33b)$$

Therefore this LC is often used for zero-difference data screening, too. The LC (2.31) theoretically works even for very long baselines and even for roving receivers. However, to reliably fix wide-lane ambiguities  $N_{ij,5}^{kl}$ , P-code measurements  $P_{ij,1}^{kl}$  and  $P_{ij,2}^{kl}$  with a good quality are indispensable.

Let us mention that the code multipliers  $\kappa_{3,5}$  and  $\kappa_{4,5}$  may be derived by introducing the phase multipliers (2.18) into the two conditions (2.33) to be satisfied. This yields

$$\kappa_{3,5} + \kappa_{4,5} = -1 \quad (2.34a)$$

$$\kappa_{3,5} + \xi \kappa_{4,5} = \xi_5 \quad (2.34b)$$

where  $\xi = \nu_1^2/\nu_2^2$  and  $\xi_5 = -\nu_1/\nu_2$ . Solving (2.34) for  $\kappa_{3,5}$  and  $\kappa_{4,5}$  leads to (2.32).

### Hybrid Dual-Band Observables

It is the decision of the analyst whether he wants to process the ionosphere-free observable  $L_3$ , one or both of the original observables  $L_1$  and  $L_2$ , or any other LC. However, it is also possible to form a LC which is somewhere between a pure  $L_3$  and a combined  $L_1/L_2$  LC by simultaneously processing  $L_1$  and  $L_2$  as modeled in (2.12a) and (2.12b), setting up ionospheric parameters  $I$ , one parameter per satellite, epoch, and baseline, and, in order to avoid singularities, constrain the parameters to a model value (usually

zero) by adopting the zero-mean hypothesis [Bock *et al.*, 1986; Schaer, 1994]. In this way, we obtain a kind of hybrid dual-band observables which allows us to smoothly switch between the two “extreme” cases ( $L_3$  and  $L_1/L_2$ ), where the transition essentially takes place when the variance  $\sigma^2(I)$  of the artificial ionospheric observations is of the same order of magnitude as the variance  $\sigma^2(L_1)$  of the original observations [Schaer, 1994]. Such observables may be very useful for ambiguity resolution [Schaer, 1994; Mervart, 1995; Mervart *et al.*, 1995].

### 2.3.4 Ambiguity Resolution

The problem of the resolution of the initial carrier phase ambiguities is by itself a field of research. Examples of Ph.D. theses dealing with ambiguity resolution are [Frei, 1991] and [Mervart, 1995]. Essential contributions to this subject are due to Teunissen [1995]. Ambiguity resolution always relies on statistical hypotheses and may be seriously affected by biases not taken into account in the observation equations. Ionospheric biases play the crucial role in this context, unless the Melbourne-Wübbena LC and, subsequently, the ionosphere-free LC is used. For that reason, let us briefly review standard ambiguity resolution techniques.

Thanks to the changing “geometry” of the GPS satellites, it is possible to separate double-difference carrier phase ambiguity parameters, initially treated as real-valued parameters, from the other parameters, like station coordinates. The motivation to fix phase ambiguities to integers becomes plausible when comparing the code observation equation (2.16b) with the corresponding phase observation equation (2.15a), assuming the term  $\lambda_3 B_{ij,3}^{kl}$  as known:

$$L_{ij,3}^{*kl} = \rho_{ij}^{kl} \quad (2.35a)$$

$$P_{ij,3}^{kl} = \rho_{ij}^{kl} \quad (2.35b)$$

The “ambiguity-fixed” double-difference phase observations, indicated by an asterisk, are essentially millimeter-accurate code observations. Frei [1991] showed that in the case of rapid static GPS positioning the formal accuracy of the ambiguity parameters (and station coordinates) is primarily a function of the baseline occupation time  $\tau$ . These accuracies are proportional  $\tau^{-1}$  or  $\tau^{-3/2}$ , assuming the number of epochs or the data sampling rate to be constant, respectively. This results tells us also that ambiguity resolution is increasingly important and more difficult for shorter occupation times  $\tau$ . It is under such conditions that sophisticated ambiguity resolution strategies like that of Frei [1991] or Teunissen [1995] are of vital importance.

But even when processing 24-hour sessions, ambiguity resolution clearly improves the estimates of the remaining, non-ambiguity parameters, which are strengthened due to the reduction of unknown parameters and the corresponding increase of the degree of freedom. Mervart [1995] showed, on the basis of variance-covariance analyses and experimental studies, that the most prominent improvement concerns the east-west component

of station coordinates where one may gain a factor of about two compared to “ambiguity-float” solutions (for 24-hour sessions). Note that for shorter sessions the gain is more significant. To obtain best possible results, one is therefore obliged to perform ambiguity resolution even if long sessions are processed.

At present, only three IGS ACs perform ambiguity resolution on the global IGS network, namely CODE, officially since 25 June 1995 (GPS week 807), JPL, since 21 April 1996 (GPS week 850), and GFZ, since 16 October 1998 (GPS week 971).

### Directly Resolving L1 and L2 Ambiguities on Short Baselines

For short baselines with lengths up to several kilometers, one may try to neglect the ionospheric refraction. This leads to the following, simplified phase observation equations:

$$L_{ij,1}^{kl} = \rho_{ij}^{kl} + \lambda_1 N_{ij,1}^{kl} \quad (2.36a)$$

$$L_{ij,2}^{kl} = \rho_{ij}^{kl} + \lambda_2 N_{ij,2}^{kl} \quad (2.36b)$$

In the case of a static observation scenario with an occupation time longer than about one hour, it is usually no problem to fix the ambiguity parameters  $N_{ij,1}^{kl}$  and  $N_{ij,2}^{kl}$  to the correct integers because the corresponding confidence intervals deduced from the variance-covariance information normally contain exactly one integer which is then considered to be the correct one. This approach also works for single-band data, because the ambiguity parameters  $N_{ij,1}^{kl}$  and  $N_{ij,2}^{kl}$  are treated independently.

### The Fast Ambiguity Resolution Approach (FARA)

If only few minutes or, in the extreme case, only two epochs of dual-band phase observations are available, ambiguity resolution becomes more demanding because each confidence interval generally includes a selection of integers resulting in a tremendous number of possible ambiguity vectors. The Fast Ambiguity Resolution Approach (FARA) developed by *Frei and Beutler* [1990] allows to reliably resolve the initial phase ambiguities under such circumstances. The “backbone” of FARA is that it makes rigorously use of the complete variance-covariance information, especially for the geometry-free LC, the difference of the phase observation equations (2.36a) and (2.36b), which describes a particular LC of the dual-band ambiguities  $N_{ij,1}^{kl}$  and  $N_{ij,2}^{kl}$  with a few-millimeter accuracy, namely:

$$L_{ij,1}^{kl} - L_{ij,2}^{kl} = \lambda_1 N_{ij,1}^{kl} - \lambda_2 N_{ij,2}^{kl} \quad (2.37)$$

Not only the geometry-free LC but also all possible differences between ambiguities are checked and the candidates of statistically significant combinations are rejected. Mainly due to the above relationship—it corresponds to (2.25a) leaving out the double-difference ionospheric refraction term  $\xi_4 I_{ij}^{kl}$ —the dimension of the ambiguity search space can be approximately reduced by a factor of two resulting in a significant reduction of

the number of ambiguity vectors to be checked. The ambiguity vector which yields the smallest post-fit RMS error of unit weight is classified as the correct one—if, in addition, certain statistical criteria are met. This implies that either all ambiguities can be resolved or none (if FARA fails). For that reason, the distance between the new point and the reference station should be chosen as short as possible, because this is the user’s only way to limit the influence of the ionosphere, neglected in (2.36) and (2.37). For short baselines, the differenced ionosphere-induced errors increase in good approximation proportionally to the baseline length [Schaer, 1994].

### The LAMBDA Method

The LAMBDA (Least-squares AMBiguity Decorrelation Adjustment) method developed by Teunissen [1995] is mathematically equivalent to FARA, but it involves an ingenious integer transformation of the ambiguities prior to the actual search. Since the shape and orientation of the ambiguity search ellipsoid is dictated by the variance-covariance matrix of the ambiguities, one may realize an ambiguity search space that is nearly spherical by decorrelating the ambiguities. As a result, the search for integers can be carried out in a very fast and efficient way.

### Resolving Wide-Lane and Subsequently Narrow-Lane Ambiguities

By first resolving the wide-lane ambiguities  $N_5$  (2.29) by using the wide-lane LC (2.27) and then the narrow-lane ambiguities  $N_1$  (2.30) using the ionosphere-free LC (2.16a) and taking into account the previously resolved ambiguities  $N_5$ , the dual-band ambiguities  $N_1$  and  $N_2$  may be successfully fixed even on rather long baselines. Assuming an ionospheric error of half a cycle on  $L_2$ , the corresponding error on  $L_5$  still amounts to only 0.110 cycles. This arithmetic example, based on Table 2.2, demonstrates that the resolution of the wide-lane ambiguities is still possible when the ionospheric errors on  $L_1$  and  $L_2$  become too large to directly resolve the basic ambiguities  $N_1$  and  $N_2$ . The wide-lane approach is particularly useful if “mean” ionospheric refraction is taken into account by applying an ionosphere model.

Once the wide-lane ambiguities  $N_5$  are fixed, ionospheric refraction is no longer of importance. However, because of the short wavelength  $\lambda_3$  of the “narrow lane,” the geometric term  $\rho'_{ij}{}^{kl}$  of observation equation (2.16a) has to be known or estimated precisely, implying that adequate modeling of the troposphere and the use of precise GPS ephemerides become increasingly important for longer baselines.

### Pseudo-Range Approach

Using the Melbourne-Wübbena LC (2.31) to resolve the wide-lane ambiguities  $N_5$  leads to an ionosphere-independent approach. This approach relies on the availability of high-quality code measurements.

As in the previously discussed method, the resolution of the narrow-lane ambiguities  $N_1$  has to be performed in a subsequent step using the ionosphere-free LC. Because the percentage of resolved narrow-lane ambiguities cannot exceed that of the resolved wide-lane ambiguities, a percentage of towards hundred percent of fixed wide-lane ambiguities is a prerequisite. Due to the short narrow-lane wavelength  $\lambda_3$ , the accuracy requirements in terms of the GPS orbits are considerable when resolving narrow-lane ambiguities on long baselines. Using the rule of thumb by *Bauersima* [1983]

$$\frac{\delta l}{l} = \frac{\delta \rho}{\rho} \quad (2.38)$$

where

$\delta l$  is the maximum orbit-induced error in the baseline component,

$l$  is the baseline length,

$\delta \rho$  is the maximum orbital error to be expected, and

$\rho \approx 20\,000$  km is the altitude of the GPS satellites,

one can roughly estimate the maximally allowed baseline length that still guarantees a successful resolution of the narrow-lane ambiguities for a particular orbit quality.

If a maximum orbit-induced error of  $\delta l = 1$  cm, a tenth of  $\lambda_3$ , is tolerated and if the maximum orbital error is assumed to be  $\delta \rho = 10$  cm (or  $\delta \rho / \rho = 5$  ppb), the maximum baseline length is obtained to  $l = 2000$  km. Note that this approximate limit concerning the baseline length is tremendously reduced if broadcast orbits instead of precise orbits are used.

### The Quasi-Ionosphere-Free (QIF) Ambiguity Resolution Strategy

The QIF strategy allows to directly resolve the basic phase ambiguities  $N_1$  and  $N_2$  on long baselines without making use of P-code measurements. It was developed by *Schaer* [1994] and *Mervart* [1995]. The “quasi-ionosphere-free” ambiguity resolution strategy can cope with larger ionospheric errors than the traditional phase-based wide-lane method, namely errors up to two  $L_5$ -cycles minus a given search width. Unlike the two-step ambiguity resolution procedure via wide-lane and narrow-lane LCs, the QIF strategy requires only one operation, where the dual-band phase observations  $L_1$  and  $L_2$  are processed together according to observation equations (2.12a) and (2.12b) and where ionospheric parameters  $I_{ij}^{kl}$  are set up, slightly constrained, and pre-eliminated epoch by epoch. The basic ambiguities  $N_1$  and  $N_2$  that meet certain statistical criteria are resolved pair by pair doing a full inversion of the updated normal equation system after each fixed ambiguity pair—thus increasing the probability to resolve the remaining

ambiguities. One essential QIF criterion concerns the deviation of the estimated quantity  $B_{ij,3}^{kl}$  in (2.17) from the “true” value  $B_{ij,3}^{*kl}$

$$\Delta B_{ij,3}^{kl} = B_{ij,3}^{kl} - B_{ij,3}^{*kl} = (\kappa_{1,5} N_{ij,1}^{kl} + \kappa_{2,5} N_{ij,2}^{kl}) - (\kappa_{1,5} N_{ij,1}^{*kl} + \kappa_{2,5} N_{ij,2}^{*kl}) \quad (2.39)$$

where  $N_{ij,1}^{*kl}$  and  $N_{ij,2}^{*kl}$  denote the true pair of integers.  $\Delta B_{ij,3}^{kl}$  is expected to be zero and may normally be determined with a few-millimeter accuracy. Because the wavelength internally used by the QIF strategy is approximately half that of the narrow-lane wavelength  $\lambda_3$ , it is of fundamental importance that all conceivable double-difference ambiguity parameters are formed and tested. The Bernese GPS Software uses an elaborate ambiguity cluster logic to manage the bookkeeping of fixed ambiguities.

The QIF ambiguity resolution strategy, designed for large-area permanent networks, is used by CODE for regional and global ambiguity resolution. To increase the percentage of ambiguities fixed by QIF, GPS-derived regional and global ionosphere maps are taken into account.

### Summary

Apart from the pseudo-range approach, all ambiguity resolution methods are influenced by ionospheric refraction. Assumptions concerning the the ionosphere—either by totally neglecting it or by assuming the remaining, unmodeled ionospheric errors to be within certain, acceptable limits—are required. Under AS, some of the receiver types do not allow for the pseudo-range approach.

The Bernese GPS Software supports all ambiguity resolution strategies presented here except for the LAMBDA method. For technical details concerning ambiguity resolution, the reader is referred to [Rothacher and Mervart, 1996].

## 2.4 Least-Squares Adjustment Recapitulated

Because we use least-squares adjustment to derive ionospheric parameters from GPS data, this particular parameter estimation algorithm is briefly recapitulated.

Based on a given mathematical model described by the vectorial model function  $\Psi$ , we may formulate the observation equation system

$$\mathbf{L} + \mathbf{v} = \Psi(\mathbf{X}) \quad (2.40)$$

or its linearized version

$$\mathbf{L} + \mathbf{v} = \Psi(\mathbf{X}_0) + \mathbf{A} \mathbf{x} \quad (2.41)$$

using the notation:

$\mathbf{L}$  is the one-dimensional array of the actual observations,

- $\mathbf{v}$  is the array of the observation corrections (or the residual vector),
- $\mathbf{L} + \mathbf{v} = \bar{\mathbf{L}}$  is the array of the adjusted observations,
- $\mathbf{X} = \mathbf{X}_0 + \mathbf{x}$  is the array of the unknown model parameters to be adjusted,
- $\mathbf{X}_0$  is the array of the approximate model parameters,
- $\mathbf{x}$  is the array of the model parameter corrections (or the solution vector) with respect to the approximate model parameters  $\mathbf{X}_0$ , and
- $\mathbf{A}$  is the first design (or Jacobi) matrix.

The first design matrix is defined by

$$\mathbf{A} = \left. \frac{\partial \Psi(\mathbf{X})}{\partial \mathbf{X}} \right|_{\mathbf{x}=\mathbf{x}_0} \quad (2.42)$$

Solving the linearized observation equation system (2.41) for the residual vector  $\mathbf{v}$  leads to the equation system

$$\mathbf{v} = \mathbf{A} \mathbf{x} - (\mathbf{L} - \Psi(\mathbf{X}_0)) = \mathbf{A} \mathbf{x} - \mathbf{l} \quad (2.43)$$

where  $\mathbf{l} = \mathbf{L} - \Psi(\mathbf{X}_0)$  corresponds to the term “observed-minus-computed” (O–C).

The stochastic model for the observations is described by

$$\mathbf{P} = \mathbf{Q}_u^{-1} = \sigma_0^2 \mathbf{C}_u^{-1} \quad (2.44)$$

where

- $\mathbf{P}$  is the weight matrix of the observations,
- $\mathbf{Q}_u^{-1}$  is the cofactor matrix of the observations,
- $\sigma_0$  is the a priori standard deviation of unit weight, and
- $\mathbf{C}_u$  is the covariance matrix of the observations.

Note that the weight matrix  $\mathbf{P}$  is a diagonal matrix, if the observations are uncorrelated. The diagonal elements of  $\mathbf{P}$  are then simply given by  $P_{ii} = \sigma_0^2/\sigma_i^2$ , where  $\sigma_i^2$  is the a priori variance of the corresponding observation. In the simplest case, when treating all observations as uncorrelated and of equal accuracy, the matrix  $\mathbf{P}$  becomes an identity matrix  $\mathbf{I}$ .

The solution of the equation system (2.43) is obtained by minimizing the scalar function  $\mathbf{v}^T \mathbf{P} \mathbf{v}$ . This is easily achieved, e. g., by introducing Lagrange multipliers and yields the normal equation system

$$(\mathbf{A}^T \mathbf{P} \mathbf{A}) \mathbf{x} - \mathbf{A}^T \mathbf{P} \mathbf{l} = \mathbf{N} \mathbf{x} - \mathbf{b} = \mathbf{0} \quad (2.45)$$

where

$\mathbf{N} = \mathbf{A}^T \mathbf{P} \mathbf{A}$  is the normal equation matrix and

$\mathbf{b} = \mathbf{A}^T \mathbf{P} \mathbf{l}$  is the right hand side of the normal equation system.

The solution vector follows as

$$\mathbf{x} = (\mathbf{A}^T \mathbf{P} \mathbf{A})^{-1} \mathbf{A}^T \mathbf{P} \mathbf{l} = \mathbf{N}^{-1} \mathbf{b} \quad (2.46)$$

The estimated standard deviation  $m_0$  of unit weight is computed as

$$m_0 = \sqrt{\frac{\mathbf{v}^T \mathbf{P} \mathbf{v}}{f}} \quad \text{if } f > 0 \quad (2.47)$$

where

$f = n - u$  denotes the degree of freedom (DOF) of the least-squares adjustment,

$n$  is the number of observations, and

$u$  is the number of adjusted model parameters.

The sum of the weighted residual squares,  $\mathbf{v}^T \mathbf{P} \mathbf{v}$ , may be computed using (2.43) or, alternatively, by

$$\mathbf{v}^T \mathbf{P} \mathbf{v} = \mathbf{l}^T \mathbf{P} \mathbf{l} - \mathbf{x}^T \mathbf{b} \quad (2.48)$$

The covariance matrix of the adjusted model parameters is given by

$$\mathbf{C}_{\mathbf{x}\mathbf{x}} = m_0^2 \mathbf{Q}_{\mathbf{x}\mathbf{x}} = m_0^2 \mathbf{N}^{-1} \quad (2.49)$$

where

$\mathbf{Q}_{\mathbf{x}\mathbf{x}}$  denotes the cofactor matrix of the model parameters and

$\mathbf{N}^{-1}$  the inverse normal equation matrix, respectively.

The estimated standard deviations of individual model parameters are

$$m_x = \sqrt{C_{xx}} = m_0 \sqrt{Q_{xx}} \quad (2.50)$$

where  $C_{xx}$  and  $Q_{xx}$  are diagonal elements of the covariance and cofactor matrices of the model parameters.

The general variance-covariance propagation law for the particular function  $\mathbf{y} = \mathbf{B} \mathbf{x} + \mathbf{y}_0$  reads as

$$\mathbf{C}_{\mathbf{y}\mathbf{y}} = \mathbf{B} \mathbf{C}_{\mathbf{x}\mathbf{x}} \mathbf{B}^T \quad (2.51)$$



Note that the covariance matrices  $\mathbf{C}$  in (2.51) may be replaced by the cofactor matrices  $\mathbf{Q}$  because of the linear relationship

$$\mathbf{C} = \sigma_0^2 \mathbf{Q} \quad (2.52)$$

where  $\sigma_0^2$  is the variance of unit weight.

For outlier detection, the cofactor (or covariance) matrix of the residual vector  $\mathbf{v}$

$$\mathbf{Q}_{vv} = \mathbf{Q}_{ll} - \mathbf{Q}_{ll} = \mathbf{P}^{-1} - \mathbf{A} \mathbf{Q}_{xx} \mathbf{A}^T \quad (2.53)$$

is of interest, especially, when the observations are differently weighted. Normalizing the residuals to

$$v' = \frac{v}{m_v} \quad \text{with} \quad m_v = m_0 \sqrt{Q_{vv}} \quad (2.54)$$

where

$m_v$  is the estimated standard deviation of the residual considered and

$Q_{vv}$  is the corresponding diagonal element of the cofactor matrix  $\mathbf{Q}_{vv}$ ,

yields normally distributed variables  $v'$ , which are characterized by a standard deviation of 1 (and an expectation value of 0). Each element of the normalized residual vector  $\mathbf{v}'$  can thus be statistically tested taking a certain significance level as basis. Note that  $m_l = m_0 \sqrt{Q_{ll}}$  is a good approximation for  $m_v$ , if  $m_i = m_0 \sqrt{Q_{ii}}$  is comparatively small.

If one is interested in the estimated RMS error of unit weight referred to a group of observations, the corresponding degree of freedom is required. The diagonal elements of the  $n \times n$  matrix

$$\mathbf{F} = \mathbf{P} \mathbf{Q}_{vv} \quad (2.55)$$

give that part of the degree of freedom contributed by each observation. The trace of  $\mathbf{F}$  hence corresponds exactly to the total degree of freedom  $f$ :

$$\sum_{i=1}^n F_{ii} = f = n - u \quad (2.56)$$

### Constraining Model Parameters

It is often necessary to constrain a particular model parameter  $X$  to a certain extent to its a priori value  $X_0$ . This may be done by introducing an “artificial” observation also called “pseudo-observation,” with a certain variance. Such pseudo-observations are, e. g., useful to introduce a priori information about the ionosphere when estimating epoch-specific ionosphere parameters  $I_{ij}^{kl}$ .

In principle, such a pseudo-observation has to be appended to the observation equation system (2.41). Because the value of  $O-C$  is zero for such a pseudo-observation—at least if its change with respect to the a priori value is used as the actual parameter, the weight

$$W = \frac{\sigma_0^2}{\sigma_{\text{abs}}^2} \quad (2.57)$$

has to be added to the corresponding diagonal element of the normal equation matrix  $\mathbf{N}$ . Moreover, the observation and DOF counters have to be incremented by 1.

### Constraining Linear Combinations of Model Parameters

In order to constrain the difference of two particular model parameters, the  $2 \times 2$  weight matrix  $\mathbf{W}$  given by

$$\mathbf{W} = \begin{pmatrix} W & -W \\ -W & W \end{pmatrix} \quad \text{with} \quad W = \frac{\sigma_0^2}{\sigma_{\text{rel}}^2} \quad (2.58)$$

has to be added to the normal equation matrix  $\mathbf{N}$ , that is, the values  $W$  and  $-W$  have to be added to the diagonal and off-diagonal elements corresponding to the two parameters involved. The observation and DOF counters should be again incremented by 1. Pseudo-observations of this type are particularly useful to limit the variability of parameters with a high temporal resolution, implying that all consecutive parameter pairs have to be constrained accordingly.

Note that in such a way any linear combination of model parameters may be constrained by introducing an appropriate weight matrix  $\mathbf{W}$ .

### Parameter Pre-Elimination

The principle of parameter pre-elimination is addressed because it will be used to “economically” handle the epoch-specific ionosphere parameters  $I_{ij}^{kl}$ . Let us arbitrarily subdivide the normal equation system (2.45) into two partial systems:

$$\begin{pmatrix} \mathbf{N}_{11} & \mathbf{N}_{12} \\ \mathbf{N}_{21} & \mathbf{N}_{22} \end{pmatrix} \begin{pmatrix} \mathbf{x}_1 \\ \mathbf{x}_2 \end{pmatrix} = \begin{pmatrix} \mathbf{b}_1 \\ \mathbf{b}_2 \end{pmatrix} \quad (2.59)$$

Assuming that we are not interested in the actual values of the solution subvector  $\mathbf{x}_2$  and that we want to keep the size of our normal equation system small, we may reduce the normal equation system (2.59) by pre-eliminating the model parameters  $\mathbf{x}_2$ . This pre-elimination step leads to the modified normal equation system

$$\tilde{\mathbf{N}}_{11} \mathbf{x}_1 = \tilde{\mathbf{b}}_1 \quad (2.60)$$

where

$\tilde{\mathbf{N}}_{11} = \mathbf{N}_{11} - \mathbf{N}_{12} \mathbf{N}_{22}^{-1} \mathbf{N}_{21}$  is the modified normal equation matrix of the remaining model parameters  $\mathbf{x}_1$ ,

$\tilde{\mathbf{b}}_1 = \mathbf{b}_1 - \mathbf{N}_{12} \mathbf{N}_{22}^{-1} \mathbf{b}_2$  is the corresponding right hand side of the normal equation system, and

$\mathbf{N}_{22}$  is the normal equation submatrix corresponding to the current parameter pre-elimination step.

It is important to know that the pre-eliminated model parameters  $\mathbf{x}_2$  were correctly taken into account, but that their estimates are no longer available in the solution vector (2.46).

The weighted sum  $\mathbf{v}^T \mathbf{P} \mathbf{v}$  may then be computed using (2.48) for the modified normal equation system (2.60):

$$\mathbf{v}^T \mathbf{P} \mathbf{v} = \tilde{\mathbf{l}}^T \mathbf{P} \tilde{\mathbf{l}} - \mathbf{x}_1^T \tilde{\mathbf{b}}_1 \quad (2.61)$$

where the term  $\tilde{\mathbf{l}}^T \mathbf{P} \tilde{\mathbf{l}} = \mathbf{l}^T \mathbf{P} \mathbf{l} - \mathbf{b}_2^T \mathbf{N}_{22}^{-1} \mathbf{b}_2$  has to be updated for each parameter pre-elimination step performed.

### Manipulating and Stacking Normal Equation Systems

It may be a very economic procedure to combine solutions on the normal equation level. By saving the arrays  $\mathbf{N}$ ,  $\mathbf{b}$ ,  $\mathbf{X}_0$ ,  $\mathbf{l}^T \mathbf{P} \mathbf{l}$  (or  $m_0$ ),  $n$ ,  $u$ , and the associated parameter characterization for each individual normal equation system, it is possible to subsequently manipulate and stack a set of normal equation systems in a mathematically correct way [Brockmann, 1997].



# 3. Extracting Ionospheric Information from GPS Data

## 3.1 The Earth's Ionosphere

The Earth's ionosphere is defined as that part of the upper atmosphere where sufficient ionization exists to affect the propagation of radio waves. With slight exaggeration, the ionosphere may be considered as lying between the Earth's neutral atmosphere and the Sun's fully ionized atmosphere, in which the Earth is embedded. Whereas the wave propagation through the neutral atmosphere (or troposphere) mainly depends on pressure, temperature, and water vapor content, the wave propagation through the ionosphere is primarily affected by the number of free electrons along the ray path. It is a well-known property of the ionosphere that its structure and peak electron density vary strongly with time, geographic location, and certain solar and geomagnetic disturbances. The dynamics of the ionosphere is remarkable. Variations of, e.g., one to two orders of magnitude in the electron content are not rare events.

### 3.1.1 Ionization Processes and Vertical Profile

Solar radiation plays a key role in the formation of the ionosphere. The ionization, the breaking away of electrons from atoms and molecules, is primarily caused by the impact of solar ultraviolet radiation. Because the absorption of ultraviolet light increases with decreasing altitude and increasing number of neutral atmospheric molecules, respectively, a layer of maximum electron density results.

#### **Ionospheric Regions and Layers**

The peak electron density usually occurs in the F region which begins at about 150 kilometers above the Earth's surface. The sunlit F region is split up into the F1 layer and the F2 layer, which are produced by extreme ultraviolet light. Below the F region we find the E region, produced by soft X-rays. Often patches of ionization in the E region

occur, which do not seem to be related to the normal day-time E layer. This phenomenon is known as “sporadic E.” The lowest region, the D region, contains both the D layer, produced by hard X-rays, and the cosmic ray (or C) layer.

In the F2 layer, we usually find the maximum electron density. The region below the F2 layer containing the series of distinct shells D, E, and F1, is collectively referred to as the bottomside of the ionosphere; the region above it is denoted the topside of the ionosphere. Owing to the pervasive influence of gravity, the ionosphere is to first order horizontally stratified, practically covering the region between approximately 50 and 1500 kilometers above the Earth’s surface. At higher altitudes, the number of free electrons is marginal, at least compared to that of the dominant F layers. In fact, the upper boundary of the ionosphere is not well defined since the electron density thins into the plasmasphere and subsequently into the interplanetary plasma.

### Chapman Profile

For the simplest case of a parallel, monochromatic beam of solar radiation ionizing a one-component isothermal gas in a horizontally stratified shell, the rate of production of ion pairs is given by the Chapman function [Davies, 1989]

$$q(h, \chi) = q_0 e^{(1-z-\sec \chi e^{-z})} \quad \text{with} \quad z = \frac{h - h_0}{\Delta h} \quad (3.1)$$

where

$q(h, \chi)$  is the ion production rate,

$h$  is the altitude,

$\chi$  is the zenith angle with respect to the Sun,

$q_0$  is the ion production rate at  $z = 0$ ,

$z$  is the scaled altitude,

$h_0$  is the reference height of maximum ion production when the Sun is overhead (or  $\chi = 0$ ), and

$\Delta h$  is the scale height.

The ion production rate  $q_0$  is given by

$$q_0 = \frac{\phi(\infty) \eta}{\Delta h e} \quad (3.2)$$

where

- $\phi(\infty)$  is the solar flux density outside the atmosphere in units of photons per unit area,
- $\eta$  is the number of ion pairs produced per photon, and
- $e$  is the base of the natural exponential function.

The altitude  $h_{\max}$  of the maximum ion production is obtained by differentiating the Chapman function (3.1), which yields

$$h_{\max} = h_0 + \Delta h z_{\max} \quad \text{with} \quad z_{\max} = \ln \sec \chi \quad (3.3)$$

The peak of the ion production is

$$q_{\max} = q_0 \cos \chi \quad (3.4)$$

In the E and F1 layers, ions may be assumed to recombine with electrons at a rate which depends quadratically on the electron density  $N_e$ . Omitting the term due to transportation processes, the following continuity equation holds:

$$\frac{dN_e}{dt} = q - \alpha N_e^2 \quad (3.5)$$

where  $\alpha$  is the mean recombination coefficient for molecular ions. Note that (3.5) is not valid at high levels in the ionosphere—with low densities. There, the loss rate depends linearly on  $N_e$ .

In photochemical equilibrium, that is, when  $dN_e/dt = 0$ , the electron density distribution corresponding to the Chapman function (3.1) is

$$N_e(z, \chi) = N_{e,0} e^{\frac{1}{2}(1-z-\sec \chi e^{-z})} \quad \text{with} \quad N_{e,0} = \left(\frac{q_0}{\alpha}\right)^{\frac{1}{2}} \quad (3.6)$$

where  $N_{e,0}$  is the electron density at  $z = 0$ . This distribution is called alpha-Chapman or simply Chapman layer [*Rishbeth and Garriott, 1969*].

The altitude of the maximum electron density is identical to that of the maximum ion production given in (3.3). The peak of the electron density is

$$N_{e,\max}(\chi) = N_{e,0} \cos^{\frac{1}{2}} \chi \quad (3.7)$$

It is important to mention that although most of the assumptions underlying the simple Chapman layer do not apply in the upper atmosphere, the Chapman theory is an invaluable guide in providing a useful reference [*Kelley, 1989*].

The ion production rate (3.1) and the resulting electron density distribution (3.6) are shown in Figures 3.1 and 3.2, assuming a reference altitude of  $h_0 = 350$  km, a scale height of  $\Delta h = 100$  km, and the solar zenith angle  $\chi = 0$ , meaning that the altitude  $h_{\max}$  equals

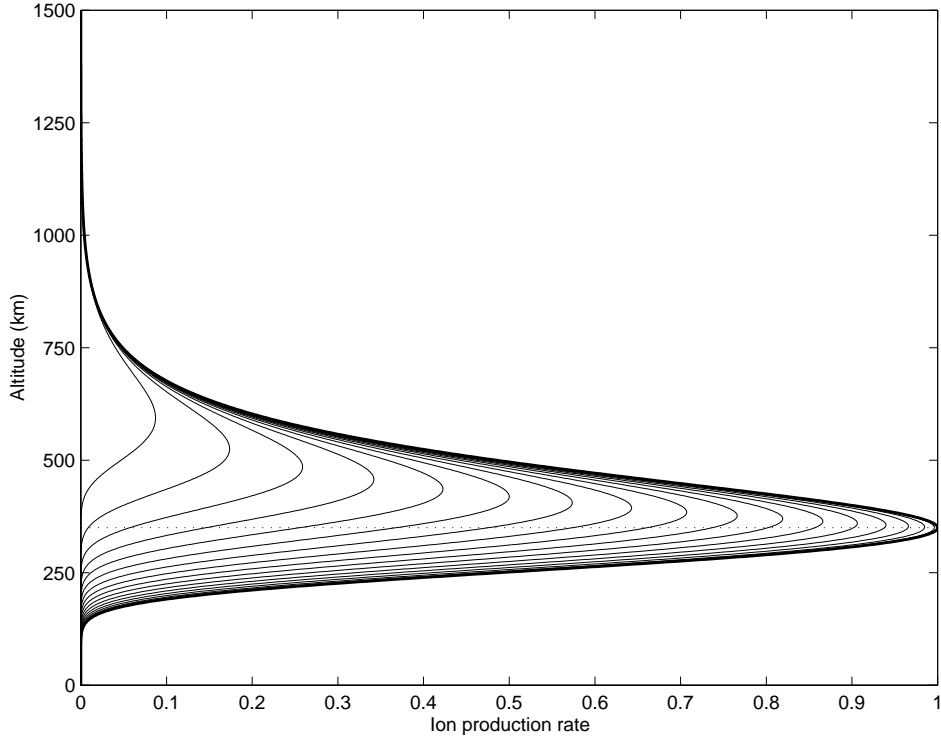


Figure 3.1: Chapman ion production rate for solar zenith angles  $\chi$  of  $0^\circ$ , and  $5^\circ$  to  $85^\circ$  in steps of  $5^\circ$ .

$h_0$  indicated by the dotted line. Profiles for solar zenith angles of  $5^\circ$ ,  $10^\circ$ ,  $15^\circ$ , ...,  $85^\circ$  are drawn with thinner lines. The ion production rate and the electron density are labeled in units of  $q_0$  and  $N_{e,0}$ , respectively. Changing the intensity of the solar flux  $\phi(\infty)$  changes the peak values  $q_{\max}$  and  $N_{e,\max}$ , but does not affect the corresponding altitude  $h_{\max}$ .

Inspecting the electron density distribution (3.6) reveals that at noon  $N_{e,\max}$  theoretically reaches its maximum, and  $h_{\max}$  its minimum. Once the solar radiation source is absent, the electron density decreases. On the “obscured” hemisphere, the electron density should be low and fairly stable. We see that the electron density strongly depends on the relative position of the Sun and the solar zenith angle  $\chi$ , respectively, implying a pronounced diurnal variation as well as a seasonal variation in the electron concentration. This dependence of the ionospheric state on the solar position can be effectively used for temporal and spatial modeling of electron density.

After ionization, the free electrons tend to react with other molecules, which implies that not only photochemical processes but also transportation processes determine the spatial distribution of electrons and ions in the ionosphere. The prevailing vertical electron



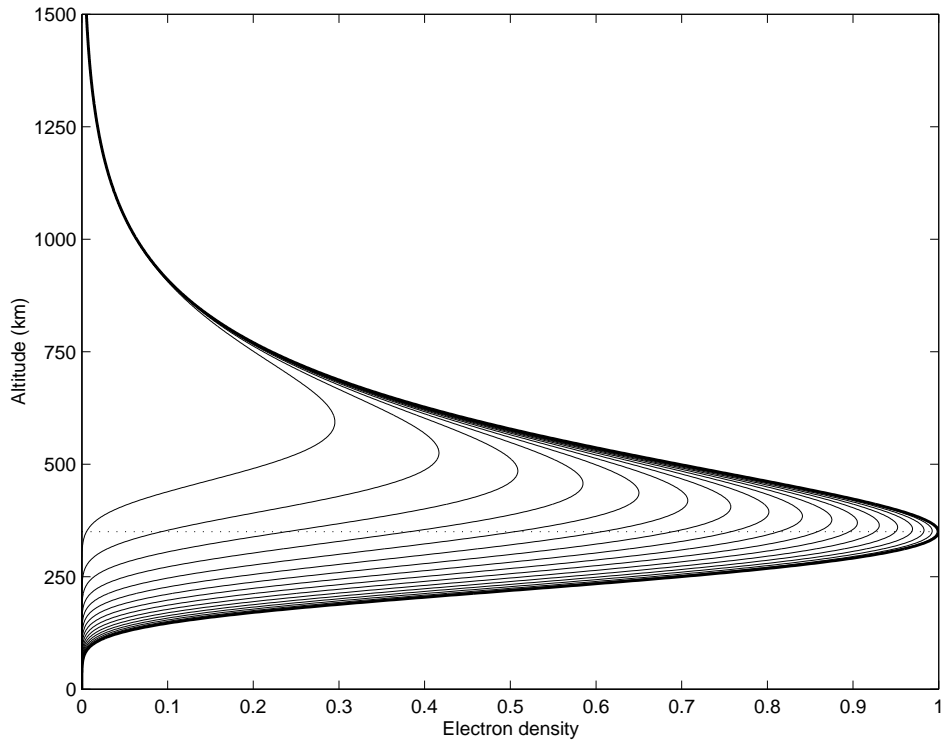


Figure 3.2: Vertical electron density distribution of a Chapman layer for solar zenith angles  $\chi$  of  $0^\circ$ , and  $5^\circ$  to  $85^\circ$  in steps of  $5^\circ$ .

density profiles may hence differ from profiles expected by the Chapman theory.

For transportation processes, the Earth's magnetic field is of crucial importance. The motion of a charged particle in the geomagnetic field is a combination of gyration around a magnetic field line, bouncing along a field line, and drifting azimuthally around the Earth. Therefore, it seems reasonable to use geomagnetic coordinates for the global description of the electron density.

### The Earth's Magnetic Field

Near the surface of the Earth, the geomagnetic field may be approximated by an earth-centered dipole. At altitudes higher than a few earth radii, however, the magnetic field lines get distorted by the solar wind. The dipole axis intersects the surface of the Earth at the south and north geomagnetic poles. The intersection between the plane through the earth center perpendicular to the dipole axis and the earth surface is called geomagnetic (or dip) equator. According to the International Geomagnetic Reference Frame, IGRF 95,

the geographic latitude and east longitude of the north geomagnetic (or dip) pole are  $79.41^\circ$  and  $-71.64^\circ$  for the epoch 1998.5, slowly moving with about  $+0.03^\circ$  and  $-0.07^\circ$  per year.

### **Geographic Regions of the Ionosphere**

Peak values of electron density usually are encountered in the equatorial region of the ionosphere, normally in the early afternoon. There are also regions of very high electron concentrations at geomagnetic latitudes of about  $\pm 20^\circ$  during the early evening. Their maxima are referred to as the equatorial anomaly. Plasma instability phenomena occurring in the equatorial F region are grouped under the generic name “equatorial spread F” (ESF). Such plasma instabilities occur primarily at night and are noticed through considerable fluctuations in the electron content, and that, interestingly, in a zone where the degree of ionization is comparatively low.

The mid-latitude ionosphere shows least variations. It is also the best observed because most of the ionosphere-sensing instruments are located in this region.

In high latitudes and in the auroral regions, the peak electron densities are considerably smaller than in lower latitudes. However, the high-latitude sector is extremely rich in plasma instabilities, which means that short-time variations of the electron density are generally much more pronounced there than at lower latitudes.

At the polar caps, where the solar zenith angle is essentially constant, a diurnal variation is still detectable. This shows that factors apart from solar illumination play a role in determining the electron density.

### **Ionospheric Irregularities**

So-called traveling ionospheric disturbances (TIDs) may cause variations in the integrated electron density of several percent. One distinguishes between

- large-scale TIDs (LSTIDs), having periods ranging from 30 minutes to 3 hours and horizontal wavelengths exceeding 1000 kilometers,
- medium-scale TIDs (MSTIDs), having periods from about 10 minutes to 1 hour and horizontal wavelengths of several hundreds of kilometers, and
- small-scale TIDs (SSTIDs), having periods of several minutes and wavelength of tens of kilometers [*Spoelstra, 1992*].

Little is known about the climatology of ionospheric irregularities. Although TIDs are often seen in mid latitudes, they are thought to be a global phenomenon.

Smallest-scale structures in the electron density distribution cause scintillation effects, rapid variations in the line-of-sight electron content. Ionospheric scintillations primarily emerge in the equatorial, high-latitude, and polar regions.

Last but not least, exceptionally vast ionospheric events, so-called ionospheric storms, may occur. These events are often coupled with severe disturbances in the magnetic field (magnetic storms) and intense solar eruptions (solar flares). An ionospheric storm usually results in a tremendous growth of the number of electrons. The pattern of ionospheric storms, where strong latitudinal and longitudinal asymmetries exist, may vary considerably from one event to the next, what makes it impossible to reasonably predict ionospheric storms.

For details related to ionosphere physics, the interested reader is referred, e. g., to [Davies, 1989; Kelley, 1989; Ratcliffe, 1972; Rishbeth and Garriott, 1969] or [Wild, 1994].

### 3.1.2 Solar Activity

Since ionization is driven largely by electromagnetic and corpuscular radiation from the Sun, it is a function of solar activity. Sunspots, first noticed by Theophrastus around 325 BC, are among the most notable phenomena on the solar surface characterizing the solar activity. Sunspots appear dark because the surface temperature is low compared to that of the ambient solar photosphere. Their life-span is highly variable. Some spots last for a few days only whereas others survive for several solar rotation periods of about 27 days.

The occurrence of sunspots is measured by the Wolf, or Zurich, sunspot number  $R$ , which is defined by

$$R = 10g + s \quad (3.8)$$

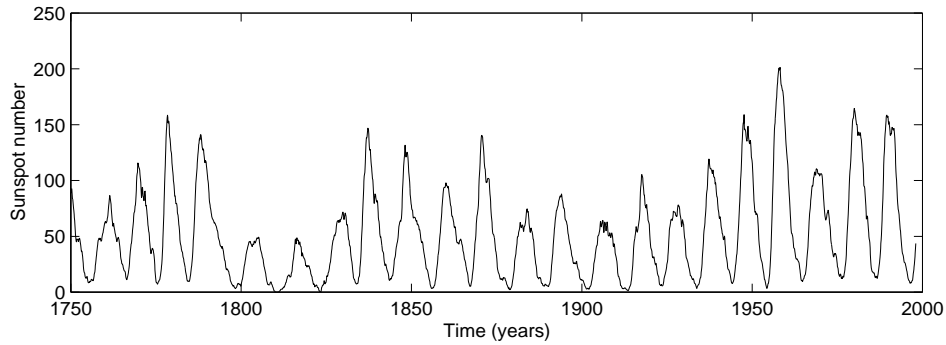
where

$g$  is the number of sunspot groups and

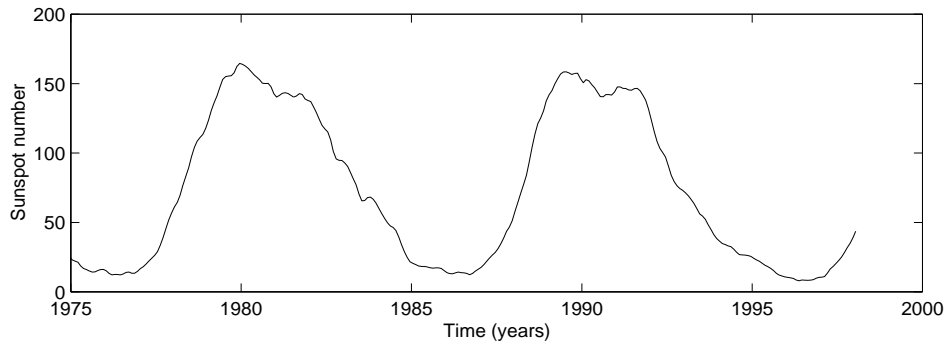
$s$  is the number of individual spots.

The division into  $g$  and  $s$  is somewhat arbitrary. Therefore the sunspot number  $R$  is to a certain amount a subjective index, depending on the observer and equipment characteristics. Nevertheless, it is valuable as a long-term index because sunspot number time series are available over several hundred years, as daily values and as monthly and yearly averages.

Figure 3.3a shows the evolution of the monthly smoothed sunspot number, obtained from *SIDC* [1998], over nearly two and a half centuries. A spectral analysis of the sunspot number time series indicates the presence of periods of about 80 years, 22 years, and 11 years, and a pronounced 27-day periodicity caused by the solar rotation. Figure 3.3b



(a) Solar cycles 1 to 22



(b) Solar cycles 21 and 22

Figure 3.3: Monthly smoothed sunspot number [*SIDC*, 1998].

reveals that the recent solar maximum occurred in 1989, that the recent minimum occurred in 1996, and that the next solar maximum—decisively influencing the ionospheric conditions—is approaching. The maximum of the solar cycle 23 is expected to occur in the time period 2000–2001.

### 3.1.3 Integrated Electron Density

The state of the ionosphere is described by the electron density  $N_e$  in units of electrons per cubic meter. For the propagation of microwaves through the ionosphere, however, the electron density integrated along the ray path, generally called total electron content (TEC), is the important ionospheric quantity. The TEC is usually expressed in TEC

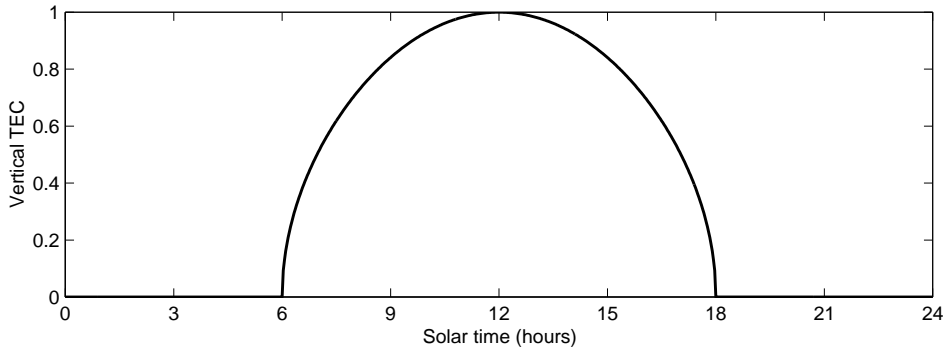


Figure 3.4: Vertical TEC  $E_v$  of a Chapman layer as a function of the solar time, in units of  $E_v(\chi = 0)$ .

units (TECU), where one TECU corresponds to  $10^{16}$  electrons contained in a cylinder aligned along the line of sight with a cross-section of one square meter. The line-of-sight or slant TEC  $E$  is the integral

$$E = \int N_e(\rho) d\rho \quad (3.9)$$

where  $N_e(\rho)$  denotes the electron density along the ray path.  $E$  in TECU gives the number of electrons in  $10^{16}$  electrons per square meter. It is important to note that the term TEC is often used to designate the vertical TEC (VTEC), that is, the slant TEC reduced to the vertical.

The vertical TEC based on the Chapman electron density profile (3.6) may be obtained by integrating

$$E_v(\chi) = \int_0^{\infty} N_e(h, \chi) dh \quad (3.10)$$

Figure 3.4 shows this integral as a function of the solar time, assuming that the geographic latitude equals the declination of the Sun.  $E_v(\chi)$  is proportional to the maximum electron density (3.7), which in turn is proportional to  $\cos^{\frac{1}{2}} \chi$ . Therefore,  $E_v(\chi)$  expressed in units of  $E_v(0)$  exactly results in  $\cos^{\frac{1}{2}} \chi$ .

In conclusion, one may say that a cosine-shaped TEC bulge co-rotating with the Sun, as postulated by *Klobuchar* [1987], should to the first order approximate the global TEC distribution on the sunlit hemisphere. However, one has to roughly know the amplitude  $E_v(\chi = 0)$ , which itself is subjected to considerable variations. During a solar cycle maximum, the vertical TEC  $E_v$  may reach values clearly above 200 TECU.

### 3.2 Wave Propagation Delays due to the Ionosphere

The minimum frequency of an electromagnetic wave penetrating an ionospheric layer is called critical (or plasma) frequency of the particular layer. The square of the critical frequency is proportional to the maximum electron density of the layer. Electromagnetic waves with frequencies below 30 MHz are reflected by the ionosphere, which means that the ionosphere is essential for radio communication. For frequencies much above 50 MHz, which penetrate the ionosphere, the ionosphere is a source of nuisance. Hence, the developers of space-based navigation systems aim at upper frequency bands on which undesirable ionospheric effects are less pronounced.

The influence of the ionosphere on electromagnetic waves with frequencies above 100 MHz has been studied in detail by several authors, e. g., by *Hartmann and Leitinger* [1984]. The most relevant results are summarized below.

The refractive index  $n$ , defined as

$$n = \frac{c}{v} \quad (3.11)$$

where

$c$  is the speed of light in vacuum and

$v$  is the speed of light in the medium,

describes the propagation of an electromagnetic wave in a given medium.

Whereas the refractive index in the troposphere, with  $n_{\text{trop}} > 1$ , is frequency-independent for microwaves, the refractive index in the ionosphere, with  $n_{\text{ion}} < 1$  for phase, depends on the frequency. This implies that the ionosphere is a dispersive medium. For GPS observations, one has to take into account that codes do not propagate with the phase velocity but with the group velocity, which means that  $n_{\text{ion}} > 1$  for code signals.

A general derivation of the refractive index in the ionosphere is given, e. g., by *Budden* [1985]. According to *Brunner and Gu* [1991], the refractive index  $n_{\text{ion}}$  can be expanded in the reciprocal frequency of the electromagnetic wave as

$$n_{\text{ion}} = 1 - \frac{C_X}{2} N_e \nu^{-2} \pm \frac{C_X C_Y}{2} N_e H_0 \cos \theta \nu^{-3} - \frac{C_X^2}{8} N_e^2 \nu^{-4} \quad (3.12)$$

with the constants

$$C_X = \frac{e^2}{4\pi^2 \varepsilon_0 m_e} \quad (3.13a)$$

$$C_Y = \frac{\mu_0 e}{2\pi m_e} \quad (3.13b)$$

where

$N_e$	is the electron density,
$H_0$	is the magnetic field strength,
$\theta$	is the angle between the propagation direction of the electromagnetic wave and the vector of the geomagnetic field,
$e$	is the charge of one electron,
$\varepsilon_0$	is the permittivity in the vacuum,
$m_e$	is the mass of electrons, and
$\mu_0$	is the permeability in the vacuum.

(3.12) has been derived from the Appleton-Hartree formula for  $n_{\text{ion}}^2$  and includes all terms whose magnitude is larger than one ppb for GPS observations. The different signs for the third-order term account for two possible polarization modes.

Because the third- and fourth-order terms of (3.12) are orders of magnitude smaller than the second-order term, the terms  $O(\nu^{-3})$  are usually ignored. Therefore (3.12) may be reduced to

$$n_{\text{ion}} = 1 - \frac{C_X}{2} N_e \nu^{-2} \quad (3.14)$$

Integrating the refractive index  $n$ , including both  $n_{\text{ion}}$  and  $n_{\text{trop}}$ , along the ray path yields the measured range  $\rho'$  between receiver and satellite

$$\rho' = \int n(\rho) d\rho \quad (3.15)$$

Based on the TEC definition (3.9), we can express the measured range  $\rho'$  as

$$\rho' = \rho + \Delta\rho_{\text{trop}} + \Delta\rho_{\text{ion}} \quad \text{with} \quad \Delta\rho_{\text{ion}} = \mp \frac{C_X}{2} E \nu^{-2} \quad (3.16)$$

where

$\rho = \int d\rho$  is the geometric distance between receiver and satellite,

$\Delta\rho_{\text{trop}} = \int (n_{\text{trop}}(\rho) - 1) d\rho$  is the path delay due to the troposphere,

$\Delta\rho_{\text{ion}}$  is the path delay due to the ionosphere,

$C_X/2 \approx 40.3 \text{ m}^3 \text{ s}^{-2}$  is a proportionality factor based on the constant  $C_X$  (3.13a),

$E = \int N_e(\rho) d\rho$  is the line-of-sight TEC in electrons per square meter, and

$\nu^{-2}$  is the reciprocal square of the frequency of the propagating electromagnetic wave.

If  $E$  is specified in TECU,  $C_x/2 \approx 40.3 \cdot 10^{16} \text{ m s}^{-2} \text{ TECU}^{-1}$ .

The signs in the range correction (or wave propagation delay)  $\Delta\rho_{\text{ion}}$  in (3.16) corresponds to the phase advance and the group delay, respectively. To be specific, the ionospheric range correction is

- *negative* for phase observations, that is, the measured range is shorter than the geometric range, and
- *positive* for code observations, that is, the measured range is longer than the geometric range.

The difference between the ionosphere-corrected range measurement  $L_3$  based on the LC (2.13), where the second-order term of the ionosphere is eliminated, and the geometric range  $\rho$  is called residual range error (RRE)  $\Delta L_3$ :

$$\Delta L_3 = L_3 - \rho \tag{3.17}$$

To keep (3.17) simple, the term  $\rho$  includes all non-ionospheric corrections. The RRE  $\Delta L_3$  obviously contains all higher-order terms of the ionosphere, among them the effects due to the geomagnetic field and due to differential ray-path bending caused by two separate paths of  $L_1$  and  $L_2$ . Simulations made by *Brunner and Gu* [1991] using ray-tracing techniques have shown that the RRE may reach values of several centimeters at low elevation angles and under extreme ionospheric conditions.

Nevertheless, one may say that the “ionosphere-reducing” LC (2.13) proved in practice to be an excellent approximation. This is not amazing because forming single and double differences also reduces higher-order effects of the ionosphere. On short baselines, it will probably never be possible to detect higher-order effects. On very long baselines, however, it will perhaps be possible to prove their existence when the TEC reaches a very high level during the periods of maximum activity..

Let us point out that for our applications the approximation (3.14) for the refractive index  $n_{\text{ion}}$  is undoubtedly adequate. On the other hand, reasonable TEC information might be useful to model RRE corrections when analyzing the “ionosphere-free” data of global networks, because that is essentially the only unknown information related to the higher-order terms  $O(\nu^{-3})$  in (3.12) [*Brunner and Gu*, 1991].

### 3.2.1 Effect on Linear Combinations

Let us define the constant  $\xi_E$  that gives the ionospheric path delay per TECU referred to the first GPS frequency  $\nu_1$ :

$$\xi_E = \frac{C_x}{2} \nu_1^{-2} \approx 0.162 \text{ m/TECU} \quad \text{with} \quad \nu_1 = 1.57542 \text{ GHz} \tag{3.18}$$



Table 3.1: Ionospheric path delay caused by 1 TECU of free electrons.

LC	Ionospheric path delay		
	(m)	(cycles)	(ns)
$L_1$	0.162	0.853	0.542
$L_2$	0.267	1.095	0.892
$L_4$	-0.105	-1.948	-0.354
$L_5$	-0.208	-0.248	-0.695

Table 3.1 gives the ionospheric path delay corresponding to a line-of-sight TEC of one TECU for the LCs  $L_1$ ,  $L_2$ ,  $L_4$  (2.23), and  $L_5$  (2.27). The path delays expressed in meters per TECU are equal to  $\xi_E$ ,  $\xi \xi_E$ ,  $\xi_4 \xi_E$ , and  $\xi_5 \xi_E$ , respectively, using the factors  $\xi$ ,  $\xi_4$ , and  $\xi_5$  defined in (2.7), (2.24), and (2.28). The ionospheric path delays are also given in units of cycles and nanoseconds in Table 3.1.

With the help of Table 3.1, the ionospheric errors specified in Table 2.2, in meters and cycles, may now be specified as 6.159 and 1.172 TECU, respectively.

### 3.2.2 Effect on Single-Frequency Baseline Solutions

If one processes a GPS baseline using  $L_1$ -only data and neglecting ionospheric refraction, one has to expect an apparent reduction of the resulting baseline vector length, assuming that short-periodic ionospheric refraction effects tend to average out. This scale bias introduced in a single-frequency GPS network solution due to unmodeled ionospheric refraction may be calculated by the following formula [Beutler *et al.*, 1987]:

$$\frac{\delta l_{\text{ion}}}{l} = -\frac{C_X}{2} \frac{E_V}{R \cos z_{\text{max}}} \frac{1}{\nu^2} \quad (3.19)$$

where

$\delta l_{\text{ion}}$  is the ionosphere-induced distance bias to be expected,

$l$  is the length of the baseline vector,

$C_X/2 \approx 40.3 \cdot 10^{16} \text{ m s}^{-2} \text{ TECU}^{-1}$  is a proportionality factor,

$E_V$  is the average vertical TEC above the baseline,

$R$  is the length of the geocentric receiver vectors (or approximately the earth radius),

$z_{\text{max}}$  is the maximum satellite zenith distance imposed in the processing, and

Table 3.2: Ionosphere-induced scale bias of single-frequency GPS network solutions when neglecting the ionosphere.

LC	Ionosphere-induced scale bias [ppm/TECU]			
	$z_{\max} = 85^\circ$	$z_{\max} = 80^\circ$	$z_{\max} = 75^\circ$	$z_{\max} = 70^\circ$
$L_1$	-0.29	-0.15	-0.10	-0.07
$L_2$	-0.48	-0.24	-0.16	-0.12
$L_5$	+0.38	+0.19	+0.13	+0.10

$\nu$  is the frequency of the processed GPS data.

(3.19) shows that the ionosphere-induced scale bias  $\delta l_{\text{ion}}/l$  is a function of the average vertical TEC  $E_v$  above the baseline, the maximum zenith distance  $z_{\max}$ , and, last but not least, the LC analyzed.

Table 3.2 provides the scale biases  $\delta l_{\text{ion}}/l$  in ppm per TECU, calculated using formula (3.19), for the LCs  $L_1$ ,  $L_2$ , and  $L_5$  according to (2.27) and for four maximum zenith distances  $z_{\max}$ . When processing code—instead of phase—double-difference observations, the sign of  $\delta l_{\text{ion}}/l$  has to be changed.

Example: For an  $L_1$ -phase solution with  $z_{\max} = 75^\circ$  and an average TEC  $E_v = 10$  TECU, one may expect a baseline shortening of about  $-1.0$  ppm (or  $-1.0$  mm/km).

If only single-frequency data is available, local TEC models derived from data of one or more nearby operating dual-frequency GPS stations are very efficient in removing or greatly reducing the ionosphere-induced scale bias under moderate and homogeneous ionospheric conditions [Wild, 1994]. For small high-precision GPS networks, with a maximum extent of several kilometers, like the 3-dimensional test network of Turtmann in the Swiss alps, we recommend to use—even if dual-frequency data is available— $L_1$ -data together with a TEC model [Beutler *et al.*, 1995a]. The reason lies in the trade-off between the basic observable  $L_1$  and the ionosphere-free LC  $L_3$  (2.13), which does not only have a noise about 3 times as large as  $L_1$  but also considerably amplifies systematic effects due to multipath, antenna phase center offsets and variations, etc.

### 3.3 Single-Layer Model and Mapping Function

It is close to impossible to establish height-dependent profiles of electron densities using ground-based GPS observations. Such a profiling would be possible with data from a low-earth orbiter (LEO) when it tracks a GPS satellite that is observed to set (or rise) through the Earth's atmosphere until it is occulted by the Earth's limb [Melbourne *et al.*, 1994; Yunck and Melbourne, 1995]. The GPS signal is both bent and retarded,

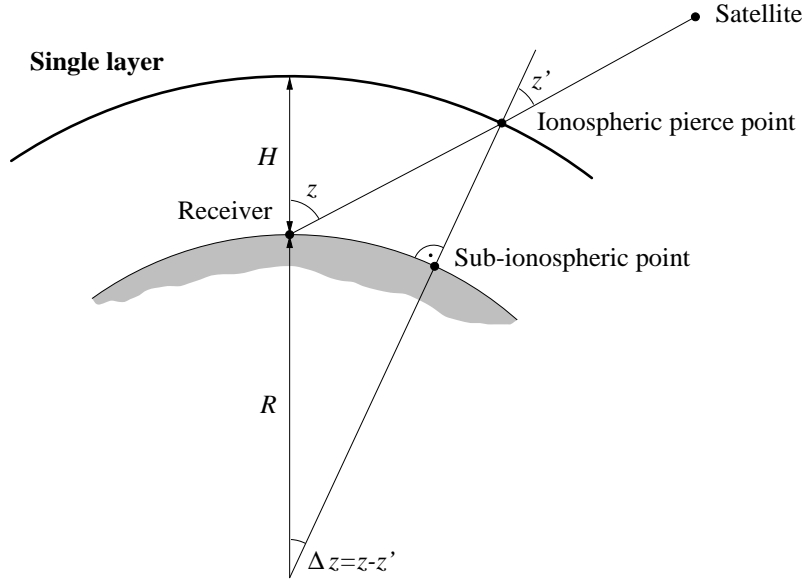


Figure 3.5: Single-layer model for the ionosphere.

causing a delay in arrival at the LEO, which is associated in turn with vertical profiles of atmospheric parameters. Having a full GPS constellation, such occultation events occur frequently. Several hundred globally distributed occultation events may be observed each day by a single LEO in a polar orbit. Ionosphere tomography is not our purpose, however.

For absolute TEC mapping using ground-based GPS data, the TEC along the vertical is of main interest. Because GPS basically provides measurements of slant TEC, an elevation-dependent mapping function

$$F(z) = \frac{E(z)}{E_v} \quad \text{with} \quad E_v = E(0) \quad (3.20)$$

which describes the ratio between the slant TEC  $E(z)$  and the vertical TEC  $E_v$  is required. Such a mapping function  $F(z)$  allows to convert  $E(z)$  to  $E_v$  and vice versa.

In order to refer the resulting vertical TEC  $E_v$  to specific solar-geomagnetic coordinates, the so-called single-layer (or thin-shell) model is usually adopted for the ionosphere. The single-layer model is outlined in Figure 3.5. We assume that all free electrons are contained in a shell of infinitesimal thickness at altitude  $H$ . The altitude  $H$  of this idealized layer is usually set to 350, 400, or 450 kilometers, approximately corresponding to the altitude of maximum electron density.

From Figure 3.5 we conclude that the relationship between  $z'$ , the satellite's zenith distance at the ionospheric pierce point, and  $z$ , the zenith distance at the receiver's

Table 3.3: Semi-diameter of the ionospheric cap probed by a single GPS station.

$z_{\max}$ ( $^{\circ}$ )	$z'_{\max}$ ( $^{\circ}$ )	$\Delta z_{\max}$ ( $^{\circ}$ )	$R \Delta z_{\max}$ (km)	$F(z_{\max})$
70	61.37	8.63	960	2.09
75	64.45	10.55	1170	2.32
80	66.90	13.10	1460	2.55
85	68.51	16.49	1830	2.73
90	69.07	20.93	2330	2.80

location, is given by

$$\sin z' = \frac{R}{R + H} \sin z \quad (3.21)$$

where

$R \approx 6371$  km is the mean earth radius and

$H$  is the height of the single layer.

Assuming the satellite distribution to be homogenous over the entire sky, the semi-diameter of the ionospheric cap probed by a single receiver is basically defined by the maximum central angle  $\Delta z_{\max} = z_{\max} - z'_{\max}$ . The semi-diameters  $\Delta z_{\max}$  in degrees and  $R \Delta z_{\max}$  in kilometers resulting for various maximum zenith distances  $z_{\max}$  are given in Table 3.3, actually assuming a centroid height of  $H = 450$  km. It is remarkable how sparsely the ionosphere is probed by a single receiver. For  $z_{\max} = 80^{\circ}$ , the diameter of the ionospheric cap reaches almost 3000 kilometers.

The area of such an ionospheric cap in steradians is given by

$$A = 2 \pi (1 - \cos \Delta z_{\max}) \quad (3.22)$$

According to (3.23),  $n_A \approx 80$  GPS tracking stations would be sufficient to sound out the entire ionosphere of the Earth, when we allow for  $z_{\max} = 80^{\circ}$ :

$$n_A = \frac{4 \pi}{A} = \frac{2}{1 - \cos \Delta z_{\max}} \quad (3.23)$$

### 3.3.1 GPS Satellite Visibility and Probed Ionospheric Centroid

Because GPS orbital planes have an inclination of  $55^{\circ}$  with respect to the Earth's equator, the satellite sky distribution depends very much on the geographic latitude of the observer. From the space point of view, one may illustrate the GPS satellite constellation by a truncated sphere with a radius equal to the semi-major axis of the satellite orbits

[*Santerre, 1991*]. Figure 2.3, which shows the GPS satellite trajectories projected on the Earth's surface, makes clear that this truncated sphere is bounded by the envelopes at  $\pm 55^\circ$ .

The projection of this truncated sphere on the observer's hemisphere is shown in Figure 3.6 for various geographic latitudes. In the latitude-dependent plots, showing azimuth versus zenith distance, the shaded areas are the zones where no GPS satellites are visible. In addition, elevation cut-off circles are plotted in  $5^\circ$ -intervals. It is clear that the “north (or south) hole” is exactly tangent to the local zenith at a latitude of  $55^\circ$  (or  $-55^\circ$ ). This may be seen in Figure 3.6e (or 3.6i). Similar figures may be found in [*Santerre, 1991*].

For ionospheric mapping, the satellite sky distribution projected on the single layer is of interest. Figure 3.7 provides this information, showing azimuth versus absolute distance. Elevation cut-off circles are plotted again with solid lines, but they are complemented by two distance marks at 1000 and 2000 kilometers, plotted with dotted lines. Figure 3.7 is based on a single-layer height of 450 kilometers. Therefore, it is fully compatible with Table 3.3. Note that Figure 3.7—correspondingly re-scaled—may be applied to tropospheric mapping, too.

### 3.3.2 Ionospheric Mapping Functions

Ionospheric mapping functions are generally defined by (3.20), that is, by the TEC ratio  $E(z)/E(0)$ . Using the Chapman function (3.1) and the TEC definition (3.9) to describe the slant TEC  $E(z)$  and vertical TEC  $E(0)$ , the limit of  $F(z)$  for  $\Delta h \rightarrow 0$  leads to the so-called single-layer model (SLM) mapping function

$$F(z) = \frac{1}{\cos z'} = \frac{1}{\sqrt{1 - \sin^2 z'}} \quad \text{with} \quad \sin z' = \frac{R}{R + H} \sin z \quad (3.24)$$

where  $z'$  is the satellite's zenith distance at the point where the single layer is pierced. For the single-layer height  $H$  in (3.21) we then obtain  $H = h_0$ . Values of the SLM mapping function evaluated at a few low elevation angles are given in the last column of Table 3.3.

The mapping function suggested by *Klobuchar* [1987] for the GPS broadcast ionosphere model approximates the SLM mapping function for  $z$  between  $0^\circ$  and  $85^\circ$  within about two percent, taking a single-layer height of  $H = 350$  km as basis. The broadcast model mapping function may be written as

$$F(z) = 1 + 2 \left( \frac{z + 6}{96} \right)^3 \quad (3.25)$$

where  $z$  is the zenith distance of the satellite at the receiver location, expressed in degrees.

Still another TEC mapping function was proposed by *Clynch et al.* [1989]. This  $Q$ -factor mapping function is represented by an even polynomial fitted in the least-squares sense

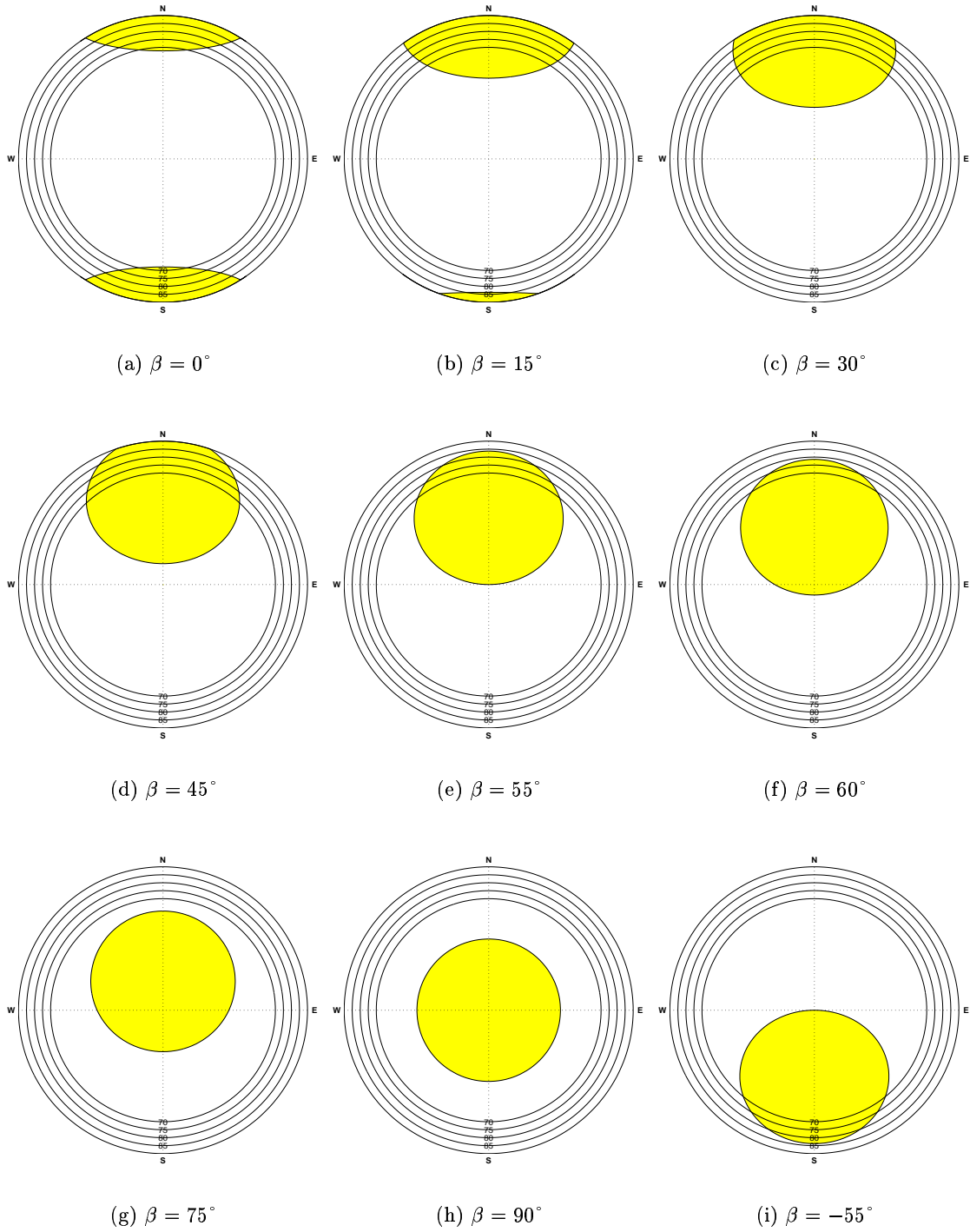


Figure 3.6: GPS satellite visibility as a function of the geographic latitude  $\beta$ .

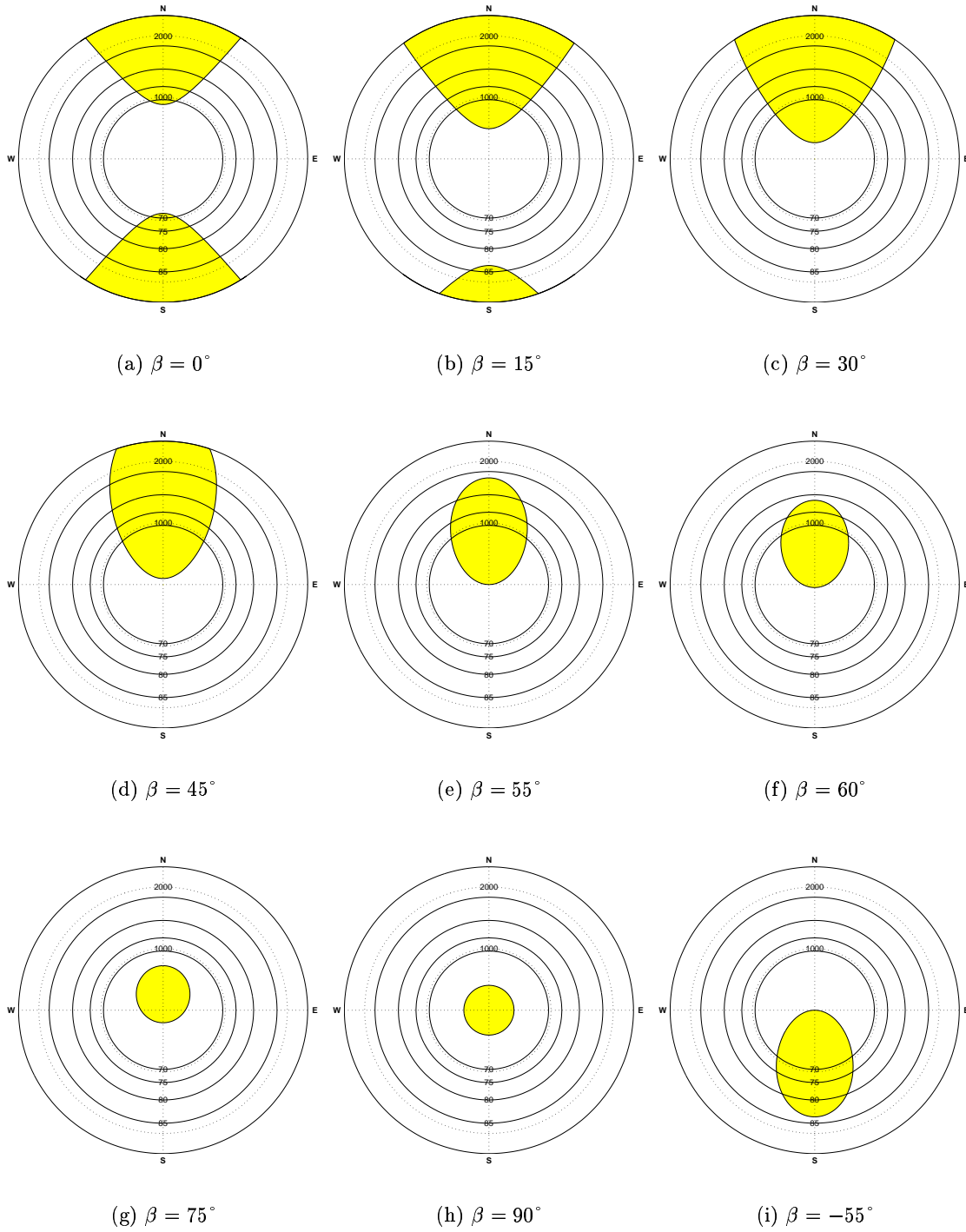


Figure 3.7: GPS-probed part of the ionospheric centroid as a function of the geographic latitude  $\beta$ .

to TEC ratios obtained when assuming a uniform electron density distribution between altitudes of 200 and 600 kilometers. It may be written as

$$Q(z) = \sum_{i=0}^3 a_i \left(\frac{z}{90}\right)^{2i} \quad (3.26)$$

where  $z$  is again in degrees. The four polynomial coefficients are:  $a_0 = 1.0206$ ,  $a_1 = 0.4663$ ,  $a_2 = 3.5055$ , and  $a_3 = -1.8415$ . It is unconventional that  $a_0 \neq 1$  and therefore  $Q(z = 0) = a_0 \neq 1$ .

For comparison purposes, the mapping function based on a Chapman profile (3.1) with  $h_0 = 350$  km,  $\Delta h = 100$  km, and  $\chi = 0$ , which is drawn as a thick line in Figure 3.1, is included. Based on (3.6), (3.9), and (3.10), the Chapman profile mapping function may be formulated as

$$F(z, \chi) = \frac{E(z, \chi)}{E_v(\chi)} \quad \text{with} \quad E(z, \chi) = \int_0^{\infty} N_e(h, \chi) \sec z'(h) dh \quad (3.27)$$

where  $z'(h)$  denotes the satellite's zenith distance at altitude  $h$ , which may be computed using (3.21). Because the peak electron density  $N_{e,0}$  obviously cancels in the TEC ratio  $E/E_v$ ,  $N_{e,0}$  may be set to unity here.

The numerical integration of the slant TEC  $E(z)$  in (3.27) may be performed with a Gaussian quadrature technique [Beutler, 1998]. This integration technique is very powerful and provides results of highest precision.

The four ionospheric mapping functions discussed above are compared in Figure 3.8. The SLM mapping function is shown for altitudes  $H$  of 350, 400, and 450 km. It is clear that the higher the height  $H$  of the layer, the smaller  $F(z)$  becomes in (3.24). Unlike the slopes of the broadcast model mapping function and the  $Q$ -factor mapping function, those of the SLM mapping function and the Chapman profile mapping function decrease significantly at large zenith distances.

In order to better see the errors of the various mapping functions, the deviations in percent with respect to the SLM mapping function at  $H = 350$  km are shown in Figure 3.9. We notice that the SLM mapping function at  $H = 350$  km generally overestimates the Chapman profile mapping function with  $h_0 = H$  (and  $\Delta h > 0$ ), that is, the vertical TEC  $E_v$  derived from slant TEC  $E$  would be underestimated. On the other hand, one recognizes that the SLM mapping function at  $H = 428.8$  km indicated by the dotted line matches the Chapman profile mapping function remarkably well. The reason is that the altitude  $H$  of 428.8 km corresponds to that altitude  $h$  of the reference Chapman profile where 50% of the vertical TEC  $E_v$  is reached. Incidentally, the vertical electron density distribution of our reference Chapman profile contains at  $h = 800$  km about 91.6% of the TEC, at  $h = 1000$  km 96.9%, and at  $h = 1500$  km 99.7%.

Due to the polynomial representation of the broadcast model mapping function and the  $Q$ -factor mapping function, both reveal an "unsettled" pattern compared to the others.



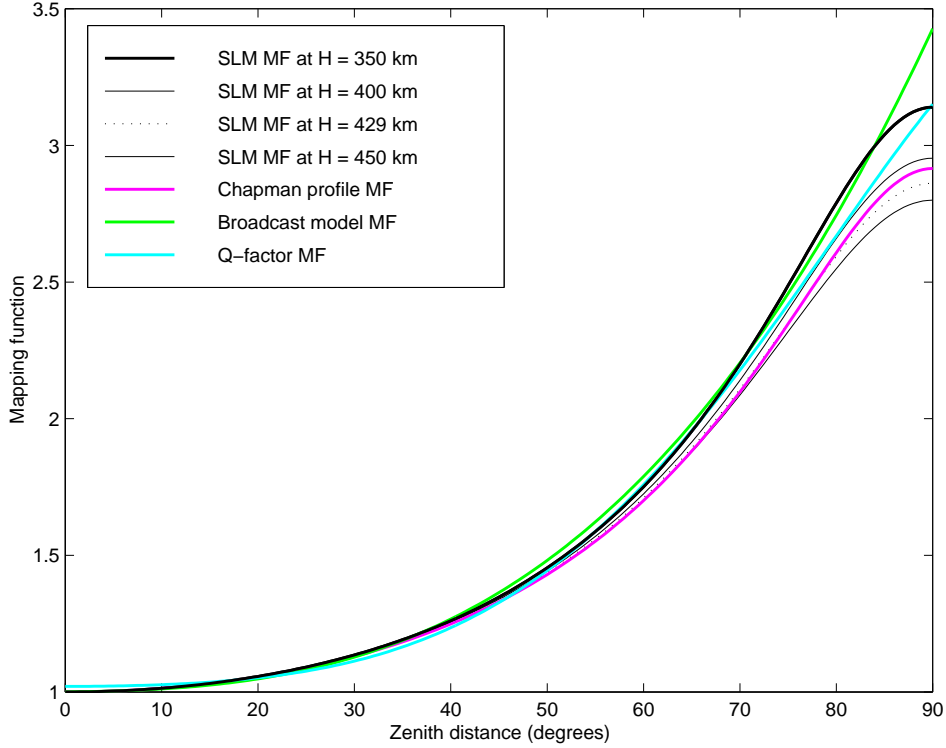


Figure 3.8: Ionospheric mapping functions compared.

Moreover, for both polynomial mapping functions,  $F(z = 0) \neq 1$ . There are no obvious advantages for using either the broadcast model or the  $Q$ -factor mapping function. The computation of the correct SLM mapping function is comparably simple.

For completeness, we also quantify the centroidal height of the Chapman profile (3.1):

$$h_{\text{cen}}(\chi) = \frac{1}{E_v(\chi)} \int_0^{\infty} N_e(h, \chi) h dh \quad (3.28)$$

where  $E_v(\chi)$  is given by (3.10). For  $h_0 = 350$  km,  $\Delta h = 100$  km, and  $\chi = 0$ , the integral (3.28) yields  $h_{\text{cen}}(0) \approx 477.0$  km.

In order to prove that the SLM altitude  $H$  of 428.8 km almost optimally approximates the Chapman profile mapping function (3.27),  $H$  has been adjusted in the least-squares sense for various zenith distance ranges  $(0, z_{\text{max}})$ , where  $z_{\text{max}}$  denotes the maximum zenith distance. The resulting SLM altitudes  $H_{\text{opt}}$  and the corresponding maximum deviations  $\Delta F_{\text{max}}$  in percent are listed in Table 3.4.

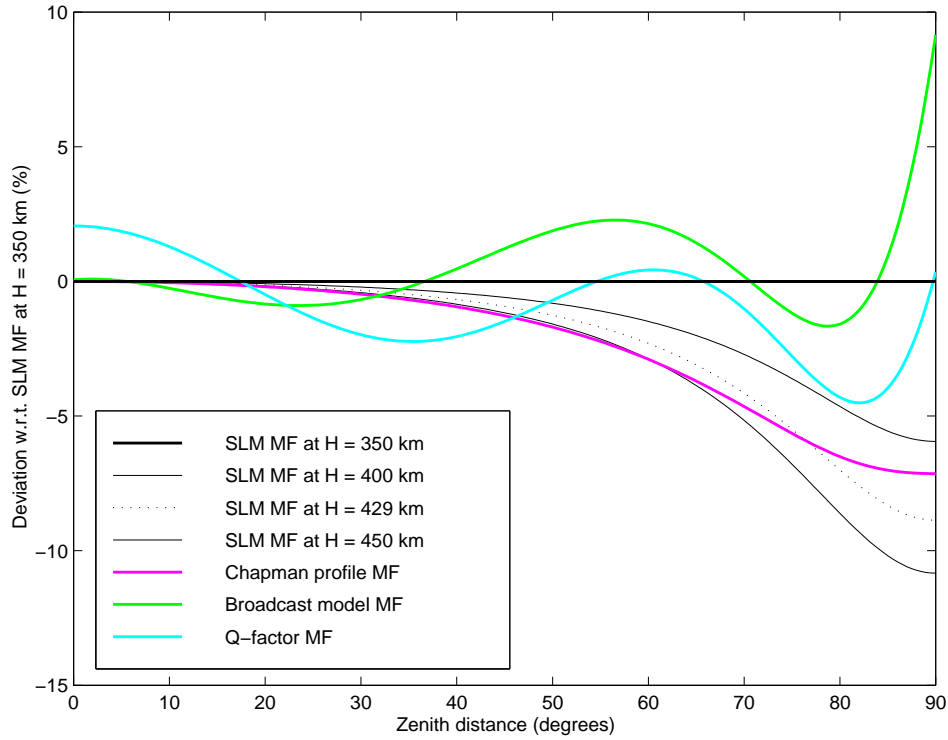


Figure 3.9: Deviations of ionospheric mapping functions with respect to the single-layer model mapping function at  $H = 350$  km.

Table 3.4: Altitudes  $H_{\text{opt}}$  for the SLM mapping function best fitting the reference Chapman profile mapping function.

$z_{\text{max}}$ ( $^{\circ}$ )	$H_{\text{opt}}$ (km)	$\Delta F_{\text{max}}$ (%)
70	445.9	0.34
75	439.7	0.55
80	432.5	0.83
85	425.3	1.07
90	420.1	0.99

Our investigation shows that the Chapman profile mapping function (3.27) may be approximated by a SLM mapping function (3.24) within about one percent, if the SLM altitude  $H$  is well chosen. This in turn means that it is not worthwhile to numerically integrate the Chapman profile mapping function (3.27), keeping in mind that real

Table 3.5: Altitudes  $H_{\text{opt}}$  and factors  $\alpha_{\text{opt}}$  for the modified SLM mapping function best fitting the reference Chapman profile mapping function.

$z_{\text{max}}$ ( $^{\circ}$ )	$H_{\text{opt}}$ (km)	$\alpha_{\text{opt}}$	$\Delta F_{\text{max}}$ (%)
70	411.3	0.9907	0.036
75	406.4	0.9895	0.052
80	403.1	0.9886	0.054
85	403.1	0.9886	0.069
90	407.0	0.9903	0.406

TEC profiles may still considerably differ from a Chapman profile. The computation of the SLM mapping function is simple, therefore we consider this mapping function as appropriate when the height  $H$  is well chosen.

In order to demonstrate that we may approximate the reference Chapman profile mapping function with an unsophisticated mapping function even more precisely than it is possible with the SLM mapping function, let us modify (3.21) to

$$\sin z' = \frac{R}{R + H} \sin(\alpha z) \quad (3.29)$$

where  $\alpha$  is a correction factor which is close to unity. The mapping function we propose is based on the SLM mapping function (3.24), however, using the reduced zenith distance  $z'$  computed according to (3.6). Consequently, this mapping function corresponds to a modified SLM mapping function.

Table 3.5 list altitudes  $H$  as well as factors  $\alpha$  simultaneously adjusted for various zenith distance ranges  $(0, z_{\text{max}})$ . It is remarkable that our modified SLM mapping function  $F = F(H_{\text{opt}}, \alpha_{\text{opt}})$  provides obliquity factors which are about one order of magnitude more consistent with respect to our reference than those of  $F = F(H_{\text{opt}})$  listed in Table 3.4. For  $z_{\text{max}} = 80^{\circ}$ , the least-squares adjustment yields  $H_{\text{opt}} = 403.1$  km and  $\alpha = 0.9886$ . The corresponding maximum deviation  $\Delta F_{\text{max}}$  is about half a part per thousand. Figure 3.10 shows the deviations of this modified SLM mapping function and the SLM mapping function at  $H = 428.8$  km with respect to the reference Chapman profile mapping function.

The agreement is excellent, but we have to keep in mind that the altitude  $h_{\text{max}}$  of the maximum electron density may depend on the solar zenith angle  $\chi$ . One might argue that other values for the parameters  $h_0$  and  $\Delta h$  should be used. The methods described in this section could be used to optimize the ionospheric mapping function.

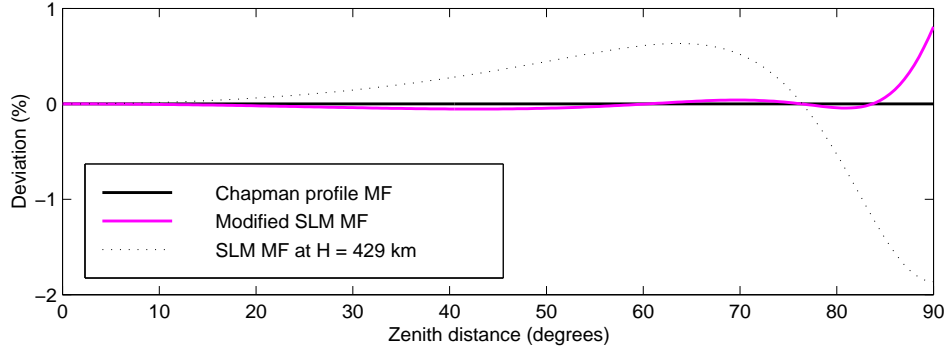


Figure 3.10: Deviation of the modified SLM mapping function with respect to the reference Chapman profile mapping function.

### 3.4 Observation Equations for Absolute TEC Determination

In order to rewrite the observation equations (2.24) and (2.25) for absolute TEC determination, the ionospheric term  $I_i^k$  has to be replaced by

$$I_i^k = \xi_E E_i^k = \xi_E F(z_i^k) E_v(\beta_i^k, s_i^k) \quad (3.30)$$

where

$\xi_E \approx 0.162$  m/TECU is the constant (3.18),

$E_i^k$  is the slant TEC between receiver  $i$  and satellite  $k$ ,

$F(z_i^k)$  is the ionospheric mapping function (3.20) evaluated at the zenith distance  $z_i^k$ , and

$E_v(\beta_i^k, s_i^k)$  is the vertical TEC at the ionospheric pierce point associated with the solar-geomagnetic coordinates  $(\beta, s)$ , that is, the geomagnetic latitude  $\beta$  and the sun-fixed longitude  $s$ .

Subsequently, the ionospheric observation equations (2.24) for zero-difference phase and code observations may be rewritten as

$$L_{i,4}^k = -\xi_4 \xi_E (F(z) E_v(\beta, s))_i^k + B_{i,4}^k \quad (3.31a)$$

$$P_{i,4}^k = +\xi_4 \xi_E (F(z) E_v(\beta, s))_i^k + c(\Delta b^k - \Delta b_i) \quad (3.31b)$$

and the observation equation (2.25a) for double-difference phase observations read as

$$L_{ij,4}^{kl} = -\xi_4 \xi_E (F(z) E_v(\beta, s))_{ij}^{kl} + B_{ij,4}^{kl} \quad (3.32)$$

where  $\xi_4 \xi_E \approx -0.105$  m/TECU. Note that  $(\dots)_i^k$  in (3.31) indicates the zero-difference operator;  $(\dots)_{ij}^{kl}$  in (3.32) is the double-difference operator illustrated by (2.11).

For zero-difference code observations, phase-smoothed according to (2.8), the ionospheric observation equation is identical with (3.31b):

$$\tilde{P}_{i,4}^k = +\xi_4 \xi_E (F(z) E_v(\beta, s))_i^k + c(\Delta b^k - \Delta b_i) \quad (3.33)$$

The *unknown* parameters in the GPS observation equations (3.31), (3.32), and (3.33) are the absolute TEC information  $E_v(\beta, s)$  and in addition either

- the satellite and receiver differential code biases (DCBs)  $\Delta b^k$  and  $\Delta b_i$  or
- the ambiguity parameters  $B_{i,4}^k$  and  $B_{ij,4}^{kl}$ , respectively.

Therefore, one cannot directly derive absolute TEC information  $E_v(\beta, s)$  from single-epoch GPS data. To separate  $E_v(\beta, s)$  from DCBs or ambiguity parameters, one is forced to process data that covers a longer time span.

## 3.5 Total Electron Content Parameterization Methods

### 3.5.1 Local TEC Representation

Two-dimensional Taylor series expansions are used to locally represent the vertical total electron content  $E_v(\beta, s)$ :

$$E_v(\beta, s) = \sum_{n=0}^{n_{\max}} \sum_{m=0}^{m_{\max}} E_{nm} (\beta - \beta_0)^n (s - s_0)^m \quad (3.34)$$

where

$(\beta, s)$  are the solar-geographic coordinates of the ionospheric pierce point,

$n_{\max}, m_{\max}$  are the maximum orders of the two-dimensional Taylor series expansion in latitude and longitude.

$E_{nm}$  are the unknown coefficients of the Taylor series expansion, and

$(\beta_0, s_0)$  are the coordinates of the origin of the expansion.

More details related to this TEC parameterization method may be found, e. g., in [*Georgiadou and Kleusberg, 1988; Wild, 1994; Warnant, 1996; Komjathy, 1997*].

### 3.5.2 Global TEC Representation

The TEC representation (3.34) is not well suited to globally parameterize the Earth's TEC. As an alternative we propose a spherical harmonic (SH) expansion [*Schaer et al.*, 1995]:

$$E_v(\beta, s) = \sum_{n=0}^{n_{\max}} \sum_{m=0}^n \tilde{P}_{nm}(\sin \beta) \left( \tilde{C}_{nm} \cos(ms) + \tilde{S}_{nm} \sin(ms) \right) \quad (3.35)$$

where

$\beta$  is the geographic or preferably geomagnetic latitude of the intersection point of the line of sight with the single layer,

$s = \lambda - \lambda_0$  is the sun-fixed longitude of the ionospheric pierce point,

$\lambda$  is the longitude of the ionospheric pierce point,

$\lambda_0$  is the longitude of the Sun,

$n_{\max}$  is the maximum degree of the SH expansion,

$\tilde{P}_{nm} = N_{nm} P_{nm}$  is the normalized associated Legendre function of degree  $n$  and order  $m$ ,

$N_{nm}$  is the normalization function,

$P_{nm}$  is the classical, unnormalized Legendre function, and

$\tilde{C}_{nm}, \tilde{S}_{nm}$  are the unknown SH coefficients and global ionosphere map (GIM) parameters, respectively.

The normalization function  $N_{nm}$  may be written according to [*McCarthy*, 1996] as

$$N_{nm} = \sqrt{\frac{(n-m)!(2n+1)(2-\delta_{0m})}{(n+m)!}} \quad (3.36)$$

where  $\delta$  denotes the Kronecker delta.

It can be shown that the mean vertical TEC  $\bar{E}_v$  of the global TEC distribution (3.35) is generally represented by the zero-degree SH coefficient  $\tilde{C}_{00}$ :

$$\bar{E}_v = \frac{1}{4\pi} \int_0^{2\pi + \frac{\pi}{2}} \int_{-\frac{\pi}{2}}^{\frac{\pi}{2}} E_v(\beta, s) \cos \beta d\beta ds = N_{00} \tilde{C}_{00} = \tilde{C}_{00} \quad \text{with} \quad N_{00} = 1 \quad (3.37)$$

Consequently, it is possible to deduce the global number of ionospheric electrons from the coefficient  $\tilde{C}_{00}$  using the relationship

$$n_e = 4\pi R'^2 \bar{E}_v \quad (3.38)$$

where  $R' = R + H$  is the radius of the spherical single layer. Note that  $n_e$  is obtained in units of  $10^{16}$ , if  $R'$  and  $\tilde{C}_{00}$  are given in meters and TECU, respectively.

The number of GIM parameters  $\tilde{C}_{nm}$  and  $\tilde{S}_{nm}$  in the SH expansion (3.35) is given by the simple expression

$$u_E = (n_{\max} + 1)^2 \quad (3.39)$$

or, if the SH expansion (3.35) is truncated at the maximum order  $m_{\max} \leq n_{\max}$ , by

$$u_E = (n_{\max} + 1)^2 - (n_{\max} - m_{\max})(n_{\max} - m_{\max} + 1) \quad (3.40)$$

$n_{\max}$  and  $m_{\max}$  also dictate the spatial resolution of a truncated SH expansion:

$$\Delta\beta = \frac{2\pi}{n_{\max}} \quad (3.41a)$$

$$\Delta s = \frac{2\pi}{m_{\max}} \quad (3.41b)$$

where

$\Delta\beta$  is the resolution in latitude and

$\Delta s$  is the resolution in sun-fixed longitude and local time, respectively.

Both the local and the global TEC representation presented in (3.34) and (3.35) are handled in the Bernese GPS Software [*Rothacher and Mervart, 1996*]. Because such a TEC representation is referred to a certain time interval, one has to estimate one set of TEC parameters for each time interval of interest. Alternatively, it is possible to refer the individual sets of global TEC parameters to certain nominal epochs, which means that in this case the TEC parameters are linearly interpolated between consecutive nominal epochs. Figure 3.11 illustrates the two different parameterization models.

The global TEC representation (3.35) is appropriate for regional ionospheric mapping, as well [*Schaer et al., 1995*]. Because a network of GPS stations within a certain longitude range scans the ionosphere over a full cycle in the  $s$ -coordinate during 24 hours, a single set of “global” TEC parameters allows it to describe a regional TEC distribution for 24 hours. The local TEC representation (3.34), on the other hand, is only applicable when referring it to a fraction of a day.

### 3.5.3 Other Global TEC Parameterization Methods

In the following we briefly highlight the different global TEC parameterization methods that are used by the GPS-ionosphere groups at JPL (Jet Propulsion Laboratory), ESA (European Space Agency), EMR (Energy, Mines and Resources), UPC (Polytechnical University of Catalonia), and UNB (University of New Brunswick).

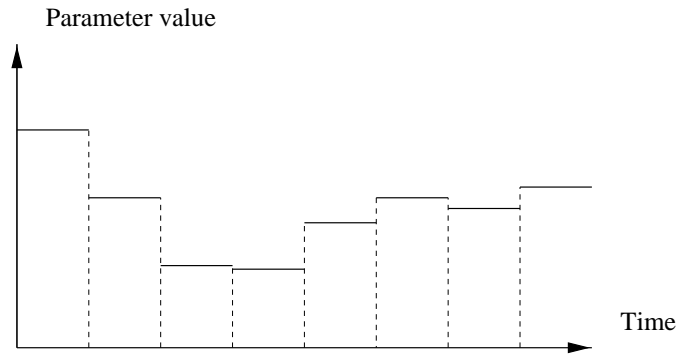
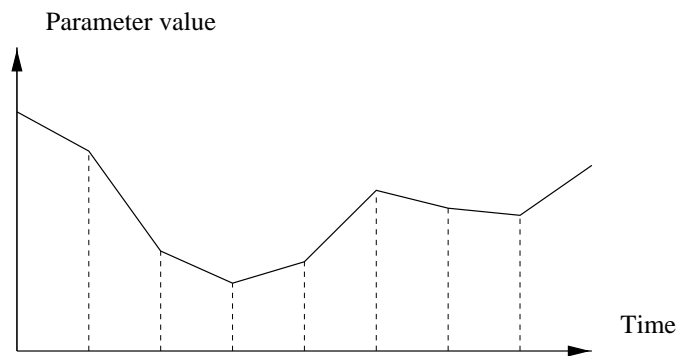
(a) Piece-wise, *constant* functions(b) Piece-wise, *linear* functions

Figure 3.11: Two methods for parameterizing time-dependent parameters.

JPL describes the ionosphere by TEC values at the vertices of an almost uniform grid [Mannucci *et al.*, 1998]. The TEC at each vertex evolves stochastically with time where the time correlations between updates have to be specified. The spatial variation of the TEC between the vertices is modeled as linear. JPL also used SH expansions [Wilson *et al.*, 1995].

ESA uses Gauss-type exponential functions [Feltens *et al.*, 1996, 1998]. A disadvantage of these functions is that they are not linear in the unknown parameters.

EMR subdivides the surface into cells of constant TEC [Gao *et al.*, 1994]. UPC uses a similar method, referring the cells to two layers, however [Hernandez-Pajares *et al.*, 1998]. Discontinuities at the cell boundaries are unavoidable.

UNB uses a local TEC representation of low order for each station and subsequently does an interpolation between the station-specific TEC estimates to provide a global



TEC distribution [Komjathy, 1997].

Let us mention, last but not least, the TEC parameterization method used for the GPS broadcast ionosphere model [Klobuchar, 1987]. There the global TEC distribution may be written as

$$E_v(\beta, s) = \begin{cases} E_{\min} + E_{\text{amp}}(\beta) \cos s' & \text{if } |s'| < \frac{\pi}{2} \\ E_{\min} & \text{else} \end{cases} \quad (3.42)$$

where

$(\beta, s)$  are the solar-geomagnetic coordinates of the ionospheric pierce point, namely the geomagnetic latitude  $\beta$  and the sun-fixed longitude  $s$  (or the local time minus 12 hours),

$E_{\min} \approx 9.2$  TECU is the nighttime TEC, corresponding to an ionospheric delay of 5 ns at L1,

$E_{\text{amp}}(\beta)$  is the amplitude,

$s' = 2\pi(s - s_0)/\tau(\beta)$  is the phase angle, and

$\tau(\beta)$  is the “period” of the cosine function.

According to the Klobuchar model, the diurnal maximum TEC is assumed to be generally at 14:00 local time, that is, at  $s_0 = 2$  h.

Eight ionospheric coefficients are broadcast by the GPS satellites. They represent the amplitude  $E_{\text{amp}}(\beta)$  and the period  $\tau(\beta)$  of the cosine function in (3.42) by cubic polynomials:

$$E_{\text{amp}}(\beta) = \begin{cases} \frac{c}{\xi_E} \sum_{i=0}^3 a_i \beta^i & \text{if } E_{\text{amp}}(\beta) \geq 0 \\ 0 & \text{else} \end{cases} \quad (3.43a)$$

$$\tau(\beta) = \begin{cases} \sum_{i=0}^3 b_i \beta^i & \text{if } \tau(\beta) \geq \tau_{\min} \\ \tau_{\min} & \text{else} \end{cases} \quad (3.43b)$$

where  $\tau_{\min} = 20$  h is the minimum period. Note that the factor  $c/\xi_E$  is introduced in (3.43a), because the coefficients  $a_i$  are provided in seconds of ionospheric delay at L1.  $c$  is the speed of light and  $\xi_E$  is the constant (3.18).

The mapping function belonging to the GPS broadcast ionosphere model is given by (3.25), a polynomial approximation for the SLM mapping function (3.24) at  $H = 350$  km.

For global ionospheric mapping, the TEC representation (3.42) is inappropriate, because it is not linear in the free parameters  $a_i$  and  $b_i$ .

### 3.6 Variance-Covariance Study Concerning Different Ionospheric GPS Observables

In this section, we study the formal accuracy of the TEC coefficients as a function of the observation type by playing off the phase observation equation (3.31a) against the code observation equation (3.31b).

This variance-covariance study is based on GPS data simulated for a single mid-latitude station assuming the currently available 27-satellite constellation. The corresponding dual-frequency phase and code observations, sampled every 5 minutes, cover 24 hours. The observation RMS error is assumed to be elevation-dependent:

$$\sigma(z) = \frac{\sigma(0)}{\cos z} \quad (3.44)$$

where

$z$  is the zenith distance of the satellite referred to and

$\sigma(0)$  is the RMS error of an observation at zenith.

$\sigma(0) = 2$  mm is assumed for phase,  $\sigma(0) = 0.2$  m for code observations. This implies that the RMS error reaches about 12 mm and 1.2 m, respectively, at  $z_{\max} = 80^\circ$ . In the variance-covariance analyses, all observations are weighted according to the law

$$P(z) = P(0) \cos^2 z \quad (3.45)$$

where  $P(0)$  is the weight of an observation at zenith.

The TEC is parameterized by one SH expansion (3.35) of degree 5 adopting the SLM mapping function (3.24). The number of TEC parameters to be determined is given by (3.39), that is, by  $(5 + 1)^2 = 36$ . Although the SH TEC representation is stationary with respect to the sun-fixed frame, it models the temporal variation of TEC in our case, because the single station probes at any time only a certain solar longitude band. It is obvious that the TEC distribution is idealized to be rather smooth and that possible short-term fluctuations of the TEC are plainly disregarded. The resulting formal accuracies are therefore expected to be very optimistic. Nevertheless, they should reflect the actual value of different GPS observables in a qualitative way.

Seven different processing scenarios were investigated. They may be grouped into three main categories:

- case A: processing only phase data (3.31a),
- case B: processing only code data (3.31b), and
- case C: processing phase and code data together.

Table 3.6: Comparison of the smallest formal uncertainties of the vertical TEC  $E_v(\beta, s)$ , the satellite DCBs  $\Delta b^k$ , the receiver DCB  $\Delta b_i$ , and the ambiguity biases  $B_{i,4}^k$ .

Case	$\sigma_{\min}(E_v)$ (TECU)	$\sigma_{\min}(\Delta b^k)$ (ns)	$\sigma(\Delta b_i)$ (ns)	$\sigma_{\min}(B_{i,4}^k)$ (mm)	$u_{\text{tot}}$
A	0.00796	–	–	0.864	84
B1	0.62200	0.168	0.204	–	64
B2	0.54400	–	0.178	–	37
B3	0.30400	–	–	–	36
C1	0.00786	0.144	0.032	0.864	112
C2	0.00785	–	0.031	0.864	85
C3	0.00783	–	–	0.862	84

Case C corresponds—more or less—to the case of processing phase-smoothed code data (3.33).

For cases B and C involving code observations, we distinguish in addition whether (1) both the 27 satellite DCBs (differential code biases) and the receiver DCB are estimated, (2) only the receiver DCB is estimated, or (3) all DCBs are considered as known. Each estimated DCB is represented by one parameter (per day). The DCB as well as the TEC estimates would be less accurate if a higher temporal resolution would be assumed for DCB parameters. Unlike DCBs, ambiguity biases  $B_{i,4}^k$  must be solved for in any case, because these will be different from one satellite pass to the next one. As a minimum, one bias per satellite pass (and receiver) has to be determined. In our example, we have 48 ambiguity biases.

Table 3.6 lists the essential results of this variance-covariance study, namely the smallest formal uncertainties of the vertical TEC  $E_v(\beta, s)$ , the satellite DCBs  $\Delta b^k$ , the receiver DCB  $\Delta b_i$ , and of the ambiguity biases  $B_{i,4}^k$ . The last column of this table gives, moreover, the total number  $u_{\text{tot}}$  of unknown parameters for each case.

As quality measure for the TEC determination, we use the formal accuracy  $\sigma_{\min}(E_v)$  which gives the smallest uncertainty of the vertical TEC  $E_v$  in the  $(\beta, s)$ -space. It is clear that the solar-geomagnetic coordinates  $(\beta, s)$  associated with  $\sigma_{\min}(E_v)$  lie within the station-specific latitude band probed. Comparing case B with case A clearly shows that the phase-only processing is highly superior to the code-only processing. We hereby conclude that the popular conception that absolute TEC determination mainly depends on “absolute” range (or code) measurements is wrong.

The ratio of 100 between code and phase RMS error is rather optimistic, if we keep in mind that code accuracy may be severely reduced, e. g., by multipath. For TEC determination, the B-to-A accuracy ratio is about 80 for the case B1 and is still about 40 for the case B3. Because the receiver DCBs  $\Delta b_i$  seem to be less stable in practice than those of the satellites, case B3/C3 is a rather unrealistic scenario. In case C, we do

not much gain for the ionosphere parameters. The formal accuracy of the receiver DCB  $\Delta b_i$  is considerably improved, however. Because all DCBs may be shifted by a common bias, we generally refer them to the overall mean of the satellite DCBs  $\Delta b^k$ , which is assumed to be zero, by introducing the condition

$$\frac{1}{u_{\Delta b}} \sum_{k=1}^{u_{\Delta b}} \Delta b^k = \Delta b_{\text{ref}} \quad \text{with} \quad \Delta b_{\text{ref}} = 0 \quad (3.46)$$

where  $u_{\Delta b}$  is the number of observed satellites.

If data of  $n$  globally distributed stations is simultaneously processed in a similar way, one may expect that in the cases B1 and C1 the formal accuracy  $\sigma(\Delta b^k)$  of the satellite DCBs is improved by approximately a factor of  $\sqrt{n}$ . Even then, the accuracies of the TEC parameters and the receiver DCBs do not significantly improve, provided that  $n$  station-specific TEC representations are set up. If global TEC representations are set up, additional correlations are induced via the common TEC parameters.

The results of Table 3.6 are confirmed by actual TEC and DCB estimates. Because the simulated GPS data is not contaminated by the ionosphere, the estimated local TEC distribution may—and actually does—deviate from zero within statistical limits. These deviations are characterized by the formal accuracies listed in Table 3.6.

In summary, we may say that either phase observations (3.31a), as exclusively used by, e. g., *Wild* [1994], or phase-smoothed code observations (3.33) are recommended for absolute TEC determination. Code observations (3.31b) only contribute for retrieving DCBs in a significant way.

## **Part II**

# **GPS-Derived Ionospheric Information—Results**



# 4. Time Series of CODE Ionosphere Products

## 4.1 IGS Data Processing at CODE—An Overview

All global and European ionosphere products developed in the context of this research work have been fully integrated in the automatic IGS data processing scheme at CODE. We give an overview at the beginning of this chapter.

There are three levels of daily processing steps. In chronological order, they are addressed as

- *rapid*,
- *final*, and
- *European* IGS data processing.

### 4.1.1 Rapid IGS Data Processing

The rapid IGS data processing is initiated by an FTP command which is executed shortly after 00:00 UT. The corresponding computer job runs during the whole day and downloads the newly available RINEX (Receiver-INdependent EXchange) observation files of the last day via Internet from the three global IGS data centers. It is followed by the computer job controlling the rapid IGS data processing, which is submitted in the early morning. Whenever a time-dependent minimum number of complete RINEX observation files is reached, the corresponding BPE (Bernese Processing Engine) job is started. On average, data from about 60 IGS stations are processed in this way on each day. A simplified flow chart of the rapid IGS data processing at CODE is shown in Figure 4.1. The ionosphere-related processing steps are emphasized by shading.

First, the RINEX observation files are converted into BGS binary observation files. Code preprocessing is based on the ionosphere-free code observation equation (2.15b) and yields epoch-specific receiver clock offsets  $\Delta t_i$  for synchronization purposes. Apart from

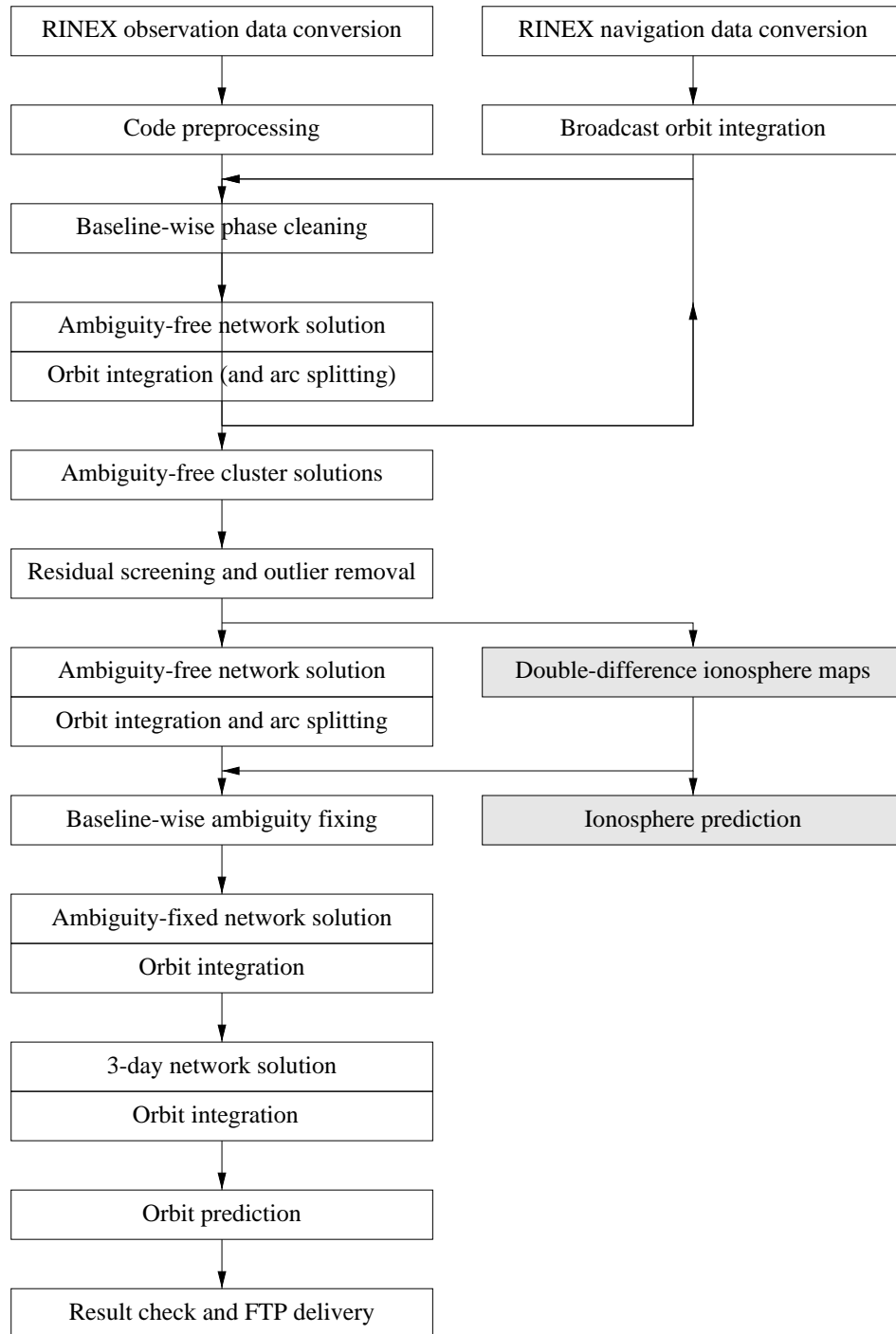


Figure 4.1: Flow chart of the rapid IGS data processing at CODE.



the ionospheric solution and the ambiguity fixing, all subsequent solutions are based on the ionosphere-free phase observation equation (2.16a). The mathematical correlations of double-difference observations within a baseline are always correctly modeled; those within a network or a baseline cluster are usually taken into account when computing final solutions. Generally, an elevation cut-off angle of  $10^\circ$  is used and all observations are weighted according to elevation using (3.45). The set of linearly independent baselines to be formed is found by minimizing the sum of all baseline lengths, which leads to “shortest” baselines. With regard to the first orbit improvement, one additional iteration is performed. Outliers are then removed based on normalized residuals (2.54). While the ambiguity-free network solution is computed, global ionosphere maps (GIMs) are derived by analyzing the geometry-free LC of phase observations (see (2.25a) and (3.32)). The ionosphere prediction procedure, which follows the rapid GIM estimation, will be explained in detail in Chapter 5. The GIMs are subsequently taken into account for fixing phase ambiguities using the QIF strategy (see section 2.3.4). After computing the ambiguity-fixed network solution, this 1-day solution is combined on the normal equation level using the program ADDNEQ with the corresponding 1-day solutions of the two preceding days. This yields a so-called 3-day solution. The resulting orbits of the third, current day are then labeled “CODE rapid orbits.” Finally, the orbits, satellite clock parameters, and earth rotation parameters (ERPs) are predicted for the two subsequent days. The rapid IGS data processing is finished by checking results for plausibility and delivering the rapid and 2-day predicted orbit and ERP products via Internet to the IGS AC coordinator. These products, complemented by the 1-day predicted products and the rapid and predicted GIM information, are also made available via anonymous FTP at CODE. The corresponding FTP address is `ftp://ubclu.unibe.ch/aiub$ftp/code/`. It is worth mentioning that there is an option to use the 1-day predicted orbits of the previous run as a priori orbit information for the next day. This option is normally not used.

The rapid IGS data processing, serving up to six VAX/Alpha computers in parallel, takes about 3–4 hours and is usually completed well before 12:00 UT. The rapid GIM production alone takes about half an hour. The BPE-supported parallel processing is particularly efficient for processing steps that may be performed cluster by cluster, or even baseline by baseline.

### 4.1.2 Final IGS Data Processing

The rapid orbits subsequently flow as a priori orbits into the final IGS data processing which is schematically given in Figure 4.2. Unlike the rapid IGS data processing, the final processing scheme includes various sequential BPE jobs which may be grouped into a double-difference and a zero-difference processing sequence.

The evolution of the number of IGS stations processed daily by CODE is shown in Figure 4.3 over a time span of about 2.5 years. We notice a steadily increasing number

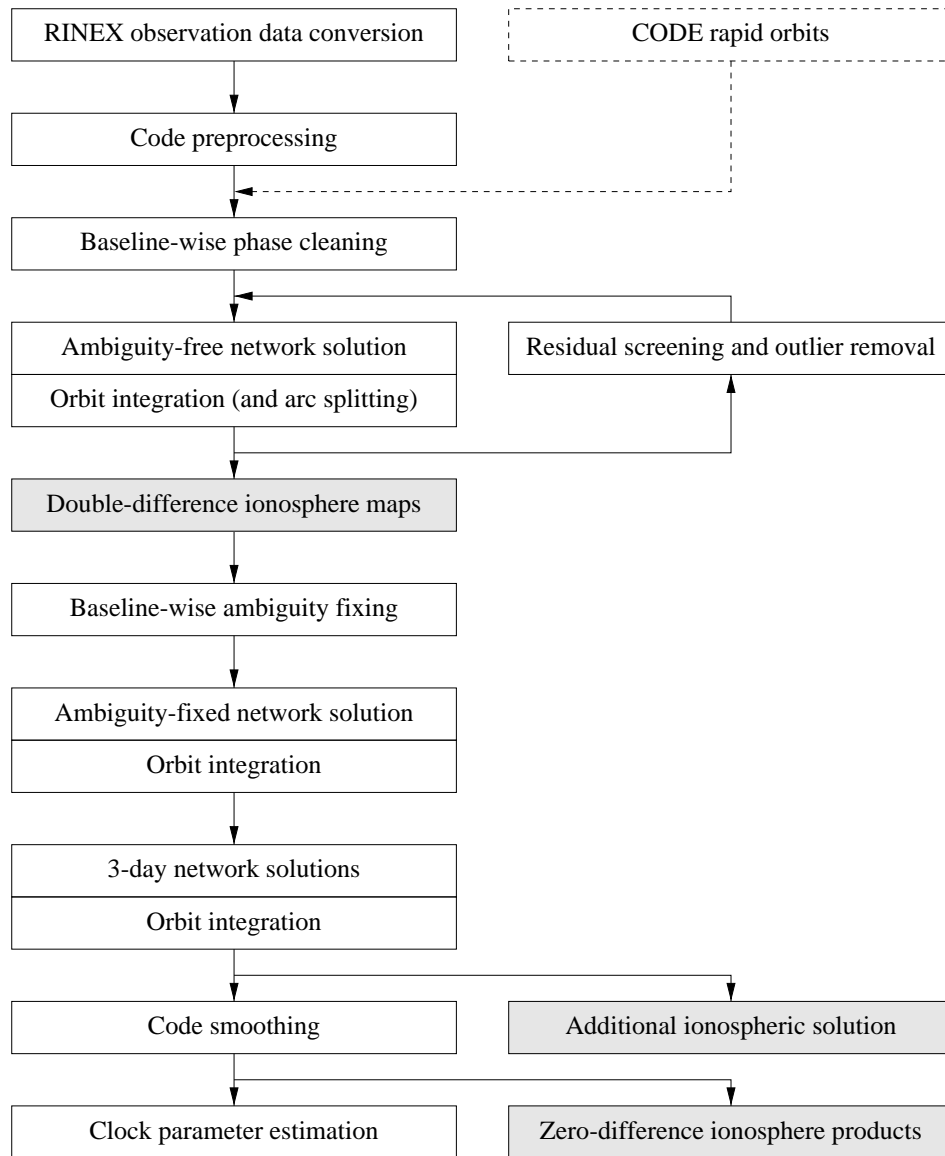


Figure 4.2: Flow chart of the final IGS data processing at CODE.

of stations which, however, shows a few remarkable slumps caused by public holidays, temporary connection difficulties, or a breakdown of an IGS global data center. A corresponding spectral analysis reveals a pronounced 7-day period, confirming that there is still some human interaction in the data management. The GPS tracking network processed by CODE consists at present of about 130 stations, the global distribution of which is given in Figures 2.5 and 4.4. Figure 4.4 indicates the probed ionospheric regions by dot-

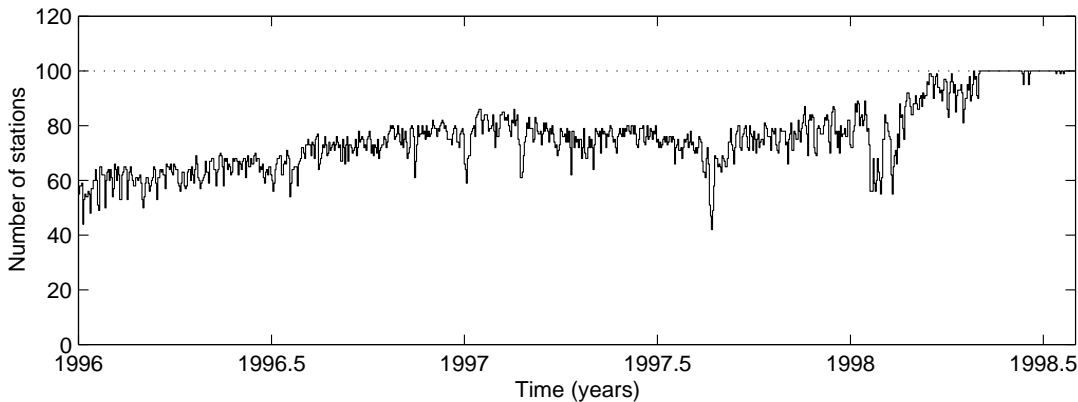


Figure 4.3: Number of IGS stations daily processed by CODE, from January 1996 to July 1998.

ted circles—ignoring the GPS-specific “north and south holes” as shown in Figure 3.7 for certain station latitudes. As from spring of 1998, an upper limit of 100 stations is imposed on the double-difference processing. If more than 100 stations are available for a particular day, first the data completeness and secondly a priority list are used to decide whether a station is actually included or not. The number of stations processed in the zero-difference processing is usually 80, which is the maximum number presently manageable. The corresponding priority list allows the selection according to the needs concerning the processing of zero differences and code measurements, respectively.

In the final processing step, we use a strategy to form baselines, which searches for linearly independent baselines thereby maximizing the total number of single-difference phase observations. The GIM estimation based on double differences (3.32) happens prior to the QIF ambiguity fixing. The 3-day combination yields the “CODE final orbits” that are referred to the middle day. At the end of the double-difference processing sequence, an additional ionospheric solution is computed for test purposes.

Last but not least, a zero-difference processing step follows for the “middle” day. The code smoothing is accomplished by (2.8), primarily using the Melbourne-Wübbena LC analogous to (2.31) for data screening. Epoch-specific satellite and station clock parameters  $\Delta t^k$  and  $\Delta t_i$  are adjusted by analyzing (2.15b) and by taking into account the final orbits, station coordinates, and tropospheric information stemming from the double-difference processing. The zero-difference ionosphere products are based on geometry-free, phase-smoothed code observations according to (3.31b) and (3.33), and include differential code bias (DCB) information  $\Delta b^k$  and  $\Delta b_i$  as a by-product.

The final IGS data processing at CODE is performed with a delay of about 4 days after collecting the observations of the middle day of the 3-day solutions. Keeping in mind

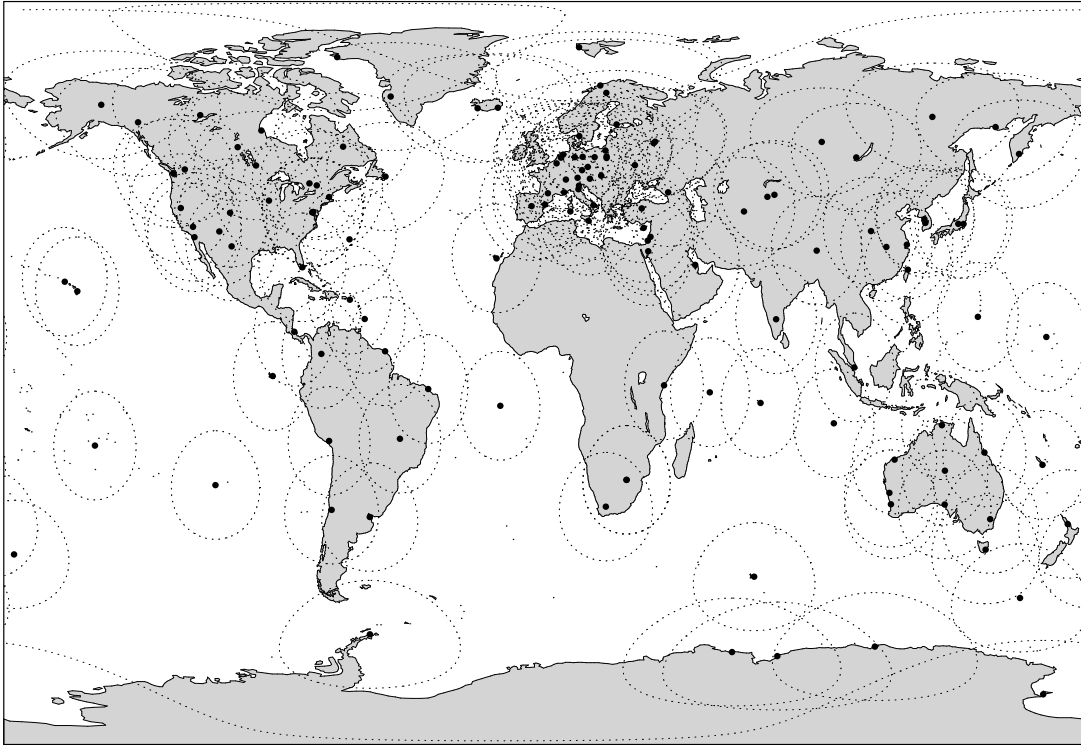


Figure 4.4: Globally distributed IGS stations processed by CODE and GPS-probed ionospheric regions.

that all ionospheric solutions are daily solutions, this means that the phase-derived final GIMs are available within about 3 days of the observations.

The IGS final products of CODE—consisting of orbits, ERPs, station coordinates in SINEX format, satellite clocks, tropospheric information, and ionosphere maps and satellite DCBs in IONEX format (see also section 4.2.5)—are delivered weekly to the CDDIS. All these products are daily products, except for the station coordinates which refer to one GPS week and therefore stem from a 7-day combination.

### 4.1.3 European IGS Data Processing

Unlike the global processing schemes in Figures 4.1 and 4.2, the regional, *European* IGS data processing, which follows approximately one week behind the final processing is performed without orbit improvement. The processing steps are similar to those of the global processing: baseline-wise phase cleaning, ambiguity-free cluster solutions, residual screening and outlier removal, ambiguity-free network solution, regional ionosphere map

based on (3.32), baseline-wise ambiguity fixing, ambiguity-fixed network solutions. In addition, an “ambiguity-fixed” ionosphere map is derived. All European solutions are daily solutions, except for the 7-day combination of the station coordinates, CODE’s contribution to EUREF, which is computed once a week. The European GPS network processed by CODE consists of about 40 stations.

Let us finally mention that various solutions with different settings and features are computed in addition for test purposes as part of both the European and the global IGS data processing. These solutions, which are produced in parallel, are used to examine new, refined processing strategies. We refer to, e. g., [Rothacher *et al.*, 1998b], who compare different processing strategies for regional GPS networks.

It seems important to point out that ionospheric mapping does not require precise orbits, because the ionospheric (or geometry-free) LC totally eliminates the geometric component. Even so, one needs orbital information, because it is required to compute the obliquity factors  $F(z)$  as well as the coordinates  $(\beta, s)$  of the intersection points with the single layer, but even broadcast orbits would serve this purpose. When looking at the processing schemes more closely, one may notice, however, that the ionospheric processing steps indirectly benefit from precise orbits, because the data screening is always based on the ionosphere-free LC containing the geometric component. This aspect should not be underestimated, because a data screening based on the geometry-free LC would suffer from unpredictable short-time variations of the TEC.

## 4.2 CODE Ionosphere Products

The current CODE ionosphere products include:

- rapid GIMs (**RG** solution) based on double-difference data (3.32),
- final GIMs (**G1** solution) also based on (3.32),
- GIMs including satellite and station DCBs (**Z1** solution) based on zero-difference data (3.33),
- station-specific ionosphere maps including satellite and station DCBs (**Z1N** solution) based on (3.33),
- European ionosphere maps (**EG** solution) based on (3.32),
- “ambiguity-fixed” European ionosphere maps (**EQ** solution) based on (3.32), and
- 1-day and 2-day predicted GIMs (**G11/G12** solution) based on the time series of the **G1** solutions and the three most recent **RG** solutions.

Note that **RG**, **G1**, **Z1**, etc., are internal solution IDs.

Table 4.1: CODE ionospheric solutions, the maximum degree  $n_{\max}$  and order  $m_{\max}$  of the SH expansion, the period  $\Delta t$  of validity, the total number  $u$  of TEC and DCB parameters estimated each day, and TEC parameter constraints  $\sigma_{E,\text{abs}}$  and  $\sigma_{E,\text{rel}}$ .

Solution ID	$n_{\max}$	$m_{\max}$	$\Delta t$ (h)	$u_E$	$u_{\Delta b^k}$	$u_{\Delta b^i}$	$\sigma_{E,\text{abs}}$	$\sigma_{E,\text{rel}}$
RG/G1	12	8	2	1788	–	–		X
Z1	12	8	2	1788	27	80		X
Z1N	4	4	24	2000	27	80	X	
EG/EQ	12	8	24	149	–	–	X	
G11/G12	12	8	2	1788	–	–		

#### 4.2.1 TEC Parameterization and Estimation

Let us briefly state the most important aspects concerning the TEC parameterization and estimation. The elevation cut-off angle of  $10^\circ$  and the observation weighting model (3.45) are adopted for the ionospheric solutions too. The vertical TEC is parameterized exclusively by SH expansions (3.35) which refer to a solar-geomagnetic frame. Slant TEC is reduced with the SLM mapping function (3.24), setting the layer height to  $H = 450$  km.

Table 4.1 gives the maximum degree and order of the SH expansion and the total number of SH coefficients estimated each day for various solution types. The number of SH coefficients per TEC representation (3.35) is given by relations (3.39) or (3.40), which is 149 for a GIM and 25 for a station-specific map, respectively. The period of validity  $\Delta t$  of a single set of TEC parameters is 2 hours for all GIMs, that is, 12 sets of TEC parameters have to be estimated each day. The 24-hour regional and station-specific TEC maps are both described by one “global” TEC representation (3.35). For the Z1N solution, the total number  $u_E$  of TEC parameters is consequently  $80 \cdot 25 = 2000$ , assuming the number of processed stations to be 80. The satellite and station DCBs are represented by daily constants. This leads to  $27 + 80$  DCB parameters per day with a constellation of 27 satellites.

In order to avoid singularities in the low-degree SH coefficients when deriving regional and station-specific TEC maps, small constraints (2.57) of, e. g., 100 TECU are imposed on all SH coefficients. This is indicated by an “X” in the column labeled  $\sigma_{E,\text{abs}}$ . When deriving several global TEC maps per day, one has to expect unreasonable—very high or negative—TEC estimates in regions where at times no stations are located. We avoid such problems by limiting the variations between consecutive global TEC maps with relative constraints (2.58) between consecutive TEC parameters of the same degree and order. Because we deal with normalized SH coefficients, we may use a common  $\sigma_{E,\text{rel}}$  for all global TEC parameters. The a priori sigma  $\sigma_{E,\text{rel}}$  must be found experimentally by producing global TEC maps with different  $\sigma_{E,\text{rel}}$  and taking, e. g., the extent of regions

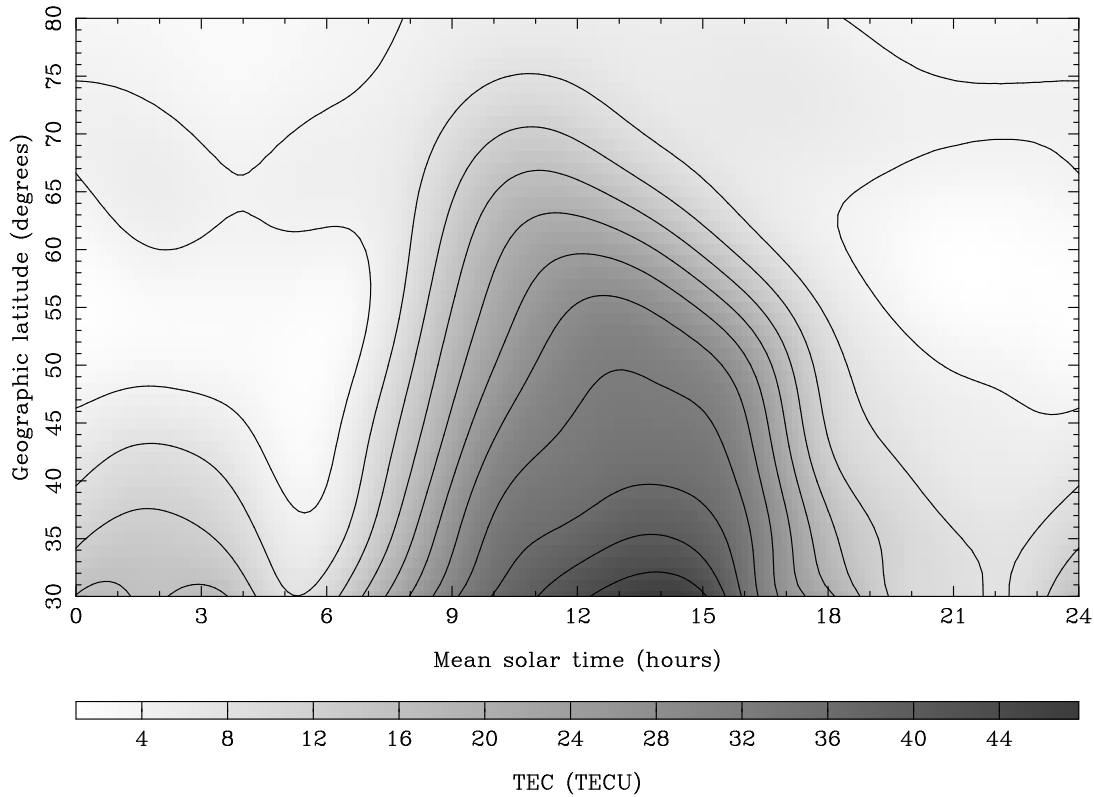


Figure 4.5: 24-hour European TEC map for November 14, 1998.

with negative TEC as an indication. After extensive tests, we use  $\sigma_{E,\text{rel}} = 0.03$  TECU. It is essential that such “relative” pseudo-observations do not affect the “absolute” TEC determination. Relative constraints are based on the basic assumption of a “frozen-in” ionosphere co-rotating with the Sun for unprobed ionospheric regions.

## 4.2.2 Examples of CODE TEC Maps

### European TEC Maps

An example for a European TEC map (EQ solution) is given in Figure 4.5 for November 14, 1998. Remember that EQ TEC maps are derived from ambiguity-fixed double-difference phase observations of about 40 European IGS stations. The vertical TEC is given as a function of the mean solar time, corresponding to a mean sun-fixed longitude  $s$  plus 12 hours, and the geographic latitude. Contour lines are given for every 4 TECU in accordance with the tick marks of the gray-scale bar. The TEC reaches its maximum around local noon. We recognize, however, that the corresponding point in time depends

rather strongly on the latitude. Furthermore, we clearly see a pronounced north-south gradient. The TEC considerably increases towards lower latitudes and reaches about 48 TECU on that particular day at the latitude of  $30^\circ$ .

### Station-Specific TEC Maps

We do not show individual station-specific Z1N TEC maps here, because they may be handled and visualized in a similar way as 24-hour European TEC maps. Apart from the different observation type used, the only difference compared to the EG/EQ TEC maps is that each Z1N TEC map is represented by less SH coefficients and covers a narrower latitude range.

### Global TEC Maps

A series of 12 2-hourly global TEC snapshots for January 17, 1998, taken at 01:00, 03:00, 05:00, 07:00, 09:00, 11:00, 13:00, 15:00, 17:00, 19:00, 21:00, and 23:00 UT, is shown row by row in Figure 4.6. The corresponding GIMs (Z1-like solution) were derived from phase-smoothed zero-difference code observations of 79 globally distributed IGS stations. The only difference to a current Z1 solution is that the SH expansion (3.35) was referred to a solar-geographic frame at that time, instead of the solar-geomagnetic frame currently used. As in Figure 4.5, dark areas indicate high TEC and reach values slightly above 50 TECU on that particular day. Nevertheless, the typical TEC structure co-rotating with the Sun, which may be bifurcated, follows the geomagnetic equator indicated by the dotted line fairly well, despite using a solar-geographic reference frame. Figure 4.6 indicates that a solar-geomagnetic reference frame is more appropriate. On the other hand, it also shows that the choice of the sun-fixed reference frame is not that crucial—if a subdaily temporal resolution is attained. In terms of spatial resolution, (3.41a) tells us that we are able to resolve TEC structures which are separated by  $\Delta\beta = 360^\circ/12 = 30^\circ$  in latitude. Because the equatorial anomaly exhibits a peak-to-peak distance which is of this order, it may be resolved with a SH expansion of degree 12. The bifurcation of the TEC bulge due to the equatorial anomaly is also recognizable in Figure 4.6.

The 7th global TEC snapshot of Figure 4.6, corresponding to 13:00 UT, is shown in Figure 4.7 in a larger scale. The TEC maximum is crossing the Greenwich meridian, whereas the Sun's subpoint is already at a longitude of  $-15^\circ$ , neglecting the equation of time. However, it is normal that the TEC bulge follows the Sun's subpoint with a certain lag.

### Global RMS Maps

The formal accuracy of the TEC estimation may be computed for any coordinates  $(\beta, s)$  by applying the general variance-covariance propagation law (2.51) to the variance-covariance matrix of the adjusted SH coefficients. Figure 4.8 shows 2-hourly global



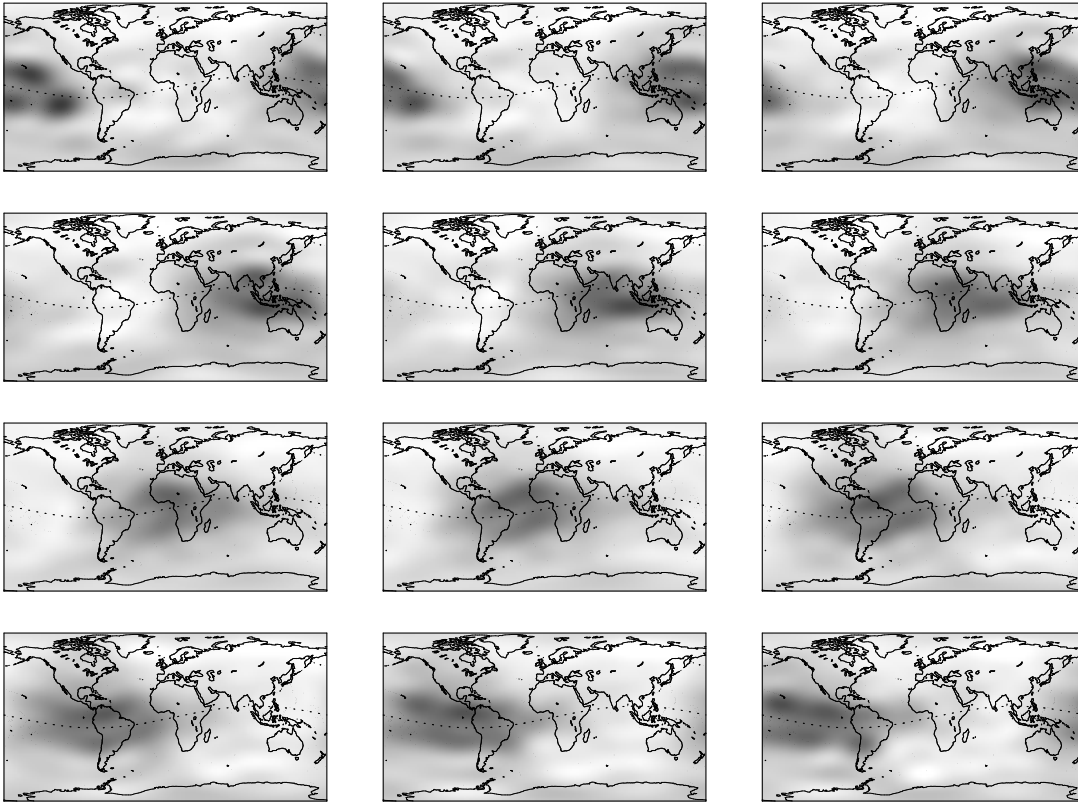


Figure 4.6: 2-hourly global TEC snapshots for January 17, 1998, taken at 01:00, 03:00, 05:00, ..., 23:00 UT.

snapshots of the formal RMS errors which are associated with the TEC maps shown in Figure 4.6. The lighter the shading, the better is the formal TEC accuracy. The RMS errors vary in this case by approximately one order of magnitude. It is obvious that the RMS structure primarily reflects the station coverage. It is thus not astonishing that the TEC over Europe and North America is comparatively well determined, whereas extended ionospheric regions exist, mainly over the open sea, where the TEC does not get probed in situ. It is interesting that isolated stations, like O'Higgins in Antarctica, may be clearly identified on the basis of a bright spot in the RMS picture of Figure 4.8.

### 4.2.3 Data Formats

All ionospheric solutions—with the exception of the predictions—are computed using the main parameter estimation program GPSEST of the Bernese GPS Software [Rothacher and Mervart, 1996]. The CODE ionosphere products are available in the form of BGS

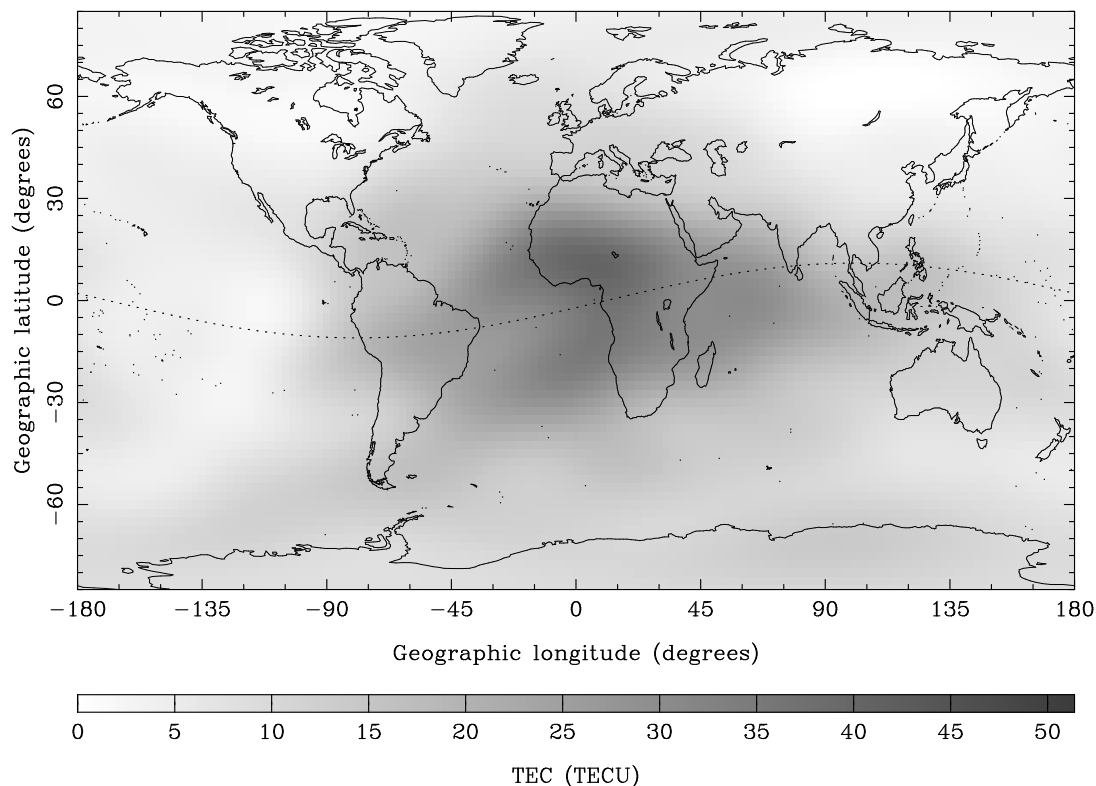


Figure 4.7: Global TEC on January 17, 1998 at 13:00 UT.

ionosphere and DCB files. Extracts from an ionosphere and a DCB file are given in Figures 4.9 and 4.10. The ionosphere files essentially contain the normalized SH coefficients of the TEC representation (3.35). They may contain several sets of SH coefficients either referring to different periods of validity or to different stations. The DCB files contain the DCB estimates for satellites and receivers. Each receiver DCB is labeled by a 4-character ID and the IERS DOMES number of the corresponding station. Note that the characters “G” and “R” are used to distinguish between GPS and GLONASS DCB information.

Many ionosphere files are also converted into IONEX files, namely: the rapid GIMs (RG solution), the final GIMs (G1 solution), the zero-difference GIMs (Z1 solution), the European maps (EG solution), and the predicted GIMs. IONEX files essentially contain TEC grid maps which are referred to an earth-fixed frame and particular epochs. The satellite DCB estimates which are included in the global IONEX files stem from the corresponding Z1N solution or, if such a solution is not yet available, from a moving 7-day DCB combination of the most recent Z1N solutions. The G1 ionosphere product is complemented subsequently with the corresponding 1-day DCB estimates. Furthermore, a

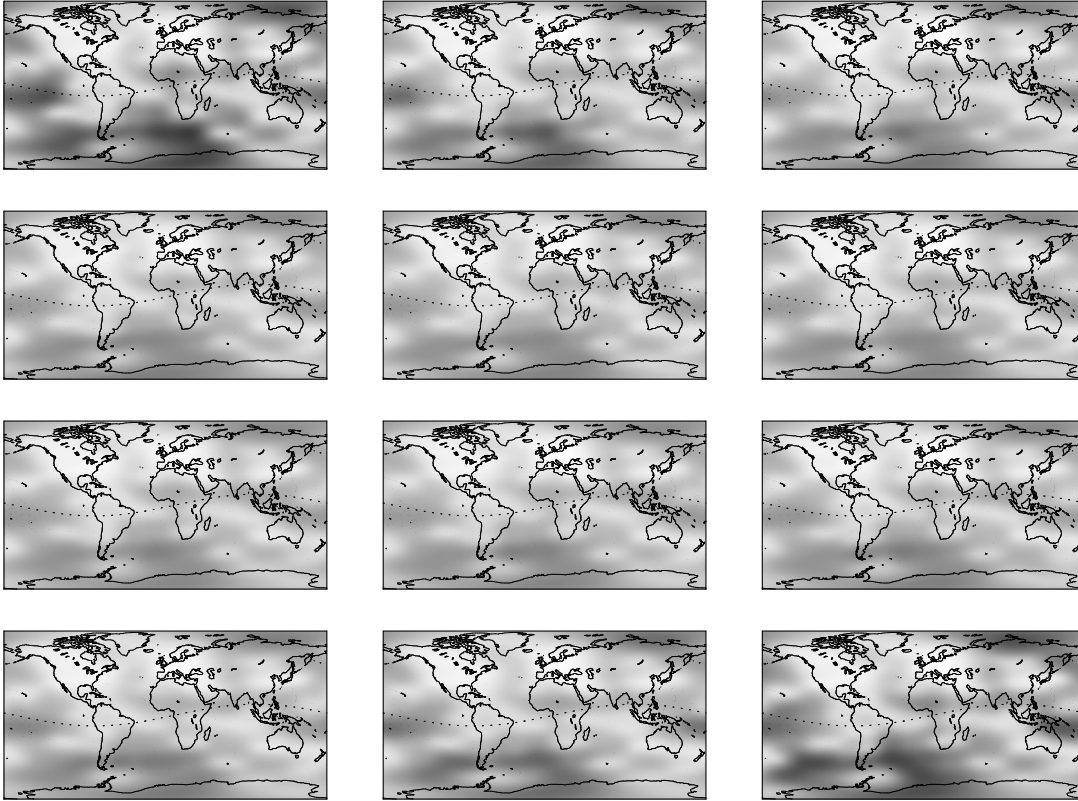


Figure 4.8: 2-hourly global RMS snapshots for January 17, 1998, taken at 01:00, 03:00, 05:00, ..., 23:00 UT.

moving 7-day DCB comparison is made to provide realistic, satellite-specific information about the RMS accuracy of the daily DCB estimation.

#### 4.2.4 IGS IONEX Files

At present, the IONEX product based on the G1 GIMs and the Z1N DCBs is considered as our official IGS ionosphere product and is delivered weekly to CDDIS. IGS IONEX files as of DOY 152, 1998 may be found under <ftp://cddisa.gsfc.nasa.gov/pub/gps/products/ionex/YYYY/DDD/CCCGDDD0.YYi.Z>, where YYYY is the 4-digit year, CCC is the AC ID, DDD is the DOY, and YY is the 2-digit year; the “Z” indicates a compressed file. IGS IONEX files do not only fulfill the IONEX standard but also satisfy additional IGS-specific criteria that make it easier to compare and combine GIMs within the IGS [Feltens and Schaer, 1998]. One essential criterion concerns the epochs the TEC grid maps have to be referred to, namely 01:00, 03:00, 05:00, ..., 23:00 UT of each day.

CODE'S GLOBAL IONOSPHERE INFORMATION FOR DAY 152, 1998				05-JUN-98 02:51
-----				
MODEL NUMBER / STATION NAME	:	1521-01		
MODEL TYPE (1=LOCAL,2=GLOBAL,3=STATION)	:	2		
MAXIMUM DEGREE OF SPHERICAL HARMONICS	:	12		
MAXIMUM ORDER	:	8		
DEVELOPMENT WITH RESPECT TO				
GEOGRAPHICAL (=1) OR GEOMAGNETIC (=2) FRAME	:	2		
MEAN (=1) OR TRUE (=2) POSITION OF THE SUN	:	1		
MAPPING FUNCTION (0=NONE,1=1/COS)	:	1		
HEIGHT OF SINGLE LAYER AND ITS RMS ERROR (KM)	:	450.00	0.00	
COORDINATES OF EARTH-CENTERED DIPOLE AXIS				
LATITUDE OF NORTH GEOMAGNETIC POLE (DEGREES)	:	79.41		
EAST LONGITUDE (DEGREES)	:	-71.64		
PERIOD OF VALIDITY				
FROM EPOCH / REFERENCE EPOCH (Y,M,D,H,M,S)	:	1998 06 01 00 00 00		
TO EPOCH	:	1998 06 01 02 00 00		
LATITUDE BAND COVERED				
MINIMUM LATITUDE (DEGREES)	:	-88.73		
MAXIMUM LATITUDE (DEGREES)	:	86.87		
ADDITIONAL INFORMATION				
NUMBER OF CONTRIBUTING STATIONS	:	100		
NUMBER OF CONTRIBUTING SATELLITES	:	27		
ELEVATION CUT-OFF ANGLE (DEGREES)	:	10		
MAXIMUM TEC AND ITS RMS ERROR (TECU)	:	41.11	0.37	
COMMENT / WARNING	:			
COEFFICIENTS				
DEGREE	ORDER	VALUE (TECU)	RMS (TECU)	
0	0	12.63992828	0.0448	
1	0	3.21952829	0.0418	
1	1	6.00803877	0.0441	
12	-8	0.01343537	0.0141	
CODE'S GLOBAL IONOSPHERE INFORMATION FOR DAY 152, 1998				05-JUN-98 02:51
-----				
MODEL NUMBER / STATION NAME	:	1521-02		
12	-8	0.04504099	0.0117	
CODE'S GLOBAL IONOSPHERE INFORMATION FOR DAY 152, 1998				05-JUN-98 02:51
-----				
MODEL NUMBER / STATION NAME	:	1521-03		
12	-8	0.03860867	0.0142	

Figure 4.9: BGS ionosphere (ION) file g1\_98152.ion.

#### 4.2.5 The Ionosphere Map Exchange (IONEX) Format

IONEX is an internationally adopted format for the exchange of two- or even three-dimensional ionosphere maps [Schaer *et al.*, 1998a]. It was developed by the IGS Ionosphere Working Group and approved by the IGS community. The IONEX format has similar characteristics as the RINEX format [Gurtner, 1994].

Each IONEX file consists of a header section and a data section. The header section is placed at the beginning of the file and contains descriptive information which is valid for the entire file. The data section then contains the actual TEC information as TEC

CODE'S STATION-SPECIFIC IONOSPHERE INFO FOR DAY 152, 1998		06-JUN-98 17:37	
-----			
DIFFERENTIAL (L1-L2) CODE BIASES FOR SATELLITES AND RECEIVERS:			
PRN / STATION NAME	VALUE (NS)	RMS (NS)	
*** *****	*****	***	*****
G01	-0.595	0.009	
G02	-1.835	0.009	
G03	0.182	0.009	
G31	1.267	0.009	
G ALBH 40129M003	14.893	0.072	
G ALGO 40104M002	2.714	0.078	
G AMCT 40472S003	4.123	0.083	
G	ZWEN 12330M001	-1.013	0.077

Figure 4.10: BGS DCB file z1n98152.dcb.

grid maps, usually giving the TEC values in units of 0.1 TECU. Extracts from an IGS IONEX file are shown in Figures 4.11 and 4.12. Figure 4.11 shows an IONEX header section which may also contain satellite DCB information and technique-related auxiliary data. Figure 4.12 finally contains a few fragments of the corresponding global TEC and RMS grid maps.

If the grid is dense enough, the spatial interpolation of the TEC grid maps may be performed by using the four-point formula [Abramowitz and Stegun, 1972]

$$E(\lambda, \beta) = (1 - p)(1 - q)E_{0,0} + p(1 - q)E_{1,0} + q(1 - p)E_{0,1} + pqE_{1,1} \quad (4.1)$$

where

$E(\lambda, \beta) = E(\lambda_0 + p\Delta\lambda, \beta_0 + q\Delta\beta)$  is the TEC interpolated at the desired geographic longitude  $\lambda$  and latitude  $\beta$ ,

$E_{i,j}$  are the four nearest TEC grid values as depicted in Figure 4.13,

$(\lambda_0, \beta_0)$  are the geographic coordinates associated with  $E_{0,0}$ ,

$p, q$  are multipliers within the interval  $[0, 1]$ , and

$\Delta\lambda, \Delta\beta$  are the grid widths in longitude and latitude.

For further information about the IONEX format, we refer to [Schaer et al., 1998a]. This article also includes guidelines concerning the temporal interpolation of TEC grid maps as well as a short description of IONEX reading and writing Fortran-77 modules. Meanwhile a subroutine to spatially and temporally interpolate IONEX TEC information is available too.

1.0	IONOSPHERE MAPS	GPS	IONEX VERSION / TYPE
DCBINX V4.1	AIUB	14-JUL-98 14:58	PGM / RUN BY / DATE
CODE'S GLOBAL IONOSPHERE INFORMATION FOR DAY 152, 1998			COMMENT
The global ionosphere maps are generated on a daily basis			DESCRIPTION
by the Center for Orbit Determination in Europe (CODE),			DESCRIPTION
University of Berne, Switzerland.			DESCRIPTION
The TEC is modeled with a spherical harmonic expansion up			DESCRIPTION
to degree 12 and order 8 referring to a solar-geomagnetic			DESCRIPTION
reference frame. The 12 2-hour sets of 149 ionosphere			DESCRIPTION
parameters per day are derived from GPS carrier phase data			DESCRIPTION
of the global IGS (International GPS Service) network.			DESCRIPTION
Contact address: stefan.schaer@aiub.unibe.ch.			DESCRIPTION
1998	6	1 1 0 0	EPOCH OF FIRST MAP
1998	6	1 23 0 0	EPOCH OF LAST MAP
7200			INTERVAL
12			# OF MAPS IN FILE
COSZ			MAPPING FUNCTION
10.0			ELEVATION CUTOFF
Doubly differenced GPS carrier phase			OBSERVABLES USED
100			# OF STATIONS
27			# OF SATELLITES
6371.0			BASE RADIUS
2			MAP DIMENSION
450.0	450.0	0.0	HGT1 / HGT2 / DHGT
87.5	-87.5	-2.5	LAT1 / LAT2 / DLAT
-180.0	180.0	5.0	LON1 / LON2 / DLON
-1			EXPONENT
TEC/RMS values in 0.1 TECU; 9999, if no value available			COMMENT
DIFFERENTIAL CODE BIASES			START OF AUX DATA
01	-0.595	0.064	PRN / BIAS / RMS
02	-1.835	0.028	PRN / BIAS / RMS
03	0.182	0.045	PRN / BIAS / RMS
31	1.267	0.036	PRN / BIAS / RMS
DCB values in ns; sum of all values constrained to zero			COMMENT
DIFFERENTIAL CODE BIASES			END OF AUX DATA
			END OF HEADER

Figure 4.11: Header section of the IGS IONEX file `codg1520.98i`.

#### 4.2.6 Automatically Updated WWW Site Showing CODE GIMs

The computer job that executes the ionosphere prediction procedure, shaded in Figure 4.1, also includes a procedure that automatically updates the ionosphere-related CODE WWW site <http://www.cx.unibe.ch/aiub/ionosphere.html> [Schaer, 1998a]. E.g., the most recent rapid and final CODE GIMs are visualized there on the basis of the corresponding IONEX files.

#### 4.2.7 History of the CODE Ionospheric Solutions

The computer scripts to automate the G1 GIM production were prepared at the end of 1995. Since January 1, 1996, the G1 GIM estimation procedure is running in an operational mode. The first GIMs were 24-hour GIMs represented by a SH expansion of degree 8 referring to a solar-geographic frame. The SLM altitude was set to 400 kilometers. At that time, an elevation cut-off angle of  $20^\circ$  was used and all observations were

1															START OF TEC MAP	
1998	6	1	1	0	0											EPOCH OF CURRENT MAP
	87.5	-180.0	180.0	5.0	450.0											LAT/LON1/LON2/DLON/H
114	114	114	114	114	114	114	114	114	114	114	113	113	113	113	112	
112	112	111	111	111	110	110	109	109	109	108	108	107	107	107	106	
106	105	105	105	105	104	104	104	104	104	104	104	104	104	104	105	
105	105	106	106	106	107	107	108	108	109	109	110	110	111	111	111	
112	112	113	113	113	113	114	114	114								
	85.0	-180.0	180.0	5.0	450.0											LAT/LON1/LON2/DLON/H
120	120	120	120	120	119	119	119	119	118	118	118	117	117	117	116	
116	115	115	114	113	113	112	111	110	110	109	108	107	106	105	105	
104	103	102	102	101	101	101	100	100	100	100	100	100	101	101	101	
102	103	103	104	105	106	107	108	109	110	111	112	113	114	115	116	
117	118	118	119	119	120	120	120	120								
	82.5	-180.0	180.0	5.0	450.0											LAT/LON1/LON2/DLON/H
127	127	126	126	125	124	124	123	123	122	122	121	121	121	120	120	
120	119	118	118	117	116	115	113	112	111	109	108	107	105	104	103	
102	101	100	99	99	98	98	97	97	97	97	97	98	98	99	99	
100	101	103	104	105	107	108	110	112	113	115	117	119	120	122	123	
124	125	126	127	127	128	128	127	127								
-87.5-180.0 180.0 5.0 450.0															LAT/LON1/LON2/DLON/H	
40	41	42	43	43	44	44	45	45	45	46	46	46	46	45	45	
45	45	44	43	43	42	41	41	40	39	38	37	36	35	34	33	
32	31	30	29	28	27	27	26	25	24	24	23	23	23	22	22	
22	22	22	22	23	23	24	24	25	25	26	27	28	29	30	31	
32	33	34	35	36	37	38	39	40								
1															END OF TEC MAP	
2															START OF TEC MAP	
1998	6	1	3	0	0											EPOCH OF CURRENT MAP
	87.5	-180.0	180.0	5.0	450.0											LAT/LON1/LON2/DLON/H
127	127	127	127	127	126	126	126	126	126	125	125	125	125	124	124	
123	123	123	122	122	121	121	121	120	120	119	119	119	118	118	118	
117	117	117	117	117	117	117	117	117	117	117	117	117	118	118	118	
119	119	120	120	121	121	122	122	123	123	124	124	125	125	125	126	
126	126	126	127	127	127	127	127	127								
-87.5-180.0 180.0 5.0 450.0															LAT/LON1/LON2/DLON/H	
44	45	45	46	47	47	47	48	48	48	48	47	47	47	46	46	
45	45	44	43	42	41	41	40	39	38	37	36	36	35	34	33	
33	32	32	31	31	30	30	30	29	29	29	29	29	29	29	29	
29	30	30	30	31	31	31	32	32	33	33	34	35	35	36	37	
38	39	39	40	41	42	43	43	44								
12															END OF TEC MAP	
1															START OF RMS MAP	
1998	6	1	1	0	0											EPOCH OF CURRENT MAP
	87.5	-180.0	180.0	5.0	450.0											LAT/LON1/LON2/DLON/H
2	2	2	2	2	2	2	2	2	2	2	2	2	2	2	2	
2	2	2	2	2	2	2	2	2	2	2	2	2	2	2	2	
2	2	2	2	2	3	3	3	3	3	3	3	3	3	3	3	
3	3	3	3	3	3	3	3	3	3	3	3	3	3	3	2	
2	2	2	2	2	2	2	2	2	2	2	2	2	2	2	2	
-87.5-180.0 180.0 5.0 450.0															LAT/LON1/LON2/DLON/H	
5	5	5	5	5	5	5	5	5	5	5	5	5	5	5	5	
5	5	5	5	5	5	5	5	5	5	5	5	5	5	5	5	
5	5	5	5	5	5	5	5	5	5	5	5	5	5	5	5	
5	5	5	5	5	5	5	5	5	5	5	5	5	5	5	5	
5	5	5	5	5	5	5	5	5	5	5	5	5	5	5	5	
12															END OF RMS MAP	
															END OF FILE	

Figure 4.12: Data section of the IGS IONEX file codg1520.98i.

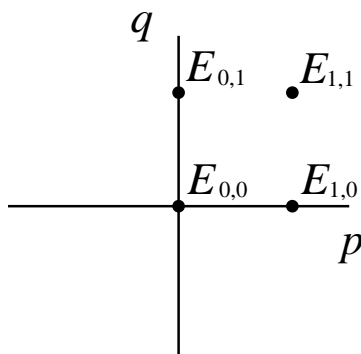


Figure 4.13: Bivariate interpolation using the four nearest TEC grid values  $E_{i,j}$ .

equally weighted. Furthermore, two other global ionospheric solutions were computed: the solution called **Q1**, which is equivalent to an ambiguity-fixed **G1** solution, and the **G1H** solution. The **G1H** solution corresponds to a **G1** solution, solving in addition for one global SLM height parameter.

A re-processing of the entire IGS data set of the year 1995 was performed by the beginning of 1996 computing the **G1**, **Q1**, and **G1H** solutions for each day. Supported by the Bernese Processing Engine (BPE), six parallel CPUs, and a powerful data archive system, this re-processing could be performed within about one week. As a result of this effort, ionospheric solutions are available from January 1, 1995 onwards.

European, **EG/EQ** TEC maps (see section 4.2) are routinely derived since DOY 344, 1995. The first **EG/EQ** TEC maps were represented by a SH expansion of degree 5. However, the maximum degree was increased to 8 on DOY 364, 1996, resulting in 81 instead of 36 TEC parameters per day to represent the regional TEC. As of DOY 95, 1997, an elevation cut-off angle of  $15^\circ$  has been chosen for the **EG/EQ** solutions.

The production of phase-derived GIMs was integrated into the rapid IGS data processing scheme at the end of June 1996. Rapid, **RG** GIMs have thus been produced by CODE starting with DOY 183, 1996.

At the end of September 1997, CODE began to generate global IONEX files. Before that time, only BGS ionosphere files were made available. However, non-BGS users could also apply CODE ionosphere maps with the help of a manual [Schaer, 1997].

At the beginning of October 1997, the elevation cut-off angle was generally decreased from  $20^\circ$  and  $15^\circ$ , respectively, to  $10^\circ$  for all solutions.

**Z1** GIMs derived from zero-difference observations are computed on a regular basis since DOY 295, 1997. Since DOY 296, 1997, a solution like **Z1**, processing only night-time data and therefore called **Z1N**, is computed as well. The initial motivation to produce **Z1N** solutions was to get more reliable DCB results, in view of the temperate ionospheric



climate on the night hemisphere. However, this solution type was subject to an essential change of its characteristics. Since DOY 22, 1998, the Z1N solution type is based on station-specific TEC representations of degree 3 now processing the data without any restriction. The maximum degree was increased to 4 on DOY 239, 1998, increasing the number of TEC parameters by approximately 50%.

At the end of January 1998, the maximum degree of the SH expansion was increased from 8 to 12 to improve the spatial resolution of the TEC representation in latitude. This change affected the RG, G1/Q1/G1H, Z1, and EG/EQ solutions.

At the end of March 1998, the temporal resolution of the TEC parameterization for the RG, G1, and Z1 solutions was considerably increased from 24 to 2 hours, thereby imposing relative constraints on the SH coefficients. Moreover, for these as well as the EG/EQ solutions, the reference frame was changed from a solar-geographic to a solar-geomagnetic system; the a priori SLM height was increased from 400 to 450 kilometers. The production of Q1/G1H solutions was stopped.

Since June 1, 1998, compressed IGS IONEX files containing G1 TEC and RMS maps are delivered to CDDIS. The approximate size of a uncompressed IGS IONEX file is 0.8 MB, or 0.4 MB if it contains no RMS maps. Its compressed version is about 4–6 times smaller. A global ionosphere file uses about 100 kB, a Z1N ionosphere file containing station-specific TEC information about 200 kB.

All BGS ionosphere files from old G1 solutions were converted into IONEX files at the beginning of July 1998. The uninterrupted, full time series of G1 TEC maps is thus available in the IGS-approved IONEX format, too. Two restrictions have to be mentioned, however. First, it is not possible to reconstruct RMS maps using the ION-to-IONEX conversion program because of missing covariance information. We save only variance information in ionosphere files, and therefore, RMS maps, if desired, would have to be re-computed with the program GPSEST. Secondly, GIMs with a 24-hour resolution are represented by only one IONEX grid map referring to 12:00 UT, because such GIMs may be simply rotated in longitude to obtain grid maps at other epochs. Note that the IONEX interpolating subroutine may account for this rotation [*Schaer, 1998a*].

In summary, we may say that the time series of the CODE ionospheric solutions are rather inconsistent in view of the considerable number of changes and refinements carried out. But this is also true for all other solutions computed by CODE. Therefore, a complete re-processing of the IGS data using the most up-to-date processing strategies should be aimed at to obtain consistent and improved time series of geodetic and atmospheric parameters.

### 4.3 Selected Global TEC Parameters

Because the amount of global TEC data based on G1 solutions is tremendous, we will concentrate on a few time series of selected TEC parameters notwithstanding their incon-

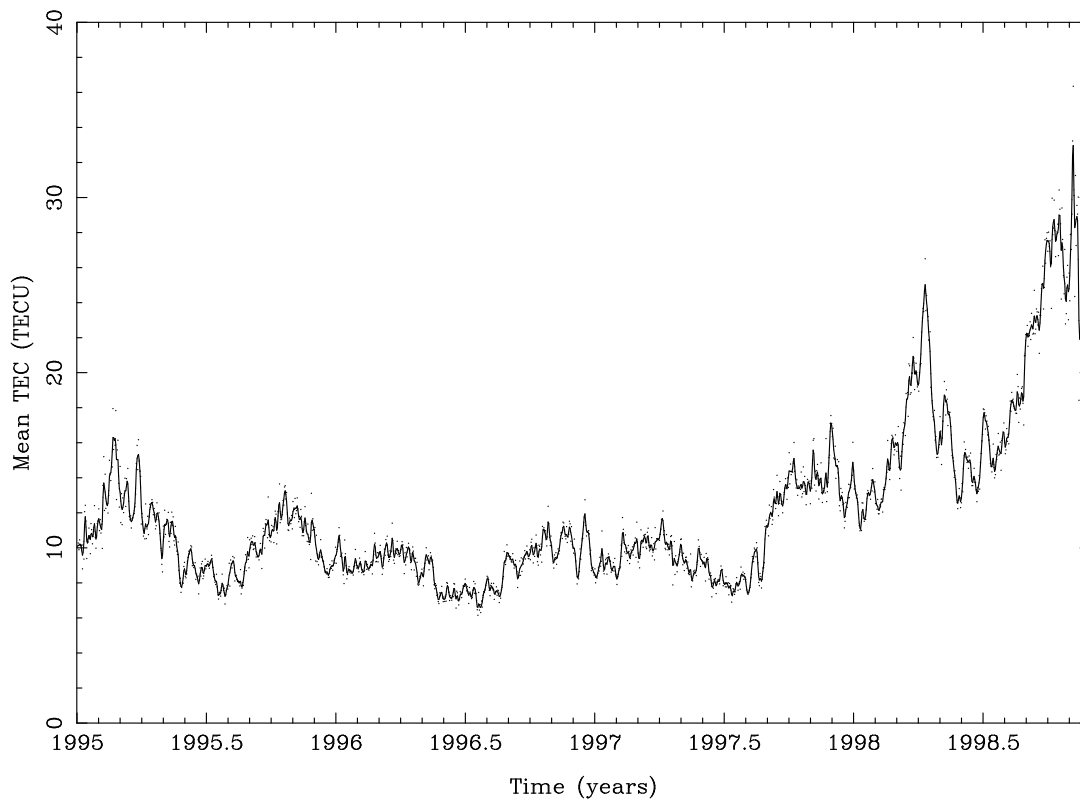


Figure 4.14: Mean vertical TEC of the Earth's ionosphere computed by CODE, from January 1995 to November 1998.

sistencies. The current length of the series of G1 solutions of almost 4 years is remarkable, compared to a solar cycle of 11 years, however, it is still relatively short. Nevertheless, such a time series of several years related to GPS-derived global TEC is unique and has not yet been seen up to now.

### 4.3.1 Mean TEC of the Earth's Ionosphere

An essential parameter to describe the state of the Earth's ionosphere is the mean vertical TEC  $\bar{E}_v$  (3.37), represented by the zero-degree coefficient  $\tilde{C}_{00}$  of the SH expansion (3.35). The importance of this particular TEC parameter is evident from the linear relationship (3.38) between  $\bar{E}_v$  and  $n_e$ , the global number of free ionospheric electrons.

Figure 4.14 shows the evolution of the mean vertical TEC during a period of low solar activity, namely from January 1995 to November 1998. Figure 4.14 is probably one of the most important figures of our analysis, as it documents the global state of the

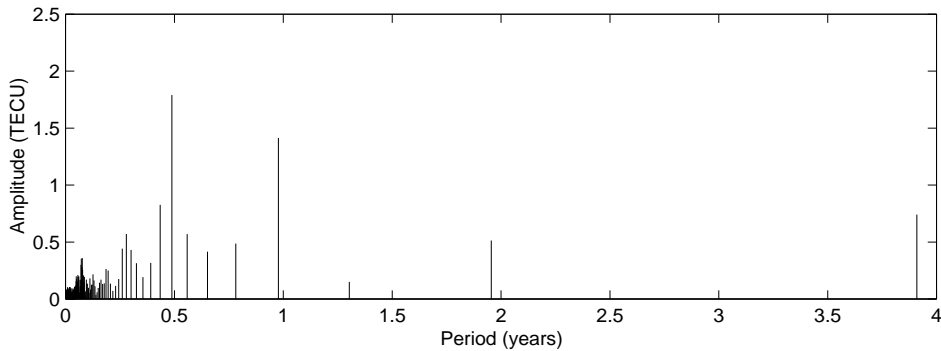


Figure 4.15: Amplitude spectrum of the mean TEC.

ionosphere over almost 4 years. Dots indicate the daily estimates or, in the case of a 2-hour resolution, daily averages. The solid line of smoothed daily estimates has been added to better see the behavior of the mean TEC. We perform signal smoothing by computing moving averages using a Gaussian kernel as weighting function:

$$\tilde{s}(t) = \frac{\sum_{i=1}^n W(t_i) s(t_i)}{\sum_{i=1}^n W(t_i)} \quad \text{with} \quad W(t_i) = \exp\left(-\frac{(t_i - t)^2}{2 \Delta t^2}\right) \quad (4.2)$$

where

$\tilde{s}(t)$  is the smoothed signal evaluated at time  $t$ ,

$s(t_i)$  is the measured signal referred to time  $t_i$ , and

$W(t_i)$  is the Gaussian kernel, and

$\Delta t$  is the characteristic width of the Gaussian kernel.

$\Delta t$  was set to 1 day to compute the smoothed signal shown in Figure 4.14.

Figure 4.14 reveals that we passed the recent ionospheric minimum activity period in the summer of 1996. It is impressive how large the dynamics of the ionosphere is—even during a solar minimum. Pronounced short-term as well as long-term fluctuations may be observed.

Before interpreting these fluctuations, let us have a look at the amplitude spectra in Figures 4.15 and 4.16 that were obtained from a spectral analysis of the mean TEC. The long-term trend caused by the 11-year solar cycle and an offset were removed from the signal prior to the spectral analysis.

In Figure 4.15 we notice two periods with highly significant amplitudes, namely a semi-annual and an annual one. The amplitude of the semi-annual component reaches almost

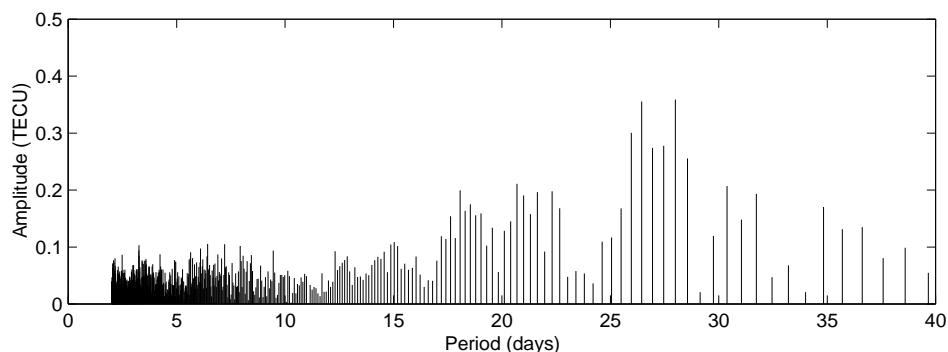


Figure 4.16: Amplitude spectrum of the mean TEC, for periods below 40 days.

2 TECU. Both components are caused by annual, semi-annual, and seasonal anomalies which have been known for a long time [*Rishbeth and Garriott, 1969*].

Over the world as a whole, there exists a 7% annual variation of solar ionizing flux, with the maximum in January, due to the variation of the sun-earth distance. In addition, there is a seasonal or winter anomaly: the TEC of the F2 layer tends to be larger in winter than in summer. This is a day-time phenomenon and vanishes at night. The winter anomaly is expected to be the more pronounced the higher the solar activity is. The semi-annual variation—the maxima of which occur around the equinoxes—remains definitively evident at solar minimum. Possible causes for these TEC anomalies are: variations in the neutral air temperature, seasonal changes in the concentration of atomic oxygen, etc.

In Figure 4.16, showing the amplitude spectrum for periods below 40 days, prominent peaks may be noticed around 27 days. These periods are caused by sunspots co-rotating with the Sun's surface. The associated peak is spread over a certain range of periods because the angular velocity varies with solar latitude. In the end, one has to be aware of the fact that the phase of the 27-day signal continuously changes due to sunspots randomly appearing and disappearing. Consequently, the real amplitudes associated with the Sun's rotation may be considerably larger than those reflected by the spectral analysis. This is confirmed by Figure 4.14.

### Summary

The long-term variation in the TEC in Figure 4.14 is clearly due to the variation of the sunspot number in the same time period (see also section 6.4). We note that the maxima of the semi-annual variation coincide remarkably well with the equinoxes. Minima occur at solstice, where the minima in summer are more pronounced than in winter. The short-term variations, caused by the Sun's rotation, are visible as well. We mention that

a figure similar to Figure 4.14 is regularly updated as part of the ionosphere prediction procedure. It is accessible through the CODE ionospheric WWW site [Schaer, 1998a].

### 4.3.2 Deriving Mean TEC From Global IONEX Data

It is easy to derive mean TEC values  $\bar{E}$  from global IONEX data. One merely has to compute the weighted sum

$$\bar{E} = \frac{\sum \cos \beta E_{\beta,\lambda}}{\sum \cos \beta} \quad (4.3)$$

where

- $E_{\beta,\lambda}$  is the TEC grid value associated with the geographic coordinates  $(\beta, \lambda)$  and
- $\cos \beta$  is the weighting function for the geographic latitude  $\beta$ .

The sum (4.3), which is compensated for the inhomogeneity of the grid, includes all TEC grid values  $E_{\beta,\lambda}$  referring to a certain epoch. When computing  $\bar{E}$  using (4.3), one has to take into account that IGS IONEX files contain the TEC grid values at  $\lambda = \pm 180^\circ$  twice.

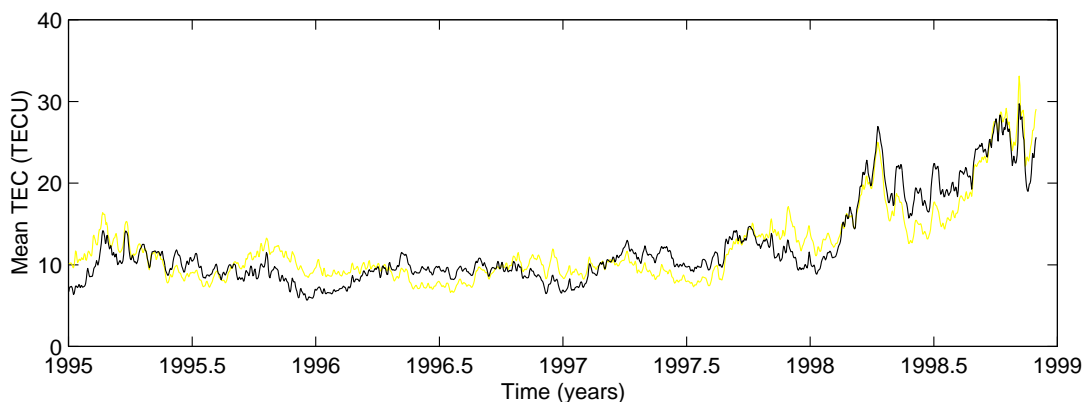
### 4.3.3 Mean TEC of the Northern and Southern Hemisphere

Formula (4.3) may also be used to compute mean TEC values related to a certain area of the globe by taking into account exclusively those TEC grid values which lie within the area of interest.

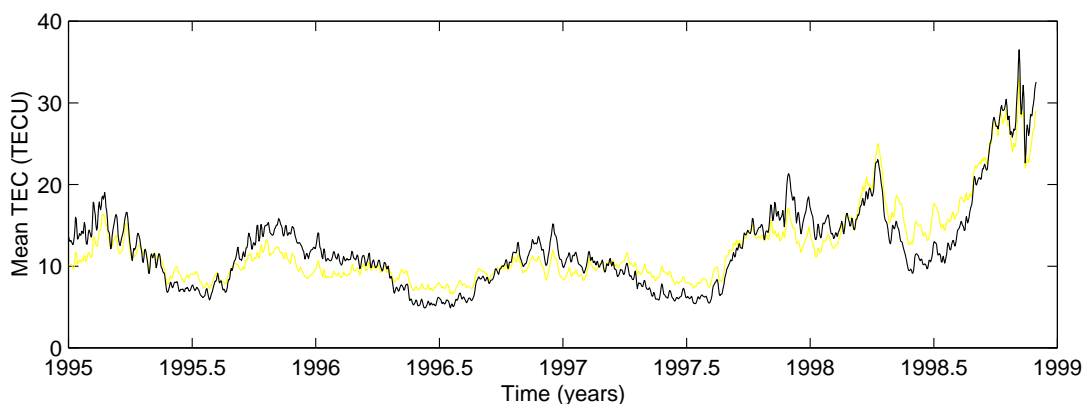
Let us discuss the mean TEC of the northern and southern hemisphere derived in such a way. The corresponding 1-day smoothed TEC values are shown in Figure 4.17. The varying declination of the Sun with respect to the Earth's equator obviously has a major impact. This is confirmed by the fact that the magnitudes of both signals significantly differ at solstice, whereas they are more or less the same at the equinoxes. Note that the light gray line gives the mean TEC of the entire sphere according to Figure 4.14. Figure 4.17 actually shows the mean TEC of the "geographic" hemispheres. As an alternative, the hemispheres which are bounded by the dip equator might be considered, in particular when looking at maps with a subdaily resolution. Diurnal variations in the mean TEC may be expected in both frames, however. Those with respect to the "geomagnetic" hemispheres are expected to be less pronounced (see also section 5.5.2).

The amplitude spectra of the mean TEC of the northern and southern hemisphere are shown in Figure 4.18. Whereas the amplitude of the semi-annual variations are of comparable size for both hemispheres, the amplitude of the annual variations are with about 4 TECU considerably larger for the southern hemisphere.

It is clear that the mean TEC related to, e. g., the day-time and night-time hemisphere might be visualized and analyzed in a similar way.



(a) Northern hemisphere



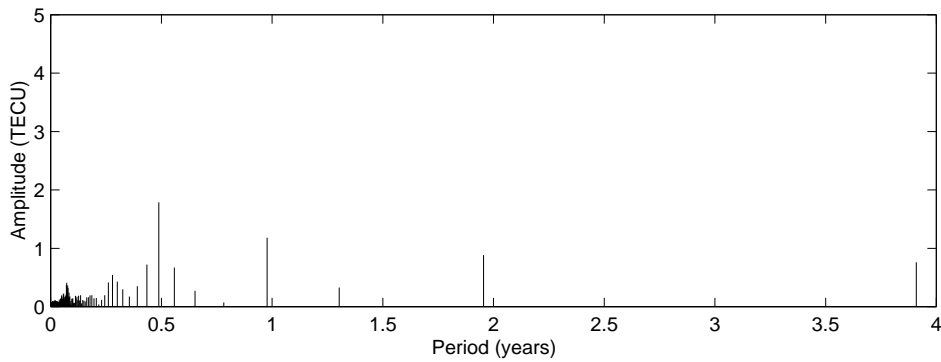
(b) Southern hemisphere

Figure 4.17: Mean TEC of both hemispheres, from January 1995 to November 1998.

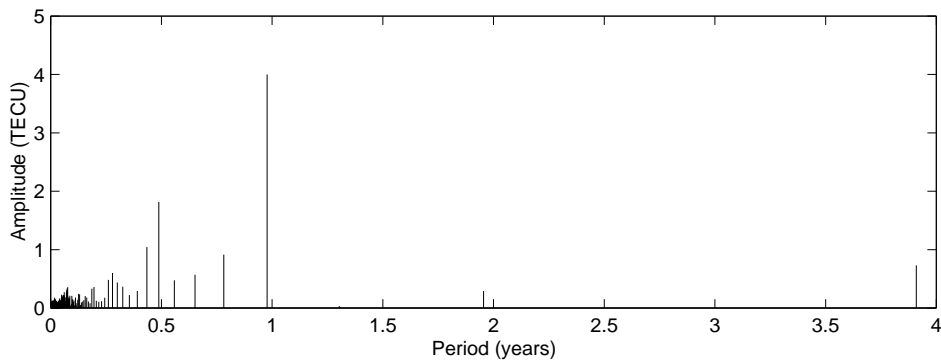
#### 4.3.4 Maximum TEC

The maximum TEC of the Earth's ionosphere may be found by searching for the maximum either in the global TEC distributions represented by (3.35) or in the global IONEX data. Note that maximum TEC values are explicitly given in the BGS ionosphere files introduced in Figure 4.9.

Figure 4.19 shows the G1-based time series of the maximum TEC. The value varies



(a) Northern hemisphere



(b) Southern hemisphere

Figure 4.18: Amplitude spectrum of the mean TEC of both hemispheres.

between approximately 20 and 150 TECU during this particular 4-year period. It is natural that short-term maxima may exceed the 1-day smoothed values given in Figure 4.19.

The corresponding amplitude spectrum is shown in Figure 4.20. The semi-annual component with an amplitude of about 10 TECU is dominant. A sunspot-driven component may be noticed in Figure 4.21, which shows the periods below 40 days. However, because the phase of the 27-day variation may continuously change, the real amplitudes of this variation are generally underestimated by spectral analyses. Strictly speaking, also the period is not well defined, because of the differential rotation of the Sun.

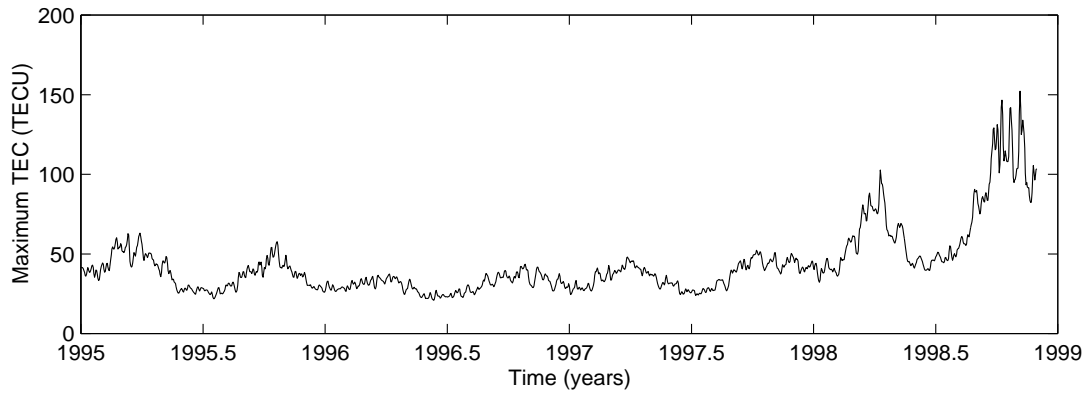


Figure 4.19: Maximum vertical TEC, from January 1995 to November 1998.

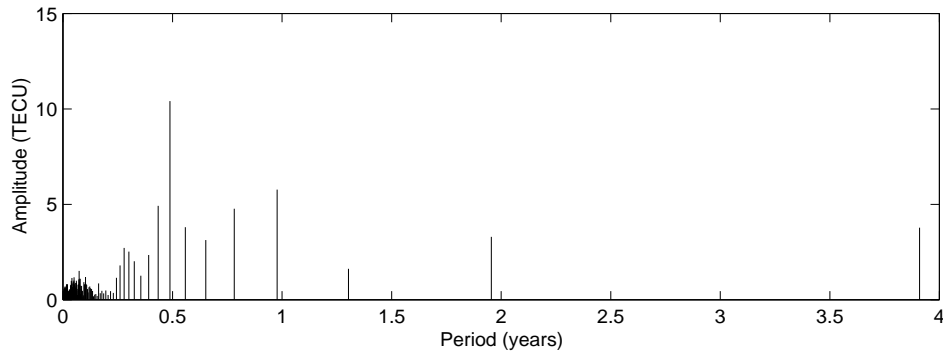


Figure 4.20: Amplitude spectrum of the maximum TEC.

### Minimum TEC

From the physical point of view, negative TEC values are not possible. The global TEC representation (3.35) may all the same result in negative TEC values. When considering their formal variances, however, the corresponding statistical confidence intervals usually extend into the positive domain of the TEC. In other words, these values are not significantly negative. Negative TEC values may sometimes occur in regions where no stations are located and where moreover the TEC itself is expected to be low. To avoid negative TEC values in our IONEX data, we simply reset them to zero.



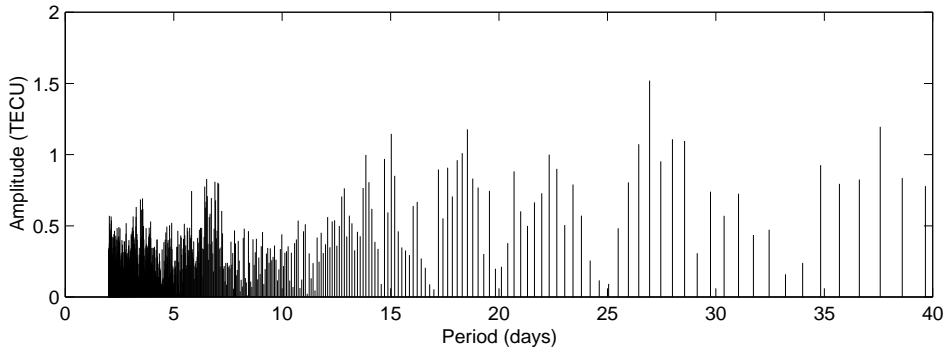


Figure 4.21: Amplitude spectrum of the maximum TEC, for periods below 40 days.

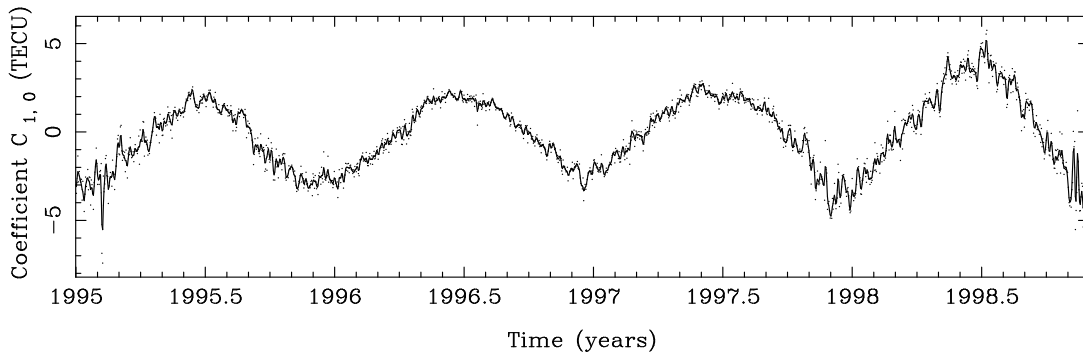


Figure 4.22: Normalized cosine coefficient  $\tilde{C}_{1,0}$ .

### 4.3.5 Higher-Degree SH Coefficients

Let us now look at G1-based time series of SH coefficients of higher degrees and orders, too. A selection of cosine and sine SH coefficients is shown in Appendix A, namely  $\tilde{C}_{0,0}$ ,  $\tilde{C}_{1,0}$ ,  $\tilde{C}_{1,1}$ ,  $\tilde{S}_{1,1}$ ,  $\tilde{C}_{2,0}$ ,  $\tilde{C}_{2,1}$ ,  $\tilde{S}_{2,1}$ ,  $\tilde{C}_{2,2}$ , and  $\tilde{S}_{2,2}$ . It would not make sense to show all higher-degree coefficients, keeping in mind that current GIMs include all terms up to  $\tilde{C}_{12,8}$  and  $\tilde{S}_{12,8}$ , respectively.

#### Zonal SH Coefficients

The first-degree coefficient  $\tilde{C}_{1,0}$ , which describes the zonal variation of the global TEC distribution, is shown in Figure 4.22. It is easily understood that the annual variation induced by the varying declination of the Sun is predominant. An offset may not be seen.

Such an offset would indicate a permanent imbalance in the global TEC distribution between the northern and southern hemisphere.

Unlike the zero-degree SH coefficient  $\tilde{C}_{0,0}$ , all coefficients of higher degrees and orders directly depend on the realization of the sun-fixed reference frame. One may therefore expect a discontinuity in the corresponding time series at the end of March 1998, when moving to a solar-geomagnetic reference frame. The main reason that no prominent jump may be detected is the 24-hour resolution maintained in Figure 4.22 which averages diurnal variations out. We postpone a discussion of the problems related to the subdaily resolution to Chapters 5 and 6.

### Sectorial SH Coefficients

Unlike zonal SH functions with  $m = 0$ , which are longitude-invariant, sectorial SH functions (with  $m = n$ ) are latitude-invariant, that is, they exclusively describe harmonics in longitudinal direction. Since the zero-degree sectorial coefficient  $\tilde{C}_{0,0}$  is constant and  $\tilde{S}_{0,0}$  disappears in (3.35), let us have a closer look at the low-degree coefficients  $\tilde{C}_{1,1}$ ,  $\tilde{S}_{1,1}$ ,  $\tilde{C}_{2,2}$ , and  $\tilde{S}_{2,2}$ . Their time series stemming from G1 solutions are included in Appendix A, namely in Figures A.3, A.4, A.8, and A.9.

The corresponding amplitude spectra are shown in Figures 4.23 and 4.24, actually for the high-frequency domain only. It may be disturbing at the first moment that the spectral analysis of these time series reveals in addition to the expected annual, semi-annual, and solar periods also an “unexpected” period in global TEC. The sharp peaks at a period around 15 days are striking. This signal is so pronounced that it is clearly visible even in the original time series. The corresponding amplitudes—always related to the normalized SH coefficients—range from about 0.15 to 0.25 TECU. Also, it is characteristic that the amplitude in  $\tilde{S}_{1,1}$  is less pronounced.

A period around 15 days reminds us of revolution period of the Moon. Since our global TEC representation is longitude-orientated towards the Sun, the so-called synodical month, the time it takes from new moon to new moon, is the relevant revolution period. A synodical month is equal to approximately 29.5306 days. The time that the Moon needs from one maximum elongation to the next corresponds therefore to  $29.5306/2 \approx 14.77$  days. This is “exactly” the period we see in our amplitude spectra of the low-degree sectorial SH coefficients. Computations solving for this period yield estimates which agree with the true value on the level of 0.01 days. We have thus demonstrated that there is a significant lunar impact on the Earth’s ionosphere! These perturbations are probably indirectly caused by atmospheric pressure variations associated with lunar gravitational tides [Rishbeth and Garriott, 1969]. These tidal waves, considered in an earth-fixed frame, respond to the well-known tidal cycle of about 12 hours 25 minutes. Another piece of evidence is, that the influence of the Moon on the ionosphere is not only confirmed by the particular period of 14.77 days but also by the coefficient-specific

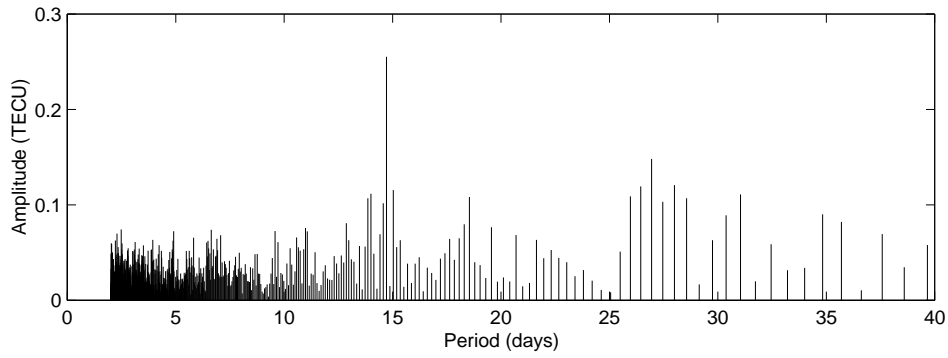
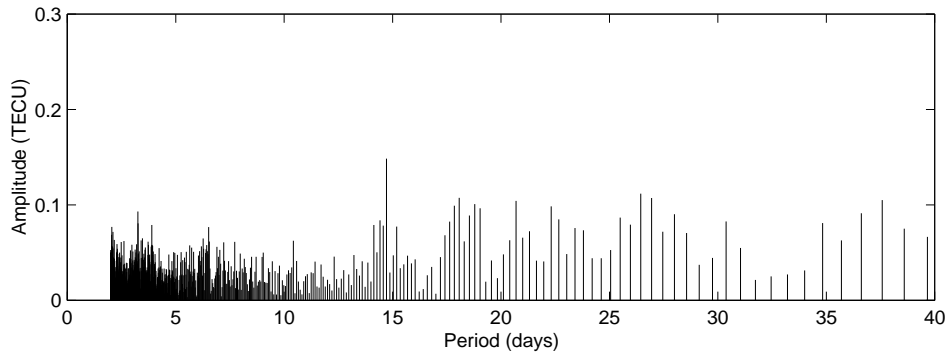
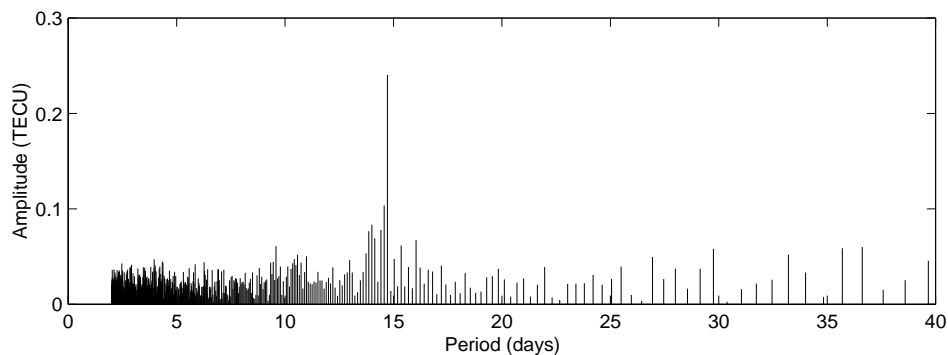
(a) Cosine coefficient  $\tilde{C}_{1,1}$ (b) Sine coefficient  $\tilde{S}_{1,1}$ 

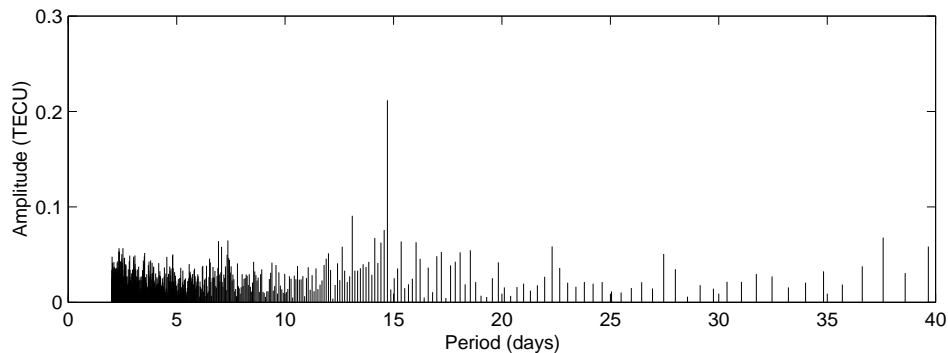
Figure 4.23: Amplitude spectrum of the sectorial SH coefficients  $\tilde{C}_{1,1}$  and  $\tilde{S}_{1,1}$ , for periods below 40 days.

phases themselves, which are in excellent agreement with the lunation cycle. Small phase shifts offer a basis for further investigations.

In this context, the advantage of using SH expansions becomes obvious. The fact that SH expansions are well suited for studying harmonic as well as resonance phenomena on a sphere are one reason why SH expansions are widely used in science.



(a) Cosine coefficient  $\tilde{C}_{2,2}$



(b) Sine coefficient  $\tilde{S}_{2,2}$

Figure 4.24: Amplitude spectrum of the sectorial SH coefficients  $\tilde{C}_{2,2}$  and  $\tilde{S}_{2,2}$ , for periods below 40 days.

## 4.4 TEC as a Function of Geographic Coordinates and Time

A user of TEC information is probably not interested in SH coefficients but in the TEC as a function of geographic coordinates and time, more precisely in  $E(\beta, \lambda, t)$ , where  $(\beta, \lambda)$  are the geographic coordinates and  $t$  is UT. If one uses IONEX data, it is relatively easy to get  $E(\beta, \lambda, t)$  since the data grid used is already referring to an earth-fixed geographic frame [Schaer *et al.*, 1998a]. In the case of using BGS ionosphere data, a transformation from  $(\beta, \lambda, t)$  into  $(\beta', s, t)$ , where  $(\beta', s)$  are the sun-fixed geomagnetic coordinates, has to be applied [Schaer, 1997]. For this purpose, the coordinates of the earth-centered

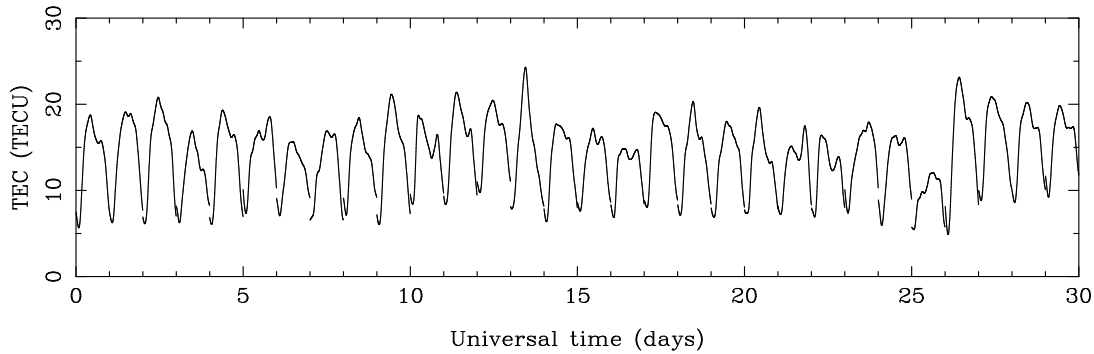


Figure 4.25: Daily TEC profiles evaluated at  $(\beta, \lambda) = (50^\circ, 7.5^\circ)$ , for June 1998.

dipole axis are included in the ionosphere files.

#### 4.4.1 Daily TEC Profiles

Let us now study the evolution of the TEC over one month at a latitude of  $50^\circ$  and a longitude of  $7.5^\circ$ , a location in Western Europe. Figure 4.25 shows the TEC stemming from EQ solutions as a function of universal time for the 30 days of June 1998. In this series of daily TEC profiles, we primarily notice a pronounced diurnal variation which is obviously due to the changing position of the Sun. The estimated TEC varies between about 5 TECU at night and 25 TECU in the early afternoon. It is interesting that consecutive TEC profiles sporadically tend to resemble each other.

From the modeling point of view, two features have to be highlighted. Each daily TEC profile is continuous from construction. However, discontinuities at the day boundaries are unavoidable because each day is processed independently. The expert may moreover recognize that the TEC estimates at 00:00 UT and at 24:00 UT are identical since the TEC representation (3.35) is “periodic” in the sun-fixed longitude  $s$  and local time, respectively. The latter aspect is admittedly a handicap for regional TEC modeling. This disadvantage is not critical as long as only night-time TEC is concerned, at least for European TEC maps.

The “double hump” around noon is typical in this season. It may be seen even more clearly in Figure 4.26 which shows the daily TEC profiles of Figure 4.25 now accumulated in one 24-hour interval of local time. A long series of similar figures may be found in [Warnant, 1996]. However, unlike Figure 4.26, those figures are based on data of one single GPS station which is located at Brussels, Belgium.

An important question in this context is: what is the temporal resolution of the EQ/EG daily TEC profiles. Let us therefore compute the time  $\Delta t$  it takes a particular sun-fixed

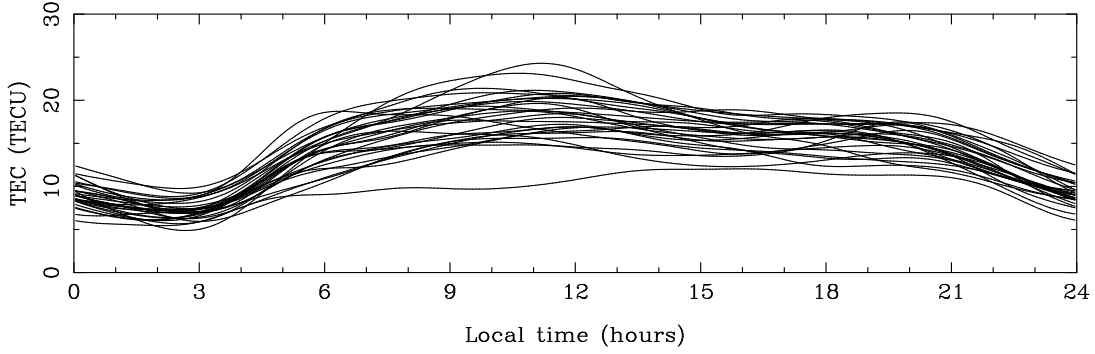


Figure 4.26: Daily TEC profiles evaluated at  $(\beta, \lambda) = (50^\circ, 7.5^\circ)$  as a function of local time, for June 1998.

ionospheric point to pass the field of view of a regional ground network:

$$\Delta t = \frac{2 \Delta \lambda_{\max} + \Delta \lambda_0}{2 \pi} \quad \text{with} \quad \sin \Delta \lambda_{\max} = \frac{\sin \Delta z_{\max}}{\cos \beta_0} \quad (4.4)$$

where

$\Delta t$  is the approximate temporal resolution of the daily TEC profile, expressed in days,

$\Delta \lambda_0$  is the extent of the ground network in longitude, or zero in the case of deriving station-specific TEC maps,

$\Delta z_{\max} = z_{\max} - z'_{\max}$  is the semi-diameter of the ionospheric cap probed by a single receiver, where  $z'_{\max}$  is given by (3.21), and

$\beta_0$  is the mean geographic latitude of the network processed.

With  $\Delta \lambda_0 \approx 45^\circ$ , (4.4) gives a  $\Delta t$  of about 6 hours for EQ/EG TEC maps. For station-specific maps near the equator, we obtain a temporal resolution of 2 hours, which should be seen in relation to the SH resolution itself.

#### 4.4.2 Monthly Averaged TEC Profiles and Day-to-Day Variability

Averaging the daily TEC profiles in Figure 4.26 yields the monthly averaged TEC profile shown in Figure 4.27 (solid line). Figure 4.27 proves once more that the TEC usually reaches its minimum in the early morning. In addition, we may quantify the day-to-day variability  $m(t)$  as a function of local time  $t$  by computing

$$m(t) = \sqrt{\frac{\sum_{i=2}^n (s_i(t) - s_{i-1}(t))^2}{n-1}} \quad (4.5)$$

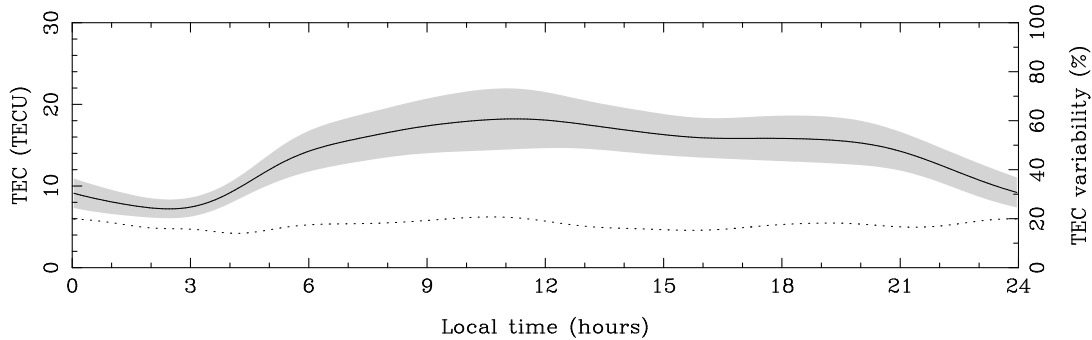


Figure 4.27: Monthly averaged TEC profile and day-to-day TEC variability evaluated at  $(\beta, \lambda) = (50^\circ, 7.5^\circ)$ , for June 1998.

where

- $s_i(t)$  is the signal associated with the  $i$ -th day and
- $n$  is the number of days involved.

(4.5) leads to RMS differences  $m(t)$  which we superimpose on the averaged signal  $\bar{s}(t)$ , that is, the shaded band in Figure 4.27 is bounded by  $(\bar{s} - m, \bar{s} + m)$ . The relative TEC variability  $m(t)/\bar{s}(t)$  in percent is included as a dotted line referring to the right-hand scale.

The function  $m(t)$  according to (4.5) does not correspond to the standard deviation with respect to  $\bar{s}(t)$ . This “day-to-day repeatability” is shown in Figure 4.28 as a shaded band and a dotted line, respectively.

What is the meaning of TEC repeatability or variability in practice? Assuming that we want to use our daily TEC information for real-time applications, the simplest approach is certainly to use either averaged information or the information of the previous day. If we use averaged TEC information, we have to expect errors which are statistically of the order of the day-to-day repeatability. On the other hand, if we use the TEC information of the previous day, the uncertainty to be expected is given by the day-to-day variability. For June 1998, e. g., we would be better off with monthly averaged TEC information, because the TEC repeatability in Figure 4.28 is approximately 10–15%, whereas the TEC variability in Figure 4.27 reaches 15–20%. It is conceivable that averaged TEC information which is referred to a period shorter than one month serves the purpose of “prediction” even better. Ionosphere prediction issues will be addressed in Chapter 5.

The CODE GIMs based on G1 as well as Z1 solutions provide the TEC for any location and time with a 2-hour resolution. From these global solutions we thus may extract TEC profiles similar to those in Figure 4.25 for regional TEC maps. Such profiles allow

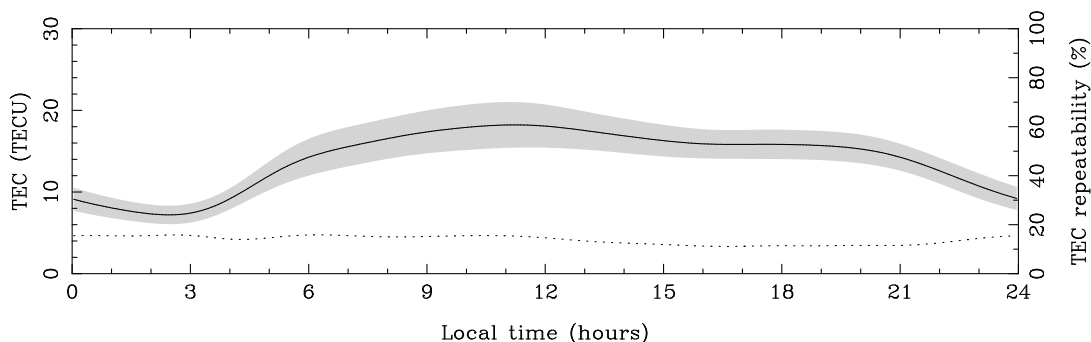


Figure 4.28: Monthly averaged TEC profile and day-to-day TEC repeatability evaluated at  $(\beta, \lambda) = (50^\circ, 7.5^\circ)$ , for June 1998.

the validation of these GIMs, an issue we will address in Chapter 6. Nevertheless, it is important to be aware of the fact that very short-term variations in the TEC, like TIDs, are not accounted for by global or regional TEC maps. In other words, our TEC estimates give a time-averaged TEC. The TEC estimates are moreover subjected to a certain measurement noise.

Last but not least, we refer to Appendix A which includes a 12-month series of monthly averaged EQ TEC profiles, namely from December 1997 to November 1998, revealing the seasonal peculiarities of the TEC evolution over Europe.

## 4.5 Estimating a Global Single-Layer Height

From January 1995 to March 1998, G1H solutions were computed, where the single-layer height was treated as an additional unknown parameter. This SLM height parameter, which affects the coordinates  $(\beta, s)$  of the ionospheric pierce points as well as the obliquity factors of the SLM mapping function  $F(z)$ , provides information about the vertical distribution of the TEC, at least in a crude form. Because the G1H solution is not linear with respect to the SLM height parameter, the TEC information stemming from the previously computed G1 solution was taken into account as a priori information.

Figure 4.29 shows the daily estimates of the global single-layer height thus obtained. Dots indicate the individual estimates; the solid line indicates the 10-day smoothed signal. As the G1H solution is an “interferometric” solution, it is not amazing that the day-to-day scattering of the SLM height estimates is quite large. An interpretation of the variations seen would be rather speculative therefore. We may note, however, that no significant long-term trend may be detected and that the average height significantly exceeds the a priori value of 400 kilometers. The average SLM height results in approx-



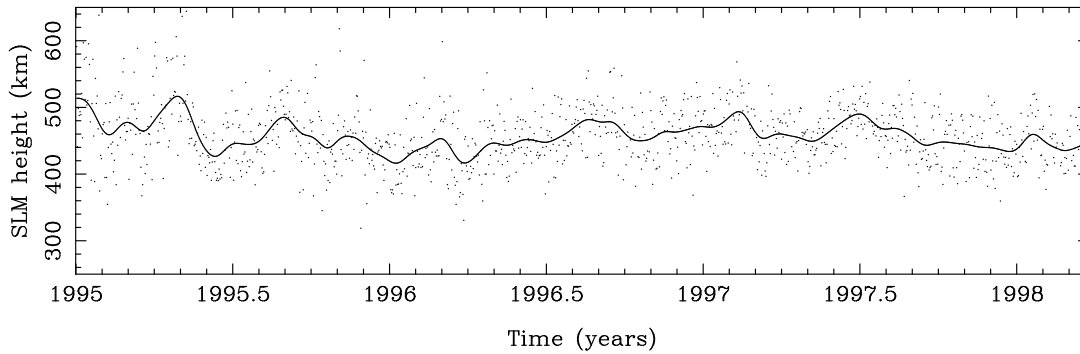


Figure 4.29: Daily estimated global single-layer heights based on G1H solutions, from January 1995 to March 1998.

imately 450 kilometers. This implies in turn that the G1H TEC estimates are larger on average than the corresponding G1 estimates based on 400 kilometers.

If we estimate SLM height parameters as part of zero-difference—instead of double-difference—solutions, the formal accuracy improves considerably. Using an adequate SLM height parameterization, one might expect that a diurnal variation and possibly a latitudinal dependence could be detected and monitored with ground-based GPS data. First attempts in this direction were made, e. g., by *Feltens* [1998]. As an alternative, one may take an ionosphere model, like IRI [*Bilitza*, 1998], to model the SLM height as it was done by *Komjathy and Langley* [1996]. In view of these problems, the exchange of SLM height maps is possible with the IONEX format as well [*Schaer et al.*, 1998a]. Without underestimating the impact of a slightly mismodeled SLM height, it may be considered as a second-order effect in ionospheric mapping. Nevertheless, one should aim at a more reasonable SLM height model in the future. One may expect that LEOs carrying GPS receivers will revolutionize atmospheric mapping in terms of vertical resolution.

## 4.6 IGS Receiver Performance in the Equatorial Region

Numerous receivers in the IGS network, in particular those located near the geomagnetic equator, severely suffer from the increased ionospheric activity—well before the next solar maximum comes within reach. Figure 4.30 gives an depressing summary of how IGS receivers perform under aggravated ionospheric conditions. The eight subfigures are referred, in 3-hour steps, to 01:30, 04:30, 07:30, ..., 22:30 LT and show the average number of GPS satellites successfully tracked by the receivers as a function of geographic latitude. “Successfully tracked” means that only one missing measurement epoch per 20 minutes is tolerated. It is alarming to see that more or less all “equatorial” receivers fail to keep track of the satellites over local noon and afternoon, which is a clear indication that the

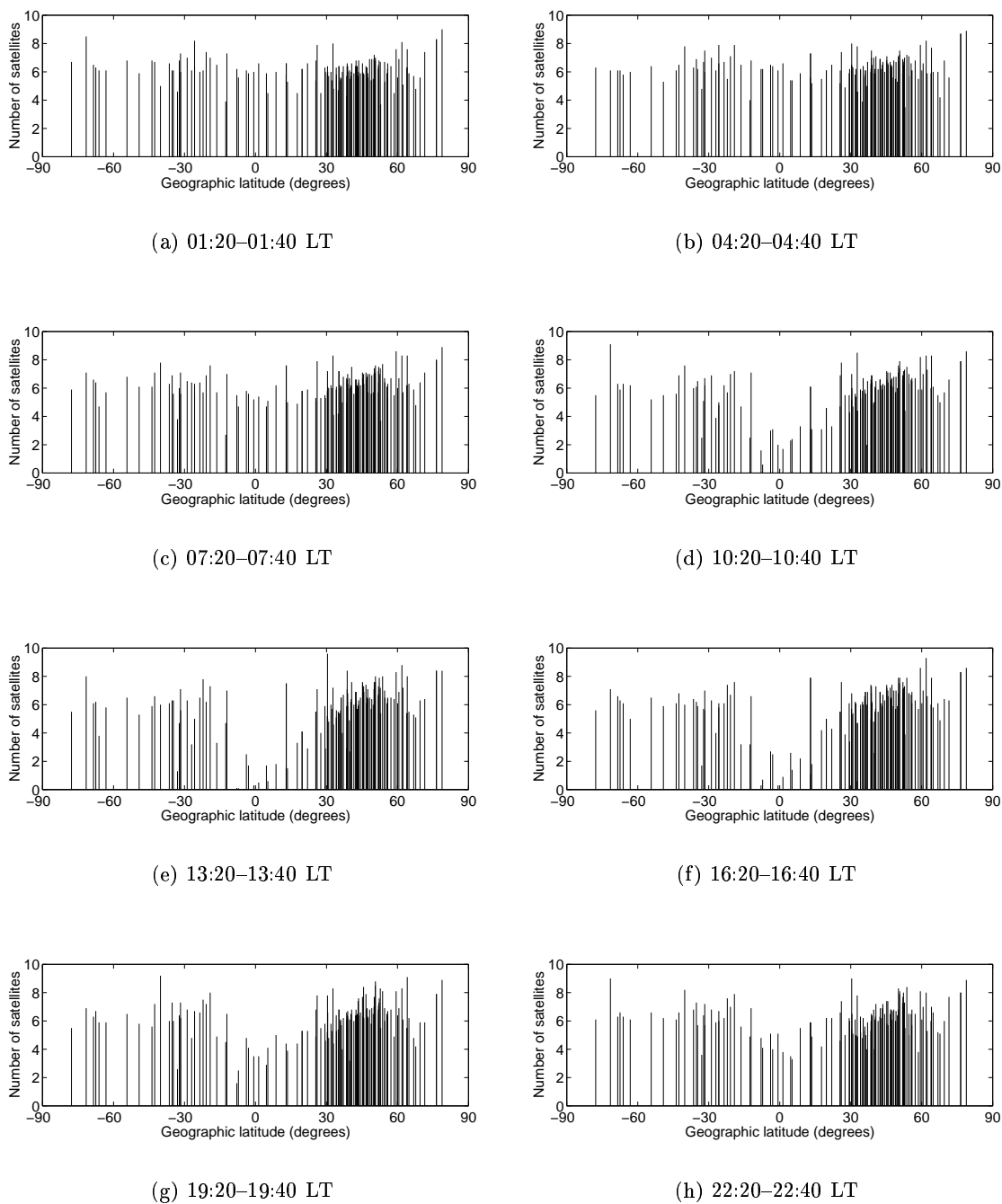


Figure 4.30: Average number of GPS satellites successfully tracked by receivers in the IGS network as a function of local time and geographic latitude, for September 1998.

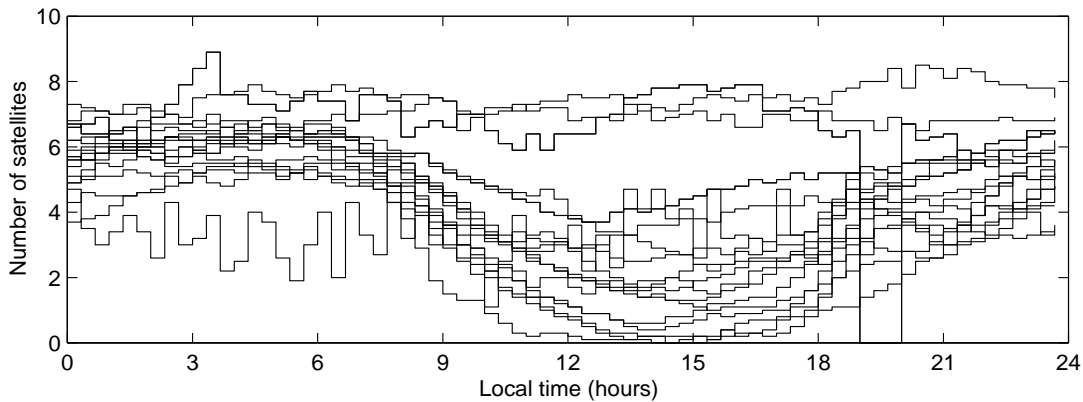


Figure 4.31: Average number of GPS satellites successfully tracked by “equatorial” receivers in the IGS network with geographic latitudes between  $-20^\circ$  and  $+20^\circ$ , for September 1998.

problem is related to the ionosphere. This performance statistics should be taken serious because it does not describe the situation for a particular day but throughout one entire month, namely September 1998.

Figure 4.31 shows the average number of satellites successfully tracked by “equatorial” receivers, located within geographic latitudes of  $\pm 20^\circ$ , as a function of local time. Some receivers temporarily loose track of all the satellites. This complication does not affect precise orbit determination too much. For ionosphere monitoring, this performance is not acceptable. Fortunately, only one receiver type performs so poorly under increased ionospheric activity. Unfortunately, it is the receiver type mainly used in the IGS network.

## 4.7 Differential Code Biases

Differential (L1–L2) code biases (DCBs) have to be taken into account when processing one-way code measurements, as in the case of the Z1 and Z1N solutions. The pre-launch measurements of satellite DCBs differ significantly from values published, e. g., by JPL [Bertiger *et al.*, 1998]. The receiver DCBs are usually unknown, unless they can be measured directly, as in the case of Rogue receivers. The history of corresponding DCB calibrations indicates that Rogue receiver DCBs are constant at the level of  $\pm 0.1$  nanoseconds, except when a part in the analog portion of the receiver is swapped out for repair and upgrade [Wilson and Mannucci, 1993].

In practice, we have to solve for satellite as well as receiver DCBs when processing one-

way code measurements—or a derivative of them—for ionospheric mapping. Although DCBs are usually treated as a nuisance, it is worthwhile to study the resulting estimates obtained as a by-product of the TEC determination in detail, because they contain information about the stability of instrumental biases over long time spans and even about the quality of the TEC determination. Apart from ionospheric mapping, precise time transfer using GPS suffers from unstable instrumental biases too. DCB values are required by single-frequency users who use IGS precise clock information, either for positioning or time transfer.

#### 4.7.1 DCBs of the GPS Spacecrafts

Because all DCBs  $\Delta b^k$  (and  $\Delta b_i$ ) may be shifted by a common bias, only the relative DCBs (e. g., relative to a reference satellite) affect ionospheric mapping and single-point positioning. However, it has a beneficial effect on the individual DCB estimates, if they are referred to the overall mean of the satellite DCBs by introducing the condition (3.46) instead of selecting one particular reference satellite. Whereas a receiver DCB is only observed by the corresponding receiver itself, a satellite DCB is theoretically observed by all involved receivers, at least on a 24-hour basis. This is why that satellite DCBs are in fact more accurately determined than receiver DCBs, provided a network of many receivers is processed. Hence,  $\Delta b_{\text{ref}}$  of (3.46) represents a very stable, but virtual bias.

It may happen from time to time that a satellite DCB estimate is missing, in particular when a satellite undergoes maintenance or is manoeuvred, not to speak of satellites which are at some time dismissed or newly launched, like PRN 8 in 1997. It is obvious that in such a case, the reference bias  $\Delta b_{\text{ref}}$  may change slightly. When comparing or combining DCB results, we therefore properly align the daily results to  $\Delta b_{\text{ref}}$  which is now based on all satellites involved. We can achieve this by considering the individual satellite DCB estimates as “observations,” setting up one common set of satellite DCB parameters and additionally one offset parameter per daily set of DCB estimates, introducing the condition (3.46) with respect to all satellites involved, and finally by adjusting the unknown parameters in the least-squares sense. This yields a combined set of satellite DCBs as well as daily DCB observations optimally aligned. The adjusted offset parameters may be further used to align the receiver DCB observations, too. In this way, we are even capable of handling DCB information referred to a completely different reference, like a particular receiver DCB. Within the IGS, it became a standard to use (3.46). If one would be interested in “absolute” DCB information, the relative DCB information has to be aligned to the calibration values of the Røgnre receivers.

Figure 4.32 shows the daily satellite DCB estimates based on the Z1N solutions for the time period from June 1998 to November 1998. They are all aligned to the combined set of satellite DCBs. The daily estimates are indicated by dots; the combined values are indicated by circles. The individual satellite DCBs vary between about  $\pm 2.5$  nanoseconds, except for PRN 13, the only Block-IIIR spacecraft in operation, for which the DCB is

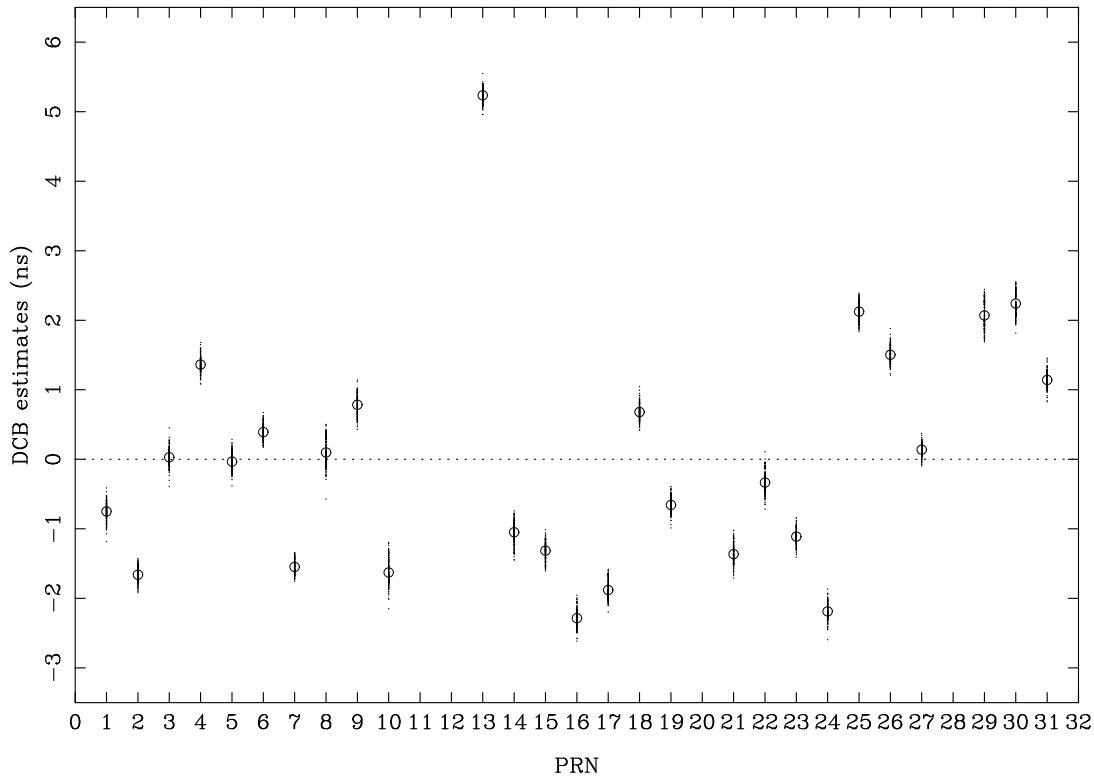


Figure 4.32: Daily DCB estimates (dots) of the GPS spacecrafts and combined values (circles) based on Z1N solutions, from June 1998 to November 1998.

roughly +5 nanoseconds. We should keep in mind that eventually only the differences between DCBs are relevant. The residuals, the individual estimates minus the combined values, are given in Figure 4.33. The dots in Figures 4.32 and 4.33 form a kind of error bars. We will see, however, that the day-to-day differences of the DCB estimates are actually smaller than one might think, because the satellite DCBs slowly vary in time.

Figures 4.34 and 4.35 show the daily DCB estimates of two particular GPS spacecrafts, namely PRN 23 and PRN 8, since the end of October 1997. In addition, the 10-day smoothed DCB values using (4.2) are given by the solid line. The figures showing the Z1N DCB results of all other PRNs are given in Appendix B. Note that these figures are all drawn to the same scale including a window of one nanosecond.

The day-to-day scatter of the DCB estimates improved quite drastically at the end of January 1998. This can be attributed to the change from night-time data processing to station-specific TEC mapping. Whereas the DCBs of PRN 23 and the other “old-established” PRNs behave quite well, the DCB of PRN 8 behaves rather badly. This is not surprising because PRN 8, which is still a Block-IIA spacecraft, was just launched on

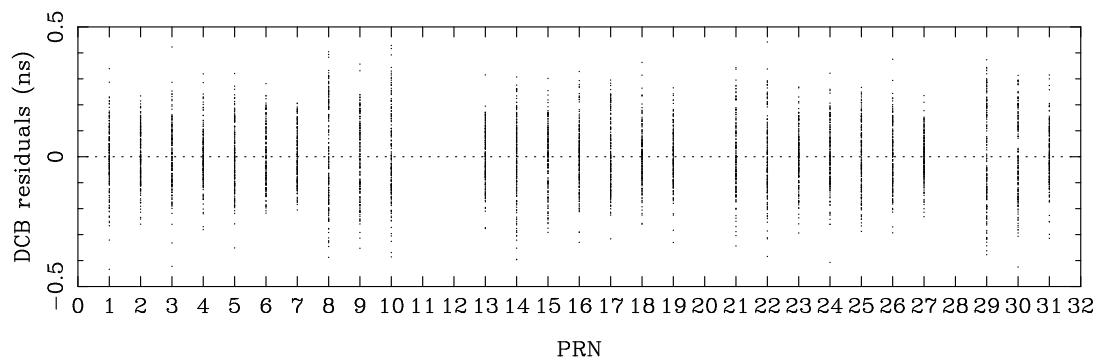


Figure 4.33: Daily DCB residuals of the GPS spacecrafts with respect to combined values based on Z1N solutions, from June 1998 to November 1998.

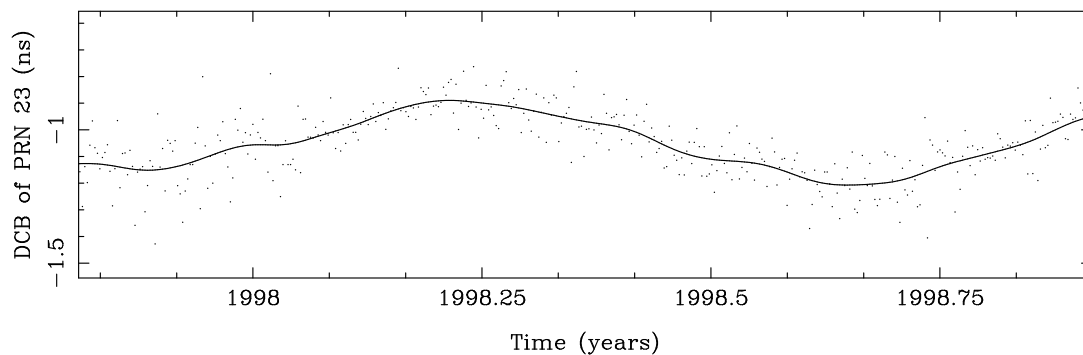


Figure 4.34: DCB of PRN 23.

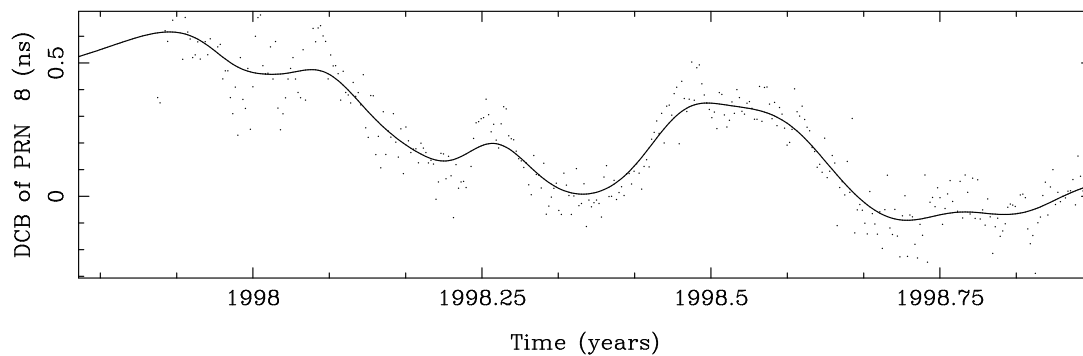


Figure 4.35: DCB of PRN 8.

Table 4.2: Combined DCB values of the GPS spacecrafts and RMS errors of the daily Z1N estimation, from June 1998 to November 1998.

PRN	DCB (ns)	RMS (ns)	PRN	DCB (ns)	RMS (ns)
1	-0.750	0.091	17	-1.879	0.077
2	-1.659	0.068	18	+0.681	0.086
3	+0.029	0.076	19	-0.656	0.075
4	+1.363	0.079	21	-1.364	0.076
5	-0.033	0.072	22	-0.334	0.086
6	+0.391	0.072	23	-1.111	0.070
7	-1.548	0.070	24	-2.188	0.073
8	+0.099	0.086	25	+2.124	0.091
9	+0.784	0.077	26	+1.504	0.087
10	-1.628	0.090	27	+0.138	0.068
13	+5.235	0.079	29	+2.070	0.091
14	-1.049	0.104	30	+2.240	0.076
15	-1.314	0.086	31	+1.141	0.079
16	-2.285	0.097			

6 November 1997 and therefore is not yet in orbit for a long time. One may expect that the DCB of PRN 8 will become more stable in future. Let us point out, in this context, that CODE already included PRN 8 into its processing scheme before broadcast orbits were available, namely on 23 November 1997. To do so, a couple of iterations had to be performed over the orbit determination procedure right at the outset. PRN 8 became officially operational on 18 December 1997.

Table 4.2 lists the 6-month combined values of the satellite DCBs which are shown in Figure 4.32 with circles. In addition to the combined DCB values, RMS errors of the daily estimates are given for each PRN. Aiming at a more realistic evaluation of the day-to-day repeatability of the satellite DCB estimates, we compute the RMS error  $m$  with respect to a strongly smoothed signal  $\tilde{s}$  using (4.2):

$$m = \sqrt{\frac{\sum_{i=1}^n (s(t_i) - \tilde{s}(t_i))^2}{n-1}} \quad (4.6)$$

where

- $t_i$  are the measurement epochs,
- $s(t_i)$  is the measured signal at epoch  $t_i$ ,
- $\tilde{s}(t_i)$  is the smoothed signal at epoch  $t_i$ , and
- $n$  is the number of measurements considered.

The use of relation (4.6) is based on the assumption that most of the long-term variations are real. Note that in our case  $\tilde{s}$  is a 10-day smoothed signal, represented by the solid lines shown in Figures 4.34 and 4.35.

The individual RMS errors in Table 4.2 are in the range of 0.068–0.104 nanoseconds, corresponding to approximately 2–3 centimeters and 0.2–0.3 TECU, respectively. It is conspicuous, however, that spacecrafts like PRN 14 and PRN 16 which exhibit a worse day-to-day DCB repeatability also show orbit modeling problems caused by partly defective momentum wheels used for attitude control. The computation of the overall RMS error results in 0.081 nanoseconds for Z1N solutions, 0.102 nanoseconds for Z1 solutions, 0.128 nanoseconds for the old Z1N solutions, where only night-time data was processed, and 0.173 nanoseconds for the old Z1 solutions without subdaily TEC resolution. Because the Z1N DCB estimation performs best, it has been chosen as the official CODE DCB solution. It is important to point out that the smoothed DCB signals derived from Z1N and Z1 solutions are very similar and that no systematic differences may be noticed. This is also substantiated by the fact that 6-month DCB combinations for both solutions agree on the RMS level of 10 picoseconds. A moving 7-day DCB comparison is computed each day to provide realistic RMS information which reflects the current uncertainty of the individual satellite DCBs.

It is interesting to note that practically all satellite DCBs show a significant long-term variation with an amplitude which is of the order of 0.1–0.2 nanoseconds. When inspecting Figures B.1 to B.27 more closely in conjunction with Figure 2.4 showing the satellite constellation, we may recognize that the phases of this possibly annual variation tend to be equal in the case of spacecrafts which are close to each other in space. It seems that the phases linearly depend on the right ascension of the ascending node and the argument of latitude, that is, the position of the orbital plane in inertial space and the position of the satellite within the plane, respectively. We know that the satellite constellation roughly repeats itself with respect to the Sun every year, neglecting the rotation of the ascending node. Consequently, the orientation of the individual satellites with respect to the Sun is subject to an annual variation, too. We may therefore conclude that this phenomenon might be caused by a “geometrical” effect that possibly gets amplified by the inhomogeneity of the ground network.

Is the mixture of C1, P1, and P2 code measurements possibly responsible for this problem? Under the regime of AS (anti-spoofing), only few receiver types, like the Ashtech Z12, actually provide P1 (Y1) and P2 (Y2) codes in addition to the C1 (C/A) code. “Cross-correlating” receivers, like the Rogue and Trimble receivers, provide C1 and “C2” codes, where “C2” is derived from  $C_1 - (P_2 - P_1)$ . It may be easily verified, however, that in both cases the DCBs are referred to the difference P1–P2, provided that P1 and P2 are used in the first case. An effect due to eclipsing satellites may be excluded, since eclipse seasons occur in a semi-annual rhythm and affect all the satellites belonging to the same orbital plane. There are a few possible reasons for long-term satellite DCB variations: mismodeled difference between L1 and L2 satellite antenna phase center



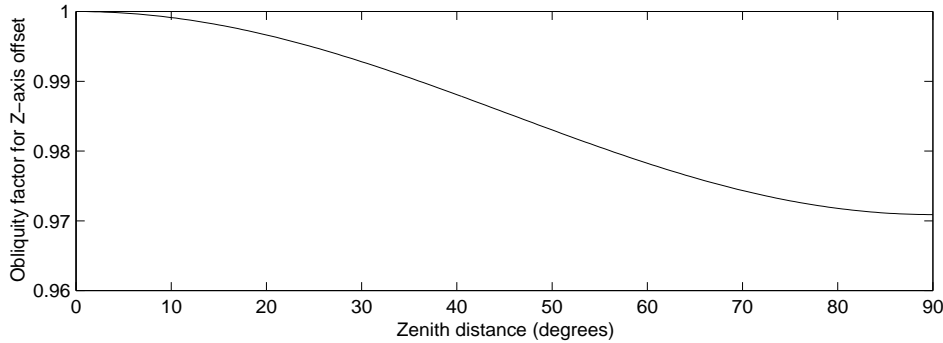


Figure 4.36: Obliquity factor for the Z-axis satellite antenna offset.

offsets, unmodeled phase windup in the zero-difference processing, elevation-dependent satellite antenna phase center variations, satellite-related multipath, temperature effect due to direct solar radiation, etc. Eventually, also an ionosphere-induced artefact cannot be excluded.

Let us briefly discuss the problem of mismodeled interfrequency satellite antenna offsets. The satellite-fixed coordinate system usually adopted has its origin in the center of mass of the satellite, the Z-axis points into the direction of the antenna array, the Y-axis corresponds to the solar panel axis, and the X-axis completes a right-hand system. We may assume that each GPS spacecraft orientates its Z-axis towards the Earth's center and its Y-axis perpendicular to the plane formed by satellite, geocenter, and Sun. The angle between the line of sight and the satellite's Z-axis (or nadir) may reach about  $14^\circ$  when observing the satellite at low elevations. By the way, this angle may be computed using (3.21) with  $R' = R + H = 26\,600$  km. Due to variations in this angle, it is possible to derive satellite antenna offsets of the various Block types or even of individual satellites from ionosphere-free GPS tracking data. Strictly speaking, this yields the ionosphere-free LC of the L1 and L2 antenna offsets, because L1 and L2 offsets may be different.

Figure 4.36 shows the obliquity factor for the Z-axis (or “vertical”) satellite antenna offset versus the zenith distance at the receiver. This obliquity factor, which is the ratio between the offset projected on the line of sight and the actual offset, results in  $\cos z'$ , where  $z'$  denotes the angle between the Z-axis and the line of sight. Figure 4.37 shows the obliquity factor for the X/Y-axis (or “horizontal”) offsets, corresponding to  $\sin z'$ . Because satellite antenna offsets are highly correlated with, e.g., satellite clock parameters, only the variation in these offsets is measurable. Figures 4.36 and 4.37 tell us that we may observe up to approximately  $1 - 0.97 = 3\%$  of the vertical satellite antenna offset and 24% of the horizontal offsets. For this reason, the horizontal offsets may be much better determined using ground-based GPS data than the vertical offsets. And these offsets are indeed significant. For Block-II/IIA spacecrafts, the IGS recommends

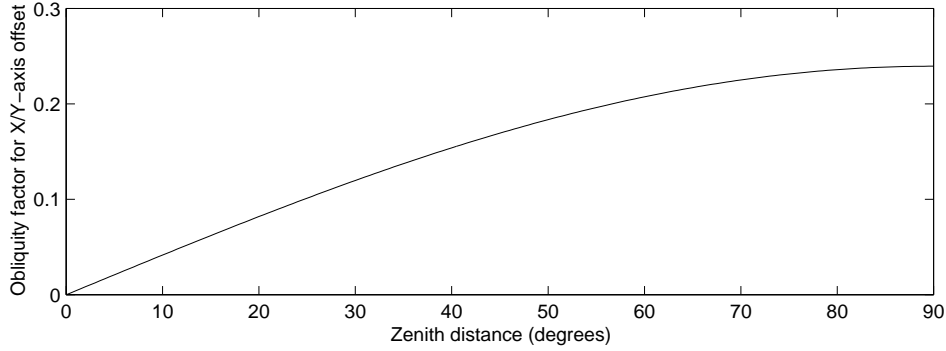


Figure 4.37: Obliquity factor for the X/Y-axis satellite antenna offset.

to use  $(X, Y, Z) = (+0.279, 0.000, +1.023)$  m when processing the ionosphere-free LC, whereas the offset vector of the Block-IIR PRN 13 may be assumed to be zero.

When estimating DCBs we must, however, analyze the geometry-free LC of GPS data and the offset values mentioned are not correct, because they refer to the ionosphere-free LC. We may, however, solve for the geometry-free LC of the L1 and L2 satellite antenna offsets, which obviously corresponds to the difference of the L1 and L2 offsets. We may use the “mapping functions” shown in Figures 4.36 and 4.37 without modification. Consequently, two satellite antenna offset vectors  $(X_3, Y_3, Z_3)$  and  $(X_4, Y_4, Z_4)$  are at our disposal from the individual L1 and L2 offsets,  $(X_1, Y_1, Z_1)$  and  $(X_2, Y_2, Z_2)$  may be derived. To keep the expression simple, we give it for the  $Z$ -component only:

$$\begin{pmatrix} Z_3 \\ Z_4 \end{pmatrix} = \begin{pmatrix} \kappa_{1,3} & \kappa_{2,3} \\ +1 & -1 \end{pmatrix} \begin{pmatrix} Z_1 \\ Z_2 \end{pmatrix} \quad (4.7)$$

where  $\kappa_{1,3}$  and  $\kappa_{2,3}$  are the coefficients (2.14) to compute the ionosphere-free LC. (4.7) allows to reconstruct the L1 and L2 satellite antenna offsets, starting from the “L3” and “L4” offsets. Solving for  $(Z_1, Z_2)$  leads to

$$\begin{pmatrix} Z_1 \\ Z_2 \end{pmatrix} = \begin{pmatrix} \kappa_{1,3} & \kappa_{2,3} \\ +1 & -1 \end{pmatrix}^{-1} \begin{pmatrix} Z_3 \\ Z_4 \end{pmatrix} = \begin{pmatrix} 1 & +\kappa_{2,3} \\ 1 & -\kappa_{1,3} \end{pmatrix} \begin{pmatrix} Z_3 \\ Z_4 \end{pmatrix} \quad (4.8)$$

$(X_4, Y_4, Z_4)$ , especially  $Z_4$ , are strongly correlated with satellite DCBs. Nevertheless, the offsets  $(X_4, Y_4, Z_4)$  extract the “geometrical” part of a bias related to the orientation of the spacecrafts. First attempts based on Z1N solutions with satellite antenna offset parameters set up for both Block-II/IIA and Block-IIR spacecrafts, indicate that a formal precision of about one centimeter for the  $Z$ -axis offset  $Z_4$  of the Block-II/IIA spacecrafts may be reached. The formal precision of  $(X_4, Y_4)$  is even slightly better. We did not

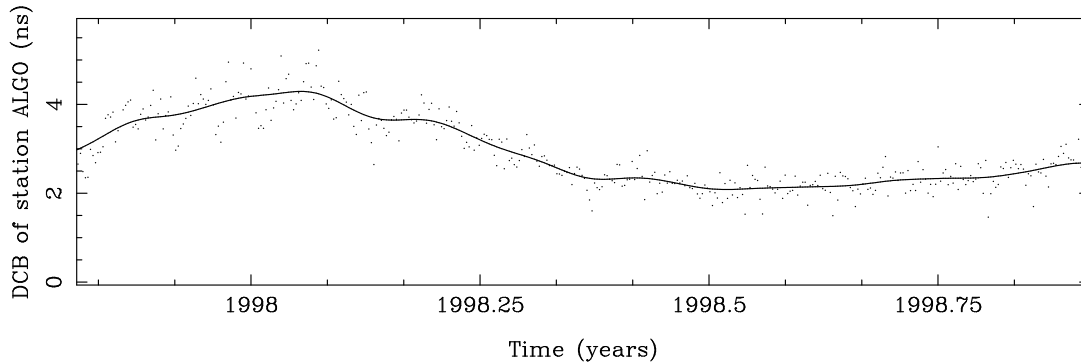


Figure 4.38: DCB of the station ALGO (Algonquin, Canada).

yet check how well G1 solutions using double differences are suited to extract satellite antenna offsets. We may expect that a double-difference estimation is in no way inferior to a zero-difference estimation, since we successfully derive “L3” satellite antenna offsets from double differences. A combination of a multitude of daily solutions is required to obtain a set of reliable satellite antenna offset estimates. One should not forget that the GPS signals are emitted by an antenna array, as seen in Figure 2.1.

#### 4.7.2 DCBs of the IGS Receivers

The day-to-day scatter of receiver DCB estimates is generally much larger than that of satellite DCB estimates. Two reasons are responsible for this. First, a receiver DCB may be less accurately determined than a satellite DCB, because it is only observed by the station itself, which is reflected by its larger formal error. Secondly, the receiver DCB estimation suffers from mismodeled TEC to a much greater extent, because the entire TEC above each receiver is relevant.

A time series for a receiver DCB obtained from Z1N solutions may be inspected in Figure 4.38. ALGO (Algonquin, Canada) is one of ten stations with very stable DCB estimates. The DCB diagrams of the nine other stations, namely CHAT, DRAO, GODE, JOZE, KOSG, NLIB, USNO, WSRT, and WTZR, may be found in Appendix B. Note that these figures show a window which always includes a range of 6 nanoseconds. The day-to-day repeatabilities of the DCB estimates, computed with (4.6) to remove the effect of long-term variations, are of the order of 0.2–0.3 nanoseconds. The values of the DCBs of the IGS receivers typically lie between  $\pm 20$  nanoseconds. Up-to-date values are given, e. g., in [Schaer, 1998a].

It is not by chance that no equatorial station appears in above top-ten list. The enlarged scatter of the DCBs of equatorial stations may be attributed to the marked dynamics of the equatorial ionosphere or the bad receiver performance in this region. It is extremely

difficult to decide whether short-term variations in DCBs are induced by the ionosphere or whether they are real.

### 4.7.3 DCBs of the GLONASS Spacecrafts

The latest development version of the Bernese GPS Software allows to process GLONASS code and phase measurements—even simultaneously with GPS data. Although the basic processing principles remain the same for GLONASS data, we have to take into account that different satellites emit their signals on slightly different frequencies, depending on a so-called channel number. The relationship is given in (2.2).

In order to clarify the effect of the differences between the GLONASS and GPS carrier frequencies, let us compare the ionospheric delay which is induced by a TEC of 100 TECU. For the GLONASS minimum and maximum frequency at L1, we obtain 15.69 and 15.44 meters, respectively, for those at L2, 25.94 and 25.53 meters. That is, starting from 100 TECU, the difference in the ionospheric delay at L1 may reach 0.25 meters, that at L2, 0.41 meters. The GPS carrier frequencies at L1 and L2 cause ionospheric errors of about 16.24 and 26.74 meters, respectively.

Since mid of July 1998, GLONASS satellite DCBs are derived on a regular basis from code measurements which are provided by the Ashtech Z18 receiver located at the Zimmerwald observatory in Switzerland. Because the Ashtech Z18 receiver provides dual-frequency measurements for both GLONASS and GPS, it makes sense to simultaneously process the data of both systems. This means that we solve each day for two sets of satellite DCB parameters and one common set of station-specific TEC parameters. Since the beginning of September 1998, we smooth the code measurements using phase measurements according to (2.8) for GLONASS data. Considerably improved DCB results are a consequence of this measure. The values thus obtained for the DCBs of GLONASS spacecrafts are of the same quality as those of the GPS counterparts, but they tend to vary a little bit more from one spacecraft to another. It is furthermore striking that two GLONASS spacecrafts supply data with a poor quality, namely those identified by slot numbers 10 and 16. The GLONASS satellite DCB estimates derived from the measurements of the Zimmerwald Ashtech Z18 receiver are available upon request.

Since October 11, 1998 (or GPS week 979), CODE is generating precise GLONASS orbits as part of the IGEX campaign in a (more or less) operational mode. CODE was the first IGEX analysis center to successfully derive precise GLONASS orbits from microwave data. There is no doubt that the secret of success lies in the combination of dual-frequency GLONASS/GPS data taking the precise CODE GPS orbits as given. At present, only Ashtech Z18 and 3S-NAV receiver data are considered by CODE. Because the 3S-NAV receiver does not provide dual-frequency GPS data, it only contributes with GLONASS data to the CODE IGEX products. In terms of a combined DCB (and TEC) determination, first tests with a Z1N-like solution type were made. Let us point out that it is mandatory to set up a GLONASS as well as a GPS DCB parameter for each GPS/

GLONASS combined receiver, because “intersystem” receiver DCBs may vary by several nanoseconds from one combined receiver to another. Consequently, two conditions of the type (3.46) are necessary to avoid singularities, preferably one for the set of GPS and one for the set of GLONASS satellite DCBs. The processing steps to generate solutions of the type Z1N (see section 4.2) including code smoothing, have already been implemented into the IGEX data processing.

## 4.8 Use of Satellite DCB Information

Satellite DCB information may be used to make precise satellite clocks—which are for obvious reasons referred to the ionosphere-free LC of code measurements—consistent with other LCs of the basic P1 and P2 code measurements. This is of particular interest for single-point positioning based on single-frequency data, when aiming at high-accuracy positioning results. The use of precise satellite clocks, orbits, as well as TEC information, e. g., in the form of IONEX maps, is of course a necessity. Because DCB information is obtained as a by-product of the TEC determination, it may be included in IONEX files [Schaer *et al.*, 1998a]. However, since receiver DCBs do not affect positioning results, only satellite DCB values are allowed in this format. For the same reason, a common shift in all satellite DCB values is not critical.

We know that each precise, “ionosphere-free” satellite clock estimate  $\Delta t^{k,3}$  does not give the true satellite clock offset  $\Delta t^k$  but is necessarily biased by  $b^{k,3}$ , the ionosphere-free LC of the basic code biases  $b^{k,1}$  and  $b^{k,2}$ :

$$\Delta t^{k,3} = \Delta t^k - b^{k,3} \quad \text{with} \quad b^{k,3} = \kappa_{1,3} b^{k,1} + \kappa_{2,3} b^{k,2} \quad (4.9)$$

In order to derive separate L1 and L2 DCB values, we may modify (4.7) by replacing the frequency-dependent satellite antenna offsets  $Z$  by the corresponding code biases  $b^k$ . This leads to

$$\begin{pmatrix} b^{k,3} \\ \Delta b^k \end{pmatrix} = \begin{pmatrix} \kappa_{1,3} & \kappa_{2,3} \\ +1 & -1 \end{pmatrix} \begin{pmatrix} b^{k,1} \\ b^{k,2} \end{pmatrix} \quad (4.10)$$

where  $\kappa_{1,3}$  and  $\kappa_{2,3}$  are the coefficients (2.14) to compute the ionosphere-free LC.  $\Delta b^k = b^{k,1} - b^{k,2}$  denotes the DCB of the satellite considered. By solving for  $b^{k,1}$  and  $b^{k,2}$ , we obtain in analogy to relation (4.8)

$$\begin{pmatrix} b^{k,1} \\ b^{k,2} \end{pmatrix} = \begin{pmatrix} \kappa_{1,3} & \kappa_{2,3} \\ +1 & -1 \end{pmatrix}^{-1} \begin{pmatrix} b^{k,3} \\ \Delta b^k \end{pmatrix} = \begin{pmatrix} 1 & +\kappa_{2,3} \\ 1 & -\kappa_{1,3} \end{pmatrix} \begin{pmatrix} b^{k,3} \\ \Delta b^k \end{pmatrix} \quad (4.11)$$

Although  $b^{k,3}$  is completely coupled with  $\Delta t^{k,3}$ , we may reconstruct “biased” satellite clock values  $\Delta t^{k,1}$  and  $\Delta t^{k,2}$  which are consistent with P1 and P2 code measurements:

$$\Delta t^{k,1} = \Delta t^k - b^{k,1} = \Delta t^{k,3} - \kappa_{2,3} \Delta b^k \quad (4.12a)$$

$$\Delta t^{k,2} = \Delta t^k - b^{k,2} = \Delta t^{k,3} + \kappa_{1,3} \Delta b^k \quad (4.12b)$$

In principle, this procedure also works for arbitrary LCs of P1 and P2 code measurements. The satellite clock  $\Delta t^{k,5}$  for the wide-lane LC is, e. g., calibrated by

$$\Delta t^{k,5} = \Delta t^k - b^{k,5} = \Delta t^{k,3} - \frac{\nu_1 \nu_2}{\nu_1^2 - \nu_2^2} \Delta b^k \quad \text{with} \quad b^{k,5} = \kappa_{1,5} b^{k,1} + \kappa_{2,5} b^{k,2} \quad (4.13)$$

where  $\nu_1 \nu_2 / (\nu_1^2 - \nu_2^2) \approx 1.984$ .

Let us finally give the complete observation equations which are valid for P1 and P2 code measurements, if precise satellite clock information is used. Let us first substitute

$$\rho_i^k - c(\Delta t^{k,3} - \Delta t_i) + \Delta \rho_{i,\text{trop}}^k = \rho''_i^k \quad (4.14)$$

in analogy to (2.6). The following one-way code observation equations then hold for P1 and P2 code measurements, using the notation (3.30) for the ionospheric correction:

$$P_{i,1}^k = \rho''_i^k + \xi_E (F(z) E_v(\beta, s))_i^k + c \kappa_{2,3} \Delta b^k \quad (4.15a)$$

$$P_{i,2}^k = \rho''_i^k + \xi \xi_E (F(z) E_v(\beta, s))_i^k - c \kappa_{1,3} \Delta b^k \quad (4.15b)$$

Theoretically, one might moreover think of introducing the effect due to the frequency-dependent satellite antenna phase center offsets. This effect is, however, much smaller than atmospheric effects.

Let us conclude this section with another remark. There are good reasons to distinguish between various code measurement types. One may assume that the satellite code biases  $b^{k,1}$  are different for P1 and C1 (C/A) code measurements. A conflict is inevitable in two respects:

- Under non-AS conditions, most receivers in the IGS network would provide C1, P1, and P2 codes. It is obvious that the IGS ACs use the P1 and P2 codes to derive precise clock information. A dual-frequency user is well-served by such a clock product. However, a single-frequency user having only C1 code measurements suffers from the inconsistency between P1 and C1, even when he applies satellite DCB information.
- In the presence of AS, we have to distinguish between a large number of cross-correlating receivers providing C1 and “C2” codes and a small number of receivers which provide C1, P1, and P2 codes. It might be an option to generate artificial “C2”-like code measurements from C1, P1, and P2 by computing  $C_1 + (P_2 - P_1)$ .

Strictly speaking, one should consider the code biases  $b^{k,C1}$ ,  $b^{k,P1}$ , and  $b^{k,P2}$ , keeping in mind, however, that the DCB  $\Delta b^k$  has a one-to-one relationship with  $b^{k,P1} - b^{k,P2}$ . This inconsistency in the IGS clock product will have to be addressed. It seems unavoidable to determine and monitor satellite-specific code biases between C1 and P1, too. This would be, by the way, an easy task when starting, e. g., from Ashtech Z12 data giving all three code observables C1, P1, and P2.

# 5. Predicting Global TEC Parameters and Maps

The state of the ionosphere may be predicted either by “extrapolation methods” or by using models which are based on a physical concept [*Ivanov-Kholodny and Mikhailov, 1986*]. In this chapter we develop an extrapolation method—where the evolution of any given global TEC parameter is estimated using a number of observations made in the past [*Schaer et al., 1998b*].

## 5.1 Mathematical Principle

Least-squares collocation, a generalization of least-squares adjustment, is well suited for predicting global TEC parameters.

Unlike the “classical” least-squares adjustment, least-squares collocation not only distinguishes between a *deterministic* and a *noise* component, but also contains a *stochastic* (or signal) component. The three components are illustrated in Figure 5.1. We distinguish between a trend function  $\Psi(t)$ , representing the deterministic component, a signal  $s$  superimposed to the trend function, representing a slowly varying stochastic component, and a noise component  $n$  of the observations, indicated by circles.  $s'$  designates the predicted signal at a certain time.

In the most general case, the signal  $s$  may be described not only in the time domain but in an arbitrary domain. Even a multi-dimensional domain may be appropriate. Below, we assume signals only vary as a function of time.

The observation equation (2.41) of the “classical” least-squares adjustment, complemented with the signal vector  $\mathbf{s}$ , may be written as

$$\mathbf{L} = \Psi(\mathbf{X}_0, t) + \mathbf{A} \mathbf{x} + \mathbf{s} + \mathbf{n} \quad (5.1)$$

or, after subtracting the term  $\Psi(\mathbf{X}_0, t)$ , as

$$\mathbf{l} = \mathbf{A} \mathbf{x} + \mathbf{s} + \mathbf{n} \quad (5.2)$$

where

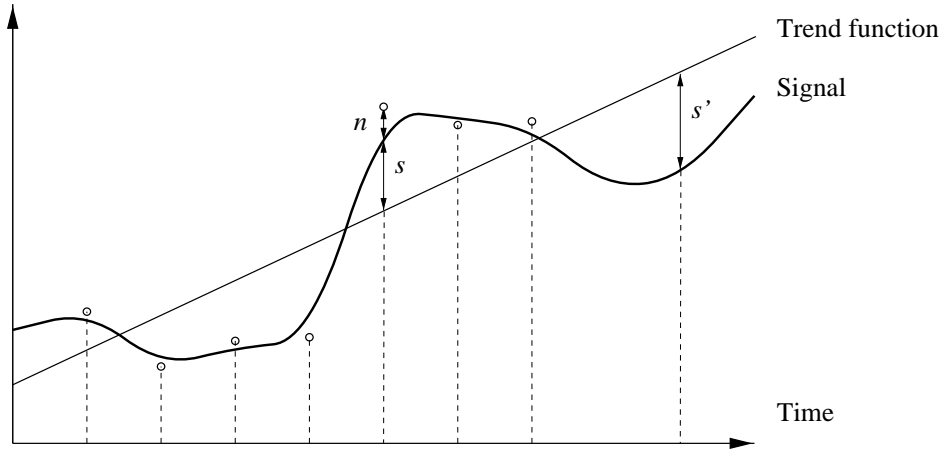


Figure 5.1: Components of the least-squares collocation: noise  $n$ , signal  $s$ , predicted signal  $s'$ , and trend function.

$l = L - \Psi(\mathbf{X}_0, \mathbf{t})$ , often also referred to “O–C”, contains the terms “observed-minus-computed”,

$L$  is the array of the observations,

$\Psi(\mathbf{X}_0, \mathbf{t})$  is a given vectorial trend function, evaluated at the approximate model parameter values  $\mathbf{X}_0$  and at the epochs  $\mathbf{t}$ ,

$A$  is the first design matrix as defined by (2.42),

$\mathbf{x}$  is the solution vector, and

$\mathbf{n}$  is the noise vector, corresponding to the residual vector  $-\mathbf{v}$  in (2.41).

The unknown model parameters  $\mathbf{X} = \mathbf{X}_0 + \mathbf{x}$  are estimated according to relation (2.46), setting  $\mathbf{P} = \mathbf{C}_u^{-1}$ :

$$\mathbf{x} = (\mathbf{A}^T \mathbf{C}_u^{-1} \mathbf{A})^{-1} \mathbf{A}^T \mathbf{C}_u^{-1} \mathbf{l} \quad (5.3)$$

where

$\mathbf{C}_{uu} = \mathbf{C}_{ss} + \mathbf{C}_{nn}$  is the total covariance matrix of the observations,

$\mathbf{C}_{ss}$  is the covariance matrix of the signal component, and

$\mathbf{C}_{nn}$  is the covariance matrix of the noise component.

Note that  $s$  and  $n$  are considered to be uncorrelated, that is,  $\mathbf{C}_{sn} = \mathbf{0}$ .



In analogy to (2.49), the covariance matrix of the adjusted model parameters is

$$\mathbf{C}_{\mathbf{x}\mathbf{x}} = \left( \mathbf{A}^T \mathbf{C}_u^{-1} \mathbf{A} \right)^{-1} \quad (5.4)$$

Finally, the signal and noise components are split by

$$\begin{pmatrix} \mathbf{s} \\ \mathbf{n} \end{pmatrix} = \begin{pmatrix} \mathbf{C}_{ss} \\ \mathbf{C}_{nn} \end{pmatrix} \mathbf{C}_u^{-1} (\mathbf{L} - \Psi(\mathbf{X}, t)) \quad (5.5)$$

where

$$\mathbf{L} - \Psi(\mathbf{X}, t) = \mathbf{l} - \mathbf{A}\mathbf{x} = \mathbf{s} + \mathbf{n} \quad (5.6)$$

In contrast to the function  $\Psi(\mathbf{X}_0, t)$  of relation (5.1),  $\Psi(\mathbf{X}, t)$  is the trend function evaluated at the adjusted model parameter values  $\mathbf{X} = \mathbf{X}_0 + \mathbf{x}$  as computed by formula (5.3).

The RMS error  $m_0$  of unit weight is defined by

$$m_0 = \sqrt{\frac{\mathbf{s}^T \mathbf{C}_{ss}^{-1} \mathbf{s} + \mathbf{n}^T \mathbf{C}_{nn}^{-1} \mathbf{n}}{2n - u}} \quad (5.7)$$

where

$n$  is the number of observations and

$u$  is the number of free parameters describing the trend function  $\Psi$ .

In order to interpolate or extrapolate the signal vector  $\mathbf{s}$ , one has to characterize—based on real data—the cross-covariance matrix  $\mathbf{C}_{s'l}$  that reflects the covariances between the predicted signal  $\mathbf{s}'$  and the “base points”  $\mathbf{L}$ . The predicted signal vector  $\mathbf{s}'$  is then obtained by

$$\mathbf{s}' = \mathbf{C}_{s'l} \mathbf{C}_u^{-1} (\mathbf{L} - \Psi(\mathbf{X}, t)) \quad (5.8)$$

and the associated covariance information, when neglecting the uncertainty of the adjusted trend function  $\Psi(\mathbf{X}, t)$ , is described by

$$\mathbf{C}_{l'l'} = \mathbf{C}_{s's'} - \mathbf{C}_{s'l} \mathbf{C}_u^{-1} \mathbf{C}_{ls'} \quad \text{with} \quad \mathbf{C}_{ls'} = \mathbf{C}_{s'l}^T \quad (5.9)$$

where  $\mathbf{C}_{s's'}$  is the autocovariance matrix of the predicted signal vector  $\mathbf{s}'$ .

At the end, we are interested in the quantity  $\mathbf{L}' = \mathbf{s}' + \Psi(\mathbf{X}, t')$ , the predicted signal added to the corresponding contribution from the trend function.

In order to describe the required covariance matrices, the function  $\gamma(t)$ , called autocovariance function (ACF), must be available. Such an autocovariance function may be empirically determined by computing averaged sums of mixed products

$$\gamma(h \Delta t) = \frac{1}{n - |h|} \sum_{i=1}^{n-|h|} s(t_{i+|h|}) s(t_i) \quad \text{for} \quad |h| = 0, \dots, n-1 \quad (5.10)$$

where

- $h \Delta t$  is the time-lag of  $s(t_{i+|h|})$  with respect to  $s(t_i)$ ,
- $h$  is the lag in units of  $\Delta t$ ,
- $\Delta t$  is the tabular interval of the time series analyzed, and
- $n$  is the number of epochs, and
- $s(t_i)$  is the signal at epoch  $t_i$ .

$\gamma(0)$  corresponds to the variance of the signal. The function  $\gamma(t)/\gamma(0)$  is a derivative of the autocovariance function and is called autocorrelation function. To guarantee that ACF-derived covariance matrices are positive definite, usually a factor of  $1/n$  instead of  $1/(n - |h|)$  is used in relation (5.10). If the trend function  $\Psi(t)$  significantly differs from zero, the observations  $L(t)$  of the signal have to be reduced prior to the ACF computation:

$$s(t) = L(t) - \Psi(t) \quad (5.11)$$

Detailed information concerning the least-squares collocation method may be found, e. g., in [Gurtner, 1992; Koch, 1988; Moritz, 1989].

## 5.2 TEC Trend Function

We use a harmonic expansion to describe the *deterministic* component of the TEC:

$$\Psi(t) = C_0 + \sum_{i=1}^n (C_i \cos(\omega_i t) + S_i \sin(\omega_i t)) \quad \text{with} \quad \omega_i = \frac{2\pi}{\tau_i} \quad (5.12)$$

where

- $\Psi(t)$  is the TEC trend function at epoch  $t$ ,
- $C_0$  is an arbitrary offset,
- $n$  is the number of periods,
- $C_i, S_i$  are the harmonic coefficients associated with the  $i$ -th period, and
- $\omega_i$  is the angular frequency related to the known period  $\tau_i$ .

The unknown model parameters  $\mathbf{X}$  in our trend function (5.12) are the offset  $C_0$  and  $n$  pairs of harmonic coefficients  $C_i$  and  $S_i$ . This leads to a solution vector (5.3) with  $2n + 1$  elements:  $\mathbf{X} = (C_0, C_1, S_1, C_2, S_2, \dots, C_n, S_n)^T$ . In order to avoid misunderstandings, it is important to point out that for each SH coefficient to be predicted an individual trend function of type (5.12) has to be introduced and adjusted.

Currently, we consider up to five periods: 11 years, 1 year, 1/2 year, 14.77 days, and 1 solar day. They describe the periodicity due to

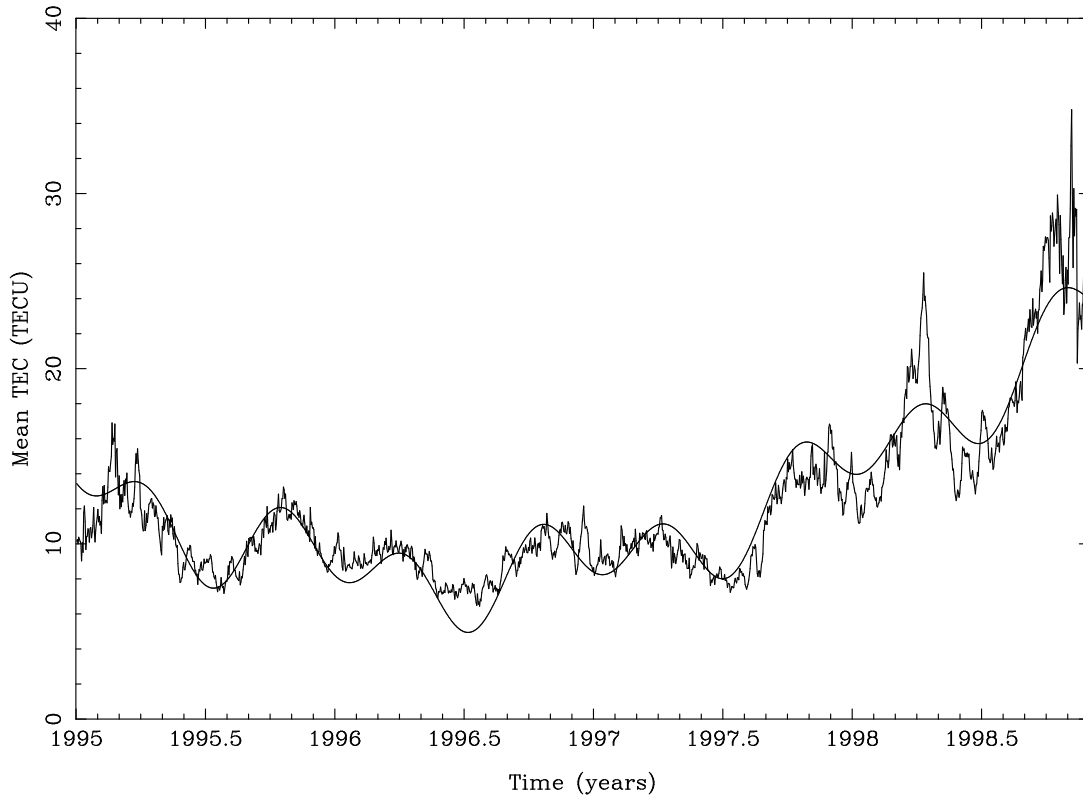
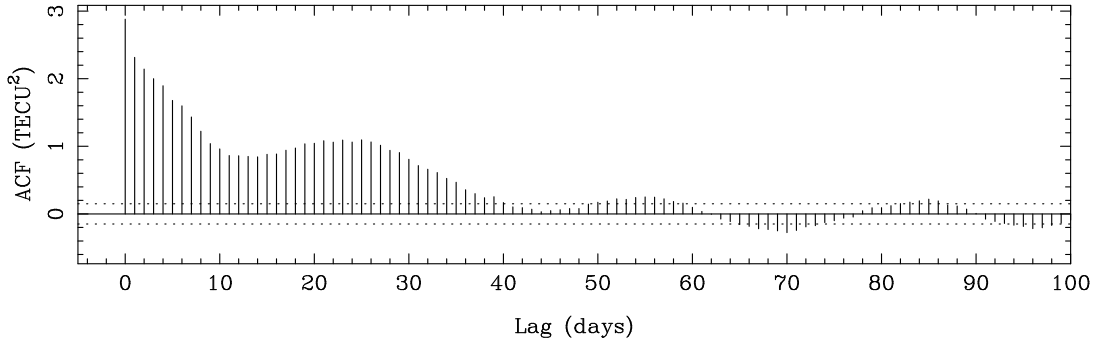
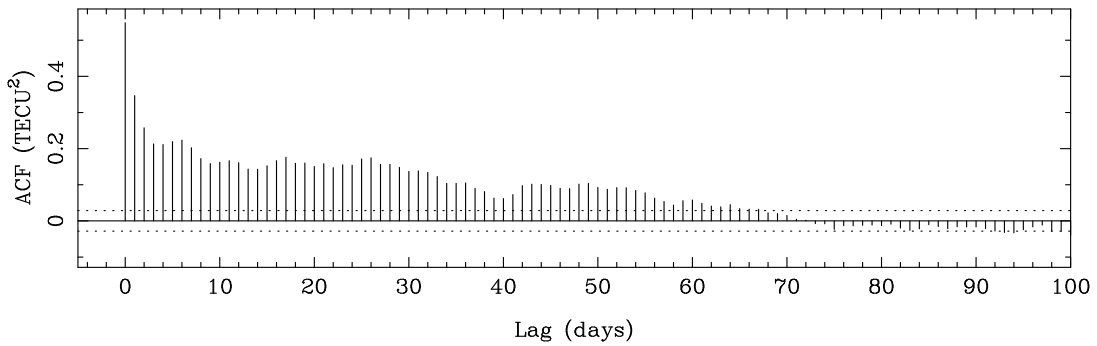


Figure 5.2: Mean TEC  $\tilde{C}_{0,0}$  and related 7-parameter trend function  $\Psi(t)$ , from January 1995 to November 1998.

- the solar cycle,
- the annual and semi-annual variation,
- the lunation cycle, and
- diurnal variations.

It only makes sense to consider the diurnal period when analyzing a time series with a subdaily resolution. Other periods, if once verified, could easily be taken into account. Because the solar rotation does not cause a real periodicity, we cannot attribute any distinct period to it.

Figure 5.2 shows the trend function  $\Psi(t)$  related to the mean TEC  $\tilde{C}_{0,0}$ , actually considering only the most dominating periods of 11, 1, and 1/2 years. It is amazing how well the 7-parameter trend function  $\Psi(t)$  follows the actual observations  $L(t)$ , but the residual signal  $s(t) = L(t) - \Psi(t)$  is still significant. This residual signal  $s(t)$  is used to derive the autocovariance function according to relation (5.10).

Figure 5.3: Autocovariance function of the SH coefficient  $\tilde{C}_{0,0}$ .Figure 5.4: Autocovariance function of the SH coefficient  $\tilde{C}_{1,0}$ .

### 5.3 Resulting Autocovariance Functions

Figures 5.3, 5.4, and 5.5 show the resulting autocovariance functions of the SH coefficients  $\tilde{C}_{0,0}$ ,  $\tilde{C}_{1,0}$ , and  $\tilde{C}_{2,0}$  for lags (or correlation times) up to 100 days. The autocovariance function  $\gamma(t)$  tells us how rapidly a particular signal  $s(t)$  decorrelates in time. Looking at the resulting autocovariance functions, the time correlations prove to be significant over a considerable time span. This is backed up by the dotted 95%-level significance bounds, drawn for  $\pm 1.96 \gamma(0)/\sqrt{n}$ , where  $n$  is the number of epochs analyzed. Moreover, the autocovariance function at  $t = 0$  gives the variance of the stochastic component  $s(t) = L(t) - \Psi(t)$ . We conclude from Figure 5.3 that the standard deviation of the signal related to the mean TEC  $\tilde{C}_{0,0}$  is  $\sqrt{\gamma(0)} \approx 1.7$  TECU. It is noticeable that the autocovariance function of the SH coefficient  $\tilde{C}_{0,0}$  also reflects the fluctuations caused by the “circulating” sunspots. This is indicated by crests of a wave at lags around 27, 54, and 81 days.

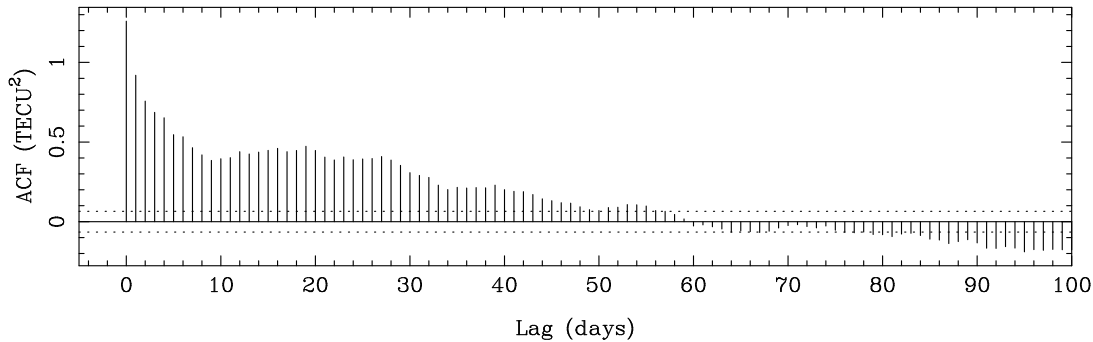


Figure 5.5: Autocovariance function of the SH coefficient  $\tilde{C}_{2,0}$ .

The autocovariance functions have been derived from the complete G1 series of TEC observations which covers about 4 years. Not all TEC observations of this series are available with a 2-hour resolution. We therefore used a special averaging procedure for the subdaily observations, which finally yield autocovariance functions with a 24-hour resolution. Our autocovariance functions derived from subdaily TEC observations must therefore contain high time correlations for lags below 24 hours, because of the a priori constraints originally defined between subsequent TEC coefficients.

## 5.4 TEC Prediction Procedure

The actual TEC prediction procedure consists of several steps. First, a series of BGS ionosphere files is read. Then, a loop over all requested SH coefficients is performed. This loop includes

- estimation of the TEC trend function (5.12),
- computation of the signal component (5.11),
- computation of the autocovariance function according to relation (5.10),
- compilation of the covariance matrices  $\mathbf{C}_u$ ,  $\mathbf{C}_{s'l}$ , and  $\mathbf{C}_{s's'}$ ,
- inversion of the covariance matrix  $\mathbf{C}_u$ ,
- estimation of the predicted signal  $s'$  and its uncertainty  $\mathbf{C}_{\nu\nu}$  based on (5.8) and (5.9),
- addition of the predicted TEC signal to the extrapolated TEC trend, and
- listing of the prediction results.

At the end, a BGS ionosphere file containing the predicted TEC information may be created. By performing the least-squares collocation step for each coefficient of the SH expansion (3.35), using the same prediction length, by merging the predicted coefficients to a full set of global TEC parameters, and by writing a corresponding GIM file, we obtain a procedure that allows us to predict entire GIMs! A software tool solving that task has been developed and documented in [Schaer *et al.*, 1998b].

Let us add a few comments concerning the individual computation steps. In the least-squares adjustment of the  $2n + 1$  auxiliary parameters defining the TEC trend function, the TEC observations are treated as uncorrelated. It may occur that one or more of the periods in (5.12) do not really exist in the time series of a particular SH coefficient. However, this impairs neither the long-term nor the short-term prediction as long as the corresponding harmonic coefficients  $C_i$  and  $S_i$  (or amplitudes  $\sqrt{C_i^2 + S_i^2}$ ) are small. We mention that we refer the individual TEC observations  $L(t)$  to the middle epoch of each 2-hour (or 24-hour) time interval of the original parameter binning.

For two reasons we use for short-term predictions only a limited number of TEC observations: (1) Keeping in mind the decorrelation in time, it does not make sense to take account of TEC observations that were made several months ago. (2) The dimension of the quadratic covariance matrix  $\mathbf{C}_U$  to be inverted directly depends on the number of TEC base points, which eventually leads to very large dimensions. Also, we should account of another “degree of freedom”: The covariance matrix  $\mathbf{C}_U$  basically consists of  $\mathbf{C}_{ss} + \mathbf{C}_{nn}$ , where  $\mathbf{C}_{ss}$  is the ACF-derived covariance matrix of the signal component and  $\mathbf{C}_{nn}$  denotes the covariance matrix of the noise component. In our case,  $\mathbf{C}_{nn}$  is a diagonal matrix which contains the formal variances provided by the primary TEC parameter estimation. As an option, those formal variances may be multiplied by a specified factor.

As least-squares collocation not only allows to predict but also to “interpolate” signals, we may use it to produce averaged global TEC maps, as well. The “smoothness” is adjustable by the factor which is applied to the variance matrix of the noise component. This factor in principle allows to switch between two extremes:

- When  $\mathbf{C}_{nn}$  is a zero matrix, the interpolated signal will correspond to the observed signal.
- When  $\mathbf{C}_{nn}$  dominates  $\mathbf{C}_{ss}$ , the interpolated signal will follow the trend function.

For obvious reasons, the variance matrix  $\mathbf{C}_{nn}$  of the noise component may have an impact on predicted TEC parameters, too.

Let us at last address the most important input parameters required by our IONANA (IONosphere ANALysis) program: a table of BGS ionosphere files, a list of a priori periods, the desired prediction length, the number of observations to be used for the actual least-squares collocation, and the multiplier for the noise component. The essential output parameters are amplitudes, phase angles, and offsets of the coefficient-specific TEC

trend functions, test factors indicating the statistical significance of the amplitudes, the variances  $\gamma(0)$ , and, naturally, the values and the formal RMS errors of the predicted SH coefficients. In addition, IONANA has a graphic output. A resulting BGS ionosphere file may be easily converted into an IONEX file.

From a theoretical point of view, one might wish to generate predictions simultaneously for all SH coefficients, implying that eventually also cross-correlations between different SH coefficients should be studied. We believe that such cross-correlations are empirically detectable. Nevertheless, the dimensions of the corresponding covariance matrices would become very large. We therefore proceed in predicting global TEC parameters coefficient by coefficient.

## 5.5 Examples

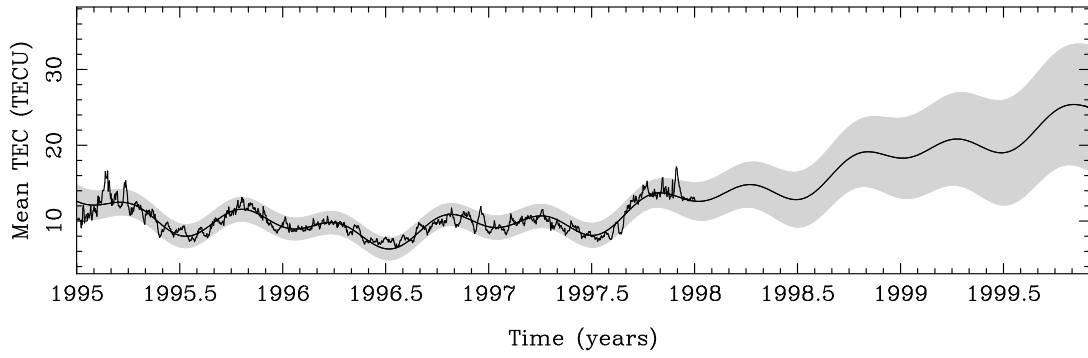
### 5.5.1 Long-Term Prediction

It is easy to understand that long-term prediction is only possible with the help of an appropriate trend function. Figure 5.6 shows the 7-parameter TEC trend function based on 35, 41, and 47 months of TEC observations. Long-term prediction is necessary to successfully extrapolate the deterministic component. This behavior is described by the trend function, when using time spans where time correlations become insignificant. Only the expectation value and the associated variance may be predicted for the signal.

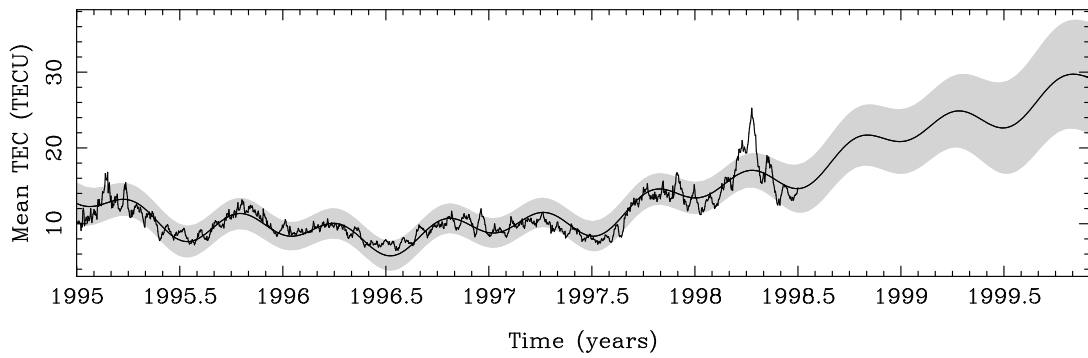
Figure 5.7 is rather speculative. It shows the evolution of the 7-parameter TEC trend function over 11 years, the principal period being due to the solar cycle. We keep in mind that a prediction of the mean TEC over such a long time interval is at the edge of science and speculation, since it is based on about 4 years of TEC observations only. Looking at Figure 3.3 which describes the evolution of the sunspot number, one may moreover expect that the increase in TEC will tend to be steeper than the decrease. Accordingly, Figure 5.7 must be interpreted with caution. This diagram, nevertheless, gives an impression of the 11-year, annual, and semi-annual variations, the amplitudes of which are estimated to  $18.3 \pm 0.2$ ,  $1.44 \pm 0.05$ , and  $1.87 \pm 0.04$  TECU, respectively. The average level (or offset  $C_0$ ) results in  $26.3 \pm 0.2$  TECU. This level is highly correlated with the 11-year amplitude estimated, indicated by the shaded confidence band becoming wider towards the next 11-year maximum (see Figures 5.6 and 5.7).

### 5.5.2 Short-Term Prediction

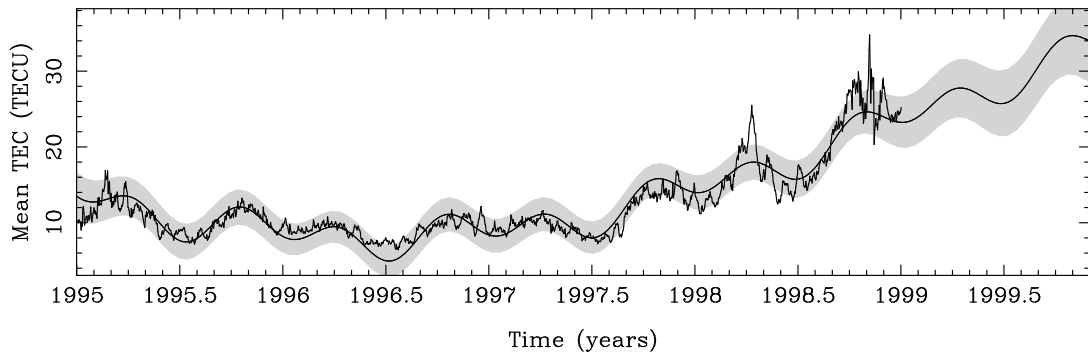
If one wishes to reliably predict a signal over short time spans, it makes sense to extrapolate not only the deterministic but also the stochastic component, provided that significant time correlations are present. Therefore, the autocovariance function is well suited as the basis for short-term prediction.



(a) January 1995 to November 1997



(b) January 1995 to May 1998



(c) January 1995 to November 1998

Figure 5.6: Long-term as well as short-term prediction of the mean TEC, based on (a) 35, (b) 41, and (c) 47 months of global TEC observations.



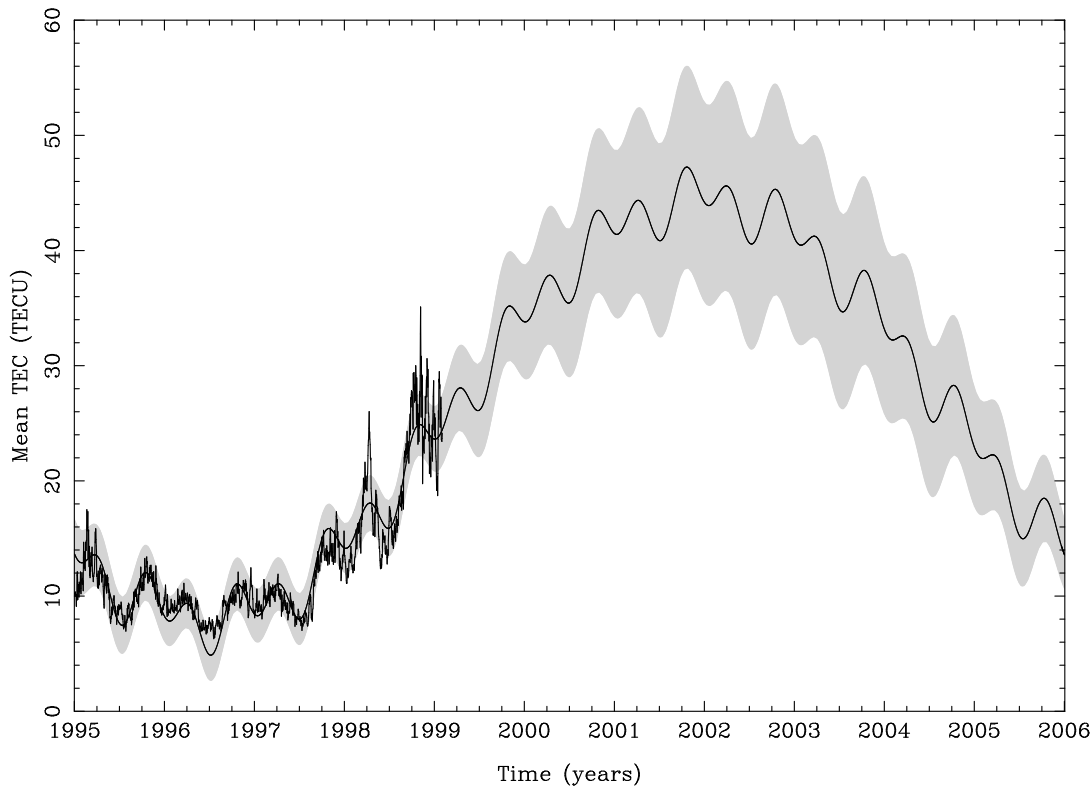
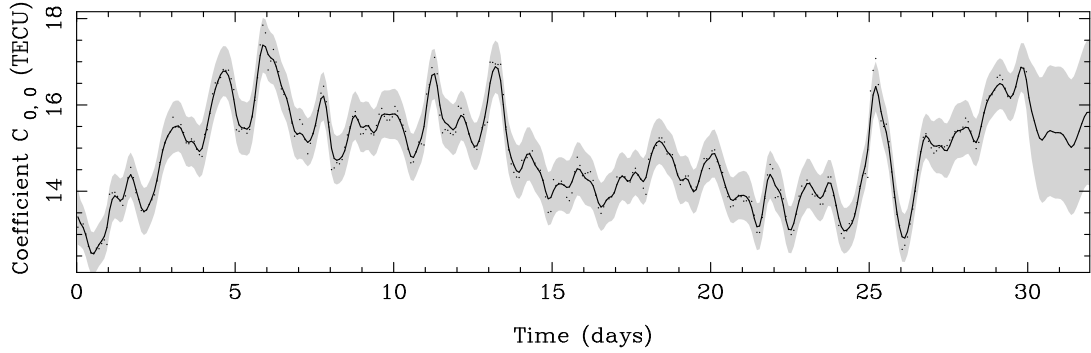


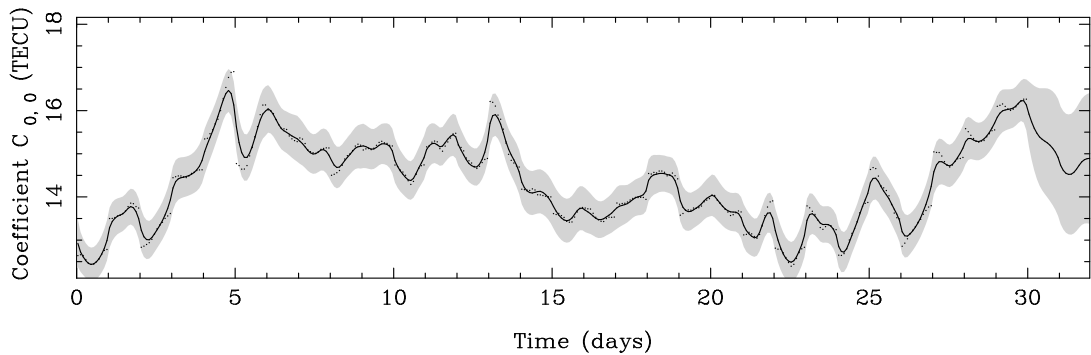
Figure 5.7: Mean TEC  $\tilde{C}_{0,0}$  and trend function  $\Psi(t)$ , fitted to 4 years of global TEC observations and extrapolated for the next 7 years.

Figure 5.8 shows the least-squares collocated signal of the SH coefficient  $\tilde{C}_{0,0}$  based on Z1 and G1 solutions for a particular month (June 1998). The solid line represents the TEC signal. It actually corresponds to an interpolated signal for the first 30 days and an extrapolated signal for the last two days. Dots indicate the original 2-hourly TEC observations. In addition, the shaded band gives the 95%-level confidence interval. This confidence interval, which increases rapidly during the last two days, demonstrates that one cannot expect miracles from the ionosphere prediction. Because the formal RMS errors provided by the primary TEC determination turn out in our experience to be very optimistic, we usually multiply them by 10 to obtain a more realistic assessment of the variance matrix  $C_{nn}$  related to the observation noise.

Figure 5.9 was generated the same way as Figure 5.8. The daily variations in the zonal SH coefficient  $\tilde{C}_{1,0}$  indicate that the geomagnetic reference frame is not perfect, either. This finding supported by the fact that the phase angle of this variation coincides with the geographic longitudes of the dip poles. When looking for a reference frame with a stationary global TEC distribution, it would be interesting to find the “symmetry axis”



(a) Z1 solutions

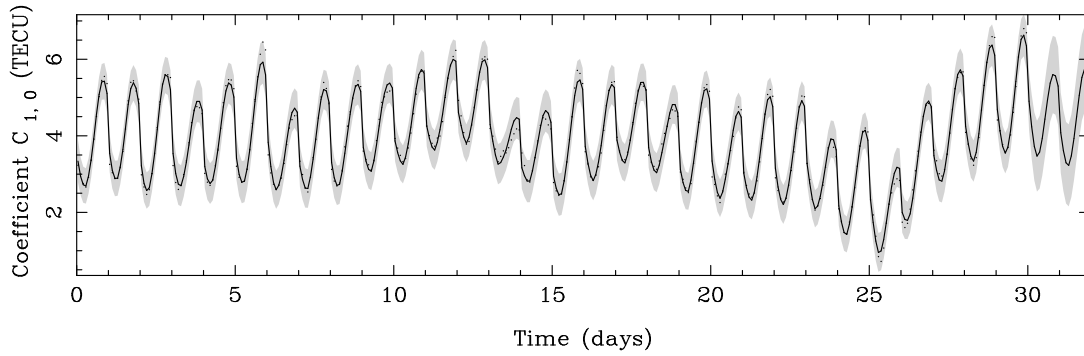


(b) G1 solutions

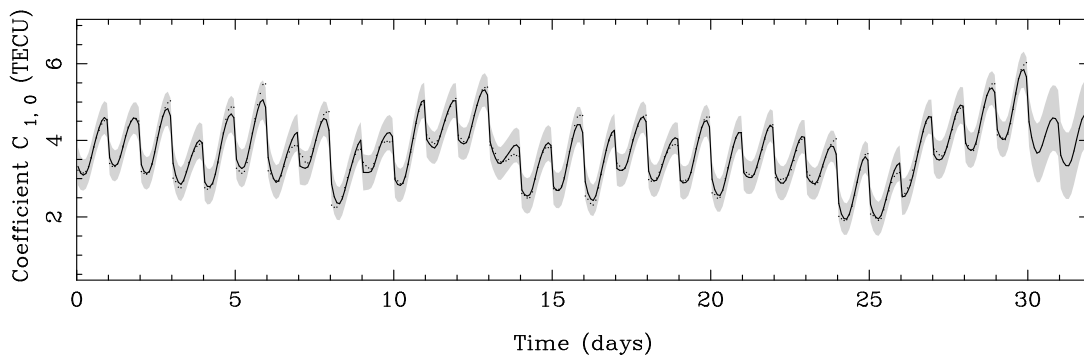
Figure 5.8: Least-squares interpolated and 2-day extrapolated SH coefficient  $\tilde{C}_{0,0}$  based on Z1 and G1 solutions, for June 1998.

where diurnal variations in  $\tilde{C}_{1,0}$  disappear or are greatly reduced. One might initially assume that this “ionospheric symmetry axis” lies somewhere between the earth rotation axis and the dip axis. The bisector of the angle between these two axes might be worth a first trial.

When comparing Figure 5.8a with 5.8b and Figure 5.9a with 5.9b we get the impression that it is difficult for the interferometric G1 TEC determination to follow the high temporal variations than the Z1 series. Although formally the same relative constraints were applied to both solutions, the diurnal fluctuations in  $\tilde{C}_{1,0}$  recovered by the G1 solutions seem to be reduced when compared to those of the Z1 solutions. Discontinuities are more pronounced in the G1 than in Z1 TEC estimates. Nevertheless, the two “mean” TEC signals agree quite well.



(a) Z1 solutions

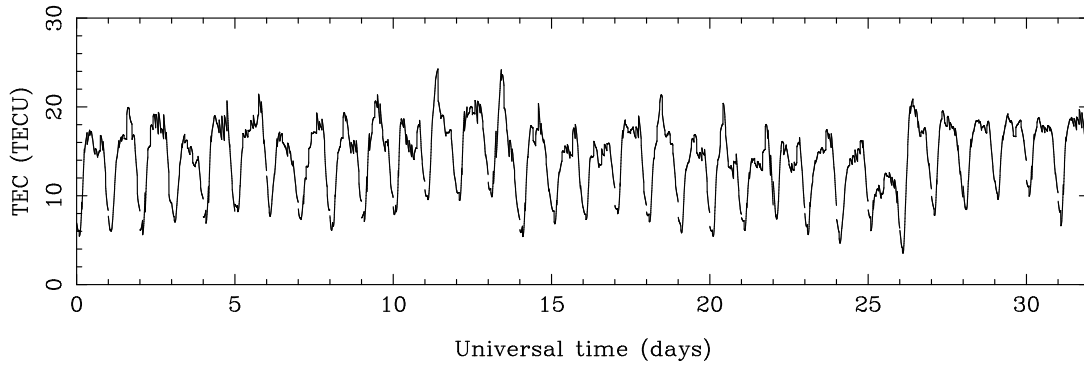


(b) G1 solutions

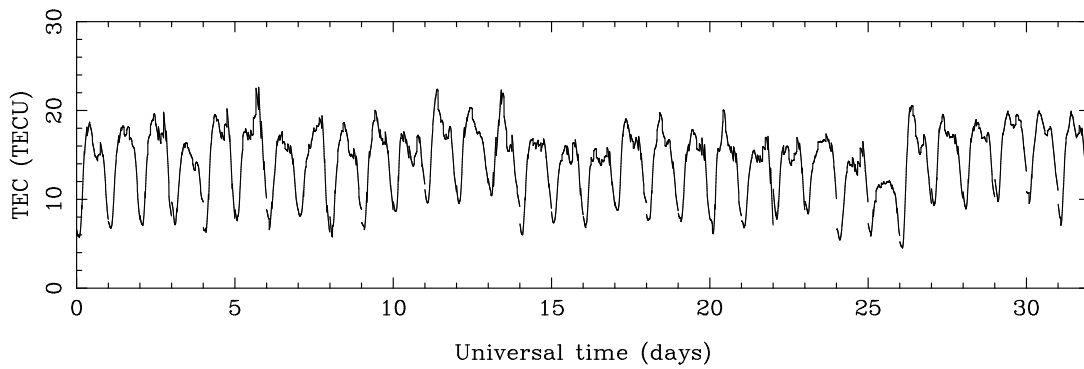
Figure 5.9: Least-squares interpolated and 2-day extrapolated SH coefficient  $\tilde{C}_{1,0}$  based on Z1 and G1 solutions, for June 1998.

An average user of ionospheric maps is probably not interested in individual SH coefficients but rather in the TEC information at a particular location. To be consistent with Figures 5.8 and 5.9 and, moreover, to Figure 4.25, we present 1-day and 2-day predicted TEC profiles evaluated at the geographic coordinates  $(\beta, \lambda) = (50^\circ, 7.5^\circ)$ , using the predicted SH coefficients. Figure 5.10a shows the prediction results derived from Z1 solutions and Figure 5.10b those derived from G1 solutions. It is nice to see that the “double maximum” around noon is reflected by the TEC prediction for the last two days. Concurrently, the discontinuities at the day boundaries are very intrusive. This unfortunately means that the discontinuities in the TEC observations are “predicted” as well.

1-day and 2-day predicted GIMs are generated and made available by CODE since mid



(a) Z1 solutions



(b) G1 solutions

Figure 5.10: 1-day and 2-day predicted TEC profiles at  $(\beta, \lambda) = (50^\circ, 7.5^\circ)$  derived from Z1 or G1 solutions of June 1998.

of June 1998 [Schaer, 1998a]. Such GIMs in the IONEX format may be of interest for real-time applications. The 1-day and 2-day predictions called G11 and G12, respectively, are based on G1 solutions which are complemented by the three most recent rapid RG solutions.

The ionosphere prediction procedure used in Figure 4.1 is kept going by the BPE that controls the rapid IGS data processing. This procedure not only derives G11 and G12 GIMs but also computes a 30-day and a one-year prediction of the mean TEC similar to Figure 5.6, creates corresponding graphics, and updates the CODE ionospheric WWW site <http://www.cx.unibe.ch/aiub/ionosphere.html> with the most recent TEC (and DCB) results.

## 5.6 Predicting DCBs for GPS Spacecrafts

Let us briefly address the question whether it would make sense to predict DCBs for GPS spacecrafts. The answer is no. ACF computations using (5.10)—and replacing in (5.11) the trend function  $\Psi(t)$  by a strongly smoothed signal  $\tilde{s}(t)$  to compensate for the still unexplained annual variation—clearly indicate that the residual signal is of random nature. This confirms that satellite DCBs seem to be stable on a level better than the standard deviation of the daily estimates, at least when averaging them over 24 hours. This standard deviation is about 0.08 nanoseconds for Z1N DCB results. We did not perform a similar study for receiver DCBs.



# 6. Validating the CODE Ionospheric Parameters and Maps

## 6.1 An Introductory Example

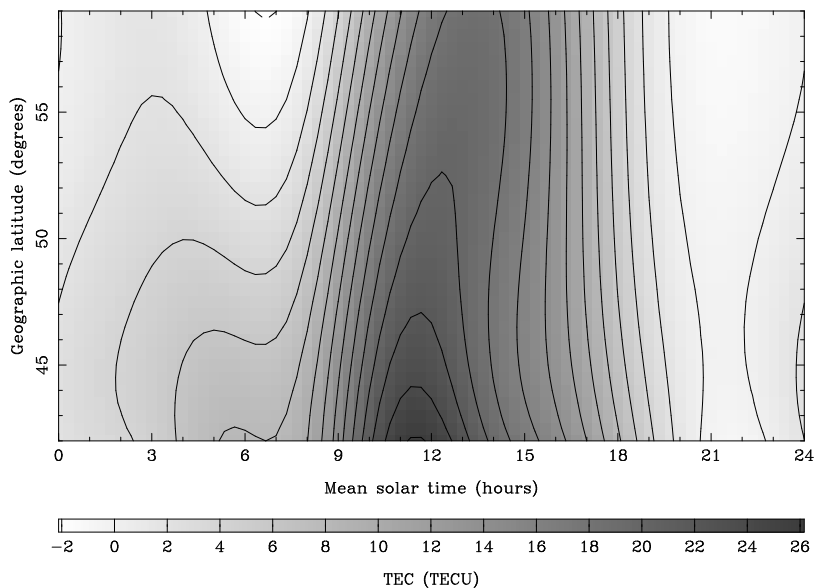
Our introductory example shall help to gain insight into the properties of

- the *deterministic* component of the TEC, represented by our TEC maps, and
- the *stochastic* component of the TEC, represented by the residuals of the modeling process.

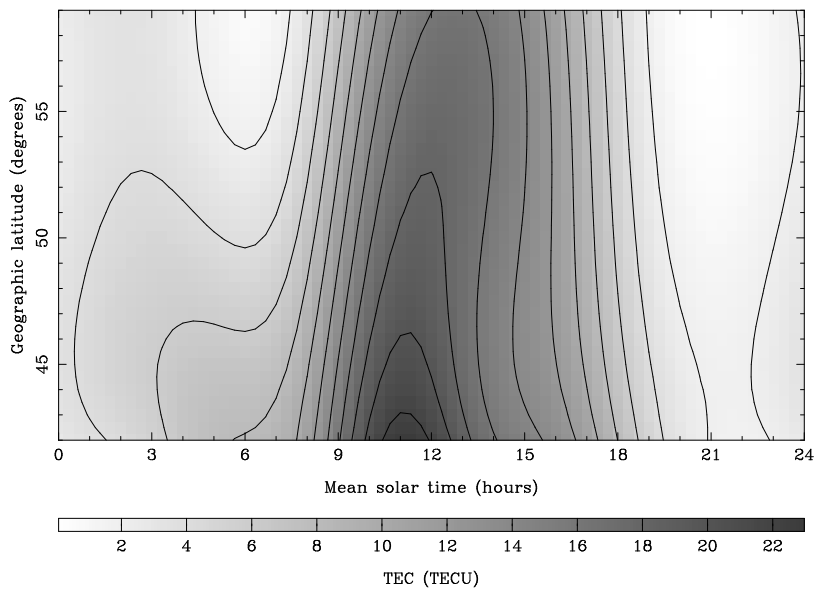
The example is based on phase measurements collected on January 25, 1994 by the two IGS sites Kootwijk, The Netherlands, and Wettzell, Germany. The length of the baseline connecting the two sites is approximately 600 kilometers. A  $20^\circ$  elevation mask was used.

### 6.1.1 Deterministic Component of the TEC

Figure 6.1 shows the baseline-specific TEC map derived from double-difference phase measurements, using a SH expansion (3.35) of degree 5. It consists of two TEC maps: (a) the map obtained from an “ambiguity-free” solution solving simultaneously for TEC and ambiguity parameters and (b) the map obtained from an “ambiguity-fixed” solution, where the previously resolved initial phase ambiguities are introduced as known integers. In this example, we had in case (a)  $36 + 42 = 78$  and in case (b) 36 unknown parameters. Although the second map (b) is expected to have a higher quality, we clearly see that the main features are the same in maps (a) and (b). A baseline must have a certain length to allow for absolute TEC determination using double-difference phase measurements. From Figure 6.1 we conclude that the differential ionospheric signal pertaining to a 600-kilometer baseline is sufficient to allow for high-quality ionosphere mapping. The mean baseline length in the IGS network is considerably longer than 600 kilometers, which means that the IGS network is well suited for ionosphere mapping using double differences.



(a) "Ambiguity-free" TEC map



(b) "Ambiguity-fixed" TEC map

Figure 6.1: Baseline-specific TEC map (before and after ambiguity resolution) derived from the baseline Kootwijk-Wetzell, for January 25, 1994.



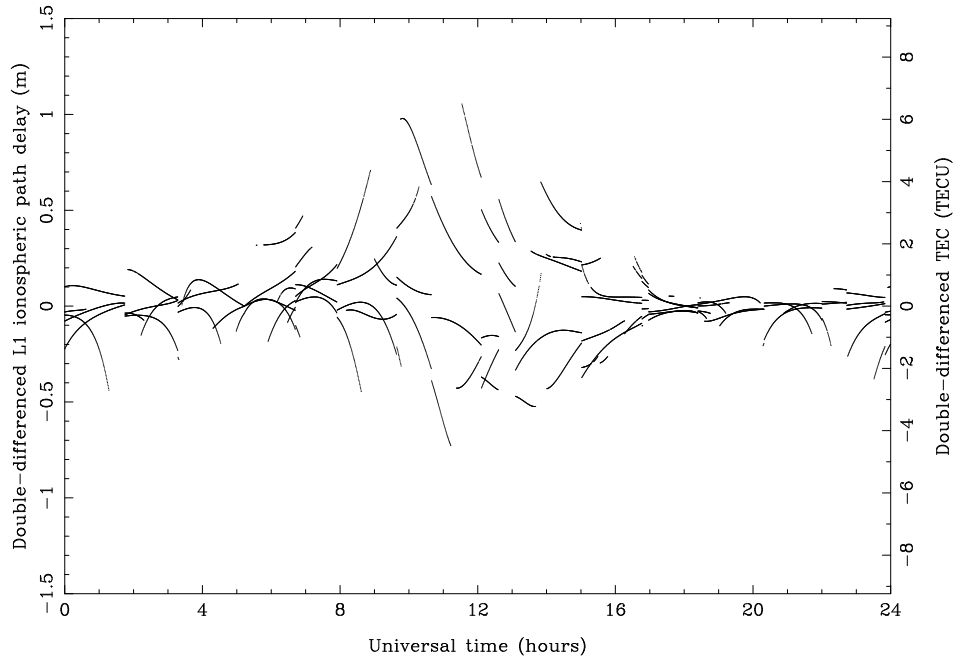


Figure 6.2: Double-differenced L1 ionospheric corrections as reflected by the Kootwijk-Wettzell TEC map, for January 25, 1994.

Let us now have a look at the double-differenced ionospheric corrections computed from the ionosphere model (3.35) underlying our baseline-specific TEC map. Figure 6.2 gives these corrections for each double-difference phase measurement. The left-hand scale gives the line-of-sight ionospheric path delay in meters on L1; the right-hand scale quantifies the corresponding TEC in TECU. The largest double-differenced ionospheric correction is more than one meter on L1 and 6 TECU, respectively.

The jumps in the corrections stem from changes of the reference satellite. Note that at each epoch we selected the satellite closest to the mean zenith as reference. Apart from these jumps, the “deterministic” ionospheric corrections are, as expected, rather smooth.

### 6.1.2 Stochastic Component of the TEC

Ambiguity resolution for January 25, 1994 is no real problem, because this particular day falls into a period where AS (anti-spoofing) was turned off. We were able to resolve all initial phase ambiguities when using both the pseudo-range approach and the QIF (quasi-ionosphere-free) strategy (see section 2.3.4). Both strategies gave identical results. As soon as these integers are known, the observation equation (2.25a) and relation (2.26) may be used to determine double-difference ionospheric corrections  $I_{ij}^{kl}$ . We call them

stochastic ionosphere parameters (SIPs). They describe the ionospheric path delay on L1. By multiplying  $I_{ij}^{kl}$  with  $\xi \approx 1.647$ , one may easily obtain the corresponding path delay on L2.

Figure 6.3a shows the epoch-specific SIPs (every 30 seconds) without taking our TEC map into account. These parameters may be determined very accurately, provided that all phase ambiguities are fixed—as in our example. We may therefore consider the SIP values in Figure 6.3a as “ionospheric truth.”

In order to obtain the “stochastic” component of the TEC, we subtract the corrections in Figure 6.2 from the SIP values in Figure 6.3a. These corrections may be computed based on the observation equation (3.32). We used the “ambiguity-fixed” TEC map. This reduction leads to the SIP values in Figure 6.3b. The remaining ionospheric path delays are principally due to a multitude of short-term fluctuations in the TEC, like TIDs (traveling ionospheric disturbances). Figure 6.4 shows the stochastic component of the TEC for the time window between 08:00 and 12:00 UT. The prevailing periods are typical for MSTIDs (medium-scale TIDs).

Figures 6.3b and 6.4 demonstrate the weakness of our TEC maps. Our TEC maps, having a limited temporal and spatial resolution, are not capable of describing unpredictable short-term fluctuations. Such short-term fluctuations are, however, crucial for GPS users trying to resolve ambiguities in the rapid-static or the kinematic mode.

Figures 6.3b and 6.4 also indicate that the GPS offers the potential for studying the stochastic behavior of the TEC [Wanninger, 1994]. By analyzing temporal differences (or triple differences) of the ionospheric LC, we may derive information about the “agitation” of the TEC [Schaer, 1996; Schaer et al., 1996b]. Note that initial phase ambiguities cancel out in such differences.

Let us briefly discuss the dual-band observation equation used for QIF ambiguity resolution (see section 2.3.4):

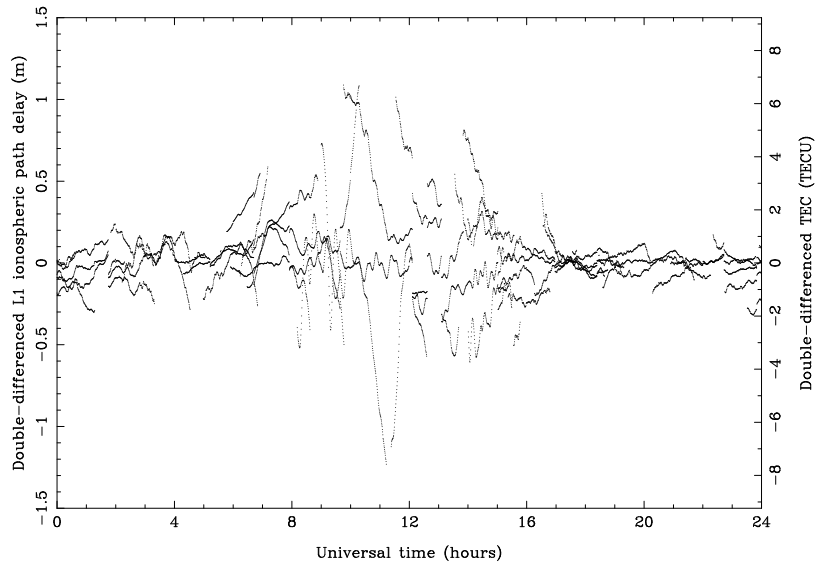
$$L_{ij,1}^{kl} = \rho_{ij}^{kl} - I_{ij}^{kl} - \xi_E (F(z) E_v(\beta, s))_{ij}^{kl} + \lambda_1 N_{ij,1}^{kl} \quad (6.1a)$$

$$L_{ij,2}^{kl} = \rho_{ij}^{kl} - \xi I_{ij}^{kl} - \xi \xi_E (F(z) E_v(\beta, s))_{ij}^{kl} + \lambda_2 N_{ij,2}^{kl} \quad (6.1b)$$

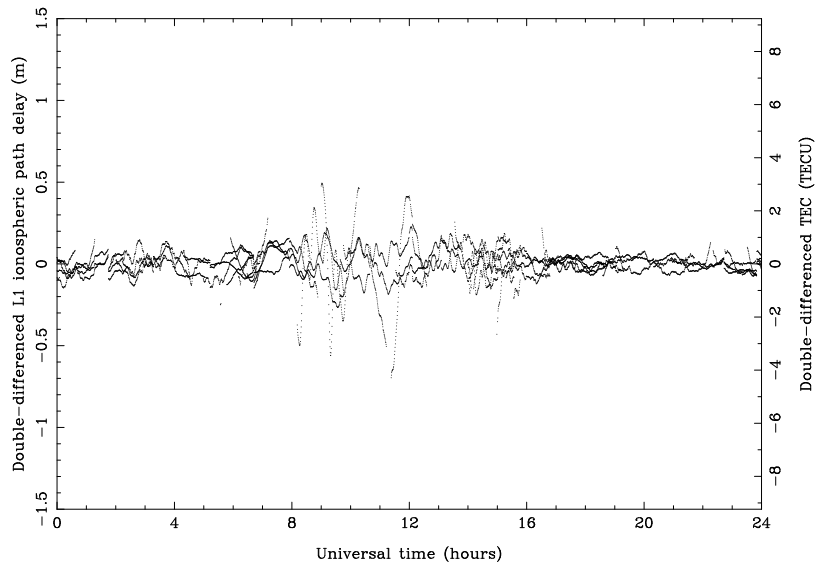
The notations in (6.1) are the same as used in (2.12) and (3.30). Whereas the estimation of epoch-specific SIPs  $I_{ij}^{kl}$  is mandatory for QIF, the consideration of a TEC map represented by  $E_v(\beta, s)$  is optional. It is important to see that the “fractional parts”  $\Delta N_{ij,1}^{kl}$  and  $\Delta N_{ij,2}^{kl}$  of the dual-band phase ambiguities, the differences between the real-valued estimates  $N_{ij,1}^{kl}$  and  $N_{ij,2}^{kl}$  and the resolved integers  $N_{ij,1}^{*kl}$  and  $N_{ij,2}^{*kl}$  indicate the remaining ionosphere-induced errors:

$$\Delta N_{ij,1}^{kl} = N_{ij,1}^{kl} - N_{ij,1}^{*kl} \quad (6.2a)$$

$$\Delta N_{ij,2}^{kl} = N_{ij,2}^{kl} - N_{ij,2}^{*kl} \quad (6.2b)$$



(a) Without TEC map



(b) With TEC map

Figure 6.3: Double-differenced L1 ionospheric path delays and double-differenced TEC on the baseline Kootwijk-Wetzell, for January 25, 1994.

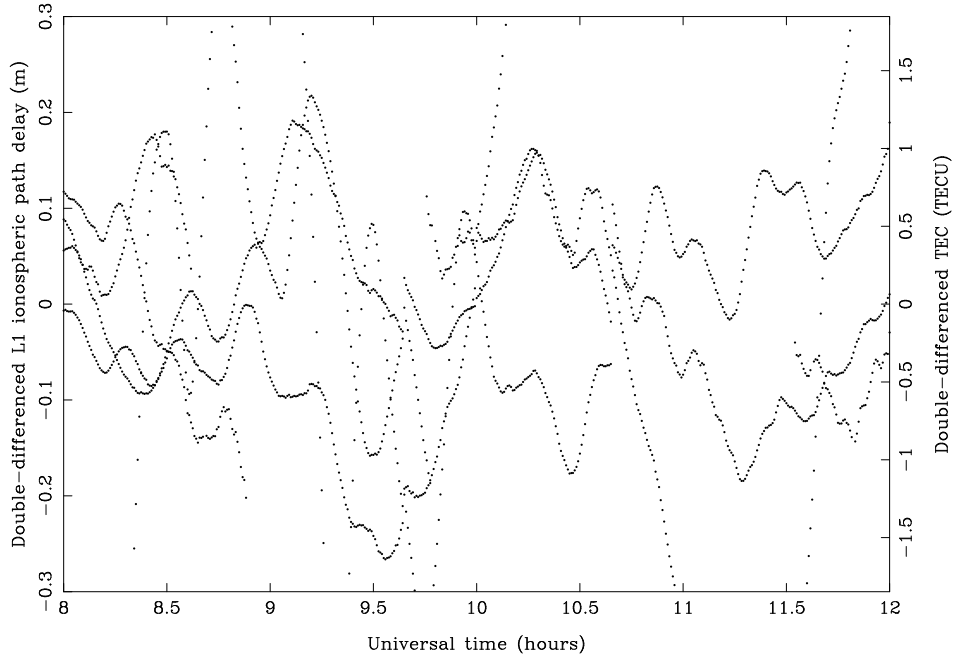


Figure 6.4: Medium-scale traveling ionospheric disturbances (MSTIDs) on the baseline Kootwijk-Wetzell, for January 25, 1994 (08:00 to 12:00 UT).

Because there is a simple relationship between  $\Delta N_{ij,1}^{kl}$  and  $\Delta N_{ij,2}^{kl}$  (see Table 2.2), we usually refer them to the wide-lane LC (2.29):

$$\Delta N_{ij,5}^{kl} = N_{ij,5}^{kl} - N_{ij,5}^{*kl} = (N_{ij,1}^{kl} - N_{ij,2}^{kl}) - (N_{ij,1}^{*kl} - N_{ij,2}^{*kl}) \quad (6.3)$$

Figure 6.5 shows two histograms of the ionosphere-induced errors: (a) one without subtracting first the deterministic component of the TEC and (b) one after taking into account our TEC map of Figure 6.1b. Unlike the traditional wide-lane ambiguity resolution, the QIF strategy can cope with ionosphere-induced errors, expressed in  $L_5$ -cycles, markedly larger than half a cycle. Using our TEC map, we may reduce the scatter of the “fractional parts” considerably. We may in this way reduce the standard deviation of  $\Delta N_{ij,5}^{kl}$  from 0.181 to 0.076  $L_5$ -cycles. Expressed in TECU, the standard deviation results in 0.75 and 0.31 TECU, respectively. Note that one  $L_5$ -cycle corresponds to approximately 4.14 TECU. It is well known that TEC maps are useful to improve phase-based wide-lane ambiguity resolution [Wild, 1993]. For the QIF strategy, the use of TEC maps makes ambiguity resolution more reliable and, moreover, allows to apply it to longer baselines, keeping in mind that the “Q(uasi)” in QIF indicates that this strategy is still sensitive to the ionosphere.

Let us specify the standard deviations of the ionospheric path delays and the corres-

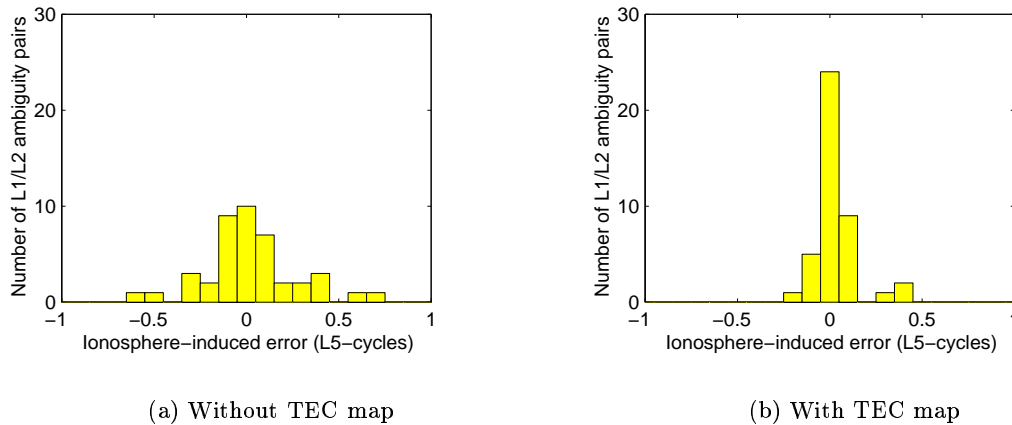


Figure 6.5: Ionosphere-induced errors related to the L1/L2 ambiguities of the baseline Kootwijk-Wetzell, for January 25, 1994.

ponding TEC values as shown in Figures 6.3 and 6.2. We obtained 0.219 meters and 1.35 TECU for Figure 6.3a which shows the full amount of the double-differenced TEC, 0.088 meters and 0.54 TECU for Figure 6.3b which shows the stochastic component, and finally 0.201 meters and 1.24 TECU for Figure 6.2 which gives the deterministic component. By taking our TEC map into account, the standard deviations of the errors related to the L1/L2 ambiguities and the ionospheric path delays were both reduced by about 60% in our example. We notice, however, that the standard deviations of the “fractional parts,” obtained to 0.75 and 0.31 TECU, are significantly smaller than 1.35 and 0.54 TECU, those of the epoch-specific SIPs, because each ambiguity parameter is referred to a time interval. By relating the standard deviation of the short-term variations to the absolute TEC level, we might eventually develop a better understanding for our TEC maps.

This introductory example shows the influence of differential TEC on a 600-kilometer baseline at mid-latitudes—during medium solar activity. For shorter baselines, these effects decrease in good approximation linearly with the baseline length [*Schaer*, 1994].

### 6.1.3 Formal Accuracy of the Double-Difference TEC Determination

What is the formal accuracy of the double-difference L1 ionospheric path delay  $I_{ij}^{kl}$  and the double-difference TEC  $E_{ij}^{kl}$  for each epoch, assuming that the L1 and L2 phase ambiguities between the two involved satellites are fixed? When analyzing the geometry-

free LC, the observation equation (2.25a) has to be used:

$$L_{ij,4}^{*kl} = -\xi_4 I_{ij}^{kl} = -\xi_4 \xi_E E_{ij}^{kl} \quad (6.4)$$

where  $\xi_4 \approx -0.647$  and  $\xi_E \approx 0.162$  m/TECU. Let us assume that the zero-difference phase measurements  $L_{i,1}^k$  and  $L_{i,2}^k$  are of the same accuracy, when expressed in meters:  $\sigma(L_{i,1}^k) = \sigma(L_{i,2}^k)$ . Consequently, the accuracy of our basic observable  $L_{ij,4}^{kl}$  may be given by  $\sigma(L_{ij,4}^{kl}) = 2^{\frac{3}{2}} \sigma(L_{i,1}^k)$ . This leads to

$$\sigma(I_{ij}^{kl}) = \frac{2^{\frac{3}{2}}}{\xi_4} \sigma(L_{i,1}^k) \quad \text{and} \quad \sigma(E_{ij}^{kl}) = \frac{2^{\frac{3}{2}}}{\xi_4 \xi_E} \sigma(L_{i,1}^k) \quad (6.5)$$

With, e. g.,  $\sigma(L_{i,1}^k) = 2$  mm, we obtain  $\sigma(I_{ij}^{kl}) \approx 8.7$  mm and  $\sigma(E_{ij}^{kl}) \approx 0.054$  TECU. It is a pity that such an accuracy may never be achieved on the zero-difference level!

In relation to  $L_{ij,1}^{kl}$ , the observable  $L_{ij,4}^{kl}$  only contains about 64.7% of the ionospheric signal, whereas  $L_{ij,2}^{kl}$  contains about 164.7%. Let us determine  $I_{ij}^{kl}$  and  $E_{ij}^{kl}$  using simultaneously the observation equations (2.12a) and (2.12b) for the original carriers L1 and L2 (ambiguities fixed):

$$L_{ij,1}^{*kl} = \rho'_{ij}{}^{kl} - I_{ij}^{kl} = \rho'_{ij}{}^{kl} - \xi_E E_{ij}^{kl} \quad (6.6a)$$

$$L_{ij,2}^{*kl} = \rho'_{ij}{}^{kl} - \xi I_{ij}^{kl} = \rho'_{ij}{}^{kl} - \xi \xi_E E_{ij}^{kl} \quad (6.6b)$$

where  $\xi \approx 1.647$ . Assuming that the doubly differenced geometric term  $\rho'_{ij}{}^{kl}$  is very precisely known, we may conclude:

$$\sigma(I_{ij}^{kl}) = \frac{2}{\sqrt{1 + \xi^2}} \sigma(L_{i,1}^k) \quad \text{and} \quad \sigma(E_{ij}^{kl}) = \frac{2}{\xi_E \sqrt{1 + \xi^2}} \sigma(L_{i,1}^k) \quad (6.7)$$

Assuming  $\sigma(L_{i,1}^k) = \sigma(L_{i,2}^k) = 2$  mm, we obtain  $\sigma(I_{ij}^{kl}) \approx 2.1$  mm and  $\sigma(E_{ij}^{kl}) \approx 0.013$  TECU. The factor of approximately 4 that we gain in accuracy when using the ambiguity-fixed dual-band observables  $L_{ij,1}^{kl}$  and  $L_{ij,2}^{kl}$  instead of the geometry-free LC  $L_{ij,4}^{kl}$  for mapping double-difference ionospheric path delays is remarkable. We have to keep in mind, however, that we assumed perfect knowledge of the term  $\rho'_{ij}{}^{kl}$ . As opposed to (6.5), (6.7) is only correct for rather short baselines. Nevertheless, in principle there must be a trade-off between both double-difference TEC determination methods, depending on the baseline length. Note that Figures 6.3 and 6.4 are both based on observation equation (6.6).

Let us point out that the dual-band observation equation (6.1) contains the entire information related to the “geometry” and TEC. It is hence possible to derive TEC maps using (6.1), as well. (6.1) thus represents the basis for a high-pass filter concerning the deterministic component of the TEC. A priori constraining the SIPs is indispensable, however, even in the ambiguity-fixed case. In other words, we are in principle able to directly split up both components of the TEC in one single processing step, even in the course of ambiguity resolution. Note that we normally pre-eliminate SIPs according to scheme (2.60) from the normal equation system when performing QIF ambiguity resolution.

Table 6.1: AC-specific offsets of the mean TEC  $\bar{E}$ , from August 28, 1998 to January 31, 1999.

AC	Offset (TECU)
COD(G1)	-0.81 (-0.12)
COD(Z1)	-1.14 (-0.45)
EMR	-0.27 (+0.42)
ESA	-1.57 (-0.88)
JPL	+3.47 (+4.16)
UPC	+0.32 (+1.01)

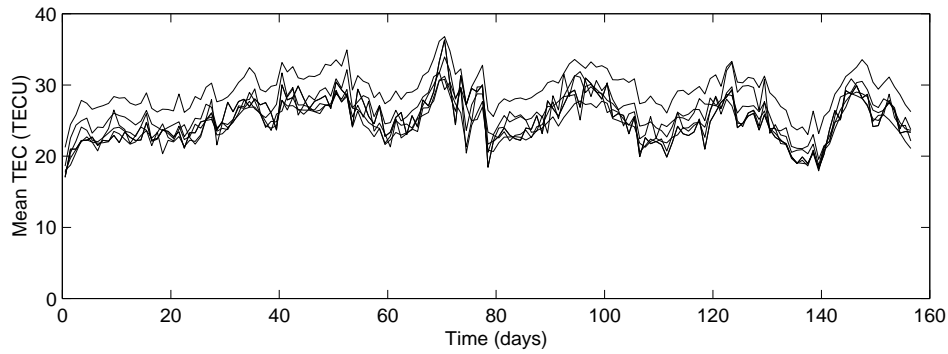
## 6.2 Comparing and Correlating CODE With IGS Global TEC Parameters and Maps

We made use of the global TEC maps produced by the IGS ionosphere ACs. This group of ACs consists, apart from CODE (Center for Orbit Determination in Europe), of NR-Can (National Resources Canada), ESA (European Space Agency), JPL (Jet Propulsion Laboratory), and UPC (Polytechnical University of Catalonia). Note that the former name of NRCan is EMR (Energy, Mines and Resources).

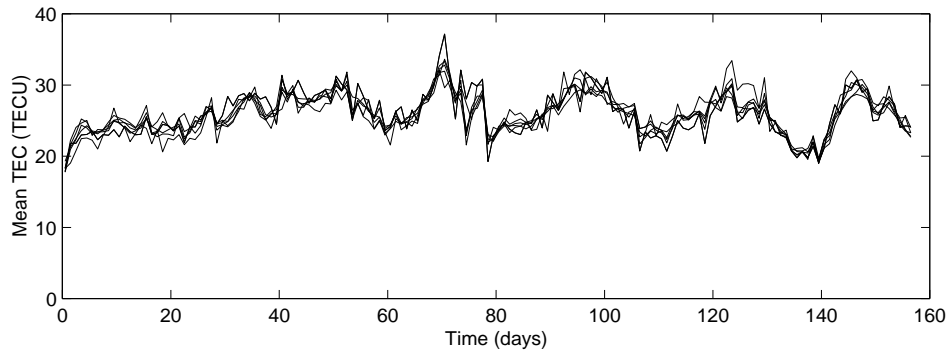
The IGS global ionosphere maps produced by each AC are made available through the CDDIS as compressed IONEX files (see sections 4.2.4 and 4.2.5). Daily IONEX files starting with June 1, 1998 may be found there. Because the EMR IONEX files had to be excluded until June 29, 1998 due to unrealistic TEC (and DCB) values and because no JPL IONEX files were available for the first 88 days, we restricted the following investigations to the time interval starting on August 28, 1998, where IONEX contributions from all five IGS ionosphere ACs were available.

### 6.2.1 Mean Total Electron Content

The mean total electron content is well suited to study the absolute calibration of global TEC maps. We therefore computed the 2-hourly mean TEC values  $\bar{E}$  according to (4.3) for each TEC product. The various time series of the daily averaged mean TEC values  $\bar{E}$  are shown in Figure 6.6a over a time interval of about five months (August 28, 1998 to January 31, 1999). We notice significant differences between the series. Table 6.1 gives the AC-specific offsets of the mean TEC  $\bar{E}$  with respect to the averaged values. The large offset of +3.47 TECU related to the JPL TEC product is striking. This offset may be attributed to the fact that JPL uses the SLM mapping function (3.24) with  $H = 550$  km [Bertiger *et al.*, 1998]. The offsets with respect to the average excluding JPL are given in parentheses. We may expect that the elevation cut-off angle used by the individual



(a) Original values



(b) Aligned values

Figure 6.6: Mean TEC  $\bar{E}$  computed by the IGS ionosphere ACs, from August 28, 1998 to January 31, 1999.

ACs influences the absolute calibration of the TEC as well. CODE, EMR, and JPL use  $10^\circ$ , ESA uses  $20^\circ$ , and UPC uses a  $0^\circ$  elevation mask. The global TEC maps derived by COD(Z1), EMR, ESA, and JPL are based on one-way phase measurements leveled to code measurements, whereas COD(G1) and UPC TEC maps are based exclusively on phase measurements, on double and zero differences, respectively.

The time series of the daily averaged mean TEC values  $\bar{E}$ , aligned using the offsets of Table 6.1, are shown in Figure 6.6b. In order to inspect the remaining differences and to become better acquainted with the properties of the mean TEC results, let us have a closer look at a particular time interval of 10 days. Figure 6.7 gives a chosen



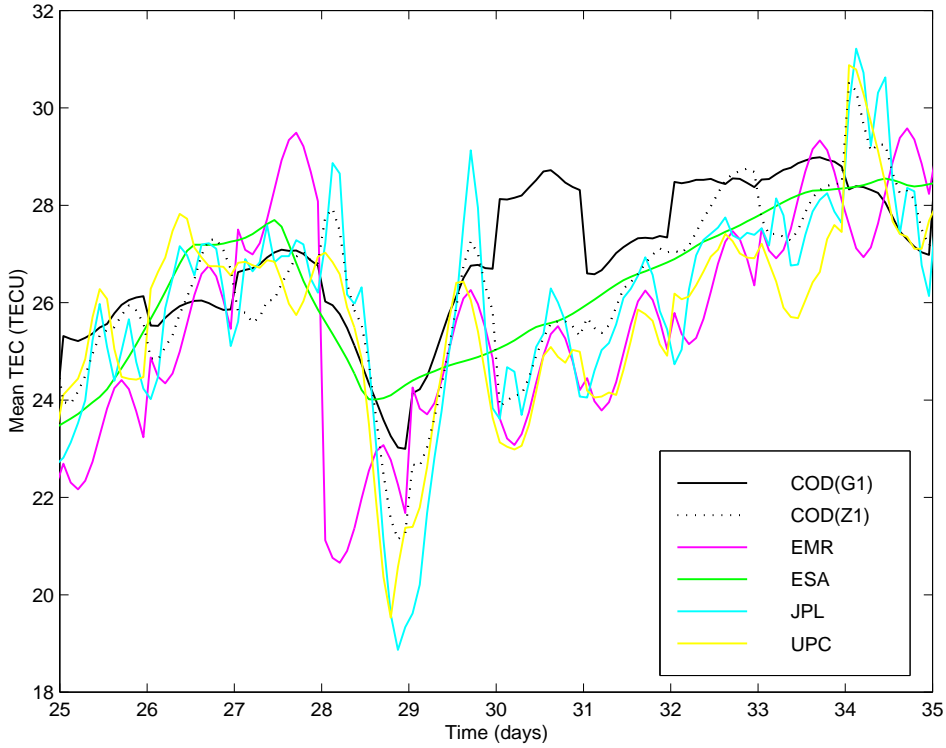


Figure 6.7: 2-hourly mean TEC  $\bar{E}$  (aligned values) computed by the IGS ionosphere ACs, from September 22 to October 1, 1998.

sample in the original 2-hour resolution from September 22 to October 1, 1998. The values were again aligned according to Table 6.1. One curve is very conspicuous because of its smoothness. This curve, produced by ESA, clearly indicates that the ESA global TEC maps underwent a heavy smoothing process. Two other curves, COD(G1) and EMR, reveal discontinuities at the day boundaries. Note that we already pointed out this problem in context of the COD(G1) TEC parameters in Chapter 5. It is strange that the EMR values show for each day a very similar signature. The remaining three curves, COD(Z1), JPL, and UPC, agree pretty well and seem to record even subdaily fluctuations.

We correlated the mean TEC results provided by the IGS ionosphere ACs with respect to each other. The correlation coefficient  $r_{xy}$  of two time series  $x$  and  $y$  may be empirically derived by computing

$$r_{xy} = \frac{\sum_{i=1}^n (x_i - \bar{x})(y_i - \bar{y})}{\sqrt{\sum_{i=1}^n (x_i - \bar{x})^2 \sum_{i=1}^n (y_i - \bar{y})^2}} = \frac{\sum_{i=1}^n x_i y_i - n \bar{x} \bar{y}}{\sqrt{(\sum_{i=1}^n x_i^2 - n \bar{x}^2) (\sum_{i=1}^n y_i^2 - n \bar{y}^2)}} \quad (6.8)$$

Table 6.2: Correlation coefficients between the mean TEC values  $\bar{E}$  of the COD(G1), COD(Z1), EMR, ESA, JPL, and UPC GIMs, from August 28, 1998 to January 31, 1999.

	G1	Z1	EMR	ESA	JPL	UPC
G1	1.000	0.861	0.750	0.863	0.844	0.835
Z1		1.000	0.800	0.876	0.909	0.871
EMR			1.000	0.813	0.809	0.763
ESA				1.000	0.884	0.868
JPL					1.000	0.933
UPC						1.000

where

- $x_i, y_i$  are the values of the two time series referring to the same epoch number  $i$ ,
- $\bar{x}, \bar{y}$  are the arithmetic mean values  $1/n \sum_{i=1}^n x_i$  and  $1/n \sum_{i=1}^n y_i$ , and
- $n$  is the number of common epochs.

Table 6.2 gives the correlation coefficients between the mean TEC values  $\bar{E}$  of the COD(G1), COD(Z1), EMR, ESA, JPL, and UPC GIMs. The highest correlation coefficient with  $r = 0.933$  resulted between JPL and UPC. The second highest coefficient with  $r = 0.909$  was obtained between COD(Z1) and JPL.

In addition, we computed the standard deviations between the mean TEC values  $\bar{E}$  of the different IGS GIMs. These standard deviations are summarized in Table 6.3. As in Table 6.2, the differences between UPC and JPL and between COD(Z1) and JPL yield the smallest standard deviations, namely 1.02 and 1.21 TECU. The largest standard deviation with 2.28 TECU resulted between COD(G1) and EMR.

We have a number of standard deviations relates to the differences between pairs of TEC products at our disposal, but at the end we would like to get an idea of the accuracy of each individual TEC product. Assuming independency of individual products, each standard deviation  $\sigma_{xy}$  of Table 6.3 may be written as  $(\sigma_x^2 + \sigma_y^2)^{\frac{1}{2}}$ , where  $\sigma_x$  and  $\sigma_y$  denote the unknown standard deviations of the individual time series  $x$  and  $y$ . Expressed as variances, the corresponding relationship is linear:  $\sigma_{xy}^2 = \sigma_x^2 + \sigma_y^2$ . This relationship allowed us to adjust the  $n = 6$  standard deviations best fitting the  $n(n - 1)/2 = 15$  standard deviations of Table 6.3. These standard deviations are given in Table 6.4. There are four series with RMS values below one TECU. For the time interval considered, the JPL series yielded the smallest value. All possible standard deviations  $\sigma_{xy}$  deduced from the adjusted values of Table 6.4 are given in Table 6.3 in parentheses. These “computed” standard deviations agree very well with the “observed” ones.

Table 6.3: Standard deviations in TECU between the mean TEC values  $\bar{E}$  of the COD(G1), COD(Z1), EMR, ESA, JPL, and UPC GIMs, from August 28, 1998 to January 31, 1999.

	G1	Z1	EMR	ESA	JPL	UPC
G1	0.00	1.64 (1.72)	2.28 (2.26)	1.65 (1.71)	1.74 (1.65)	1.78 (1.76)
Z1		0.00	1.95 (1.97)	1.37 (1.29)	1.21 (1.22)	1.40 (1.35)
EMR			0.00	1.87 (1.96)	1.91 (1.91)	2.09 (2.00)
ESA				0.00	1.32 (1.20)	1.34 (1.34)
JPL					0.00	1.02 (1.27)
UPC						0.00

Table 6.4: Adjusted standard deviations giving the accuracy of the mean TEC determination performed by the various IGS ionosphere ACs, from August 28, 1998 to January 31, 1999.

AC	RMS (TECU)
COD(G1)	1.45
COD(Z1)	0.92
EMR	1.74
ESA	0.90
JPL	0.79
UPC	0.99

### 6.2.2 Total Electron Content Above Europe

There were two main motivations to compare total electron content results above the European continent. First, it is a region with a high density of stations. Secondly, this particular region allowed us to include the CODE regional TEC products stemming from the EG and EQ solutions (see section 4.2).

We extracted the TEC values for few points around the location at  $(\beta, \lambda) = (+50^\circ, +7.5^\circ)$ , a location in Western Europe, from the COD(G1), COD(Z1), EMR, ESA, JPL, UPC, COD(EG), and COD(EQ) TEC products and computed the standard deviations of

Table 6.5: Standard deviations in TECU between TEC grid values extracted in the vicinity of  $(\beta, \lambda) = (+50^\circ, +7.5^\circ)$  from different TEC products, from August 28, 1998 to January 31, 1999.

	G1	Z1	EMR	ESA	JPL	UPC	EG	EQ
G1	0.00	1.79 (1.64)	3.11 (3.22)	3.12 (3.04)	2.08 (1.89)	2.46 (2.43)	2.08 (2.14)	1.65 (1.92)
Z1		0.00	3.35 (3.01)	2.83 (2.82)	1.08 (1.52)	1.58 (2.15)	1.93 (1.82)	1.60 (1.55)
EMR			0.00	3.02 (3.95)	3.46 (3.16)	4.04 (3.51)	3.10 (3.31)	3.24 (3.18)
ESA				0.00	3.31 (2.97)	3.38 (3.34)	3.39 (3.14)	3.29 (2.99)
JPL					0.00	1.86 (2.35)	1.83 (2.05)	1.56 (1.81)
UPC						0.00	2.63 (2.55)	2.24 (2.37)
EG							0.00	0.76 (2.08)
EQ								0.00

the resulting differences between each product pair. Let us point out that we performed neither a spatial nor a temporal interpolation of the IONEX data in order not to change the original state of the individual TEC products. In other words, we merely analyzed the differences of TEC values referring to well-defined grid points and to the times 01:00, 03:00, 05:00, ..., 23:00 UT. Note that the spatial spacing of IGS IONEX data is  $2.5^\circ$  in latitude and  $5^\circ$  in longitude (see Figures 4.11 and 4.12).

Table 6.5 gives the resulting “triangular matrix” of the standard deviations between TEC grid values extracted in the vicinity of  $(\beta, \lambda) = (+50^\circ, +7.5^\circ)$ , considering global and regional TEC products from August 28, 1998 to January 31, 1999. By far the smallest standard deviation with 1.08 TECU resulted between the COD(Z1) and the JPL TEC values, disregarding that of 0.76 TECU between the highly correlated “ambiguity-free” COD(EG) and “ambiguity-fixed” COD(EQ) values. It is worth mentioning that each standard deviation in Table 6.5 gives an average standard deviation based on all differences, taking into account one offset per product pair. The COD(Z1)-JPL offset, e.g., was obtained to be  $-4.33$  TECU. Our IONEX data comparison program also computed the standard deviations and offsets referring to 01:00, 03:00, 05:00, ..., 23:00 UT. In this way, we could observe that the standard deviation was usually minimal in the early morning and maximal in the early afternoon. As an example, the COD(Z1)-JPL standard deviation varied between 0.77 and 1.12 TECU, the time-related offset between  $-3.71$

Table 6.6: Adjusted standard deviations giving the accuracy of different TEC products for locations in Western Europe, from August 28, 1998 to January 31, 1999.

AC	RMS (TECU)
COD(G1)	1.41
COD(Z1)	0.84
EMR	2.89
ESA	2.69
JPL	1.26
UPC	1.98
COD(EG)	1.61
COD(EQ)	1.31

and  $-5.16$  TECU.

Finally, we computed the standard deviations of the TEC values referring to the eight TEC products considered. We used the same procedure explained in the previous section. Because of the high correlation between the COD(EG) and the COD(EQ) product, the corresponding variance was excluded from the adjustment. Table 6.6 lists the resulting standard deviations. The COD(Z1) TEC estimates yielded the best estimates above the European continent. Their RMS accuracy was assessed to be 0.84 TECU. It is nice that the positive impact of ambiguity resolution on the absolute TEC determination can be seen (when using double differences): the quality of the COD(EQ) TEC estimates was estimated to be approximately 20 percent better than that of COD(EG) estimates. This quality is comparable to that of JPL TEC estimates. The good ranking of the “double-difference” TEC products COD(G1), COD(EG), and COD(EQ) shows once more that these products are competitive with “zero-difference” products above a dense ground network. Table 6.5 contains in parentheses the standard deviations deduced from the adjusted standard deviations of Table 6.6.

### 6.3 Comparing CODE With JPL Global TEC Maps

This comparison of TEC maps produced by JPL and ourselves (CODE) were made to reveal possible inconsistencies between both TEC products and to furthermore clarify weaknesses of GPS-derived global TEC maps.

For this purpose, we took the COD(Z1) and JPL series of 2-hourly IONEX grid maps and computed for each individual grid point the mean difference as well as the standard deviation of the correspondingly reduced differences. As a result, we obtained 12 global maps of mean differences and 12 maps of standard deviations, referring to 01:00, 03:00,

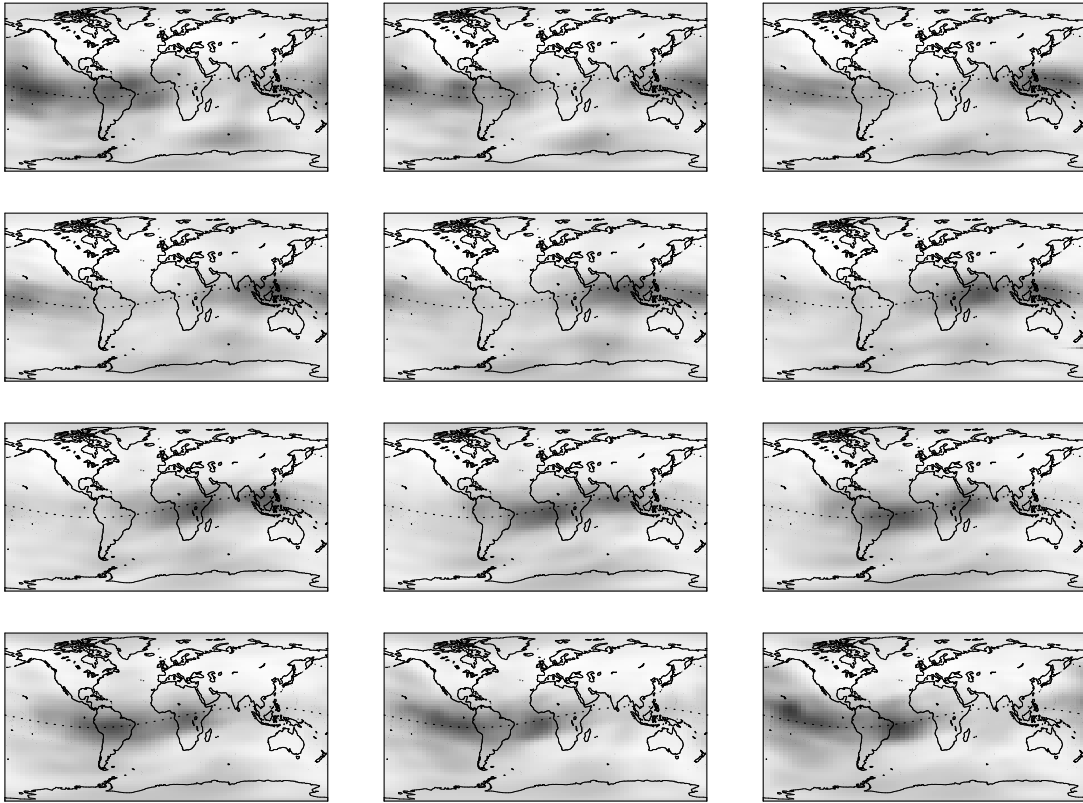


Figure 6.8: Global maps of the standard deviation between COD(Z1) and JPL GIMs referring to 01:00, 03:00, 05:00, ..., 23:00 UT each, from August 28, 1998 to January 31, 1999.

05:00, ..., 23:00 UT each. In this way we analyzed a time series of GIMs starting on August 28, 1998 and ending on January 31, 1999, which corresponds to a time interval of more than five months.

The standard deviations related to the grid points range from 0.68 TECU to about 14 TECU. Under the assumption that both TEC products have a similar accuracy, one may divide these standard deviations by  $\sqrt{2}$  to get an assessment of the individual accuracy. Figure 6.8 shows the resulting 12 global maps of the standard deviation between COD(Z1) and JPL GIMs. A gray-scale bar is provided in Figure 6.9 showing the 13:00-UT map. The darker the shading, the larger is the standard deviation. The standard deviation is small over regions with a dense station coverage, like North America, Europe, and Australia. It is generally quite large, however, in regions where no stations are located and in the equatorial zone. The weakness of the “equatorial” receivers in the IGS network is partly responsible for this observation (see section 4.6). Also, it is not amazing that

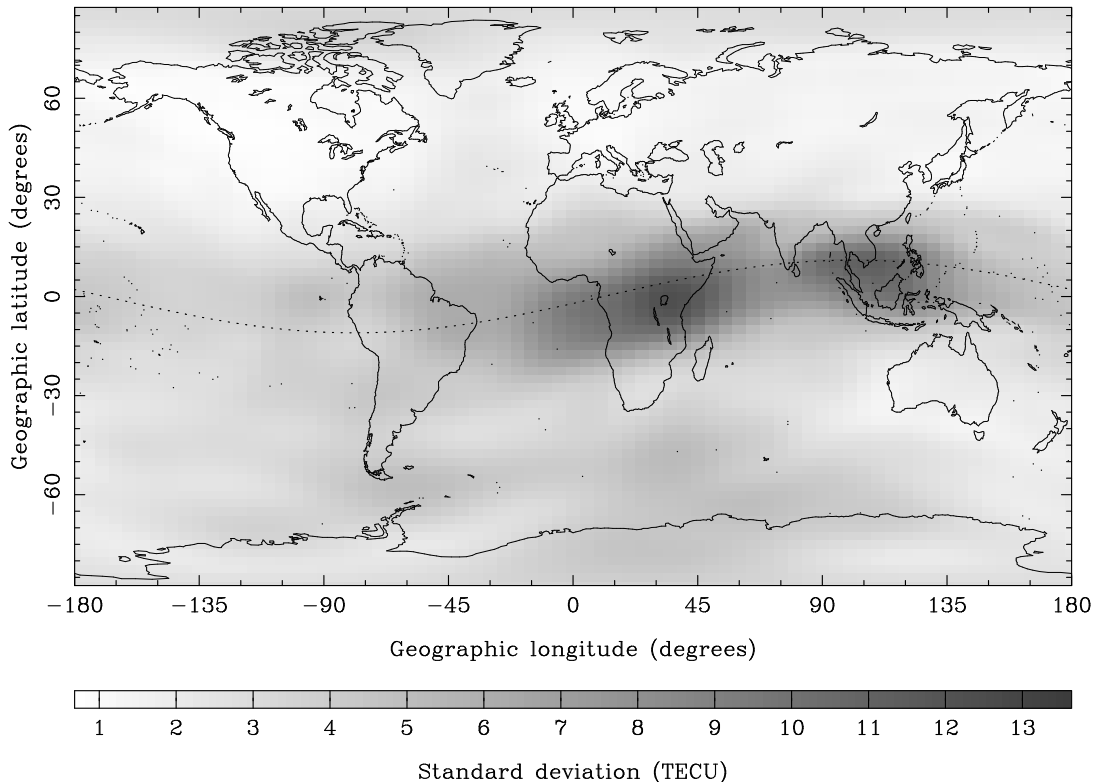
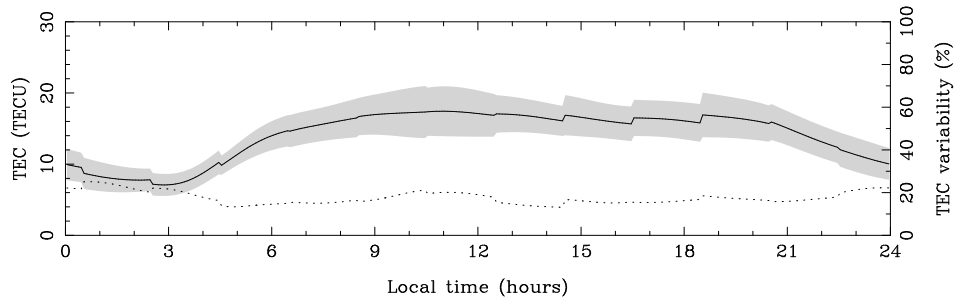


Figure 6.9: Global map of the standard deviation between COD(Z1) and JPL GIMs referring to 13:00 UT each, from August 28, 1998 to January 31, 1999.

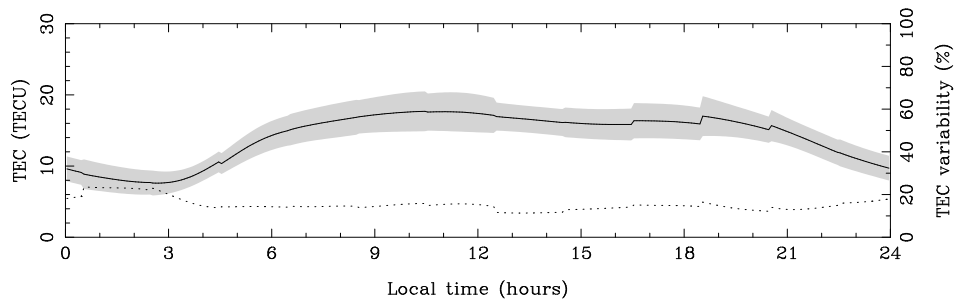
the standard deviation is higher in regions and at times where the Sun is close to the zenith, keeping in mind that the dynamics of the ionosphere is very pronounced under such circumstances.

Finally, we have to take into account that neither CODE nor JPL use all available stations to derive GIMs. Whereas JPL presently manages up to 100 stations (for ionospheric mapping), CODE has an upper limit of 80 stations in its zero-difference processing. This limit comes from restrictions due to the satellite and receiver clock parameter estimation. The 80 stations used by CODE are, by the way, not selected to optimize the global coverage. It is important to mention, however, that we could considerably increase the upper station limit in our TEC and DCB parameter estimation. Global ionospheric mapping obviously asks for using as many stations as possible.

In the same way, we also compared COD(G1) with JPL GIMs. The resulting standard deviations lie between 0.87 and 25 TECU. The comparison between the CODE GIMs Z1 and G1 yielded standard deviations between 0.83 and 19 TECU. We therefore conclude that COD(G1) GIMs, our currently official TEC product, is inferior in quality to



(a) Z1 solutions



(b) G1 solutions

Figure 6.10: Day-to-day TEC variability at  $(\beta, \lambda) = (50^\circ, 7.5^\circ)$  derived from Z1 or G1 solutions of June 1998.

the COD(Z1) GIMs which yielded standard deviations of 0.68–14 TECU compared to the JPL GIMs. Nevertheless, it is important to point out that the quality of G1 TEC estimates above dense ground networks is in no way inferior to that of Z1 estimates. This is clearly confirmed by Figure 6.10, which gives the day-to-day TEC variability, computed according to (4.5), for a location in Western Europe (see section 4.4.2). The TEC profiles based on the G1 solutions show even a smaller day-to-day variability than those produced with the Z1 solutions. This indicates that the TEC measurement noise related to the G1 solutions is not markedly larger above a dense ground network.

For completeness, we give the standard deviations of the GIMs produced by EMR, ESA, and UPC with respect to those produced by JPL. We obtained 1.35–13 TECU for EMR-JPL, 1.16–15 TECU for ESA-JPL, and 0.87–65 TECU for UPC-JPL. Note that UPC GIMs sometimes contain unreasonably high TEC values invalidating the standard deviation.

The overall mean difference (or offset) between COD(Z1) and JPL GIMs was obtained



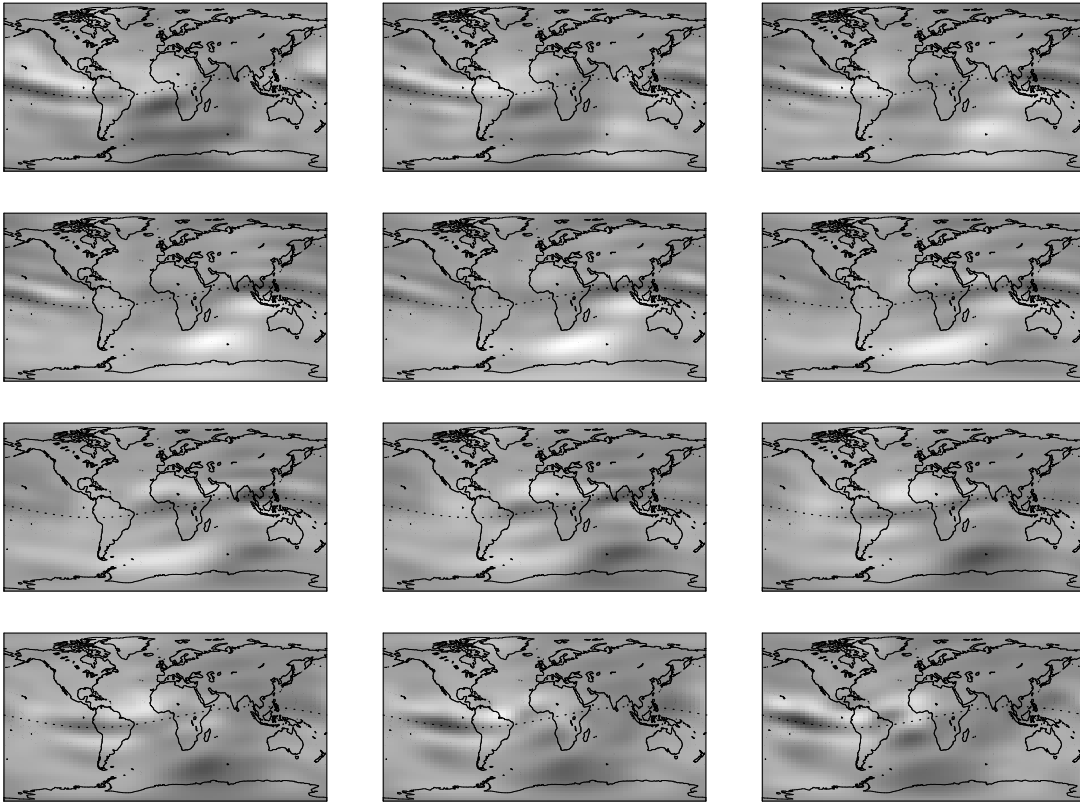


Figure 6.11: Global maps of the difference between COD(Z1) and JPL GIMs referring to 01:00, 03:00, 05:00, ..., 23:00 UT each, from August 28, 1998 to January 31, 1999.

to  $-4.61$  TECU. This offset is confirmed by the values in Table 6.1. Let us inspect the systematic differences in more detail. Figure 6.11 shows the 12 global difference maps associated with the 12 global standard deviation maps in Figure 6.8. Figure 6.12 shows the 13:00-UT map of Figure 6.11 and includes a corresponding gray-scale bar. The differences may reach about  $\pm 13$  TECU, after subtracting the overall offset of  $-4.61$  TECU. A light shading indicates a negative difference, that is, COD(Z1) GIMs underestimate the TEC (or JPL GIMs overestimate the TEC). Accordingly, a dark shading indicates a positive difference.

Whereas the degree of the shading over North America, Europe, and Australia is more or less constant from one map to another, there are regions where the shading considerably changes between maps referring to different solar times. Regions where no—or only isolated—stations are located show such a behavior. They often may be associated with the oceans. Big differences may be attributed to different assumptions made by CODE

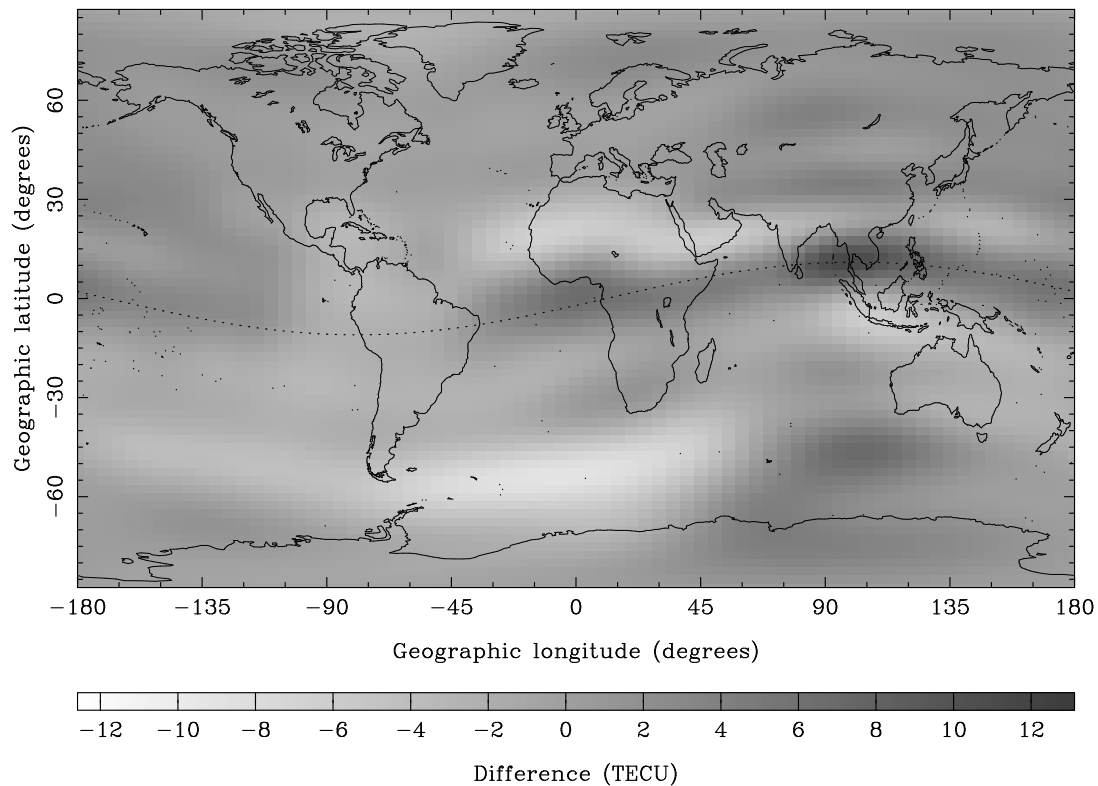


Figure 6.12: Global map of the difference between COD(Z1) and JPL GIMs referring to 13:00 UT each, from August 28, 1998 to January 31, 1999.

and JPL concerning the spatial and temporal TEC development. Another interesting feature is indicated by the light-dark-light structure in the TEC difference moving along the geomagnetic equator (dotted line). This feature is probably caused by the limited spatial resolution of the COD(Z1) GIMs in latitude. This lack of spatial resolution may lead to both an underestimation of the two crest regions of the equatorial anomaly and an overestimation of the “valley” in between. We might address this problem by increasing the maximum degree of our SH expansion.

Let us finally point out that inconsistencies in terms of absolute calibration cannot completely be removed by taking into account offsets or even maps of differences. In view of these difficulties mainly caused by different mapping functions used, absolute calibration problems should be addressed by each ionosphere AC.

## 6.4 Correlation of TEC With Solar Parameters

As the Sun is the primary “driving element” for the production of free electrons in the Earth’s ionosphere, the correlation of the global TEC level with parameters used to describe the solar activity is expected to be significant. Let us therefore study the correlations between

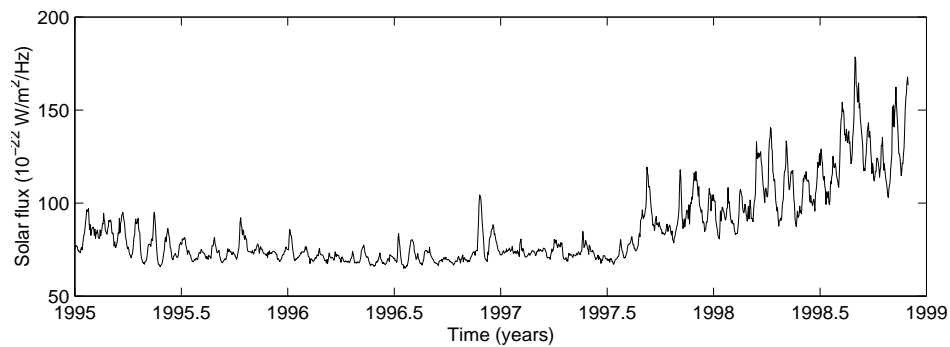
- mean TEC,
- maximum TEC (both from our GPS data analysis),
- solar flux, and
- sunspot number (both from *NGDC* [1998]).

The Sun emits radio energy with a slowly varying intensity. This radio flux changes gradually from day to day in response to the number of sunspots on the surface of the Sun. Solar flux density at 2800 MHz has been recorded routinely by the Ottawa radio telescope since 1947. Each day, values are determined at local noon and then corrected to within a few percent for factors such as antenna gain, atmospheric absorption, and background sky temperature. Beginning in 1991, the solar flux density is measured in Penticton, Canada.

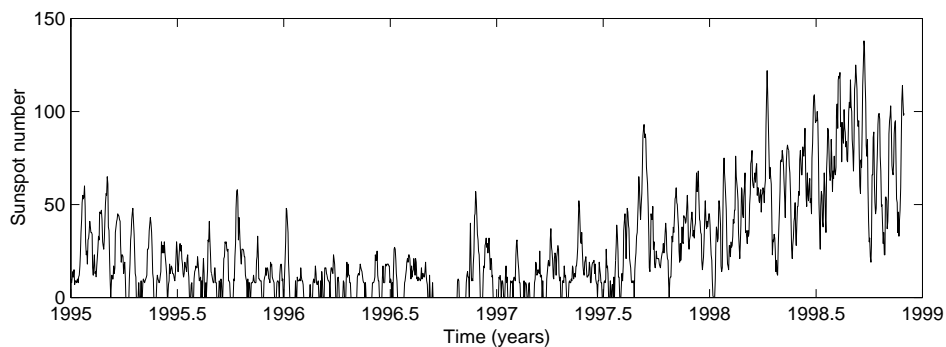
Figure 6.13 shows the Penticton 10.7-cm solar flux and the international sunspot number from January 1995 to November 1998, as obtained from *NGDC* [1998]. One usually distinguishes between “observed” and “adjusted” solar flux. Observed solar flux contains fluctuations as large as 7% that arise from the changing sun-earth distance. It influences to the same extent the production rate of free electrons in the ionosphere. In contrast, adjusted solar flux has this variation removed. It corresponds to the energy flux that would be received by a detector located at the mean sun-earth distance and is hence of interest for studying the flux on an absolute level. The solar flux we give in Figure 6.13 and the following is always the “observed” one.

We assume that the semi-annual variation in our global TEC values may be attributed to an earth-related phenomenon (see section 4.3.1). Figure 6.14 shows the “reduced” mean TEC  $\bar{E}'$  where this semi-annual term was removed for the same time period (January 1995 to November 1998).

Let us start with the hypothesis that the TEC of the ionosphere is responding with a certain lag to the solar excitation. We therefore compute the correlation coefficient (6.8) between two time series which are shifted against each other by a given number of days. The lag yielding the highest correlation is considered to be the true lag. Figure 6.15 shows the correlation coefficients of solar flux  $\phi_{\text{obs}}$  and sunspot number  $R$  relative to the reduced mean TEC  $\bar{E}'$ . The correlation coefficients are given for lags between  $-10$  and  $+10$  days. The correlation coefficients without shifting the time series is 0.892 for solar flux and



(a) Solar flux



(b) Sunspot number

Figure 6.13: Solar flux and sunspot number, from January 1995 to November 1998 [NGDC, 1998].

0.772 for sunspot number. When assuming a lag of 1 or 2 days, however, the correlation coefficients are significantly higher, 0.897 and 0.778, respectively. We therefore conclude that the global TEC level generally follows the solar activity level with a time-lag of about 1–2 days. Note that the corresponding lag vanishes when comparing solar flux and sunspot number in the same way.

Figure 6.16 shows the solar flux and sunspot number versus the reduced mean TEC to get a better impression of the correlation, assuming a lag of 1 day for the TEC level with respect to the solar activity level. The correlation of the mean TEC reduced by the semi-annual component with the observed Penticton 10.7-cm solar flux with  $r = 0.897$  is significant.

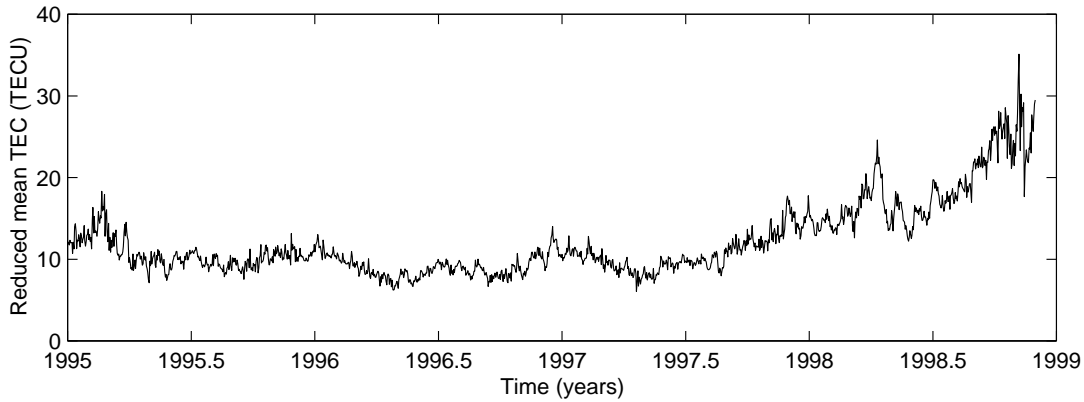


Figure 6.14: Reduced mean TEC  $\bar{E}'$  (without semi-annual component) determined by CODE, from January 1995 to November 1998.

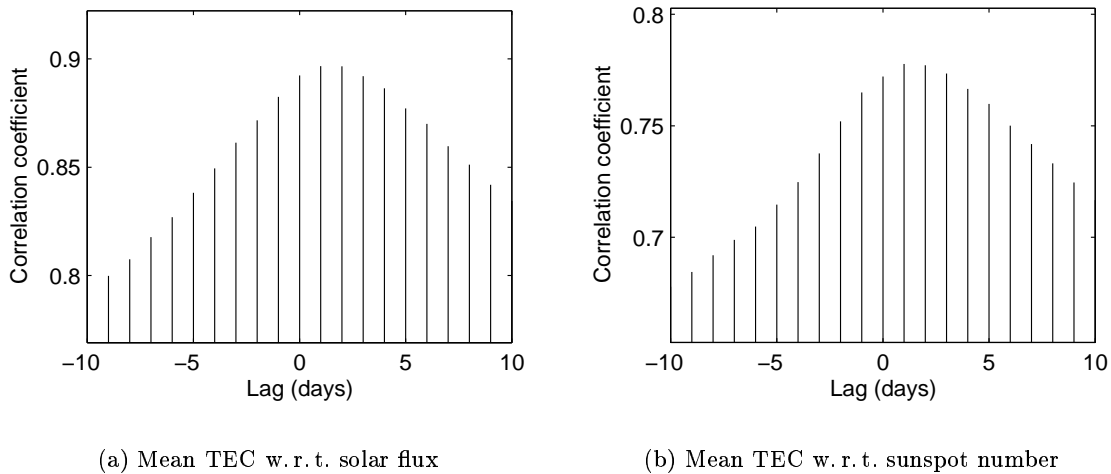


Figure 6.15: Correlation coefficients of reduced mean TEC  $\bar{E}'$  with respect to solar flux  $\phi_{\text{obs}}$  and sunspot number  $R$ , for lags between  $-10$  and  $+10$  days.

In Table 6.7, we give the correlation coefficients for all possible combinations of TEC and solar activity parameters such as mean TEC  $\bar{E}$ , reduced mean TEC  $\bar{E}'$ , maximum TEC  $E_{\text{max}}$ , reduced maximum TEC  $E'_{\text{max}}$ , observed solar flux  $\phi_{\text{obs}}$ , adjusted solar flux  $\phi_{\text{adj}}$ , and sunspot number  $R$  according to relation (3.8). Note that the correlation coefficients

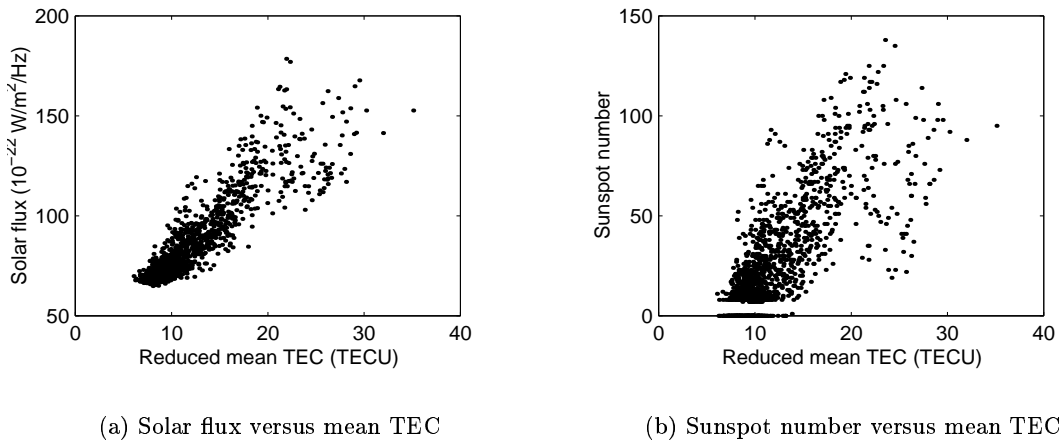


Figure 6.16: Solar flux  $\phi_{\text{obs}}$  and sunspot number  $R$  versus reduced mean TEC  $\bar{E}'$ , from January 1995 to November 1998.

Table 6.7: Correlation coefficients between mean TEC  $\bar{E}$ , maximum TEC  $E_{\text{max}}$ , observed solar flux  $\phi_{\text{obs}}$ , adjusted solar flux  $\phi_{\text{adj}}$ , and sunspot number  $R$ . Note that a dash indicates the removal of a semi-annual component.

	$\bar{E}$	$\bar{E}'$	$E_{\text{max}}$	$E'_{\text{max}}$	$\phi_{\text{obs}}$	$\phi_{\text{adj}}$	$R$
$\bar{E}$	1.000	0.960	0.946	0.903	0.874	0.854	0.750
$\bar{E}'$		1.000	0.878	0.942	0.897	0.873	0.778
$E_{\text{max}}$			1.000	0.928	0.769	0.751	0.653
$E'_{\text{max}}$				1.000	0.803	0.779	0.692
$\phi_{\text{obs}}$					1.000	0.992	0.910
$\phi_{\text{adj}}$						1.000	0.914
$R$							1.000

in Table 6.7 always assumes a time-lag of 1 or 2 days when comparing an ionospheric with a solar parameter. It is nice to see that our TEC parameters actually better correlate with  $\phi_{\text{obs}}$  which still contains the annual variation caused by the changing sun-earth distance, than with  $\phi_{\text{adj}}$ . Conversely,  $R$  seems to be slightly higher correlated with  $\phi_{\text{adj}}$  than with  $\phi_{\text{obs}}$ . This is not amazing as the sunspot number provides an absolute measure in terms of solar activity. The significantly higher correlation of the reduced TEC parameters  $\bar{E}'$  and  $E'_{\text{max}}$  with solar flux  $\phi_{\text{obs}}$  and sunspot number  $R$  supports our assumption that the semi-annual component in the global TEC level has to be attributed to an earth-related

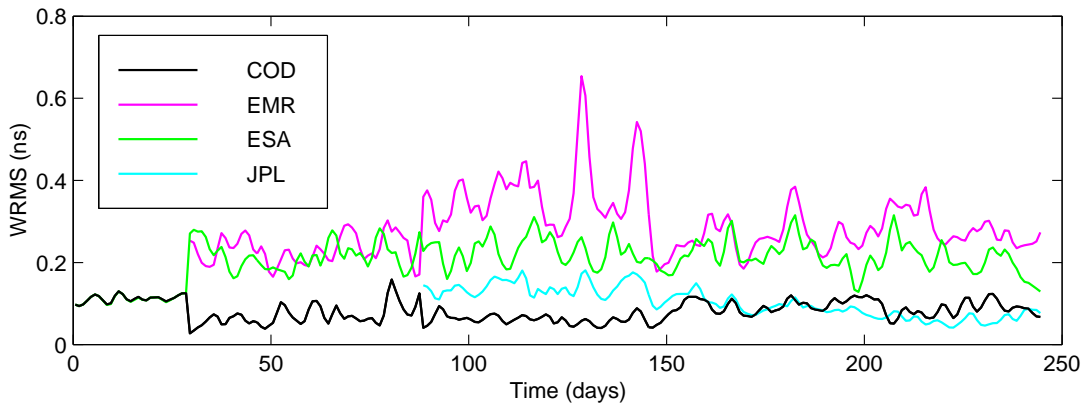


Figure 6.17: WRMS errors obtained from daily satellite DCB combinations, from June 1, 1998 to January 31, 1999.

phenomenon. The correlation between TEC parameters are, as expected, very high. The correlation coefficient between, e.g., the originally measured  $\bar{E}$  and  $E_{\max}$  reaches 0.946. No correlation could be detected between single-layer height estimates and solar parameters.

The correlation of the mean and maximum TEC with “geomagnetic indices” used to characterize the disturbance level of the geomagnetic field was studied as well. No significant correlation could be found.

## 6.5 Comparing and Combining IGS Satellite DCB Results

Four IGS ionosphere ACs supply satellite DCB values to CDDIS, namely CODE, EMR, ESA, and JPL. We therefore produced a combined set of satellite DCB values for each day, first giving equal weights to all contributions. Offset parameters to align the individual sets to a common reference were included in this adjustment as well. Group RMS errors related to each AC were computed and subsequently used to derive a weighted combination of DCB values. This second adjustment finally yields RMS errors which we call weighted RMS (WRMS) errors. These errors are an indication of the consistency of the DCB estimates supplied by the individual ACs.

This time series of WRMS errors may be inspected in Figure 6.17 over a time interval of eight months. EMR was excluded from the combination until June 29, 1998 due to unrealistic values. JPL began to supply IONEX data starting with August 28, 1998. Therefore, only two contributions were available for the first 29 days, what made a discrimination impossible. The WRMS errors referring to the subsequent days, however,

Table 6.8: Mean RMS and WRMS errors obtained from daily satellite DCB combinations, from August 28, 1998 to January 31, 1999.

AC	RMS (ns)	WRMS (ns)	Repeatability (ns)
COD(Z1N)	0.127	0.085	0.081
EMR	0.278	0.325	0.248
ESA	0.212	0.229	0.191
JPL	0.155	0.112	0.056

clearly indicate that the satellite DCB values determined by CODE and JPL perform best. They are consistent on a level of about 0.1 nanoseconds. Note that the curves in Figure 6.17 were slightly smoothed to make them more readable.

Table 6.8 summarizes the mean RMS and WRMS errors referring to the time interval where four contributions were available. For CODE, the DCB series based on station-specific TEC representations was considered. The last column of this table includes the day-to-day repeatability of the satellite DCB estimates, computed according to (4.6). Unlike the WRMS error, this repeatability only gives the AC-internal consistency. In general, WRMS and repeatability agree quite well. The fact that the outstanding repeatability of JPL's estimates is not adequately approved by our combination might be an indication that there is still an inconsistency between JPL and the other ACs. In this context, we should mention that the COD(Z1N) DCB results are derived completely independently each day, whereas the JPL daily DCB estimates are to a certain extent correlated from day to day through TEC constraints also present between subsequent days.

In addition, a series of DCB combinations was performed replacing the COD(Z1N) series by the GIM-based COD(Z1) series (see section 4.2). This led to an RMS and WRMS of 0.130 and 0.088 nanoseconds, respectively. The errors related to the other three ACs did not change significantly. The repeatability of COD(Z1) DCB estimates was obtained to be 0.102 nanoseconds. We thus conclude that the COD(Z1) and COD(Z1N) are roughly of the same quality. Last but not least, let us mention that the day-to-day repeatability of the combined DCB values resulted in 0.076 nanoseconds.



## 7. Summary, Conclusions, and Outlook

The global IGS (International GPS Service) polyhedron of permanently tracking dual-frequency GPS receivers provides a unique opportunity to derive highly accurate GPS satellite orbits, earth orientation parameters, satellite and receiver clock corrections, station coordinates and velocities, and, constantly gaining in importance, information about the Earth's atmosphere. In our analysis we studied the problems dealing with the extraction of information about the *ionosphere* using ground-based GPS/GLONASS tracking data.

Since January 1, 1996, we routinely produce daily maps of the global total electron content (TEC) distribution as part of the IGS data processing performed at the Center for Orbit Determination in Europe (CODE). These global ionosphere maps (GIMs) are derived from the same data set of doubly differenced carrier phase measurements also used for the determination of the CODE core products delivered to the IGS. To derive the ionospheric product, however, we have to analyze the so-called geometry-free linear combination, which primarily contains ionospheric information, as opposed to the ionosphere-free linear combination, which contains the "geometrical" information and practically eliminates the influence of the ionospheric refraction (ignoring higher-order terms). At present (March 1999), the GPS tracking network processed at CODE consists of more than 140 globally distributed stations.

The CODE GIMs are represented by a spherical harmonic expansion referring to a solar-geomagnetic frame, because the global TEC distribution is relatively stationary in that frame. After reprocessing all 1995 IGS data, an uninterrupted time series of daily GIMs covering a time span of more than 4 years became available and was analyzed here.

Our GIM series reveals pronounced annual and semi-annual variations in the mean TEC (see Figure 7.1). We notice maxima at equinoxes and minima at solstices. The recent period of minimum ionospheric activity was observed in summer of 1996. We furthermore notice pronounced short-term variations caused by sunspot groups randomly developing and vanishing. These fluctuations show typically periods around 27 days, associated with the rotation of the Sun. The striking ups and downs of the ionospheric activity during the latest months are caused by sunspot groups which are located in selective solar

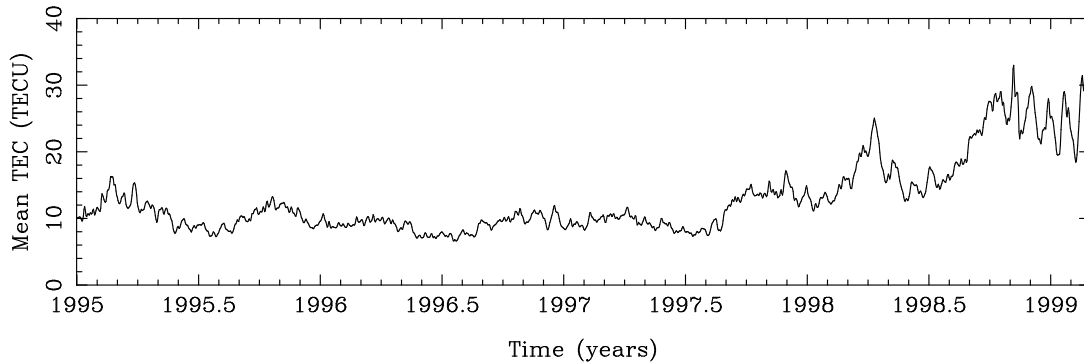


Figure 7.1: Mean vertical TEC of the Earth's ionosphere computed by CODE, from January 1995 to February 1999.

longitudes. The correlation of the CODE mean TEC level with the Penticton 10.7-cm solar flux measurements with a value of almost 0.90 proved to be very significant. In this context, we observed that the global TEC level tends to follow the solar excitation with a time-lag of 1–2 days. Finally we could demonstrate—based on a spectral analysis of low-order sectorial spherical harmonic coefficients—that there is an impact of the Moon on the ionosphere. We could detect significant TEC waves which follow the lunation cycle of about 29.53 days. Considered in an earth-fixed frame, this period corresponds to the well-known tidal cycle of about 12 hours 25 minutes. This confirms once more that a representation of the global TEC distribution by a spherical harmonic expansion has its advantages.

Based on a variance-covariance analysis studying the contribution of both phase and code measurements for high-quality absolute TEC determination, we concluded that the essential contribution stems from to phase measurements. Code measurements only contribute in a significant way for retrieving differential code biases (DCBs) of satellites and receivers. DCBs give the interfrequency difference of the instrumental P1 and P2 code biases. We described in detail how satellite DCB information may be used to make precise satellite clock values consistent with, e. g., C/A code measurements. We pointed out that one cannot avoid to determine and monitor satellite-specific code biases between C/A and P1 code measurements as well, in particular when striving for a consistent IGS satellite clock product.

Since October 1997, GIMs are concurrently derived from one-way phase measurements leveled to code measurements. The satellite DCB estimates obtained as a by-product of the “zero-difference” TEC determination show a day-to-day repeatability on the level of 0.08 nanoseconds. The annual variation in our satellite DCB estimates is not yet explained. Looking for possible causes, we discussed the effect of mismodeled interfrequency satellite antenna offsets in the “geometry-free” linear combination. First attempts

---

solving for differential satellite antenna offset parameters as part of the daily TEC determination indicated that the nadir offset parameter is formally determined with an accuracy of about one centimeter, the offsets perpendicular to the nadir axis may be determined even more accurately. As the offsets between the L1 and L2 satellite antenna phase centers may be significant, especially of the new, Block-IIIR spacecrafts, we intend to regularly derive such offset parameters in the future. It is questionable whether it is beneficial to increase the temporal resolution of DCB parameters. Once-per-revolution terms for satellites or diurnal terms for receivers might give further insights.

In March 1998, the temporal resolution of our GIM representation was considerably increased from 24 hours to 2 hours. In order to prevent unreasonable TEC estimates in regions where no stations are located, the variations between consecutive GIM parameters are limited using relative a priori constraints.

In addition to the global ionosphere products, regional TEC maps for Europe are routinely derived from double-difference data since October 1995. The “ambiguity-free” TEC maps are used to improve QIF (quasi-ionosphere-free) ambiguity resolution. “Ambiguity-fixed” maps are subsequently computed.

Since June 1, 1998, five IGS ionosphere analysis centers, among them CODE, supply global TEC maps as well as satellite DCB values in the IONEX (IONosphere map EXchange) format to the Crustal Dynamics Data Information System (CDDIS), a global data center of the IGS. IONEX, an international format for the exchange of ionosphere maps, was developed by the IGS ionosphere working group and approved by the IGS community. This interface allowed us to compare CODE TEC and satellite DCB results with those supplied by the other four IGS ionosphere analysis centers.

A five-month comparison of the mean TEC values derived from each IGS TEC product showed that there are still marked inconsistencies in terms of absolute calibration between the individual products. The differences in the mean TEC reached values up to about 5 TECU and may be attributed mainly to different mapping functions used. Nevertheless, some TEC products, among of them our “zero-difference” product, have rather small standard deviations below one TECU relative to the mean TEC values. Three products seem to reflect even subdaily fluctuations, which might be correlated with solar bursts, geomagnetic disturbances, etc.

We furthermore clarified weaknesses of GPS-derived global TEC maps by comparing the maps produced by the JPL (Jet Propulsion Laboratory) group and CODE. Systematic differences could be noticed especially above regions where no stations are located. They may be attributed to different assumptions made by the two groups concerning the spatial and temporal TEC development. The standard deviations between both TEC products range from approximately 0.7 to 14 TECU. The fact that most “equatorial” receivers in the IGS network considerably suffer from the increased ionospheric activity and frequently loose track of satellites during local noon hours may be partly responsible for large standard deviations in the equatorial zone.

Therefore, it does not make sense to assess the quality of GPS-derived GIMs by computing differences between different GIMs over the entire globe. Based on our analyses we propose that the IGS ionosphere combination center should restrict comparisons to regions with a certain density of stations, at least at the current stage.

We compared the TEC values of eight different TEC products, consisting of five “zero-difference” and three “double-difference” products, among them our two regional products, above Western Europe. We analyzed five months of IONEX data (September 1998 to January 1999). The CODE “zero-difference” TEC estimates yielded the best estimates above the European continent with an accuracy of approximately 0.8 TECU. The good ranking of the “double-difference” TEC products showed that these are competitive with “zero-difference” products above a dense ground network. In addition, the positive impact of ambiguity resolution on the absolute TEC determination could be seen: the quality of “ambiguity-fixed” TEC values was estimated to be approximately 20 percent better than that of the “ambiguity-free” solutions. It is a substantial advantage of the geometry-free linear combination that it eliminates satellite and receiver clock offsets already on the zero-difference level, unlike, e. g., the ionosphere-free linear combination, which eliminates these offsets just on the double-difference level. When analyzing the geometry-free linear combination there is no disputing that the information loss through the data differencing is detrimental, particularly above isolated stations.

Based on our validation studies, we favor our “zero-difference” GIMs. We intend to deliver these GIMs to CDDIS and to resubmit our entire “zero-difference” GIM series. As global ionospheric mapping asks for using as many stations as possible, we plan to eliminate the station number limit. We furthermore plan to increase the spatial resolution of our GIM representation and to avoid discontinuities at the day boundaries by, e. g., connecting consecutive daily ionospheric solutions on the normal equation level, eventually modeling the TEC and DCB parameters as piece-wise linear functions—instead of piece-wise constant functions.

An eight-month comparison of the satellite DCB results produced by four IGS ionosphere analysis centers indicated that our daily sets of DCB values are consistent with the daily combined sets on a level of 0.1 nanoseconds. At CODE we certainly benefit from the fact that the generation of our ionospheric solutions is fully integrated in the IGS data processing scheme. Consequently, a reliable data screening analyzing the ionosphere-free linear combination is always assured. In the zero-difference data processing, we have the medium-term goal to no longer process phase-smoothed code measurements but phase and code measurements simultaneously. Introducing previously resolved double-difference ambiguities would be the ultimate goal for zero-difference solutions.

Starting with October 11, 1998, the CODE analysis center is generating precise GLO-NASS satellite orbits as part of the IGEX (International GLONASS EXperiment) campaign using the latest version of the Bernese GPS Software which allows to process GLO-NASS code and phase measurements—simultaneously with GPS data. In this environment, we gained experience concerning the DCB and TEC determination by processing

---

data of combined GLONASS/GPS receivers. The GPS and GLONASS data processing at CODE shall be merged into one combined solution in the near future.

When getting closer to the next solar maximum the knowledge of the state of the ionosphere becomes more and more important. The access to rapid and up-to-date TEC information is required for many applications. For this reason, the CODE rapid GIMs, usually available well before 12:00 UT of the subsequent day, are applied by more and more users. These GIMs are not only used for traditional GPS data processing but also for altimetry [*Enninghorst and Rentsch, 1998*], for time transfer using common view techniques, etc. We intend to switch to a zero-difference solution for our rapid ionosphere product, as well.

The most recent CODE rapid and final GIMs may be found in a graphic form on the ionosphere-related CODE WWW site (<http://www.cx.unibe.ch/aiub/ionosphere.html>). In addition, a figure similar to Figure 7.1 is automatically updated every day. It includes, moreover, a one-year prediction of the mean TEC. Beginning in June 1998, one-day and two-day predicted GIMs are generated based on a least-squares collocation which is performed for each spherical harmonic coefficient of the global TEC representation. Predicted TEC information might be of interest for real-time applications. We presented autocovariance functions as part of our prediction apparatus. It might be an alternative to predict TEC maps based on a series of IONEX grid maps applying the same mathematical principles as for analyzing the coefficients of the spherical harmonic expansion. In such a case, a prediction step would be needed for each grid point of interest. Because the GPS broadcast ionosphere model is well-established within the GPS user community, it would also make sense to fit the associated eight parameters to our predicted GIMs and to make them available through the Internet.

In view of the progress made in GPS-based ionospheric mapping, a reprocessing of the IGS data as of 1995, 1994, 1993, or even 1992 becomes more and more important. Such a reprocessing would be beneficial to all other, non-ionospheric CODE products, as well.

It is our goal to map the ionosphere for at least the next period of high solar activity and to study in particular the impact of the ionosphere (including that of the higher-order terms) on the IGS core products. The establishment of an official IGS ionosphere product is another reason to continue with these efforts. All presented results are available upon request.

Let us mention that the solar eclipse taking place on August 11, 1999 will offer a unique opportunity to demonstrate the power of the GPS for mapping the TEC. As the zone of totality crosses Europe, the dense portion of the IGS network provides excellent conditions for monitoring this eclipse.

In our analysis we uniquely used data from ground-based GPS receivers. It easy to predict that space-borne GPS receivers on low-earth orbiters (LEOs) will revolutionize ionosphere monitoring and mapping. It will in particular be possible to obtain height-dependent profiles of the ionosphere. We expect, on the other hand, that ground-based

ionosphere monitoring will continue playing an important role to establish the total electron content.

# Acknowledgements

I would like to thank everyone who has contributed—directly or indirectly—to the realization of my Ph.D. dissertation.

I am very much indebted to PD Dr. Markus Rothacher, the head of the AIUB GPS research group and the CODE Analysis Center, for initiating me into the secrets of the Bernese GPS Software, for the numerous fruitful and inspiring discussions, and for his constructive advice.

I also would like to thank Prof. Dr. Gerhard Beutler, the supervisor and promoter of this work, for giving me the opportunity and freedom to perform this highly interesting research work, for his personal support, and for his critical but also encouraging suggestions and comments.

In addition, I would like to thank Prof. Dr. Werner Gurtner for useful discussions and proposals connected to parameter estimation issues and to the development of the IONEX format and Dr. Joachim Feltens from ESOC, the chairman of the recently established IGS Ionosphere Working Group, for the pleasant collaboration and the lively exchange of information.

Special thanks go to Timon A. Springer for this hard work connected to the automated IGS data processing every day, for many discussions, and for keeping an eye on the ionosphere-related BPE jobs. I am also grateful to Daniel Ineichen for taking charge of the daily GLONASS/IGEX data processing, and, moreover, to Erich M. Wenger, my office colleague, who will do his diploma examination by chance at the same day as my Ph.D. thesis presentation, for lots of controversial discussions concerning layout.

Finally, I express my gratitude to Gerhard Beutler and Markus Rothacher for carefully reviewing the entire manuscript. I also convey my thanks to Dr. Jan Kouba from NR-Can, former IGS Analysis Center Coordinator and visiting scientist at AIUB for several months, for reading the final version of the manuscript and for his concise remarks.

Last but not least, I would like to thank the Swiss National Science Foundation for generously supporting this work under the project number 20-47056.96.





## **Part III**

# **Appendices**



# A. Time Series of CODE Total Electron Content Parameters

## A.1 Global TEC Parameters

Figures A.1 to A.9 show the time series of CODE TEC parameters stemming from the G1 solutions (see section 4.2). The normalized SH coefficients  $\tilde{C}_{0,0}$ ,  $\tilde{C}_{1,0}$ ,  $\tilde{C}_{1,1}$ ,  $\tilde{S}_{1,1}$ ,  $\tilde{C}_{2,0}$ ,  $\tilde{C}_{2,1}$ ,  $\tilde{S}_{2,1}$ ,  $\tilde{C}_{2,2}$ , and  $\tilde{S}_{2,2}$  of (3.35) are shown in this appendix. Dots indicate the daily estimates; the solid line gives smoothed values with  $\Delta t$  set to 1 day in (4.2).

## A.2 Monthly Averaged European TEC Profiles

Figures A.10 to A.21 show European TEC profiles for 12 consecutive months based on TEC maps from EQ solutions (see section 4.2), namely from December 1997 to November 1998. The vertical TEC, given as a function of local time, is referred to a latitude of  $50^\circ$  and a longitude of  $7.5^\circ$ . The solid line indicates the monthly averaged TEC; the shaded band represents the day-to-day variability of the TEC computed according to (4.5). In addition, the dotted line gives the relative TEC variability in percent.

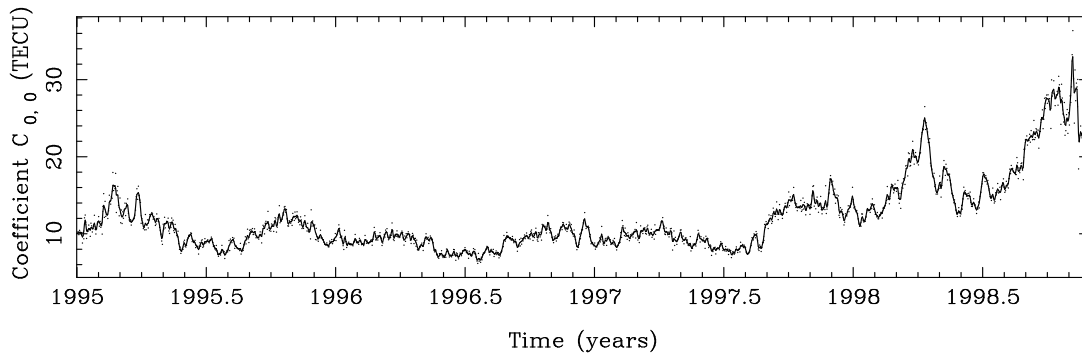


Figure A.1: SH coefficient  $\tilde{C}_{0,0}$  (or mean TEC  $\bar{E}$ ).

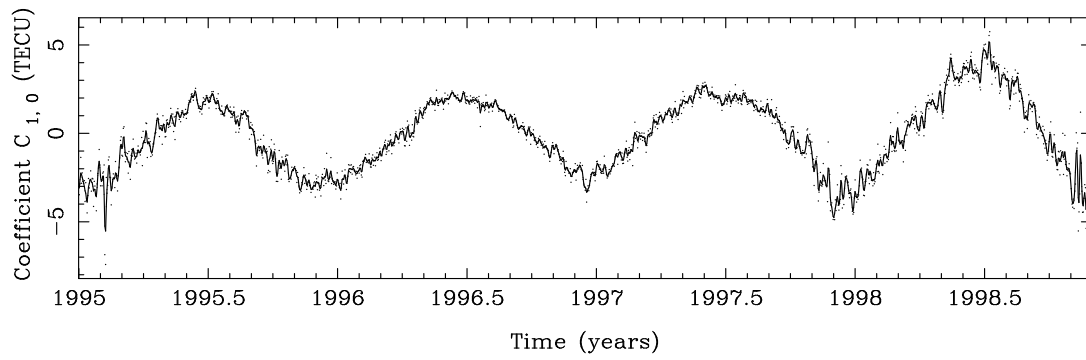


Figure A.2: SH coefficient  $\tilde{C}_{1,0}$ .

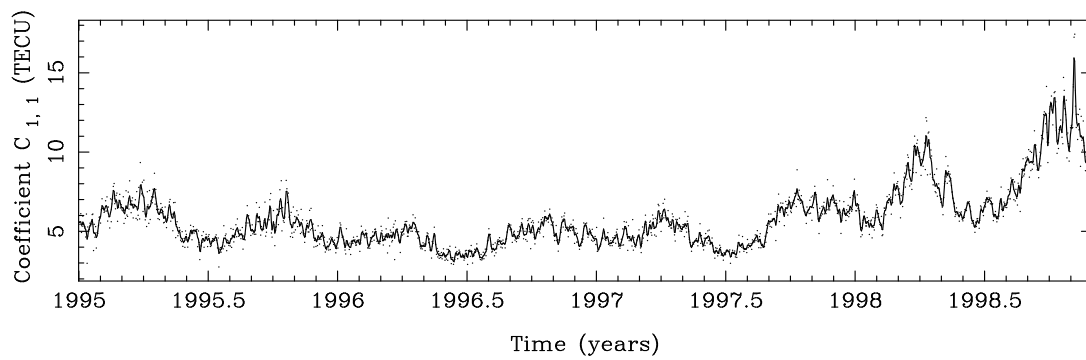


Figure A.3: SH coefficient  $\tilde{C}_{1,1}$ .

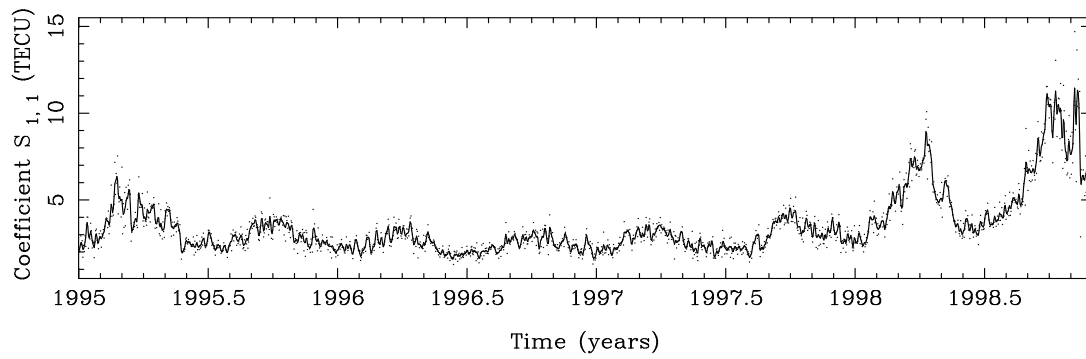


Figure A.4: SH coefficient  $\tilde{S}_{1,1}$ .

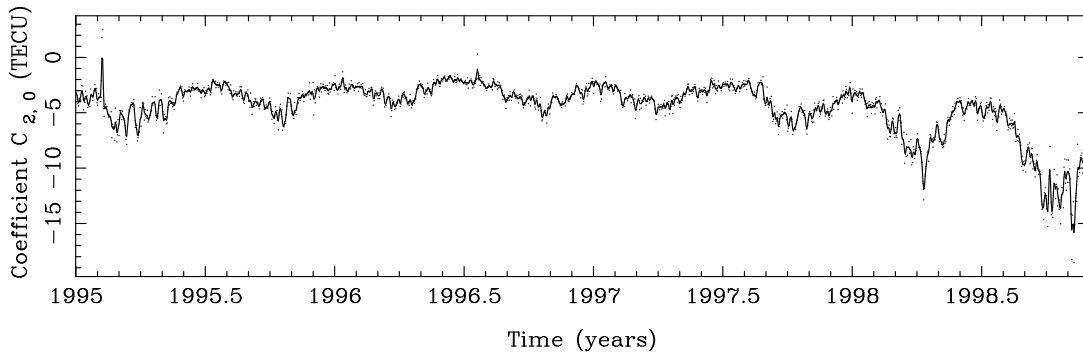


Figure A.5: SH coefficient  $\tilde{C}_{2,0}$ .

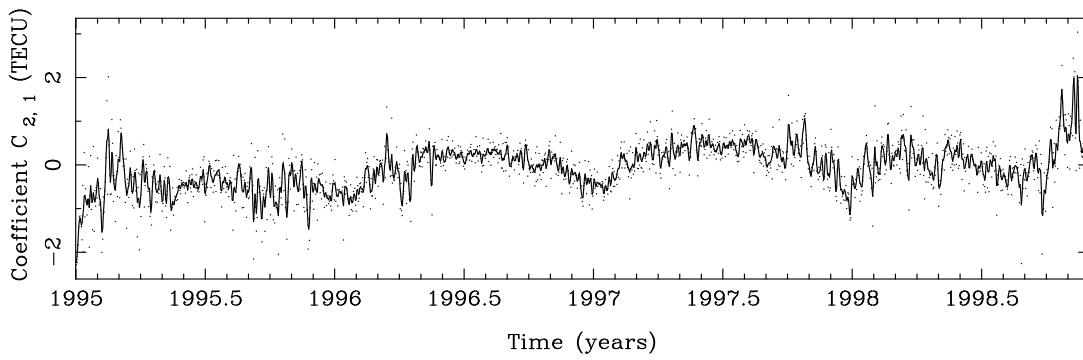


Figure A.6: SH coefficient  $\tilde{C}_{2,1}$ .

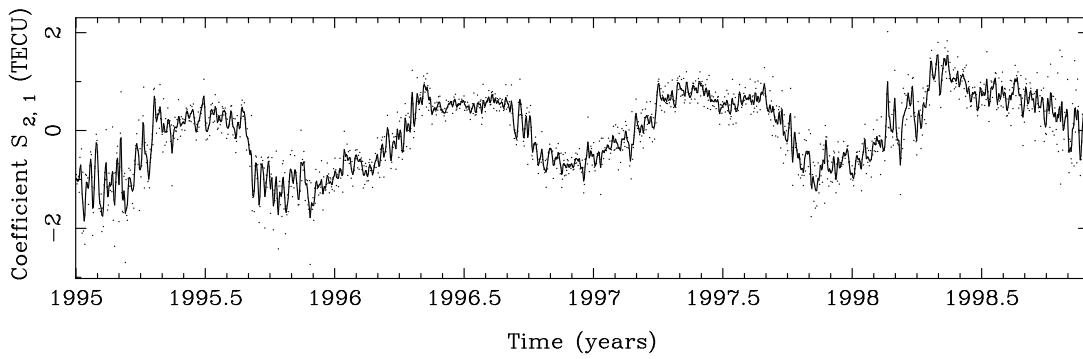


Figure A.7: SH coefficient  $\tilde{S}_{2,1}$ .

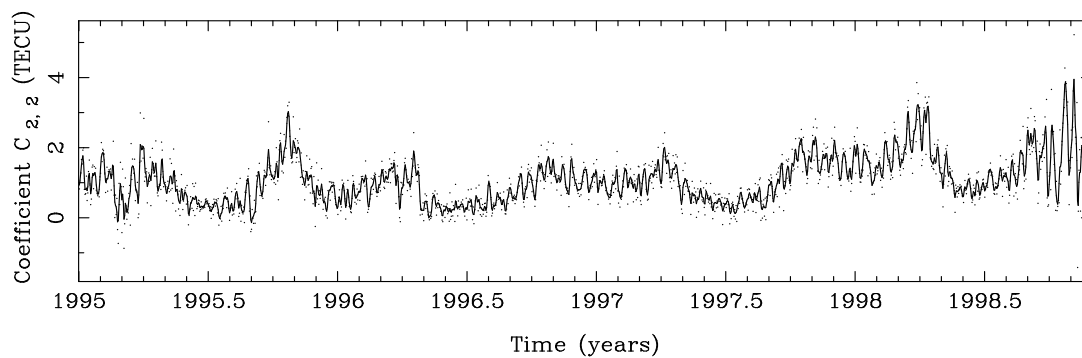


Figure A.8: SH coefficient  $\tilde{C}_{2,2}$ .

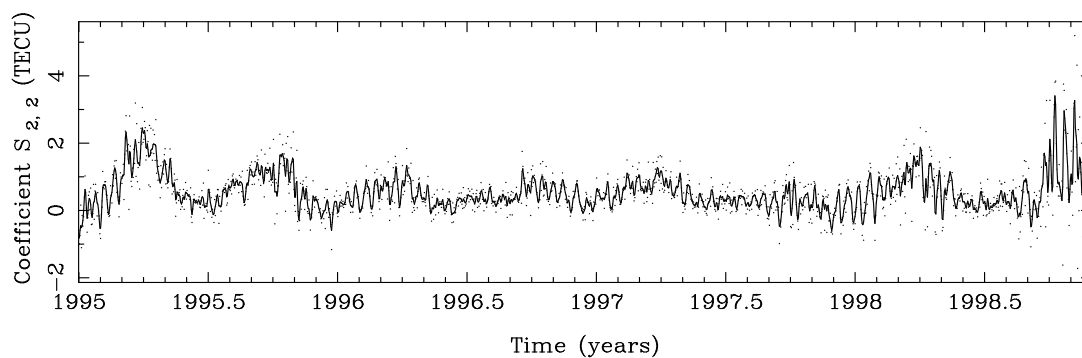


Figure A.9: SH coefficient  $\tilde{S}_{2,2}$ .

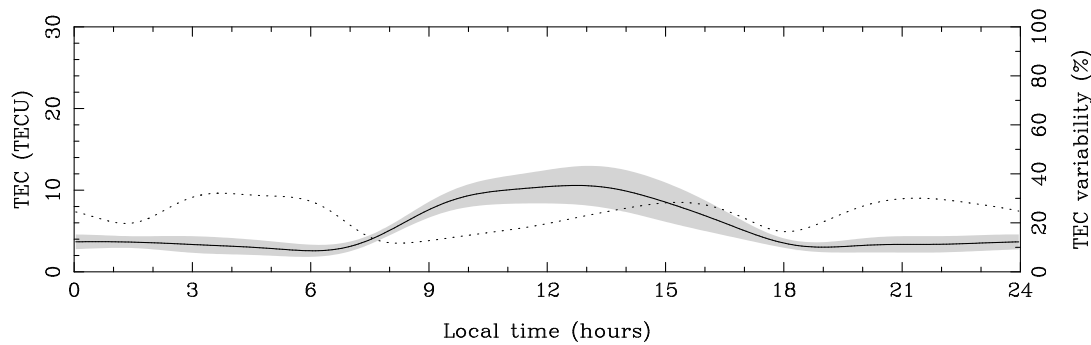


Figure A.10: Monthly averaged European TEC profile, for December 1997.

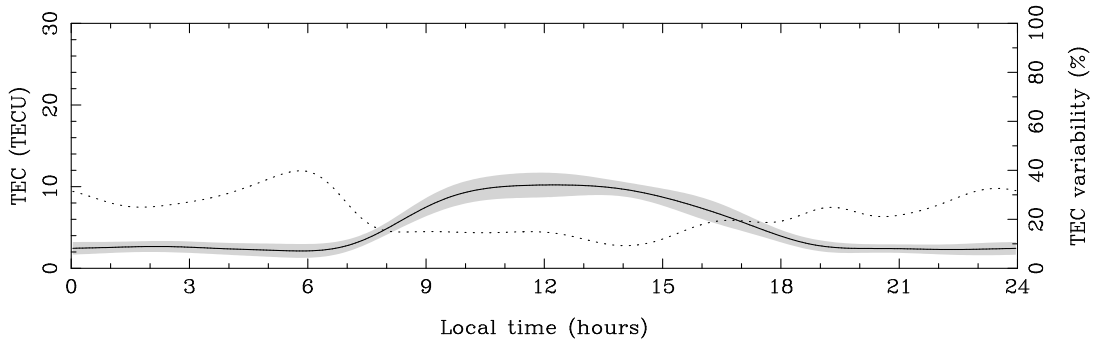


Figure A.11: Monthly averaged European TEC profile, for January 1998.

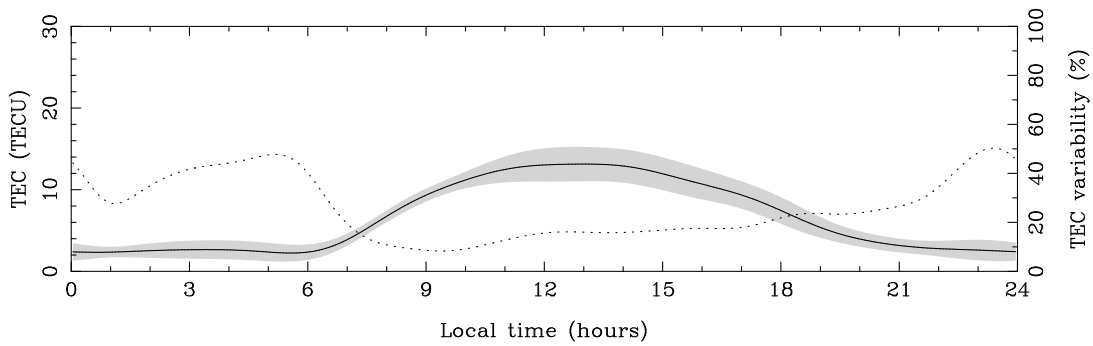


Figure A.12: Monthly averaged European TEC profile, for February 1998.

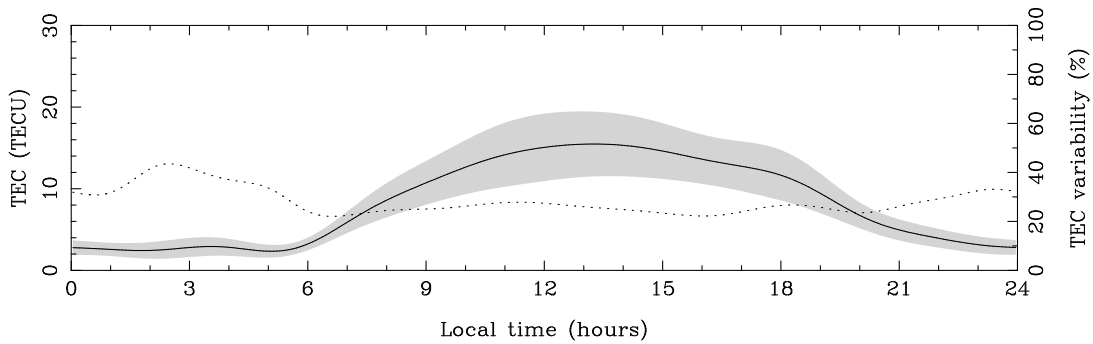


Figure A.13: Monthly averaged European TEC profile, for March 1998.

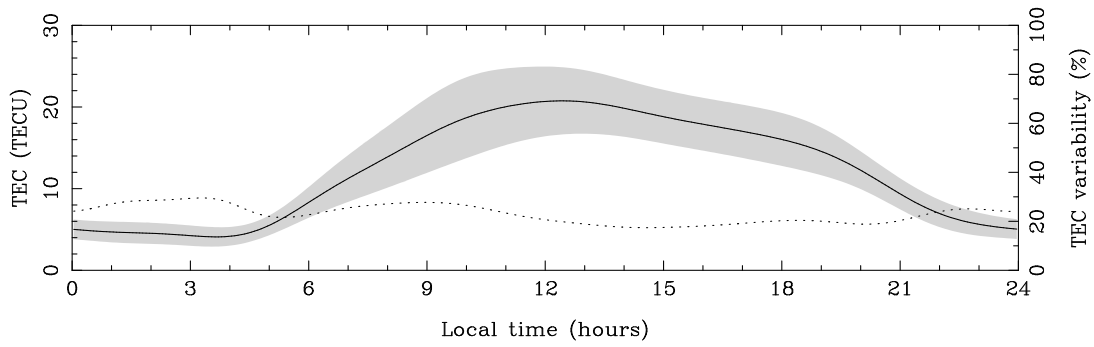


Figure A.14: Monthly averaged European TEC profile, for April 1998.

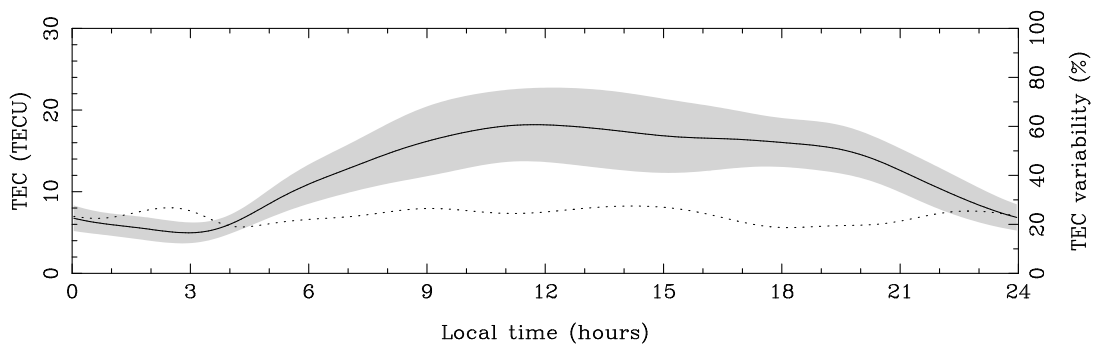


Figure A.15: Monthly averaged European TEC profile, for May 1998.

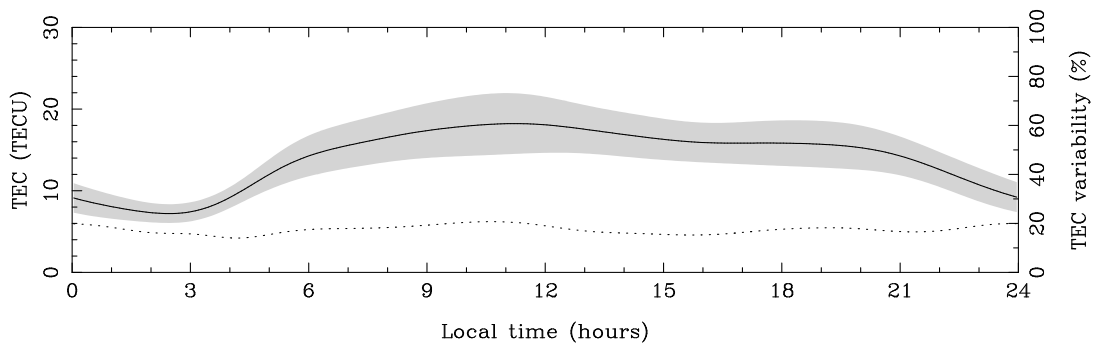


Figure A.16: Monthly averaged European TEC profile, for June 1998.



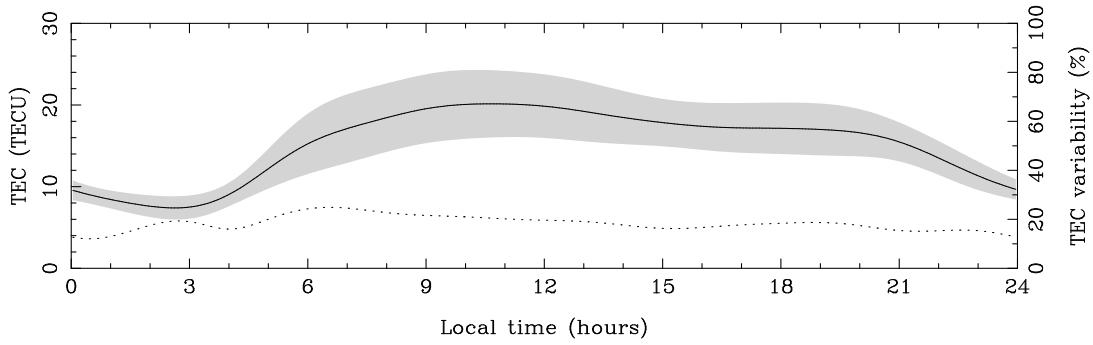


Figure A.17: Monthly averaged European TEC profile, for July 1998.

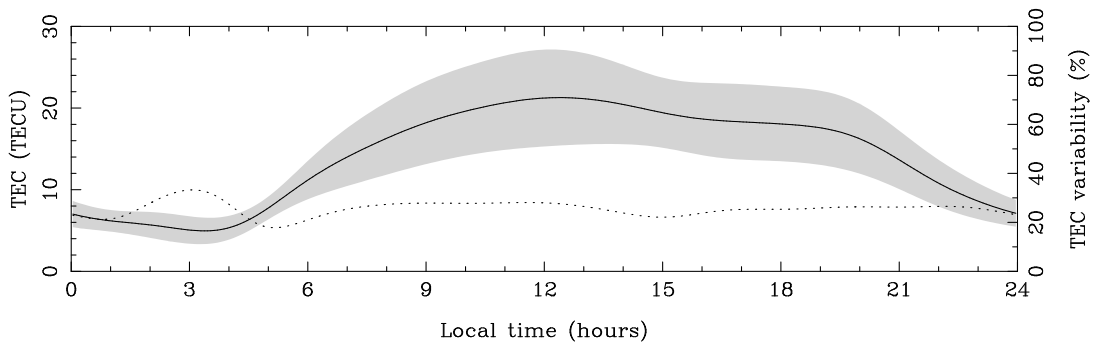


Figure A.18: Monthly averaged European TEC profile, for August 1998.

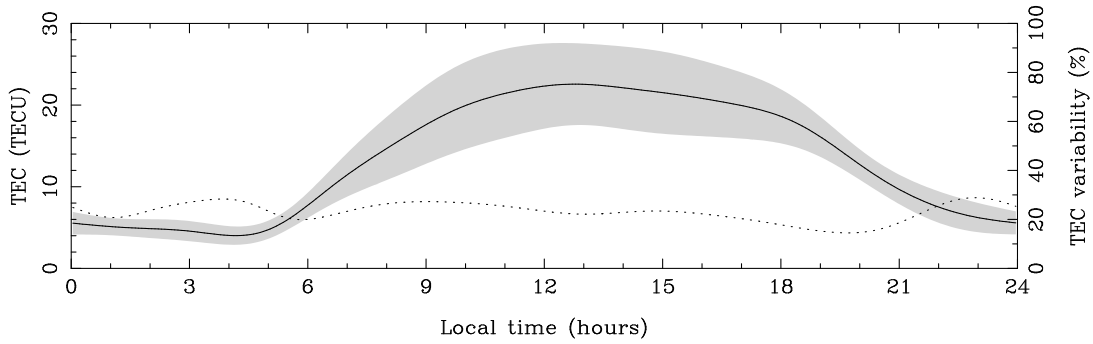


Figure A.19: Monthly averaged European TEC profile, for September 1998.

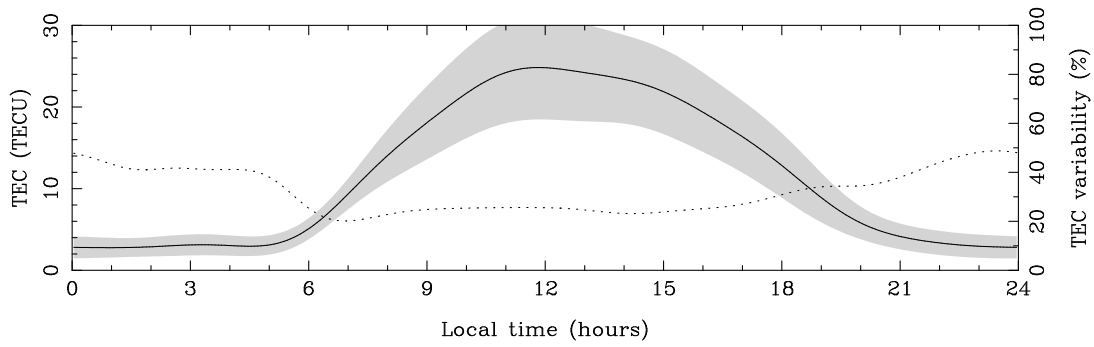


Figure A.20: Monthly averaged European TEC profile, for October 1998.

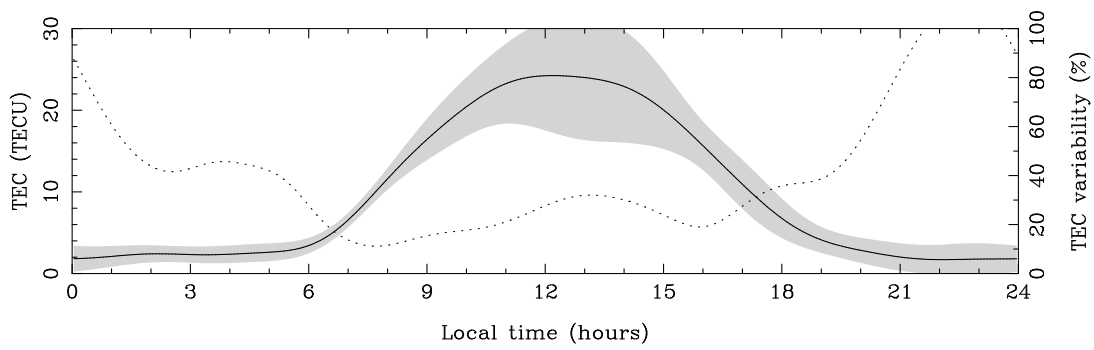


Figure A.21: Monthly averaged European TEC profile, for November 1998.

# B. Time Series of CODE Differential Code Biases

## B.1 Differential Code Biases of the GPS Spacecrafts

Figures B.1 to B.27 show the differential code biases (DCBs) of the GPS spacecrafts obtained from Z1N solutions (see section 4.2). Dots represent the daily estimates; the solid line indicates a smoothed curve setting  $\Delta t$  to 10 days in (4.2). Note that the day-to-day repeatabilities of the individual satellite DCBs are listed in Table 4.2.

## B.2 Differential Code Biases of Some IGS Stations Processed by CODE

Figures B.28 to B.37 show the DCBs of some IGS stations processed by CODE. The ten stations, the DCB estimates of which prove to be most stable are considered in this appendix, namely ALGO, CHAT, DRAO, GODE, JOZE, KOSG, NLIB, USNO, WSRT, and WTZR. The day-to-day repeatabilities of the corresponding DCB estimates are of the order of 0.2–0.3 nanoseconds.

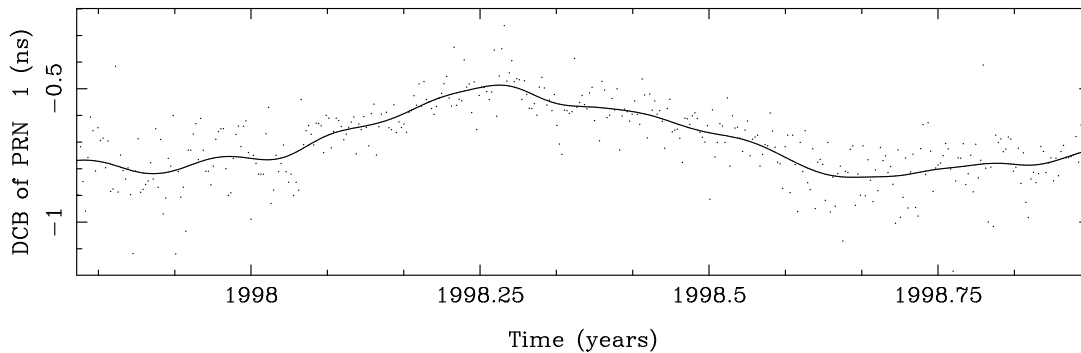


Figure B.1: DCB of PRN 1.

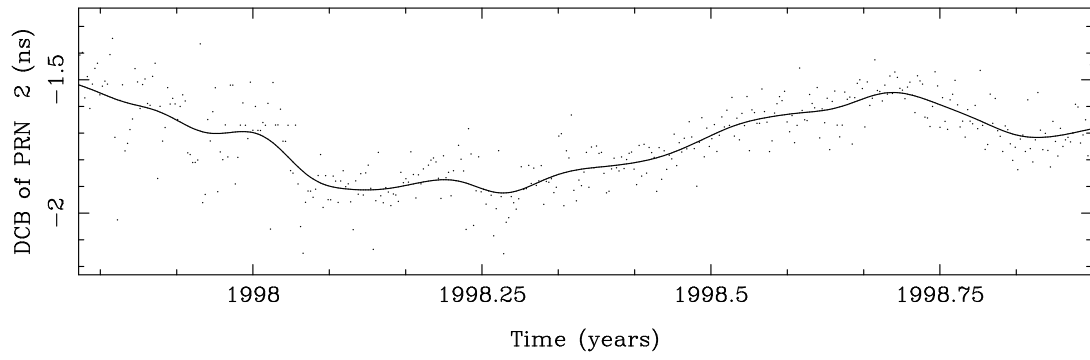


Figure B.2: DCB of PRN 2.

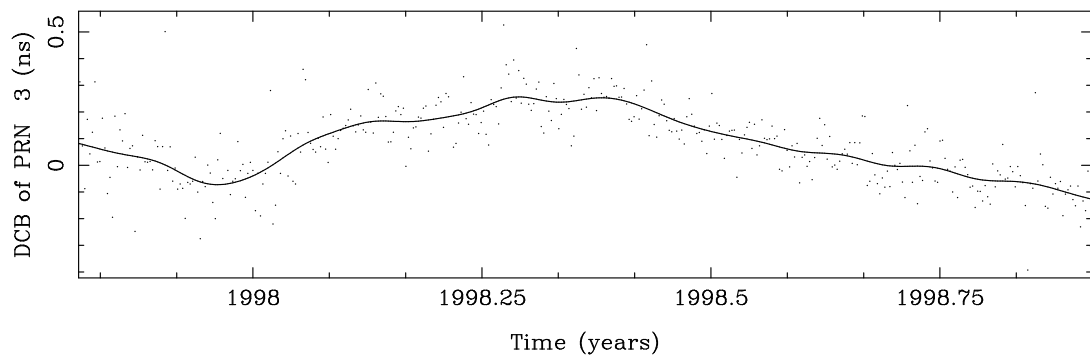


Figure B.3: DCB of PRN 3.

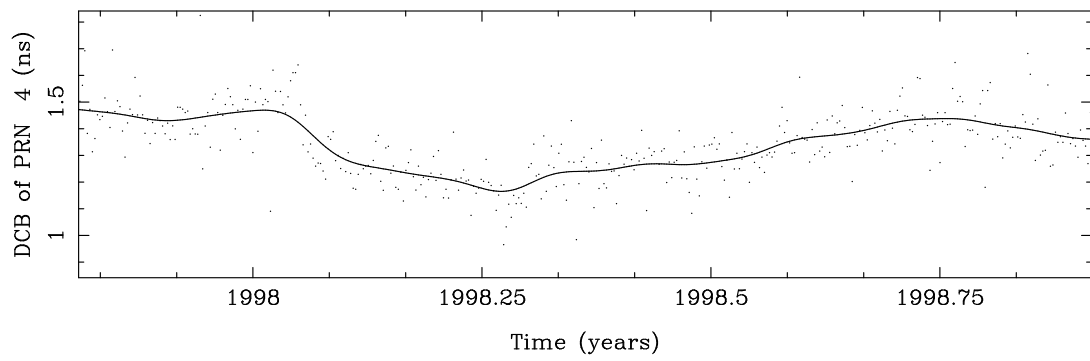


Figure B.4: DCB of PRN 4.

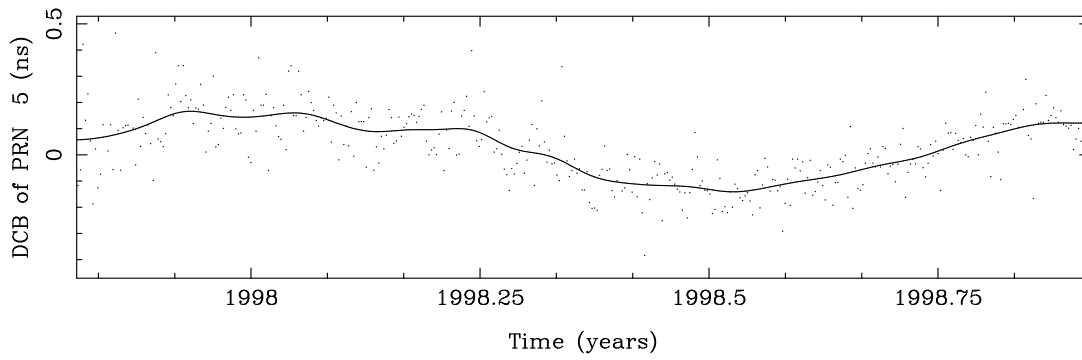


Figure B.5: DCB of PRN 5.

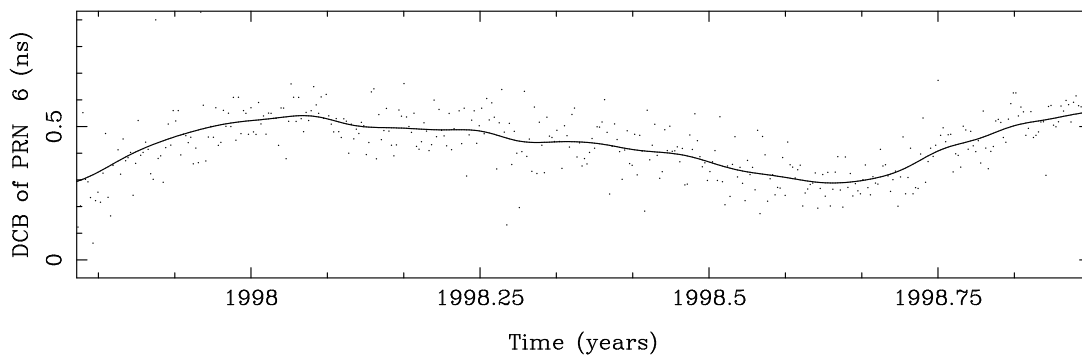


Figure B.6: DCB of PRN 6.

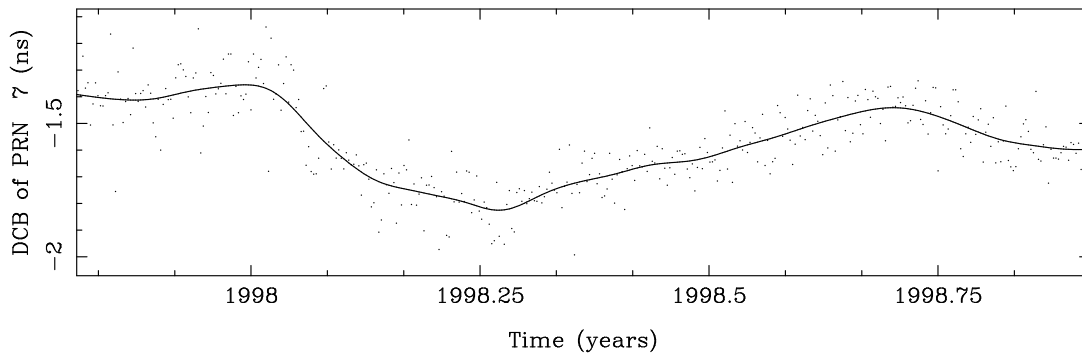


Figure B.7: DCB of PRN 7.

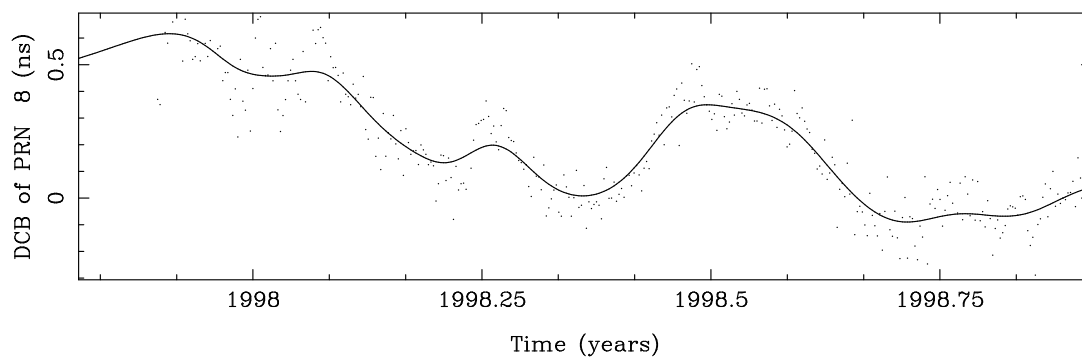


Figure B.8: DCB of PRN 8.

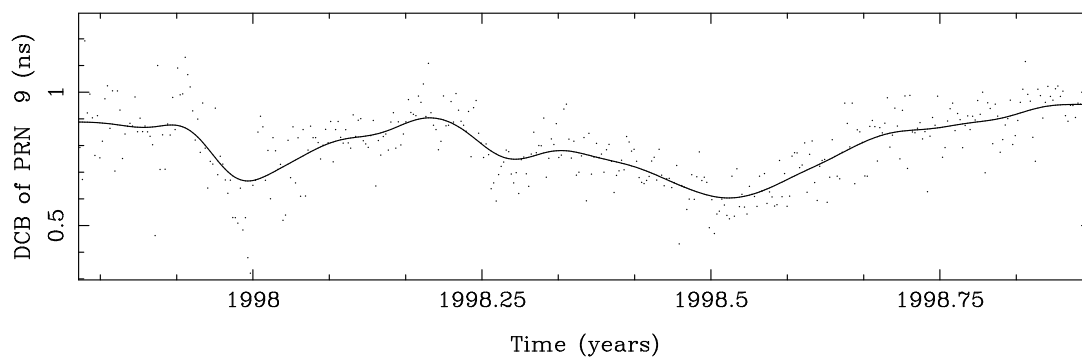


Figure B.9: DCB of PRN 9.

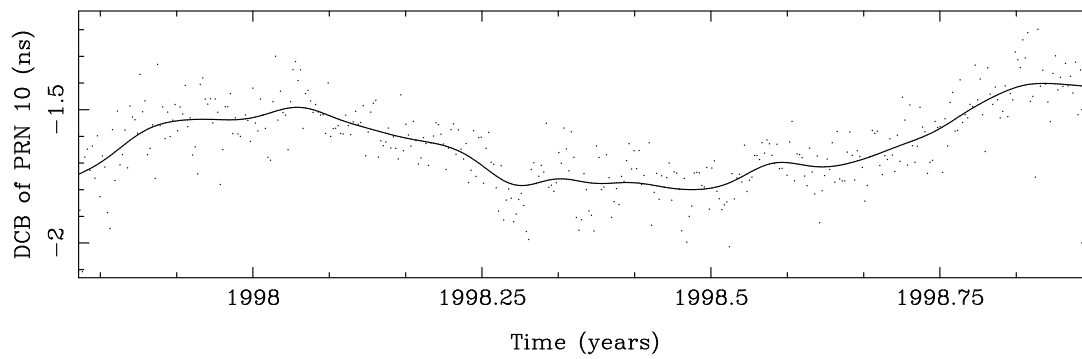


Figure B.10: DCB of PRN 10.

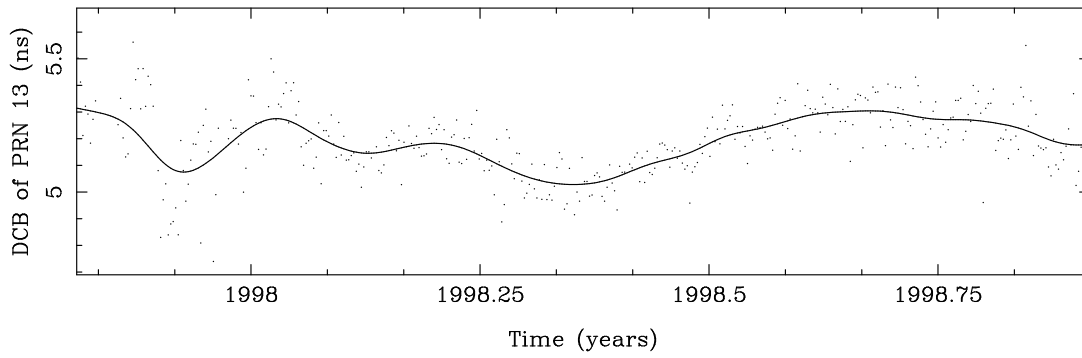


Figure B.11: DCB of PRN 13.

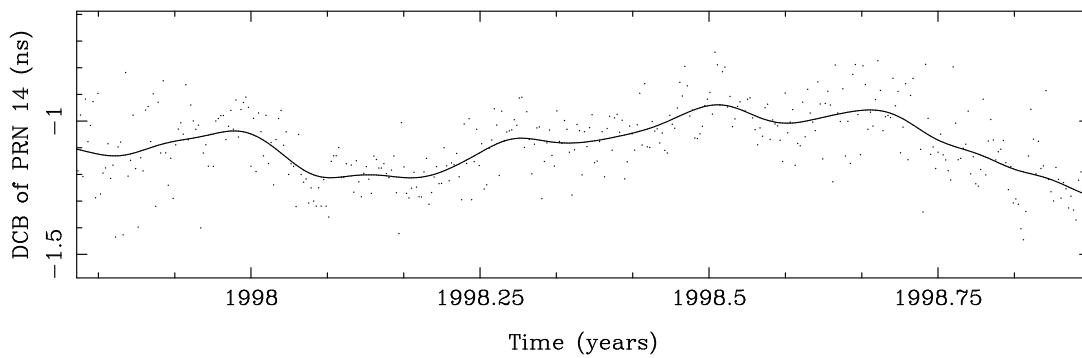


Figure B.12: DCB of PRN 14.

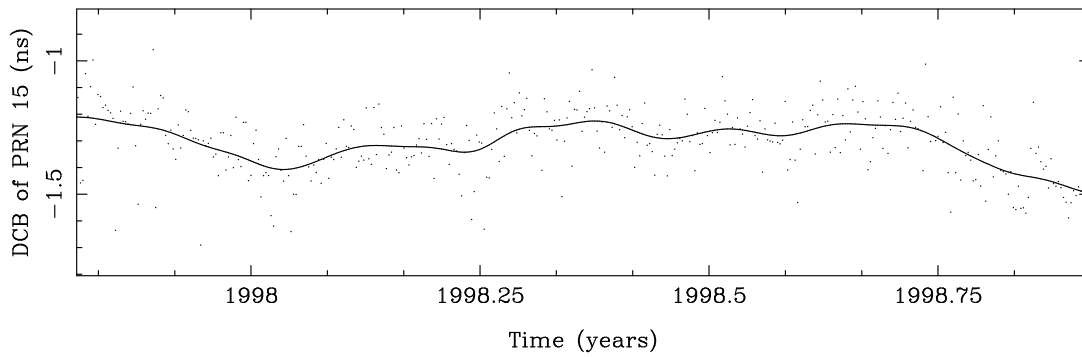


Figure B.13: DCB of PRN 15.

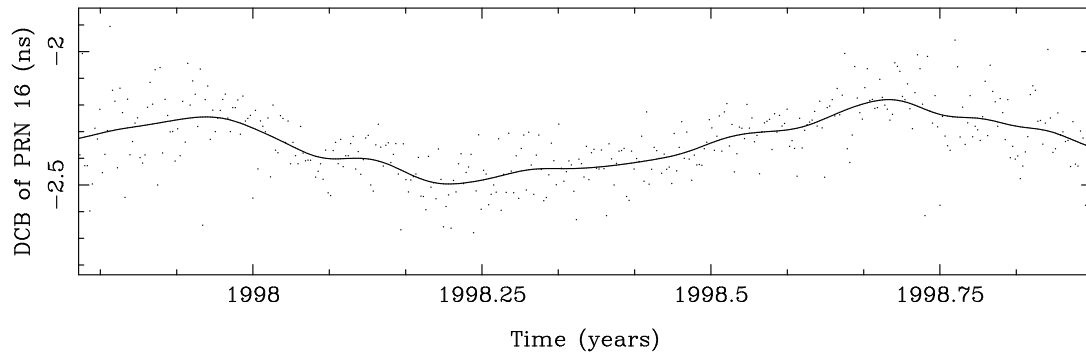


Figure B.14: DCB of PRN 16.

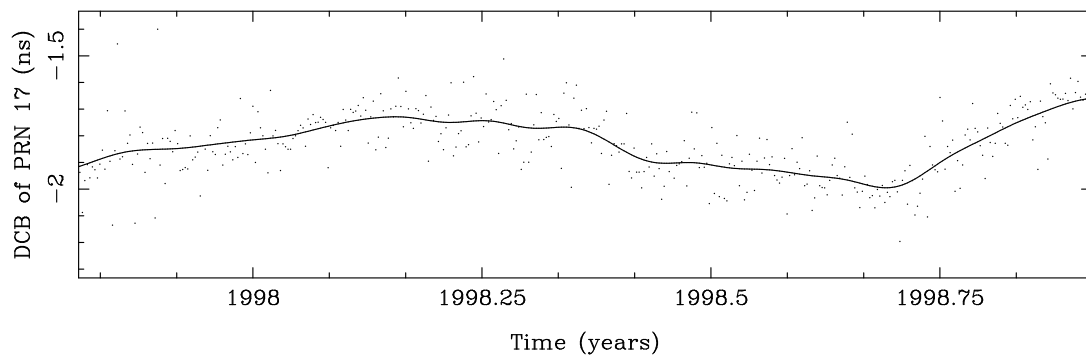


Figure B.15: DCB of PRN 17.

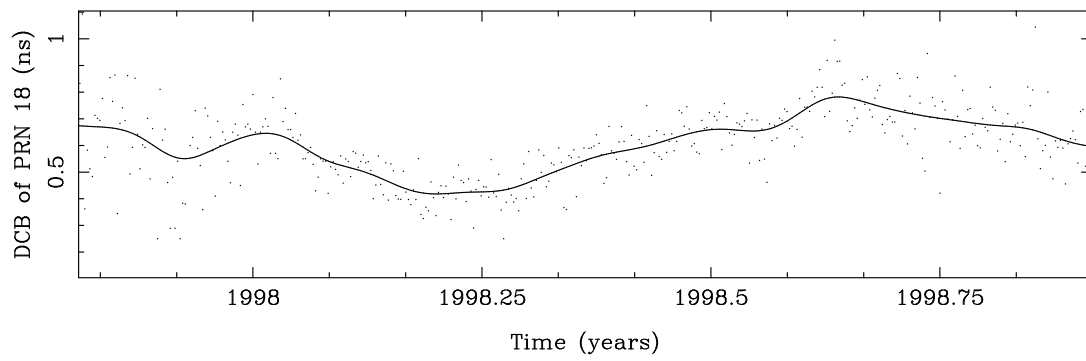


Figure B.16: DCB of PRN 18.



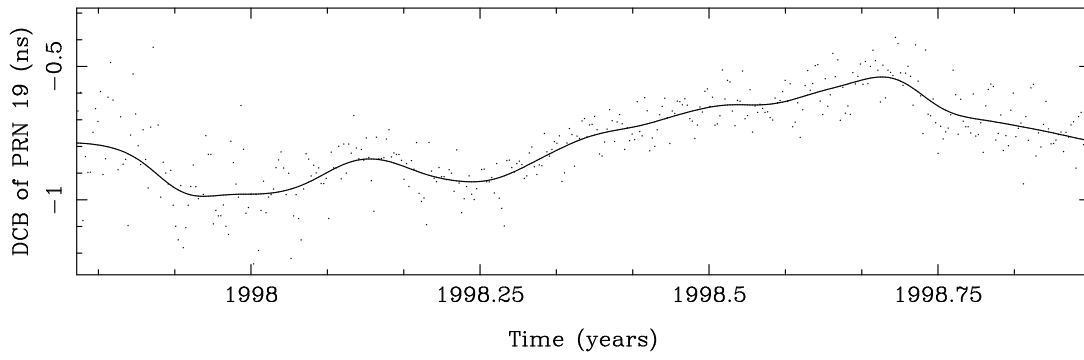


Figure B.17: DCB of PRN 19.

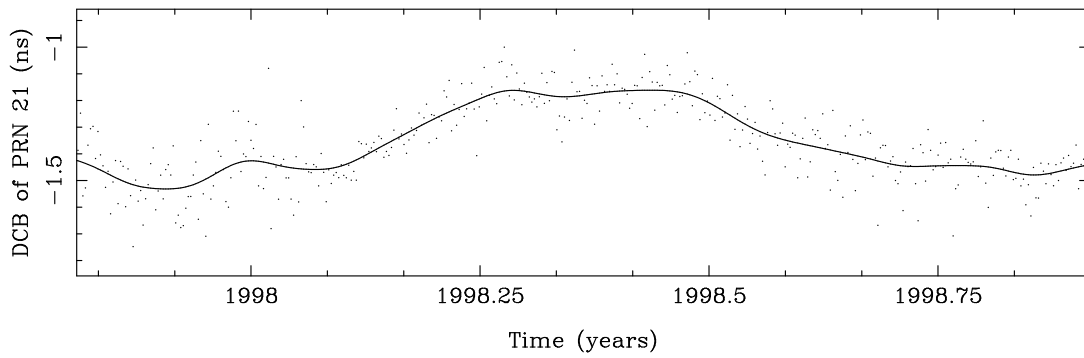


Figure B.18: DCB of PRN 21.

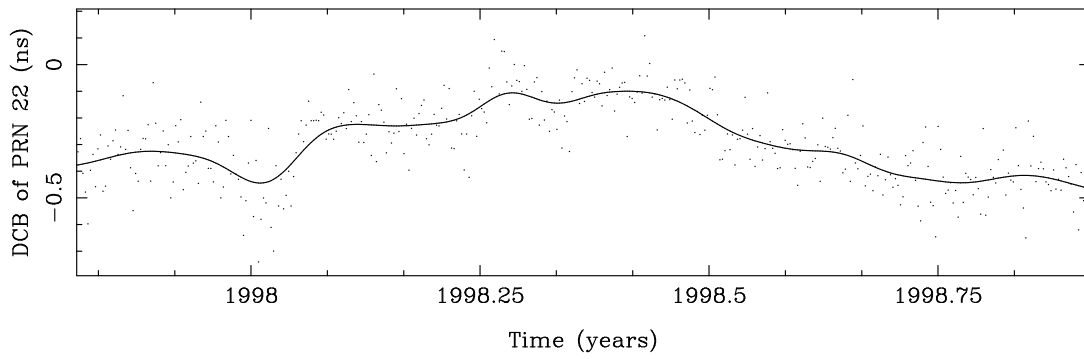


Figure B.19: DCB of PRN 22.

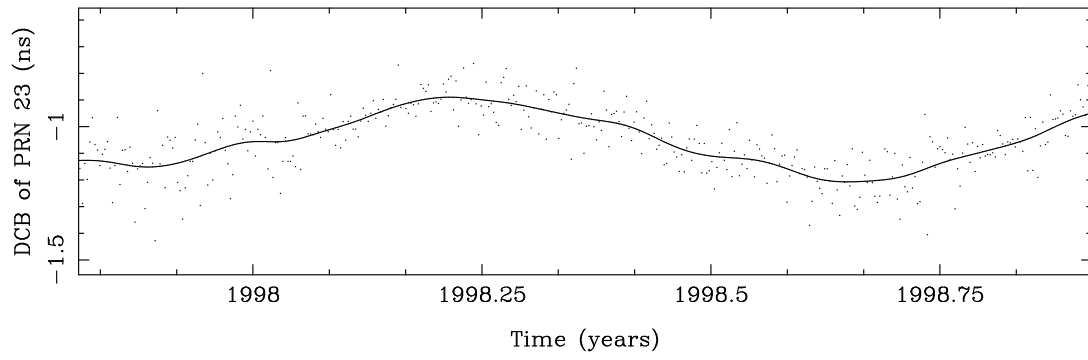


Figure B.20: DCB of PRN 23.

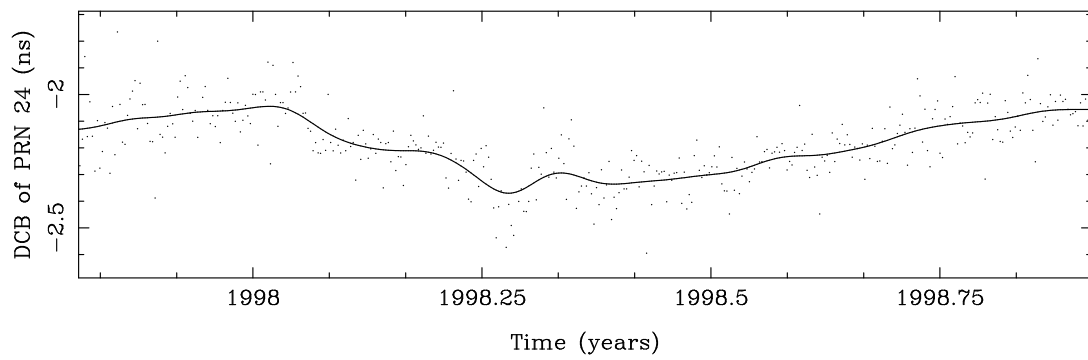


Figure B.21: DCB of PRN 24.

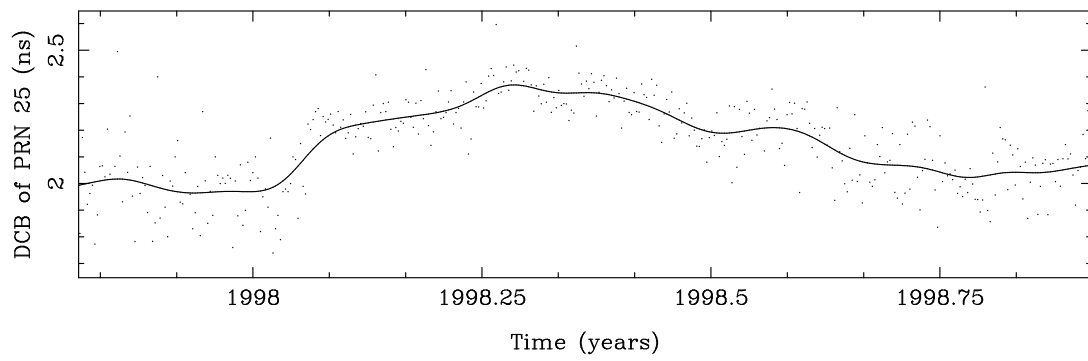


Figure B.22: DCB of PRN 25.

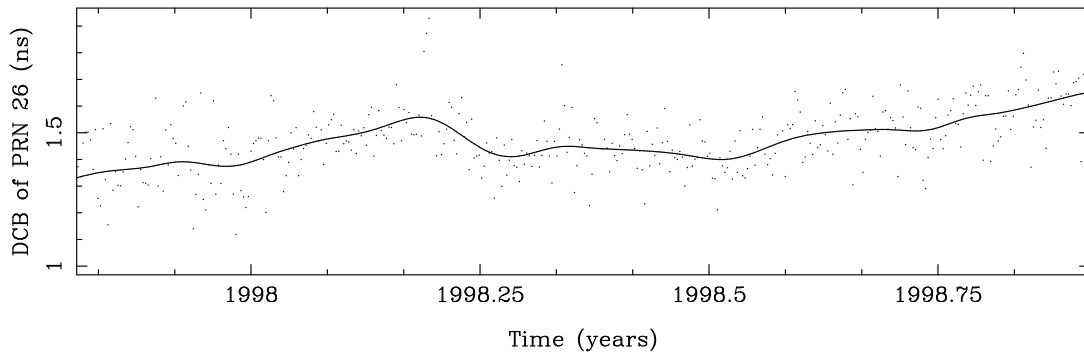


Figure B.23: DCB of PRN 26.

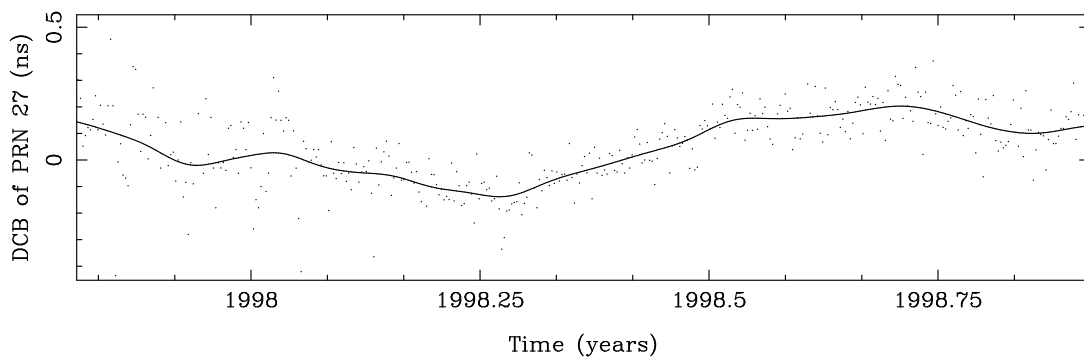


Figure B.24: DCB of PRN 27.

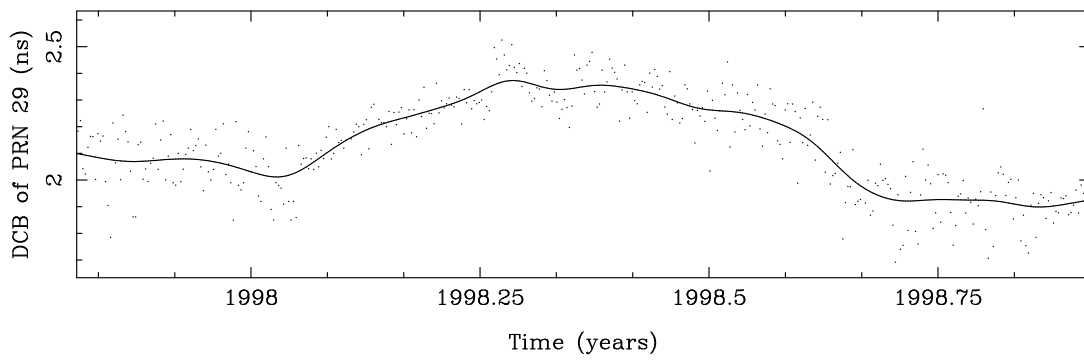


Figure B.25: DCB of PRN 29.

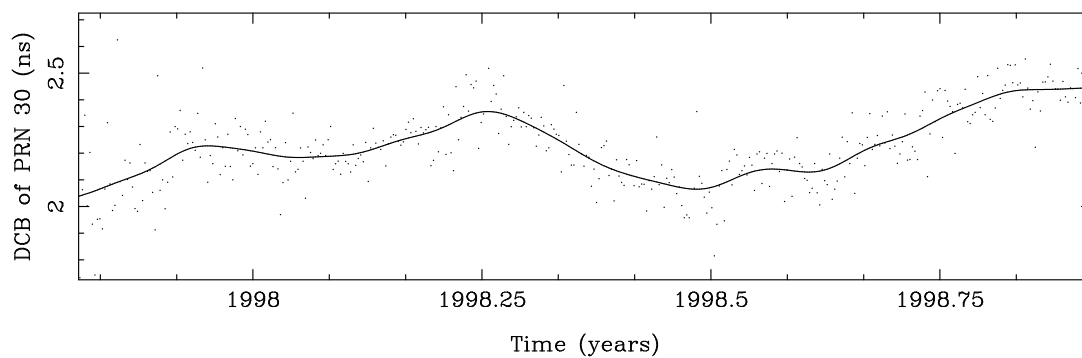


Figure B.26: DCB of PRN 30.

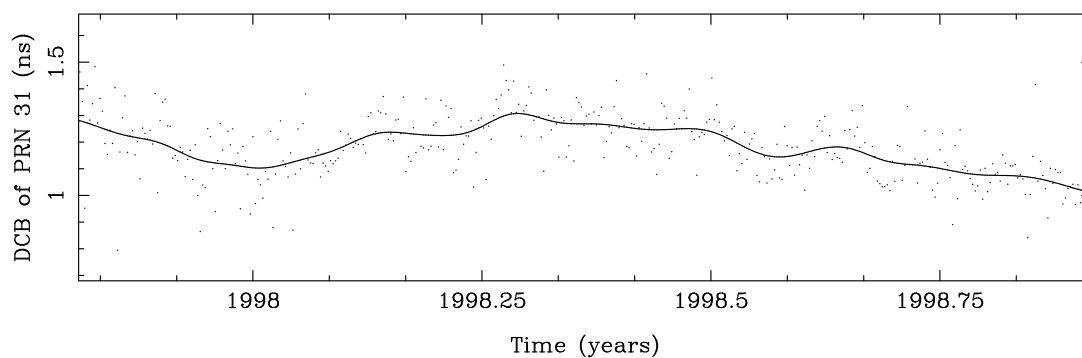


Figure B.27: DCB of PRN 31.

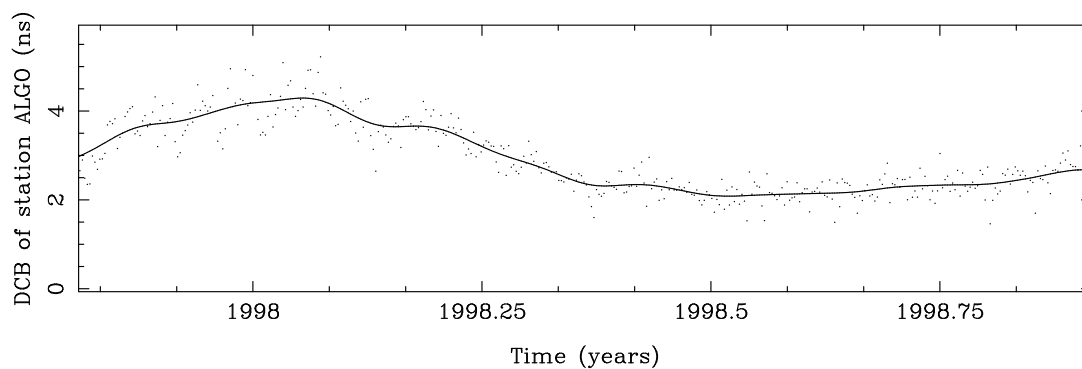


Figure B.28: DCB of the station ALGO (Algonquin, Canada).

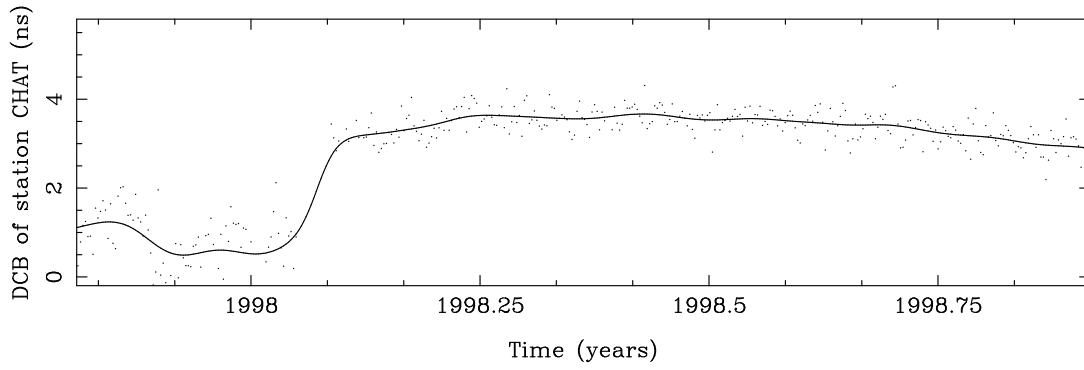


Figure B.29: DCB of the station CHAT (Chatham Island, New Zealand).

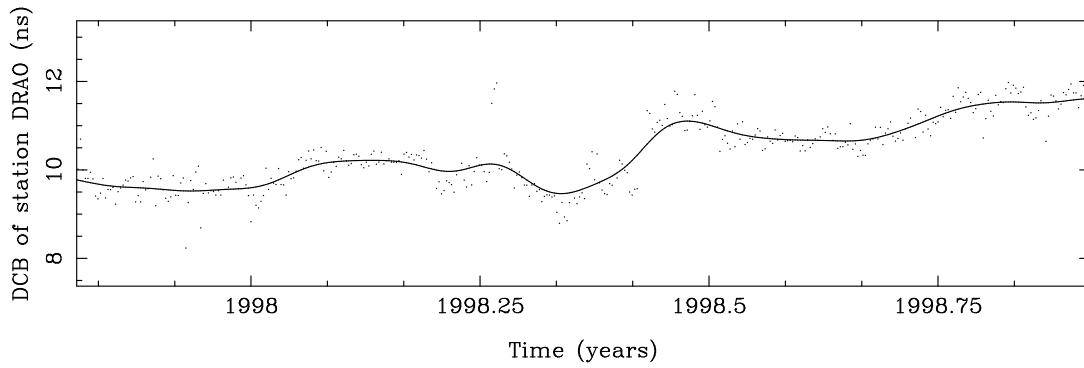


Figure B.30: DCB of the station DRAO (Dominion Radio Astrophysical Observatory, Penticton, Canada).

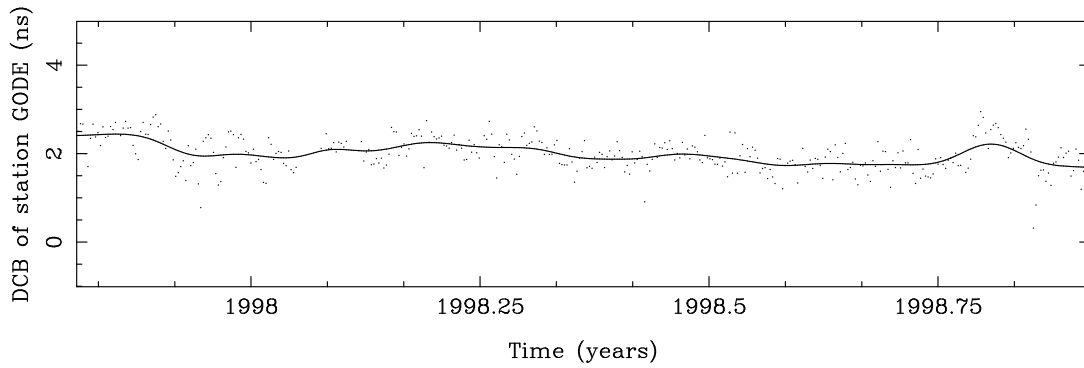


Figure B.31: DCB of the station GODE (Goddard Geophysical and Astronomical Observatory, Greenbelt, USA).

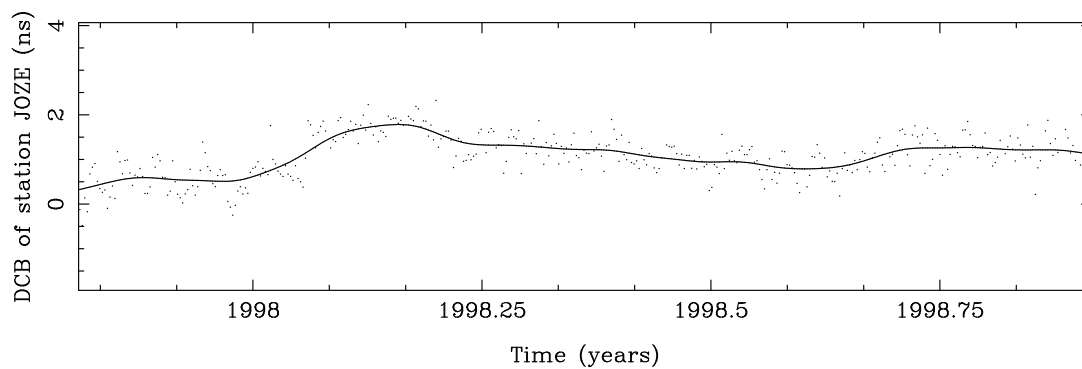


Figure B.32: DCB of the station JOZE (Jozefoslaw, Poland).

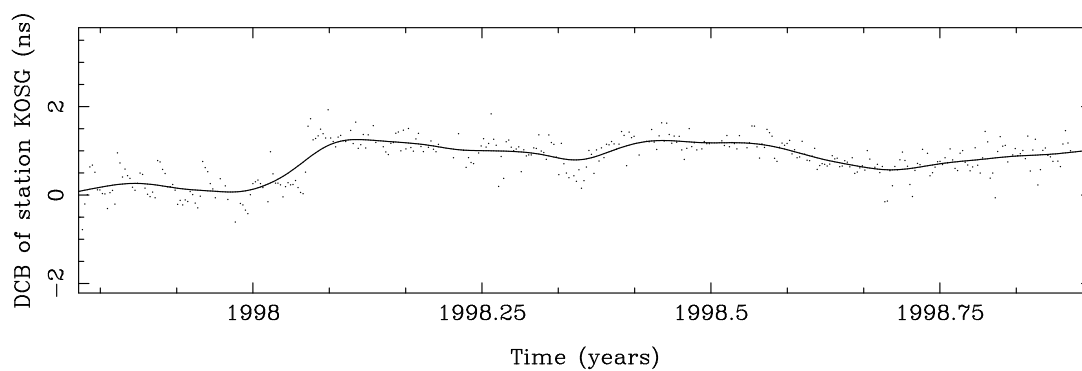


Figure B.33: DCB of the station KOSG (Kootwijk Observatory for Satellite Geodesy, The Netherlands).

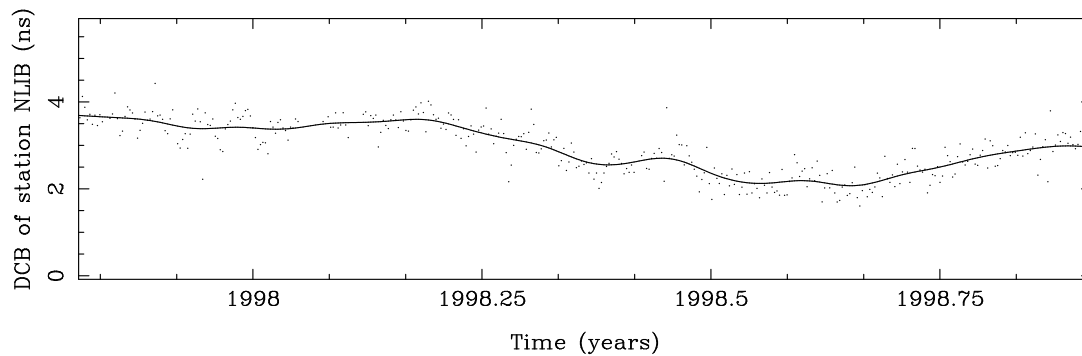


Figure B.34: DCB of the station NLIB (North Liberty, USA).

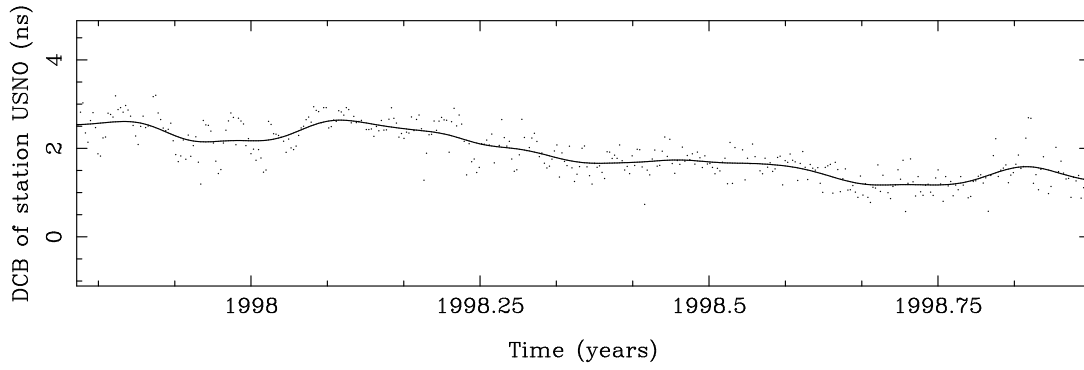


Figure B.35: DCB of the station USNO (U. S. Naval Observatory, USA).

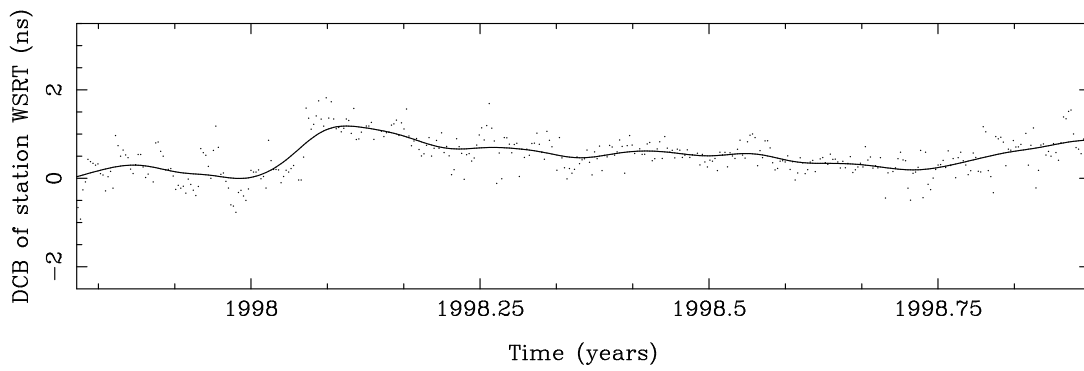


Figure B.36: DCB of the station WSRT (Westerbork Synthesis Radio Telescope, The Netherlands).

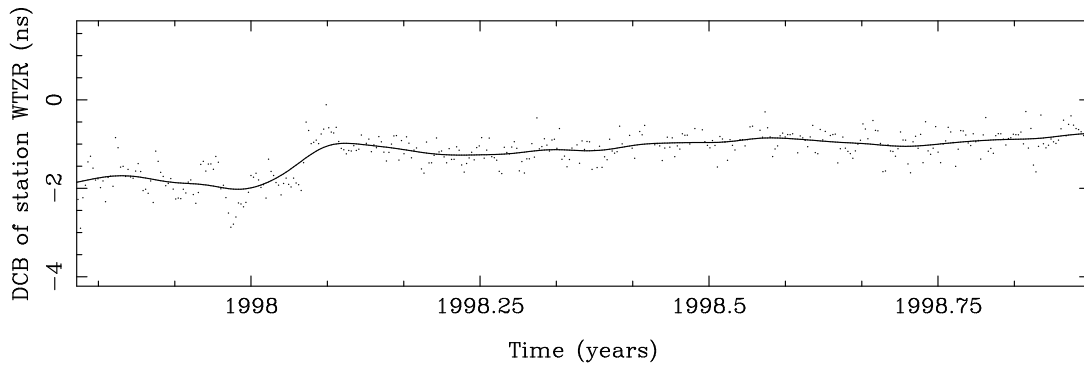


Figure B.37: DCB of the station WTZR (Wetzell, Germany).





# Bibliography

- Abramowitz, M., and I. A. Stegun (eds.) (1972), *Handbook of Mathematical Functions*, Dover, ISBN 486-61272-4.
- Bauersima, I. (1983), *NAVSTAR Global Positioning System (GPS), Teil II: Radio-interferometrische Satellitenbeobachtungen*, Vol. 10 of *Mitteilungen der Satelliten-Beobachtungsstation Zimmerwald*.
- Bertiger, W.I., Y.E. Bar-Sever, B.J. Haines, B.A. Iijima, S.M. Lichten, U.J. Lindqwister, A. J. Mannucci, R. J. Muellerschoen, T.N. Munson, A. W. Moore, L. J. Romans, B. D. Wilson, S. C. Wu, and T.P. Yunck (1998), A Real-Time Wide Area Differential GPS System, *Navigation*, 44(4), 433–447.
- Beutler, G. (1998), *Numerische Integration gewöhnlicher Differentialgleichungssysteme*, lecture notes, Astronomical Institute, University of Berne.
- Beutler, G., I. Bauersima, W. Gurtner, M. Rothacher, T. Schildknecht, and A. Geiger (1987), Atmospheric Refraction and Other Important Biases in GPS Carrier Phase Observations, in *Atmospheric Effects on Geodetic Space Measurements*, Monograph 12, pp. 15–43, School of Surveying, University of New South Wales, Kensington, Australia.
- Beutler, G., I. Bauersima, S. Botton, W. Gurtner, M. Rothacher, and T. Schildknecht (1989), Accuracy and Biases in the Geodetic Application of the Global Positioning System, *Manuscripta Geodaetica*, 14, 28–35.
- Beutler, G., W. Gurtner, M. Rothacher, U. Wild, and E. Frei (1990), Relative Static Positioning with the Global Positioning System: Basic Technical Considerations, in *Global Positioning System: An Overview*, IAG Symposium No. 102, pp. 1–23, ISBN 0-387-97266-8.
- Beutler, G., I.I. Mueller, and R. Neilan (1994), The International GPS Service for Geodynamics (IGS): Development and Start of Official Service on 1 January 1994, *Manuscripta Geodaetica*, 68, 43–51.

- Beutler, G., A. Geiger, M. Rothacher, S. Schaer, D. Schneider, and A. Wiget (1995a), *Dreidimensionales Testnetz Turtmann 1985–1993, Teil II (GPS-Netz)*, Vol. 51 of *Geodätisch-geophysikalische Arbeiten in der Schweiz*, Schweizerische Geodätische Kommission.
- Beutler, G., I. I. Mueller, and R. E. Neilan (1995b), The International GPS Service for Geodynamics (IGS): The Story, in *GPS Trends in Precise Terrestrial, Airborne, and Spaceborne Applications*, IAG Symposium No. 115, edited by G. Beutler *et al.*, pp. 3–13, Boulder, Colorado, USA, July 3–4, 1995, ISBN 3-540-60872-9.
- Beutler, G., R. Weber, U. Hugentobler, M. Rothacher, and A. Verdun (1998a), GPS Satellite Orbits, in *GPS for Geodesy*, edited by P. J. G. Teunissen and A. Kleusberg, pp. 43–109, Springer, ISBN 3-540-63661-7.
- Beutler, G., M. Rothacher, S. Schaer, T. A. Springer, J. Kouba, and R. E. Neilan (1998b), The International GPS Service (IGS): An Interdisciplinary Service in Support of Earth Sciences, *Advances in Space Research*, in press.
- Bilitza, D. (1998), International Reference Ionosphere 1995, <http://nssdc.gsfc.nasa.gov/space/model/ionos/iri.html>.
- Bock, Y., S. A. Gourevitch, C. C. Counselman III, R. W. King, and R. I. Abbot (1986), Interferometric Analysis of GPS Phase Observations, *Manuscripta Geodaetica*, 11, 282–288.
- Boucher, C., Z. Altamimi, , and P. Sillard (1998), *Results and Analysis of the ITRF 96*, IERS Technical Note No. 24, Central Bureau of IERS, Observatory of Paris, France, May 1998.
- Brockmann, E. (1997), *Combination of Solutions for Geodetic and Geodynamic Applications of the Global Positioning System (GPS)*, Vol. 55 of *Geodätisch-geophysikalische Arbeiten in der Schweiz*, Schweizerische Geodätische Kommission, Ph.D. thesis.
- Brunner, F. K., and M. Gu (1991), An Improved Model for Dual Frequency Ionospheric Correction of GPS Observations, *Manuscripta Geodaetica*, 16, 205–214.
- Budden, K. G. (1985), *The Propagation of Radio Waves*, Cambridge.
- Clynch, J. R., D. S. Coco, C. Coker, and G. J. Bishop (1989), A Versatile GPS Ionospheric Monitor: High Latitude Measurements of TEC and Scintillation, in *Proceedings of the ION GPS-89*, pp. 445–450, Colorado Springs, Colorado, USA.
- Davies, K. (1989), *Ionospheric Radio*, Vol. 31 of *IEE Electromagnetic Waves Series*, ISBN 0-86341-186-X.
- Enninghorst, K., and M. Rentsch (1998), Rapid Orbit and Altimeter Products for ERS-2, *Annales Geophysicae Supplement of the EGS 23rd General Assembly, Nice, France*, p. 356, April 20–24, 1998.

- Feltens, J. (1998), Chapman Profile Approach for 3-D Global TEC Representation, in *Proceedings of the IGS Analysis Center Workshop*, edited by J. M. Dow *et al.*, pp. 285–297, ESA/ESOC, Darmstadt, Germany, February 9–11, 1998.
- Feltens, J., and S. Schaer (1998), IGS Products for the Ionosphere, in *Proceedings of the IGS Analysis Center Workshop*, edited by J. M. Dow *et al.*, pp. 225–232, ESA/ESOC, Darmstadt, Germany, February 9–11, 1998.
- Feltens, J., J. M. Dow, T. J. Martin-Mur, C. Garcia Martinez, and M. A. Bayona-Perez (1996), Verification of ESOC Ionosphere Modeling and Status of IGS Intercomparison Activity, in *Proceedings of the IGS Analysis Center Workshop, Silver Spring, Maryland, USA*, edited by R. E. Neilan *et al.*, pp. 205–219, IGS Central Bureau, JPL, Pasadena, California, USA, March 19–21, 1996.
- Feltens, J., J. M. Dow, T. J. Martin-Mur, C. Garcia Martinez, and P. Bernedo (1998), Routine Production of Ionosphere TEC Maps at ESOC—First Results, in *Proceedings of the IGS Analysis Center Workshop*, edited by J. M. Dow *et al.*, pp. 273–284, ESA/ESOC, Darmstadt, Germany, February 9–11, 1998.
- Frei, E. (1991), *Rapid Differential Positioning with the Global Positioning System (GPS)*, Vol. 41 of *Geodätisch-geophysikalische Arbeiten in der Schweiz*, Schweizerische Geodätische Kommission, Ph.D. thesis.
- Frei, E., and G. Beutler (1990), Rapid Static Positioning Based on the Fast Ambiguity Resolution Approach FARA: Theory and First Results, *Manuscripta Geodaetica*, 15, 325–356.
- Gao, Y., P. Heroux, and J. Kouba (1994), Estimation of GPS Receiver and Satellite L1/L2 Signal Delay Biases Using Data from CACS, in *Proceedings of the International Symposium on Kinematic Systems in Geodesy, Geomatics and Navigation*, pp. 109–117, Banff, Canada, August 30–September 2, 1994.
- Gendt, G. (1998), IGS Combination of Tropospheric Estimates—Experience from Pilot Experiment, in *Proceedings of the IGS Analysis Center Workshop*, edited by J. M. Dow *et al.*, pp. 205–216, ESA/ESOC, Darmstadt, Germany, February 9–11, 1998.
- Georgiadou, Y., and A. Kleusberg (1988), On the Effect of Ionospheric Delay on Geodetic Relative GPS Positioning, *Manuscripta Geodaetica*, 13, 1–8.
- Gurtner, W. (1992), Parameterbestimmung und Schätzverfahren, lecture notes, Astronomical Institute, University of Berne.
- Gurtner, W. (1994), RINEX: The Receiver-Independent Exchange Format, *GPS World*, 5(7), 48–52, July 1994, format specifications available at <ftp://igscb.jpl.nasa.gov/igscb/data/format/rinex2.txt>.

- Habrigh, H. (1998), *Geodetic Applications of the Global Navigation Satellite System (GLONASS)*, Ph.D. thesis, Federal Agency of Cartography and Geodesy, Frankfurt, Germany, in preparation.
- Hartmann, G. K., and R. Leitinger (1984), Range Errors due to Ionospheric and Tropospheric Effects for Signal Frequencies Above 100 MHz, *Bulletin Géodésique*, 58, 109–136.
- Hernandez-Pajares, M., D. Bilitza, J. M. Juan, and J. Sanz (1998), Comparison Between IRI and GPS-IGS Derived Electron Content During 1991–97: First Results, Polytechnical University of Catalonia, Barcelona, Spain.
- Hofmann-Wellenhof, B., H. Lichtenegger, and J. Collins (1992), *GPS: Theory and Practice*, Springer, ISBN 3-211-82364-6.
- IGS (1998), *IGS Directory*, IGS Central Bureau, JPL, Pasadena, California, USA, January 1998.
- Ivanov-Kholodny, G. S., and A. V. Mikhailov (1986), *The Prediction of Ionospheric Conditions*, ISBN 390-277-2143-2.
- Kaplan, E. (ed.) (1996), *Understanding GPS: Principles and Applications*, Artech House, ISBN 0-89006-793-7.
- Kelley, M. C. (1989), *The Earth's Ionosphere: Plasma Physics and Electrodynamics*, Vol. 43 of *International Geophysics Series*, ISBN 0-12-404012-8.
- Klobuchar, J. A. (1987), Ionospheric Time-Delay Algorithm for Single-Frequency GPS Users, *IEEE Transactions on Aerospace and Electronic Systems*, 23, 325–331.
- Koch, K.-R. (1988), *Parameter Estimation and Hypothesis Testing in Linear Models*, Springer.
- Komjathy, A. (1997), *Global Ionospheric Total Electron Content Mapping Using the Global Positioning System*, Ph.D. thesis, University of New Brunswick, Fredericton, New Brunswick, Canada, Department of Geodesy and Geomatics Engineering Technical Report No. 188.
- Komjathy, A., and R. B. Langley (1996), The Effect of Shell Height on High Precision Ionospheric Modelling Using GPS, in *Proceedings of the IGS Analysis Center Workshop, Silver Spring, Maryland, USA*, edited by R. E. Neilan *et al.*, pp. 193–203, IGS Central Bureau, JPL, Pasadena, California, USA, March 19–21, 1996.
- Kouba, J. (1998), Analysis Activities, in *IGS 1997 Annual Report*, pp. 10–15, IGS Central Bureau, JPL, Pasadena, California, USA.

- Kouba, J., *et al.* (1996), SINEX—Solution-INdependent EXchange Format Version 1.00, June 30, 1996, in *Proceedings of the IGS Analysis Center Workshop, Silver Spring, Maryland, USA*, edited by R. E. Neilan *et al.*, pp. 233–276, IGS Central Bureau, JPL, Pasadena, California, USA, March 19–21, 1996, format specifications available at <ftp://igscb.jpl.nasa.gov/igscb/data/format/sinex.txt>.
- Langley, R. B. (1997), The GPS Error Budget, *GPS World*, 8(3), 51–56, March 1997.
- Leick, A. (1995), *GPS Satellite Surveying*, Wiley, ISBN 0-471-30626-6.
- Mannucci, A. J., B. D. Wilson, D. N. Yuan, C. H. Ho, U. J. Lindqwister, and T. F. Runge (1998), A Global Mapping Technique for GPS-Derived Ionospheric Total Electron Content Measurements, *Radio Science*, 33, 565–582.
- McCarthy, D. D. (ed.) (1996), *IERS Conventions*, IERS Technical Note No. 21, Central Bureau of IERS, Observatory of Paris, France, July 1996.
- Melbourne, W. G. (1985), The Case for Ranging in GPS Based Geodetic Systems, in *Proceedings of the First International Symposium on Precise Positioning with the Global Positioning System*, Rockville, Maryland, USA.
- Melbourne, W. G., E. S. Davis, C. B. Duncan, G. A. Hajj, K. R. Hardy, E. R. Kursinski, T. K. Meehan, L. E. Young, and T. P. Yunck (1994), *The Application of Spaceborne GPS to Atmospheric Limb Sounding and Global Change Monitoring*, Vol. 94-18 of *JPL Publications*, April 1994.
- Mervart, L. (1995), *Ambiguity Resolution Techniques in Geodetic and Geodynamic Applications of the Global Positioning System*, Vol. 53 of *Geodätisch-geophysikalische Arbeiten in der Schweiz*, Schweizerische Geodätische Kommission, Ph.D. thesis.
- Mervart, L., G. Beutler, M. Rothacher, and S. Schaer (1995), The Impact of Ambiguity Resolution on GPS Orbit Determination and on Global Geodynamics Studies, in *GPS Trends in Precise Terrestrial, Airborne, and Spaceborne Applications*, IAG Symposium No. 115, edited by G. Beutler *et al.*, pp. 285–288, Boulder, Colorado, USA, July 3–4, 1995, ISBN 3-540-60872-9.
- Moritz, H. (1989), *Advanced Physical Geodesy*, Wichmann.
- Neilan, R. (1995), The Organisation of the IGS, in *IGS 1994 Annual Report*, edited by J. F. Zumberge *et al.*, pp. 11–23, IGS Central Bureau, JPL, Pasadena, California, USA, September 1, 1995.
- NGDC (1998), National Geophysical Data Center, Boulder, Colorado, USA, <http://www.ngdc.noaa.gov/> or <ftp://ftp.ngdc.noaa.gov/>.
- Parkinson, B. W., and J. J. Spilker (eds.) (1996a), *Global Positioning System: Theory and Applications*, Vol. I, American Institute of Aeronautics and Astronautics, ISBN 1-56347-106-X.

- Parkinson, B. W., and J. J. Spilker (eds.) (1996b), *Global Positioning System: Theory and Applications*, Vol. II, American Institute of Aeronautics and Astronautics, ISBN 1-56347-107-8.
- Ratcliffe, J. A. (1972), *An Introduction to the Ionosphere and Magnetosphere*, Cambridge, ISBN 0-521-08341-9.
- Rawer, K., and H. Thiemann (1997), Very Long-Term Changes in the Ionosphere and Upper Atmosphere, *Advances in Space Research*, 20(11), 2101–2110.
- Rishbeth, H., and O. K. Garriott (1969), *Introduction to Ionospheric Physics*, Vol. 14 of *International Geophysics Series*.
- Rothacher, M. (1992), *Orbits of Satellite Systems in Space Geodesy*, Vol. 46 of *Geodätisch-geophysikalische Arbeiten in der Schweiz*, Schweizerische Geodätische Kommission, Ph.D. thesis.
- Rothacher, M., and L. Mervart (eds.) (1996), *Bernese GPS Software Version 4.0*, Astronomical Institute, University of Berne, Switzerland, September 1996.
- Rothacher, M., G. Beutler, E. Brockmann, W. Gurtner, L. Mervart, R. Weber, U. Wild, A. Wiget, H. Seeger, and C. Boucher (1994), Annual Report of the CODE Analysis Center for 1993, in *IERS Technical Note No. 17*, edited by P. Charlot, Central Bureau of IERS, Observatory of Paris, France, September 1994.
- Rothacher, M., R. Weber, E. Brockmann, G. Beutler, L. Mervart, U. Wild, A. Wiget, C. Boucher, S. Botton, and H. Seeger (1995a), Annual Report 1994 of the CODE Processing Center of the IGS, in *IGS 1994 Annual Report*, edited by J. F. Zumberge *et al.*, pp. 139–161, IGS Central Bureau, JPL, Pasadena, California, USA, September 1, 1995.
- Rothacher, M., W. Gurtner, S. Schaer, R. Weber, W. Schlüter, and H. O. Hase (1995b), Azimuth- and Elevation-Dependent Phase Center Corrections for Geodetic GPS Antennas Estimated from GPS Calibration Campaigns, in *GPS Trends in Precise Terrestrial, Airborne, and Spaceborne Applications*, IAG Symposium No. 115, edited by G. Beutler *et al.*, pp. 333–338, Boulder, Colorado, USA, July 3–4, 1995, ISBN 3-540-60872-9.
- Rothacher, M., G. Beutler, E. Brockmann, L. Mervart, S. Schaer, T. A. Springer, U. Wild, A. Wiget, H. Seeger, and C. Boucher (1996), Annual Report 1995 of the CODE Analysis Center of the IGS, in *IGS 1995 Annual Report*, edited by J. F. Zumberge *et al.*, pp. 151–173, IGS Central Bureau, JPL, Pasadena, California, USA, September 1996.
- Rothacher, M., T. A. Springer, S. Schaer, G. Beutler, E. Brockmann, U. Wild, A. Wiget, C. Boucher, S. Botton, and H. Seeger (1997), Annual Report 1996 of the CODE

- Processing Center of the IGS, in *IGS 1996 Annual Report*, edited by J. F. Zumberge *et al.*, pp. 201–219, IGS Central Bureau, JPL, Pasadena, California, USA, November 1997.
- Rothacher, M., T. A. Springer, S. Schaer, G. Beutler, D. Ineichen, U. Wild, A. Wiget, C. Boucher, S. Botton, and H. Seeger (1998a), Annual Report 1997 of the CODE Analysis Center of the IGS, in *IGS 1997 Technical Reports*, edited by I. Mueller *et al.*, pp. 73–87, IGS Central Bureau, JPL, Pasadena, California, USA, October 1998.
- Rothacher, M., T. A. Springer, S. Schaer, and G. Beutler (1998b), Processing Strategies for Regional GPS Networks, in *Advances in Positioning and Reference Frames*, IAG Symposium No. 118, edited by F. K. Brunner, pp. 93–100.
- Santerre, R. (1991), Impact of GPS Satellite Sky Distribution, *Manuscripta Geodaetica*, 16, 28–53.
- Schaer, S. (1994), Stochastische Ionosphärenmodellierung beim Rapid Static Positioning mit GPS, diploma thesis, Astronomical Institute, University of Berne.
- Schaer, S. (1996), Mapping the Ionosphere Using GPS at the Center for Orbit Determination (CODE), presentation held at the University of New Brunswick, Fredericton, New Brunswick, Canada, May 17, 1996.
- Schaer, S. (1997), How to use CODE's Global Ionosphere Maps, unpublished paper, Astronomical Institute, University of Berne, May 1997.
- Schaer, S. (1998a), CODE's Global Ionosphere Maps (GIMs), <http://www.cx.unibe.ch/aiub/ionosphere.html>, automatically updated WWW site.
- Schaer, S. (1998b), Towards an IGS Combined Ionosphere Product, in *IGS 1997 Annual Report*, pp. 28–29, IGS Central Bureau, JPL, Pasadena, California, USA.
- Schaer, S. and J. Feltens (1998), Terms of Reference for the IGS Ionosphere Working Group, *IRI News*, 5(3), 2–5, September 1998.
- Schaer, S., G. Beutler, L. Mervart, M. Rothacher, and U. Wild (1995), Global and Regional Ionosphere Models Using the GPS Double Difference Phase Observable, in *Proceedings of the IGS Workshop on Special Topics and New Directions*, edited by G. Gendt and G. Dick, pp. 77–92, GFZ, Potsdam, Germany, May 15–18, 1995.
- Schaer, S., G. Beutler, M. Rothacher, and T. A. Springer (1996a), Daily Global Ionosphere Maps Based on GPS Carrier Phase Data Routinely Produced by the CODE Analysis Center, in *Proceedings of the IGS Analysis Center Workshop, Silver Spring, Maryland, USA*, edited by R. E. Neilan *et al.*, pp. 181–192, IGS Central Bureau, JPL, Pasadena, California, USA, March 19–21, 1996.

- Schaer, S., M. Rothacher, and G. Beutler (1996b), Mapping the Deterministic and Stochastic Component of the Ionosphere Using GPS, *EOS Transactions of the AGU 1996 Fall Meeting*, 77(46), 142.
- Schaer, S., M. Rothacher, and G. Beutler (1996c), Global Ionosphere Maps Based on GPS Carrier Phase Data from the IGS Network Produced by the CODE Analysis Center, *EOS Transactions of the AGU 1996 Spring Meeting*, 77(17), 71.
- Schaer, S., W. Gurtner, and J. Feltens (1998a), IONEX: The IONosphere Map EXchange Format Version 1, February 25, 1998, in *Proceedings of the IGS Analysis Center Workshop*, edited by J.M. Dow *et al.*, pp. 233–247, ESA/ESOC, Darmstadt, Germany, February 9–11, 1998, format specifications available at <ftp://igscb.jpl.nasa.gov/igscb/data/format/ionex1.ps>.
- Schaer, S., G. Beutler, and M. Rothacher (1998b), Mapping and Predicting the Ionosphere, in *Proceedings of the IGS Analysis Center Workshop*, edited by J.M. Dow *et al.*, pp. 307–318, ESA/ESOC, Darmstadt, Germany, February 9–11, 1998.
- Schildknecht, T., G. Beutler, W. Gurtner, and M. Rothacher (1990), Nanosecond GPS Time Transfer Using Precise Geodetic Processing Techniques, in *Proceedings of the ION GPS-90*, pp. 149–157.
- Seeber, G. (1993), *Satellite Geodesy: Foundations, Methods, and Applications*, de Gruyter, ISBN 3-11-012753-9.
- SIDC (1998), Sunspot Index Data Center, Brussels, Belgium, <http://www.oma.be/KSB-ORB/SIDC/> or <ftp://ftpserver.oma.be/pub/astro/sidcdata/>.
- Spoelstra, T. A. T. (1992), The Ionosphere as a Refractive Medium, in *Proceedings of Symposium on Refraction of Transatmospheric Signals in Geodesy*, pp. 69–76, The Hague, The Netherlands, May 19–22, 1992.
- Springer, T. A. (1998), *Positioning, Timing, and Ranging Using the Global Positioning System*, Ph.D. thesis, Astronomical Institute, University of Berne, in preparation.
- Springer, T. A., W. Gurtner, M. Rothacher, and S. Schaer (1997), EUREF Activities at the CODE Analysis Center, in *Proceedings of the 4th International Seminar on GPS in Central Europe*, Warsaw University of Technology, Warsaw, Poland, May 7–9, 1997.
- Teunissen, P. J. G. (1995), The Least-Squares Ambiguity Decorrelation Adjustment: A Method for Fast GPS Integer Ambiguity Estimation, *Journal of Geodesy*, 70, 65–82.
- Teunissen, P. J. G., and A. Kleusberg (eds.) (1998), *GPS for Geodesy*, Springer, ISBN 3-540-63661-7.



- Wanninger, L. (1994), *Der Einfluss der Ionosphäre auf die Positionierung mit GPS*, Ph.D. thesis, University of Hanover, Germany, Wissenschaftliche Arbeiten der Fachrichtung Vermessungswesen der Universität Hannover, Nr. 201.
- Warnant, R. (1996), *Etude du comportement du Contenu Eletronique Total et ses irrégularitiés dans une région de latitude moyenne, Application aux calculs de positions relatives par le GPS*, Ph.D. thesis, Royal Observatory of Belgium, Brussels, Belgium.
- Wells, D. E., N. Beck, D. Delikaraoglu, A. Kleusberg, E. Krakiwsky, G. Lachapelle, R. Langley, M. Nakiboglu, K. P. Schwarz, J. Transquilla, and P. Vanicek (1987), *Guide to GPS Positioning*, Canadian GPS Associates, ISBN 0-920-114-73-3.
- Wild, U. (1993), Ionosphere and Ambiguity Resolution, in *Proceedings of the 1993 IGS Workshop*, edited by G. Beutler and E. Brockmann, pp. 361–369, AIUB, Berne, Switzerland, March 25–26, 1993.
- Wild, U. (1994), *Ionosphere and Geodetic Satellite Systems: Permanent GPS Tracking Data for Modelling and Monitoring*, Vol. 48 of *Geodätisch-geophysikalische Arbeiten in der Schweiz*, Schweizerische Geodätische Kommission, Ph.D. thesis.
- Willis, P., G. Beutler, W. Gurtner, G. Hein, R. Neilan, and J. Slater (1998), IGEX: International GLONASS Experiment, Scientific Objectives and Preparation, *Advances in Space Research*, in press.
- Wilson, B. D., and A. J. Mannucci (1993), Instrumental Biases in Ionospheric Measurements, in *Proceedings of the ION GPS-93*, Salt Lake City, Utah, USA, September 22–24, 1993.
- Wilson, B. D., A. J. Mannucci, and C. D. Edwards (1995), Subdaily Northern Hemisphere Ionospheric Maps Using an Extensive Network of GPS Receivers, *Radio Science*, *30*, 639–648.
- Wübbena, G. (1985), Software Developments for Geodetic Positioning with GPS Using TI-4100 Code and Carrier Measurements, in *Proceedings of the First International Symposium on Precise Positioning with the Global Positioning System*, Rockville, Maryland, USA.
- Yunck, T. P., and W. G. Melbourne (1995), Spaceborne GPS for Earth Science, in *GPS Trends in Precise Terrestrial, Airborne, and Spaceborne Applications*, IAG Symposium No. 115, edited by G. Beutler *et al.*, pp. 113–122, Boulder, Colorado, USA, July 3–4, 1995, ISBN 3-540-60872-9.



# Curriculum vitae

Name: Stefan Schaer

Geburtsdatum: 9. Juni 1965

Geburtsort: Bern

Heimatort: Trubschachen BE

1972–1976 Primarschule in Bern

1976–1981 Sekundarschule in Bern

1978–1979 Untergymnasium in Bern

1981–1985 Lehre als Vermessungszeichner beim Ingenieur- und Vermessungsbüro Luder und Perrochon in Bern, Berufsschule in Zürich

1982–1985 Berufsmittelschule in Bern

1985–1989 Studium an der Abteilung Vermessungswesen der Ingenieurschule beider Basel (IBB) in MuttENZ BL, Diplomarbeit über *Qualitätssicherung im Waggonbau mit berührungslosen 3-D-Messsystemen*, Abschluss als dipl. Vermessungsingenieur HTL

1988 Ausbildung zum Artillerie-Offizier

1989–1994 Studium an der Philosophisch-naturwissenschaftlichen Fakultät der Universität Bern im Hauptfach Astronomie und in den Nebenfächern Physik und Mathematik, Diplomarbeit über *Stochastische Ionosphärenmodellierung beim Rapid Static Positioning mit GPS*, Abschluss als Diplom-Astronom

1992–1994 Hilfsassistent am Astronomischen Institut der Universität Bern

1995–1998 Doktorand am Astronomischen Institut der Universität Bern unter der Leitung von Prof. Dr. Gerhard Beutler

